Measurements of Atmospheric Ozone, NO_2, OClO, and BrO at 80°N using UV-Visible Spectroscopy

by

Cristen Luna Frith Adams

A thesis submitted in conformity with the requirements
for the degree of Doctor of Philosophy

Graduate Department of Physics
University of Toronto

Measurements of Atmospheric Ozone, NO_2, OClO, and BrO at 80°N using UV-Visible Spectroscopy

Cristen Luna Frith Adams

Doctor of Philosophy

Graduate Department of Physics
University of Toronto

2012

Abstract

The motivation for this thesis was to study chemical and dynamical processes in the Arctic stratosphere, using data from two ground-based spectrometers (GBSs). The GBSs took atmospheric trace gas measurements at the Polar Environment Atmospheric Research Laboratory (PEARL), which is located at Eureka, Nunavut, Canada (80.05°N, 86.42°W) and operated by the Canadian Network for the Detection of Atmospheric Change. The University of Toronto GBS took measurements at Eureka on a campaign basis from 1999-2011. The PEARL-GBS was installed permanently at Eureka in 2006 and has taken measurements during the sunlit part of the year since then.

GBS and other ground-based ozone and NO_2 column measurements were compared with Atmospheric Chemistry Experiment (ACE) and Optical Spectrograph and Infra-Red Imaging System (OSIRIS) satellite measurements above Eureka. Ozone from all instruments agreed within 9.2%, while NO_2 from most instruments, including the GBS, agreed to within 20%.

On 1 August 2008, a solar eclipse of 98% totality passed over Eureka. GBS NO_2 increased to $1.84^{+0.12}_{-0.43}$ times normal levels. This agrees with a ratio of 1.91 that was calculated using a photochemical model, adjusted for reduced sunlight during the eclipse.

In spring/winter 2011, up to 47% (250 DU) ozone loss was calculated using GBS data and modeled passive ozone. This was the largest ozone loss in the 11-year GBS measurement record. GBS OClO was elevated, indicating chlorine activation and NO_2 was low, suggesting denitrification. GBS, satellite, and chemical transport model data were used to investigate the

2011 vortex breakup. NO_x transport led to middle-stratosphere ozone loss within an anticyclone. Furthermore, isolated, or "frozen-in", vortex and lower-latitude airmasses were observed following the vortex breakup.

Stratospheric BrO was retrieved from spring 2008 GBS zenith-sky measurements, using an optimal estimation technique. GBS BrO was compared with OSIRIS and Ozone Monitoring Instrument (OMI) satellite data. Discrepancies are partly attributed to bromine explosions in the boundary layer. New off-axis GBS measurements taken in spring 2010 are sensitive to boundary layer bromine. The combination of GBS stratospheric and tropospheric BrO measurements will be useful for future estimates of the Arctic bromine budget.

Acknowledgments

I've been lucky to work (and take coffee breaks) with so many lovely people throughout my PhD. Thanks to Kim Strong for guiding me through a really fun PhD project – I'm so glad that I ended up in your research group. Annemarie Fraser (aka GBS Expert of the Universe), thanks for answering my endless spectrometer questions for the past few years. Thanks also to Chris McLinden, who contributed to so many parts of this thesis. Clive Midwinter spent hours with me on the roof of the physics building and at Eureka, working on suntracker assembly and calibration – I'm grateful that I got to work with him.

The CINDI campaign in the Netherlands was a great learning experience – thanks to the many scientists who gave me advice on instrumentation and data analysis. Jennifer Hains, Mark Kroon and Ankie Piters did a great job of organizing the campaign. Thanks Maryam Akrami for working with me on all aspects of this campaign and for being a great travel-buddy.

My time at Eureka was amazing: wolf and muskox sightings, -40°C disk golf, walks to the 80°N sign, bear spray mishaps, dance parties, Easter rose-rock hunts, terrible movies, sublimation baseball, girls' nights, hilarious Wii canoe races, ptarmigans on blacktop mountain, sea-ice hockey... Thanks to everyone who's a part of these memories. I appreciate the Eureka station staff for making me feel welcome (and for keeping the dessert fridge full – chocolate mousse!). Thanks also to Jim Drummond and Kaley Walker for making these Arctic campaigns possible.

My spectrometers have always managed to break down in new and creative ways. I'm so grateful the people who have helped me trouble-shoot these problems – this, I guess, includes everyone that has ever been on campaign with me. In particular, I'd like to thank Bec Batchelor, Volodya Savastiouk, Tom McElroy, Pierre Fogal, Paul Loewen, Joseph Mendonca and Yan Tsehtik. I also appreciate all the PEARL operators who have babysat my spectrometers at Eureka, especially, Ashley Harrett, Alexei Khmel, Keith MacQuarrie, Oleg Mikailov, and Matt Okraszewski who have all spent hours in the GBS hatches. I wouldn't have much of a dataset without you.

Thanks to Tara Cunningham and Ashley Kilgour for including me in science outreach projects. Thank you also to the communities of Grise Fiord and Iqaluit for welcoming us into your classrooms.

Back in Toronto, I have also had a whole lot of support. Suri Like, Dan Weaver, and Boris Pavlovic have all contributed to the work presented in this thesis. Thanks also to Ana Sousa and Krystyna Biel – I don't think that a single week went by that I didn't pester you for something! Xiaoyi Zhao, thanks for taking over the spectrometers (despite their eccentricities)!

Thank you to Robyn Schofield and Kelly Chance for having me visit and taking the time to teach me about your BrO retrievals. Thank you also to everyone else who has provided me with advice, data, and software (and answered all of my follow-up questions). This includes (but is certainly not limited to!): Paul Kushner, Jon Abbatt, Dylan Jones, Paul Chen, Ashley Jones, Melissa Gervais, Felicia Kolonjari, Yonggang Liu, Robert Field, Thomas Walker, Rodica Lindenmaier, Florence Goutail, Andrea Pazmino, Richard Mittermeier, Gloria Manney, William Daffer, Markus Rex, Susan Strahan, Rolf Werner, Vasil Umlenski, Thomas Kurosu, Caroline Fayt, Michel Van Roozendael, Francois Hendrick, Doug Degenstein, Nick Lloyd, Chris Roth, Martyn Chipperfield, Sunny Choi, Wuhu Feng ...

Finally, thank you to everyone who distracted me from my work: the particle physicists for the "invited speaker" lunches, the basement-dwellers for giving me a social life on weekends, the GSU-ers, and those of you who were always willing to run out for a coffee. Mom, Dad, Pat, and Grandma, and the rest of my family and friends at home, thanks for all your support and giving me a break from physics! Finally, Brendan – our years in Toronto were fantastic and I look forward to our life together.

Table of Contents

List of Tables

List of Figures

List of Appendices

List of Acronyms

ACE	Atmospheric Chemistry Experiment
ACE-FTS	Atmospheric Chemistry Experiment Fourier Transform Spectrometer
ACE-MAESTRO	Atmospheric Chemistry Experiment Measurements of Aerosol Extinction in the Stratosphere and Troposphere
AIRS	Atmospheric Infrared Sounder
AMF	airmass factor
ARCTAS	Arctic Research of the Composition of the Troposphere from Aircraft and Satellites
AStrO	Arctic Stratospheric ozone Observatory
CANDAC	Canadian Network for the Detection of Atmospheric Change
CCD	charge coupled device
CFC	chlorofluorocarbon
CINDI	Cabauw Intercomparison of Nitrogen Dioxide measuring Instruments
CMAM-DAS	Canadian Middle Atmosphere Model Data Assimilation System
CTM	Chemistry Transport Model
DMP	derived meteorological product
DOAS	differential optical absorption spectroscopy
DOD	differential optical depth
DOMINO	Derivation of OMI tropospheric NO_2
DSCD	differential slant column density
DU FTS	Denver University Fourier Transform Spectrometer
EP-flux	Eliassen-Palm flux
EqL	equivalent latitude
FrIAC	frozen-in anticyclone
FTIR	Fourier transform infrared spectrometer
FTS	Fourier transform spectrometer
FWHM	full width at half maximum
GBS	Ground-Based Spectrometer
GCOS	Global Climate Observing Initiative
GEM-BACH	Global Environmental Multiscale 52 stratospheric model with the online Belgium Atmospheric CHemistry package
GEOS-5	Goddard Earth Observing System-5
GMI	Global Modeling Initiative
GOME	Global Ozone Monitoring Experiment
GPIB	general purpose interface bin
ISA	Instruments S.A. / Jobin Yvon
LUT	look-up table
MAESTRO-G	Measurements of Aerosol Extinction in the Stratosphere and Troposphere-Ground
MANTRA	Middle Atmosphere Nitrogen TRend Assessment

MAX-DOAS	multi-axis differential optical absorption spectroscopy
MCT	mercury cadmium telluride
MERRA	Modern Era Retrospective-analysis for Research and Applications
MLS	Microwave Limb Sounder
MSC-FTS	Meteorological Service of Canada Fourier Transform Spectrometer
NDACC	Network for the Detection of Atmospheric Composition Change
NDSC	Network for the Detection of Stratospheric Change
OMI	Ozone Monitoring Instrument
OSIRIS	Optical Spectrograph and Infra-Red Imaging System
PARIS-IR	Portable Atmospheric Research Interferometric Spectrometer for the InfraRed
PEARL	Polar Environment Atmospheric Research Laboratory
PEARL-GBS	Polar Environment Atmospheric Research Laboratory Ground-Based Spectrometer
PSC	polar stratospheric cloud
PV	potential vorticity
RCD	reference column density
RMS	root mean square
SAOZ	System D'Analyse par Observations Zenethales
SCD	slant column density
SCIAMACHY	SCanning Imaging Absorption spectroMeter for Atmospheric CartograpHY
SLIMCAT	Single-Layer Isentropic Model of Chemistry and Transport
SPS	SunPhotoSpectrometer
sPV	scaled potential vorticity
SZA	solar zenith angle
TOMS	Total Ozone Mapping Spectrometer
UDP	User Datagram Protocol
UT FTS	University of Toronto Fourier Transform Spectrometer
UT-GBS	University of Toronto Ground-Based Spectrometer
VCD	vertical column density
VMR	volume mixing ratio
VSLS	very short-lived substances
WMO	World Meteorological Organization

1 Introduction

The Arctic is warming at the fastest rate in the world due to the amplification of climate change through feedbacks such as the albedo-ice effect [e.g., *Hansen et al.*, 2006]. In 2007, the Arctic sea-ice extent declined to record lows, which could not be explained by current models [*Comiso et al.*, 2008]. In 2011, sea-ice reached similar lows, as shown in Figure 1.1, and arguments are emerging that we are in a new regime of low sea-ice extent [*Melsheimer et al.*, 2011]. Meanwhile, in spring 2011, an ozone hole formed in the Arctic for the first time on record [*Manney et al.*, 2011]. This occurred because the stratosphere was more isolated and low temperatures were more long-lasting than any other year on record. Within the last decade, the Arctic stratosphere experienced the four warmest and the two coldest winters since the 1970s [*Manney et al.*, 2011 and references therein].

These changes, from sea-level to the middle atmosphere, involve complex interactions between dynamics, radiation and chemistry. In order to understand these interactions, measurements of many atmospheric components over a large altitude range are necessary. Eureka, Nunavut, Canada (80.05°N, 86.41°W) is an excellent location for Arctic atmospheric studies. Weather measurements have been taken at Eureka since 1947 and indicate a surface warming of 3.2°C from 1972-2007, with a rate of +0.88°C per decade [*Lesins et al.*, 2010]. In 2005, the Canadian Network for the Detection of Atmospheric Change (CANDAC) began to install a suite of instruments at the Polar Environment Atmospheric Research Laboratory (PEARL) at Eureka to measure atmospheric constituents and parameters from 0-100 km. Prior to this, Environment Canada hosted scientific instrumentation at the same location under the name Arctic Stratospheric Ozone observatory (AStrO).

From 1999 to the present, ozone and related trace gases were measured by UV-visible spectrometers at Eureka. Ozone is just one piece of the Arctic climate puzzle: on the basic level, tropospheric ozone encourages warming through the absorption of long-wave radiation, while stratospheric ozone has a slight cooling effect, as it prevents short-wave radiation from reaching the surface [*IPCC*, 2007]. However, at a closer inspection, changes in climate affect ozone and changes in ozone affect climate in a variety of ways. These interactions involve both chemical and dynamical effects in the troposphere and stratosphere.

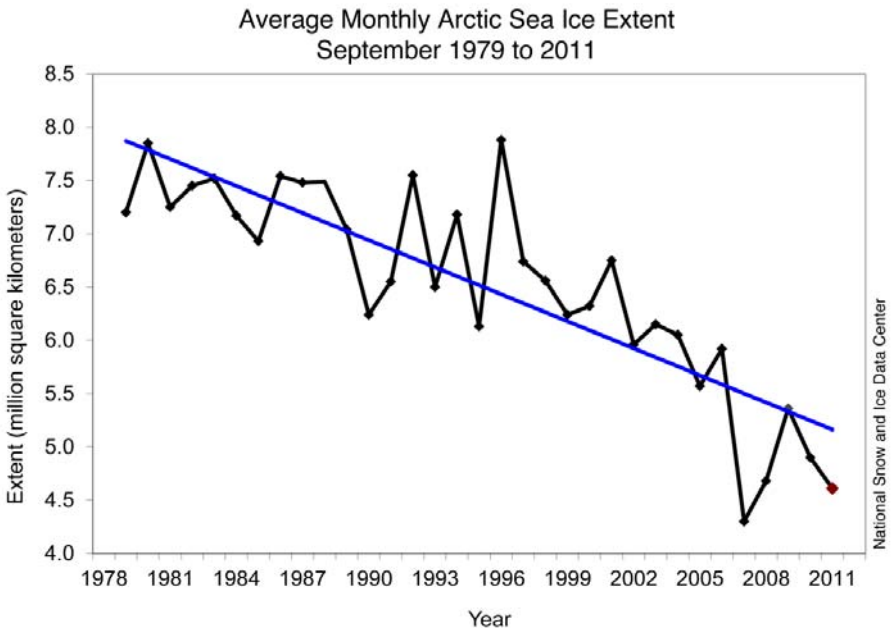

Figure 1.1: Monthly September ice extent for 1979 to 2011 shows a decline of 12.0% per decade. Figure from the National Snow and Ice Data Center [*NSIDC*, 2011].

The motivation behind this thesis is to better understand some of these mechanisms through the interpretation of ozone, NO_2, BrO and OClO columns in the Arctic measured by UV-visible spectroscopy. To produce an accurate and well-characterized dataset, instruments were tested and optimized, consistent data analysis and quality control techniques were implemented, and measurements were validated during a formal intercomparison campaign. Using the resulting 11-year dataset, the following scientific questions were addressed:

- How well do Atmospheric Chemistry Experiment (ACE) and Optical Spectrograph Infra-Red Imaging System (OSIRIS) satellite ozone and NO_2 measurements agree with ground-based measurements at Eureka?
- Is our current understanding of stratospheric odd-nitrogen photochemistry correct?
- How did the record 2011 Arctic ozone depletion compare to previous years?
- How much BrO is there above Eureka and how is it distributed in altitude?

This chapter introduces atmospheric ozone, with a focus on current understanding, open scientific questions, and UV-visible measurement techniques. Sections 1.1 and 1.2 discuss stratospheric and tropospheric ozone, respectively. The methodology behind the UV-visible measurement technique is described in Section 1.3. Section 0 provides an overview of long-term trace-gas monitoring networks and initiatives. Finally, an outline for this thesis, with a description of my contributions, is given in Section 1.5.

1.1 Stratospheric Ozone

Stratospheric ozone is essential to human life as it absorbs UV radiation that can cause cancer in humans and damage plants and crops. In 1974, catalytic cycles with chlorine were identified as a possible ozone sink [*Stolarski and Cicerone*, 1974]. In the same year, chlorofluorocarbons (CFCs) were identified as a source of active chlorine in the stratosphere and ozone depletion was predicted to occur roughly uniformly at all latitudes [*Molina and Rowland*, 1974]. Therefore, a sudden and enormous drop in ozone concentration above Halley Bay, Antarctica [*Farman et al.*, 1985a] surprised the scientific community. This severe ozone depletion, the so-called Antarctic ozone hole, was found to be caused by heterogeneous chemistry involving anthropogenic emissions of chlorine and bromine-containing species. In 1987, only two years after the discovery of the Antarctic ozone hole, the Montreal Protocol was signed to regulate emissions of ozone-depleting substances. Due to the long lifetimes of CFCs and other ozone-depleting substances in the stratosphere, the Antarctic ozone hole continues to form during late winter and early spring. Now, over twenty years after the Montreal Protocol, the severity of the ozone hole appears to be decreasing and we are entering a time of ozone recovery [e.g., *Newchurch et al.*, 2003; *Yang et al.*, 2006]. This section summarizes our current understanding of stratospheric ozone chemistry and dynamics.

1.1.1 Chemistry

Ozone depletion is typically associated with the dramatic Antarctic ozone hole. However, various catalytic cycles destroy ozone at all latitudes. While some of these cycles are part of the natural ozone balance, anthropogenic emissions of chlorine- and bromine-containing species, and N_2O enhance these cycles [e.g., *WMO*, 2011a]. Numerous catalytic cycles exist and are

reviewed in detail by *Jacob* [1999]. This section focuses on the processes which are most relevant to the polar regions.

In 1930, Chapman [1930] proposed a simple mechanism for ozone production and loss involving photochemical reactions between oxygen molecules (O_2), atomic oxygen (O), and ozone (O_3). Since atomic oxygen and ozone cycle between one another rapidly, they are often considered together as odd-oxygen or O_x. The Chapman Cycle was found to significantly over-predict ozone concentrations throughout much of the atmosphere.

Therefore, subsequent research identified catalytic ozone-depleting cycles via reactive families of hydrogen [*Bates and Nicolet*, 1950], nitrogen [*Crutzen*, 1970], chlorine [*Molina and Rowland*, 1974; *Stolarski and Cicerone*, 1974], bromine [*Wofsy et al.*, 1975; *Yung et al.*, 1980], and iodine [*Solomon et al.*, 1994]. Stratospheric hydrogen originates primarily from water vapour, which is transported from the troposphere. N_2O, produced both through natural processes in the biosphere and anthropogenic sources (e.g., agriculture), is the main contributor to reactive nitrogen. The stratospheric chlorine budget is made up mostly from anthropogenic sources, particularly CFCs. Stratospheric bromine originates approximately equally from anthropogenic sources, such as halons, and natural sources, such as methyl bromide emitted from the biosphere. Anthropogenic halogens (chlorine and bromine) are regulated under the Montreal Protocol as ozone-depleting substances. As halogen concentrations decrease and N_2O emissions increase, N_2O is becoming a significant contributor to anthropogenic ozone depletion [*Ravishankara et al.*, 2009]. Figure 1.2 shows the reaction rates for these various cycles when only gas phase chemistry is considered. Note that this figure does not apply to spring-time polar ozone depletion (e.g., the Antarctic ozone hole), which also involves heterogeneous chemistry.

Ozone loss in the middle stratosphere (~30 km) is dominated by reactive nitrogen, NO_x. NO_x comprises NO and NO_2, which cycle between one another on timescales of one minute via the following reactions:

$$NO + O_3 \rightarrow NO_2 + O_2 \tag{1.1}$$

$$NO_2 + h\nu \rightarrow NO + O \tag{1.2}$$

$$O + O_2 + M \rightarrow O_3 + M\,. \tag{1.3}$$

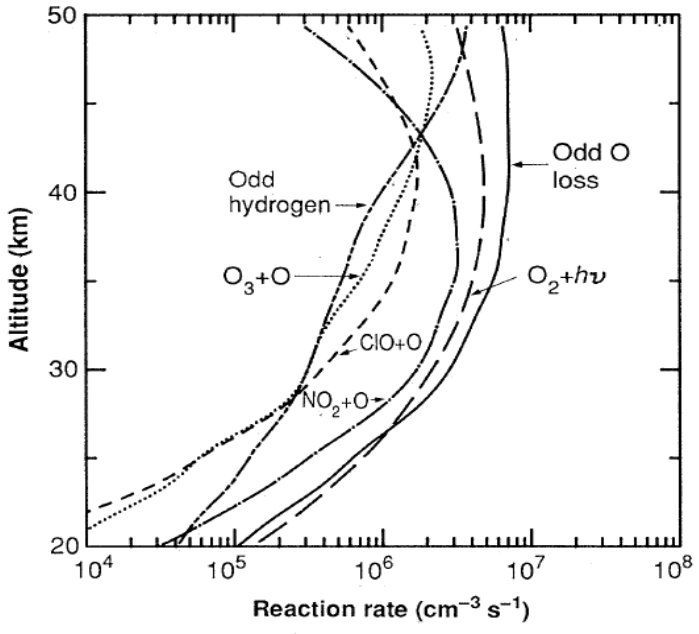

Figure 1.2: Daily average production and loss rates of O_x computed with a chemical model constrained with satellite measurements at 30°N. Heterogeneous chemistry, which is particularly significant in polar spring-time ozone depletion, is not considered. Figure from *McElroy and Salawitch* [1989].

There is no net O_x gain or loss through these processes. However, the following reaction can also occur

$$NO_2 + O \rightarrow NO + O_2 . \tag{1.4}$$

The combination of Equations 1.1 and 1.4, leads to net ozone loss

$$O_3 + O \rightarrow 2O_2 . \tag{1.5}$$

This catalytic cycle is terminated when NO_x is converted to reservoir species HNO_3 during the day and N_2O_5 overnight. Similar catalytic cycles exist for the reactive hydrogen, chlorine, bromine, and iodine families.

These reactions do not explain the Antarctic ozone hole. They require high concentrations of odd-oxygen, which are not available during polar spring, due to limited sunlight. Therefore, two

new mechanisms were proposed, both of which require high concentrations of ClO. One of these mechanisms involves the interaction between two ClO radicals [*Molina and Molina*, 1987]

$$ClO + ClO + M \rightarrow ClOOCl + M \quad (1.6)$$

$$ClOOCl + h\nu \rightarrow ClOO + Cl \quad (1.7)$$

$$ClOO + M \rightarrow Cl + O_2 + M \quad (1.8)$$

$$2 \times (Cl + O_3 \rightarrow ClO + O_2) \quad (1.9)$$

$$net: 2O_3 \rightarrow 3O_2 . \quad (1.10)$$

The other involves reactions between ClO and BrO [*McElroy et al.*, 1986; *Tung et al.*, 1986]

$$Cl + O_3 \rightarrow ClO + O_2 \quad (1.11)$$

$$Br + O_3 \rightarrow BrO + O_2 \quad (1.12)$$

$$BrO + ClO \rightarrow Br + Cl + O_2 \quad (1.13)$$

$$net: 2O_3 \rightarrow 3O_2 . \quad (1.14)$$

Typically, there is not enough ClO available for these reactions to proceed rapidly, due to chlorine deactivation via NO_2

$$ClO + NO_2 + M \rightarrow ClONO_2 + M . \quad (1.15)$$

Similarly, bromine is also sequestered by NO_2

$$BrO + NO_2 + M \rightarrow BrONO_2 + M . \quad (1.16)$$

High concentrations of ClO are possible in the lower stratosphere during polar spring since polar stratospheric clouds (PSCs) [*Solomon et al.*, 1986] can form from water and HNO_3 when temperatures drop below ~195 K. PSCs provide a surface on which chlorine reservoir species (HCl and $ClONO_2$) can be converted to active chlorine. Furthermore, PSC sedimentation

removes HNO_3 from the stratosphere. Since HNO_3 is a reservoir species for NO_2, this "denitrification" leads to low NO_2 concentrations. Therefore Equation 1.15 is suppressed and chlorine remains in its active form.

When chlorine is activated, OClO is produced via a pathway of the reaction between BrO and ClO [*Friedl and Sander*, 1989],

$$BrO + ClO \rightarrow OClO + Br . \quad (1.17)$$

The dominant sink for OClO is photolysis, which occurs rapidly. Therefore, OClO is diminished during the day.

1.1.1.1 Ozone, NO_2, BrO, and OClO

Ozone, NO_2, BrO and OClO can be measured by UV-visible spectrometers. The interplay between these species can be used to infer chlorine activation, ozone depletion, and denitrification [e.g., *Tétard et al.*, 2009]. In the middle stratosphere, NO_2 catalytically destroys ozone, while in the lower stratosphere, it deactivates chlorine, preventing ozone depletion. Since NO_2 has a short lifetime in the stratosphere, concentrations depend strongly on available sunlight, which varies greatly throughout the year in the Arctic. Therefore, it is essential to validate NO_2 measurements and photochemical models.

The concentration of OClO is determined by NO_2, BrO, and ClO. For solar zenith angle (SZA) < 90°, OClO increases linearly with ClO for fixed BrO concentrations and is therefore a good quantitative indicator of chlorine activation [*Schiller et al.*, 1990; *Schiller and Wahner*, 1996; *Sessler et al.*, 1996]. However, for SZA > 92°, OClO no longer has a linear relationship with ClO and therefore can only be used qualitatively [*Sessler et al.*, 1995].

Oetjen et al. [2011] compared the diurnal variation of ground-based OClO measurements to OClO from a photochemical stacked box model that was initialized with a chemical transport model. They found that the model qualitatively reproduced day-to-day variations in the measured OClO, but was systematically lower than the measurements, with worse agreement observed for larger SZAs and stronger chlorine activation. In an attempt to resolve these discrepancies, *Oetjen et al.* [2011] varied numerous model parameters within accuracy ranges given in the scientific literature. They found that the modeled OClO was most sensitive to

uncertainties in the ClOOCl absorption cross-section and the reaction rate of Equation 1.17. However, these parameter modifications did not reproduce the SZA-dependence of the bias between the model and the measurements. Therefore, *Oetjen et al.* [2011] concluded that the OClO measurements could not be explained by current knowledge of physical and chemical processing inside the vortex.

Although concentrations of bromine are much lower than those of chlorine, globally bromine has 45-64 times more potential for ozone destruction than chlorine per molecule [*WMO*, 2007; *Sinnhuber et al.*, 2009]. Atmospheric bromine nearly doubled due to emissions of methyl bromide and halons from 1980 to the late 1990s [*Montzka et al.*, 2003 and references therein]. Therefore, bromine is responsible for ~45% of Northern Hemisphere mid-latitude ozone reduction from 1980-2005 [*Sinnhuber et al.*, 2009]. Furthermore, the bromine-chlorine catalytic cycle causes up to half of Arctic spring-time ozone depletion [e.g., *Chipperfield and Pyle*, 1998]. There are many uncertainties in the bromine budget, as remote-sensing BrO measurements are difficult, due to the small size of the absorption features [e.g., *Aliwell et al.*, 2002] and uncertainties in the distribution between the troposphere and stratosphere [e.g., *Salawitch et al.*, 2010]. The contribution of very short-lived substances (VSLS), such as organic halogens emitted by biogenic processes in the tropical oceans, to the stratospheric bromine budget is not well understood [*WMO*, 2007 and references therein].

Salawitch et al. [2010] estimated the contribution of VSLS to the bromine budget with *in situ* tropospheric BrO measurements taken during the Arctic Research of the Composition of the Troposphere from Aircraft and Satellite (ARCTAS), Ozone Monitoring Instrument (OMI) satellite total column BrO measurements, and the Goddard Earth Observing System-5 (GEOS-5) assimilation initialized with various VSLS mixing ratios. As shown in Figure 1.3, OMI BrO total columns (x-axis) were plotted against *in situ* tropospheric BrO columns (black), and *in situ* tropospheric plus modeled stratospheric BrO columns for 0 ppt (green), 5 ppt (blue), and 10 ppt (red) of VSLS. They found that modeled stratospheric columns for 5-10 ppt of VSLS agreed best with the OMI measurements.

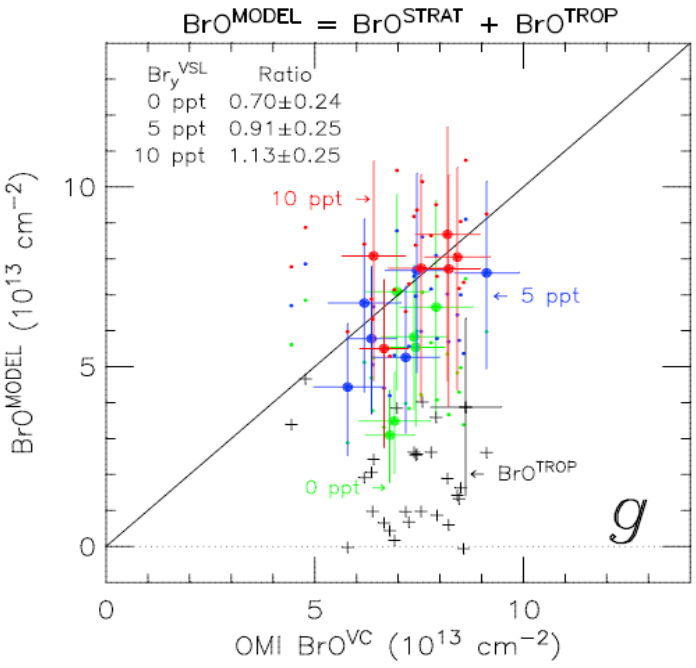

Figure 1.3: Scatter plot of spring 2008 OMI BrO total columns versus measured tropospheric BrO (black crosses) and measured tropospheric BrO plus modeled stratospheric BrO for 0 ppt (green), 5 ppt (blue), and 10 ppt (red) of VSLS. Tropospheric BrO is from ARCTAS *in situ* aircraft measurements. Modeled stratospheric BrO was calculated using CFC-12 from the GEOS-5 assimilation. For clarity, 1σ error is only shown for some of the data points. The 1-1 ratio is given by the black line and the average ratios of the modeled stratospheric plus measured tropospheric BrO over the OMI total column are indicated in black text. Figure from *Salawitch et al.* [2010].

1.1.2 Dynamics

Arctic ozone variability is governed primarily by ozone transport through the Brewer-Dobson circulation and temperatures inside the polar vortex, which determine whether PSCs form. This section provides an overview of stratospheric dynamics, based primarily on the review by *Shepherd* [2003].

Atmosphere flow tends to follow isentropes, or routes over which entropy is conserved. Potential temperature is defined as

$$\theta = T\left(\frac{P_o}{P}\right)^{R/c_P}, \tag{1.18}$$

where T and P are the temperature and pressure of the airmass, P_o is the pressure at sea-level, R is the gas constant of air, and c_p is the specific heat capacity at constant pressure. The potential temperature is the temperature that the air parcel would have if it were brought adiabatically to the reference pressure P_o for a dry ideal gas.

The middle atmosphere is stratified in entropy. Although the isentrope altitudes vary slightly with latitude, there is no adiabatic route for descent to the troposphere. Therefore air parcels tend to stay in the stratosphere for a long time.

The Brewer-Dobson circulation, proposed by *Brewer* [1949] and *Dobson* [1956], involves the zonal mean rise of air from the tropics, poleward transport, and descent in the extratropics. This circulation allows for the transport of trace gases, such as ozone and CFCs from the tropics [e.g., *Holton et al.*, 1995] and modulates Arctic ozone variability [e.g., *Tegtmeier et al.*, 2008]. The Brewer Dobson circulation is driven in the extrapropics by stationary planetary wavers propagating from the troposphere to the stratosphere. Since these planetary waves require westerly winds to propagate upward, the Brewer-Dobson circulation only occurs in the winter hemisphere, when the stratospheric polar vortex has formed.

The Brewer-Dobson circulation transports ozone-rich tropical air to the winter pole and ozone-poor air, from beneath the ozone maximum, away from the winter pole. Therefore, polar ozone concentrations increase over the winter. In the Northern Hemisphere, the Brewer-Dobson circulation is strengthened by planetary waves, which originate over large land masses and mountain ranges. Contrarily, in the Southern Hemisphere, limited topography leads to reduced Brewer-Dobson circulation. Therefore, more ozone is transported to the Arctic than Antarctica.

During winter, the polar region cools due to lack of sunlight and a large latitudinal temperature gradient forms. At the edge of this temperature gradient, a westerly flow, or winter jet develops. The region inside the winter jet is called the polar vortex and can host PSCs and active chlorine with low temperatures and dynamical isolation. As sunlight returns to the stratosphere in spring, the temperature gradient weakens and a final stratospheric warming occurs, breaking up the polar vortex.

Since planetary waves warm the stratosphere, the polar vortex is weaker in the Arctic than in Antarctica. Sudden stratospheric warmings (SSWs) [*Scherhag*, 1952] are an extreme example of the impacts of planetary waves on the polar vortex. They occur primarily in the Arctic and are described by, e.g., *Charlton and Polvani* [2007]. SSWs represent a major coupling between the troposphere and stratosphere, as they are driven by planetary waves originating in the troposphere and, in return, impact tropospheric dynamics. There are two types of SSWs: vortex splits, a division of the vortex into components of comparable size, and vortex displacements, the stretching of the vortex away from the pole. Vortex split events occur in 46% of SSWs and last up to 20 days longer than vortex displacement events [*Charlton and Polvani*, 2007].

The relative impacts of transport and chemistry on Arctic ozone variability are quantified by *Tegtmeier et al.* [2008]. They found that the dynamical supply of ozone via the Brewer-Dobson circulation is on the same order as chemical ozone loss, and both depend on planetary wave breaking in the stratosphere, as shown in Figure 1.4. This is because planetary wave breaking strengthens the Brewer-Dobson circulation and therefore increases the dynamical supply of ozone. On the other hand, planetary waves perturb and warm the vortex, preventing PSC formation and chemical ozone depletion.

1.1.3 Climate Change and Ozone Recovery

The 2010 World Meteorological Organization (WMO) Ozone Assessment [*WMO*, 2011a] predicts that the ozone column will increase over the next few decades and recover mid-century due to the decline of ozone-depleting substances. This promising forecast points to the success of the Montreal Protocol and its amendments. However, variability and uncertainty is introduced via, e.g., natural variability, the solar cycle, volcanic eruptions, trace gas emissions, and the impact of climate change on planetary waves and temperatures [e.g., *Weatherhead and Andersen*, 2006; *WMO*, 2011a]. This section reviews some of the mechanisms by which climate, stratospheric dynamics and ozone are coupled. For more comprehensive reviews, see, e.g., *Shepherd* [2007] or *WMO* [2011a].

Stratospheric ozone has had a small cooling effect on climate [*IPCC*, 2007]. However, many of the ozone-depleting substances controlled under the Montreal Protocol (e.g., CFCs and halons) have enormous global warming potentials, which are ~1000-10000 times greater than the warming potential of CO_2 [*IPCC*, 2007]. Therefore, through regulation of ozone-depleting

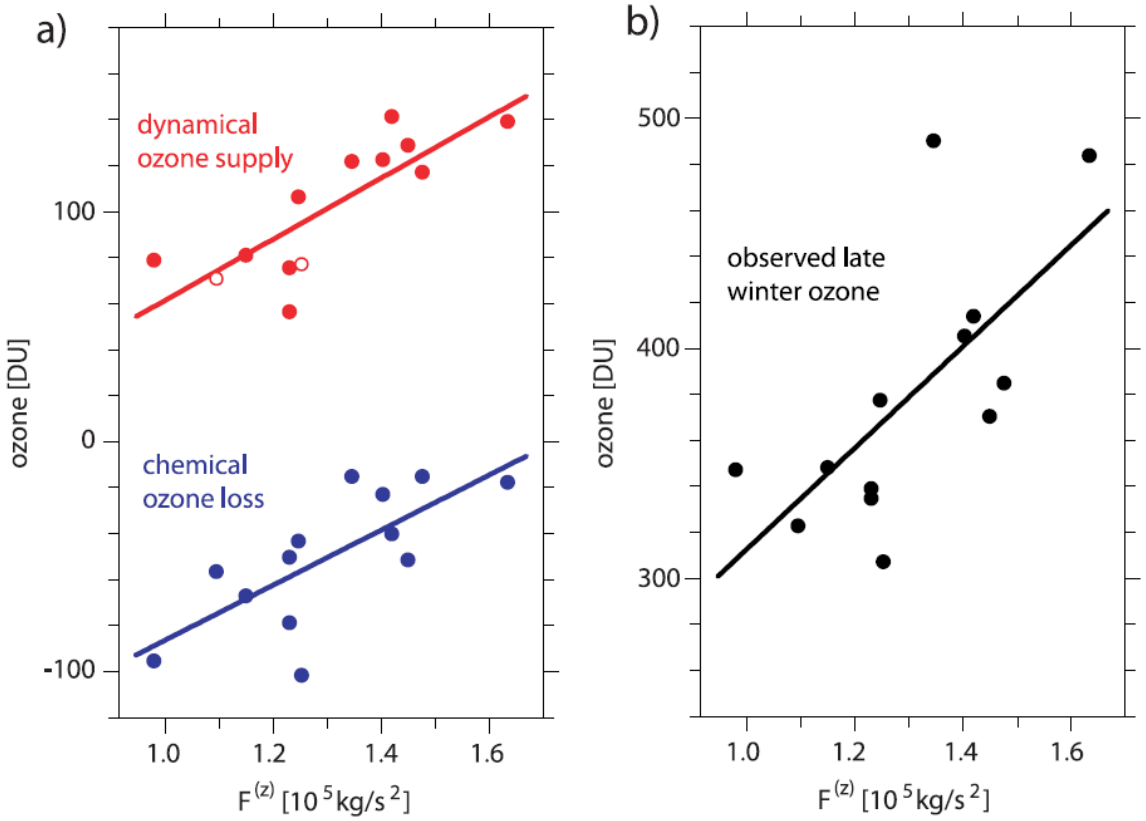

Figure 1.4: Correlation between the Eliassen Palm flux (EP-flux – a measure of planetary waves entering the stratosphere) and ozone (a) from dynamical supply (red) and chemical loss (blue) and (b) observed in winter ozone (black). Dynamical supply was calculated using a vortex-averaged diabatic decent method. Chemical loss and observed ozone were derived from vortex ozonesonde measurements taken throughout the Arctic. EP-flux was calculated from European Centre for Medium-Range Weather Forecasts (ECMWF) ERA40 reanalyses. Data are shown for winters 1991/1992 to 2003/2004. Figure from *Tegtmeier et al.* [2008].

substances, the Montreal Protocol has reduced 10 Gt of CO_2-equivalent greenhouse gases, which is five times larger than the 2008-2012 restrictions under the Kyoto Protocol [*WMO*, 2011a]. Since halogen emissions were reduced under the Montreal Protocol, anthropogenic N_2O, which is also a greenhouse gas, is now being recognized as a major ozone-depleting substance [*Ravishankara et al.*, 2009].

Randel et al. [2009] detected a cooling trend in the lower stratosphere since 1960 in satellite, radiosonde, and lidar data. The stratosphere is heated by ozone through absorption of short-wave

UV radiation and can be cooled by emitters of long-wave radiation, such as CO_2. Therefore, stratospheric cooling is consistent with increases in greenhouse gas concentrations, particularly CO_2 [e.g., *IPCC*, 2007]. Lower temperatures slow the reaction rates of homogeneous catalytic ozone depletion cycles and therefore are expected to reduce mid-latitude ozone depletion. Furthermore, *Randel et al.* [2009] measured a rapid rate of cooling in Antarctica, which is attributed to the ozone hole limiting the absorption of short-wave radiation. Furthermore, in the second half of the 21st century, the Antarctic ozone hole is expected to have 2-3 times more impact than greenhouse gas emissions on Southern Hemispheric tropospheric circulation [*Polvani et al.*, 2011]. In the Arctic, some stratospheric cooling trends were identified, but large year-to-year variability introduces uncertainties [*Randel et al.*, 2009].

There is currently no evidence that Arctic ozone depletion influences climate [*WMO*, 2011a], however climate change appears to impact Arctic ozone. The dynamical variability in the Arctic stratosphere is increasing, with warm winters getting warmer and cold winters getting colder: the four warmest and the two coldest winters since the 1970s have occurred within the last decade [e.g, *Rex et al.*, 2004; *Manney et al.*, 2011]. This variability has not been fully captured in models [e.g., *WMO*, 2011a]. Figure 1.5, taken from *Manney et al.* [2011], shows dynamical parameters related to the Arctic vortex for 1979-2011. The polar vortex in early spring 2011 was stronger than any other year on record in the Arctic or Antarctica (panel a). Furthermore, a larger fraction of the vortex was below the PSC formation temperature than any other year in the Arctic (panel b). These conditions allowed the first ever Arctic ozone hole to form.

Climate models predict that the strength of the Brewer-Dobson circulation will increase throughout the twenty-first century due to an increase in planetary wave activity [e.g., *Rind et al.*, 1998]. Enhanced Brewer-Dobson circulation is expected to modify life-times of trace gases and to change the distribution of ozone, increasing (decreasing) concentrations in the Arctic (tropics) [e.g., *WMO*, 2011a]. Therefore, Arctic ozone recovery is expected to occur from 2020-2035, with columns increasing beyond pre-1960 values later in the century [*Eyring et al.*, 2010; *WMO*, 2011a]

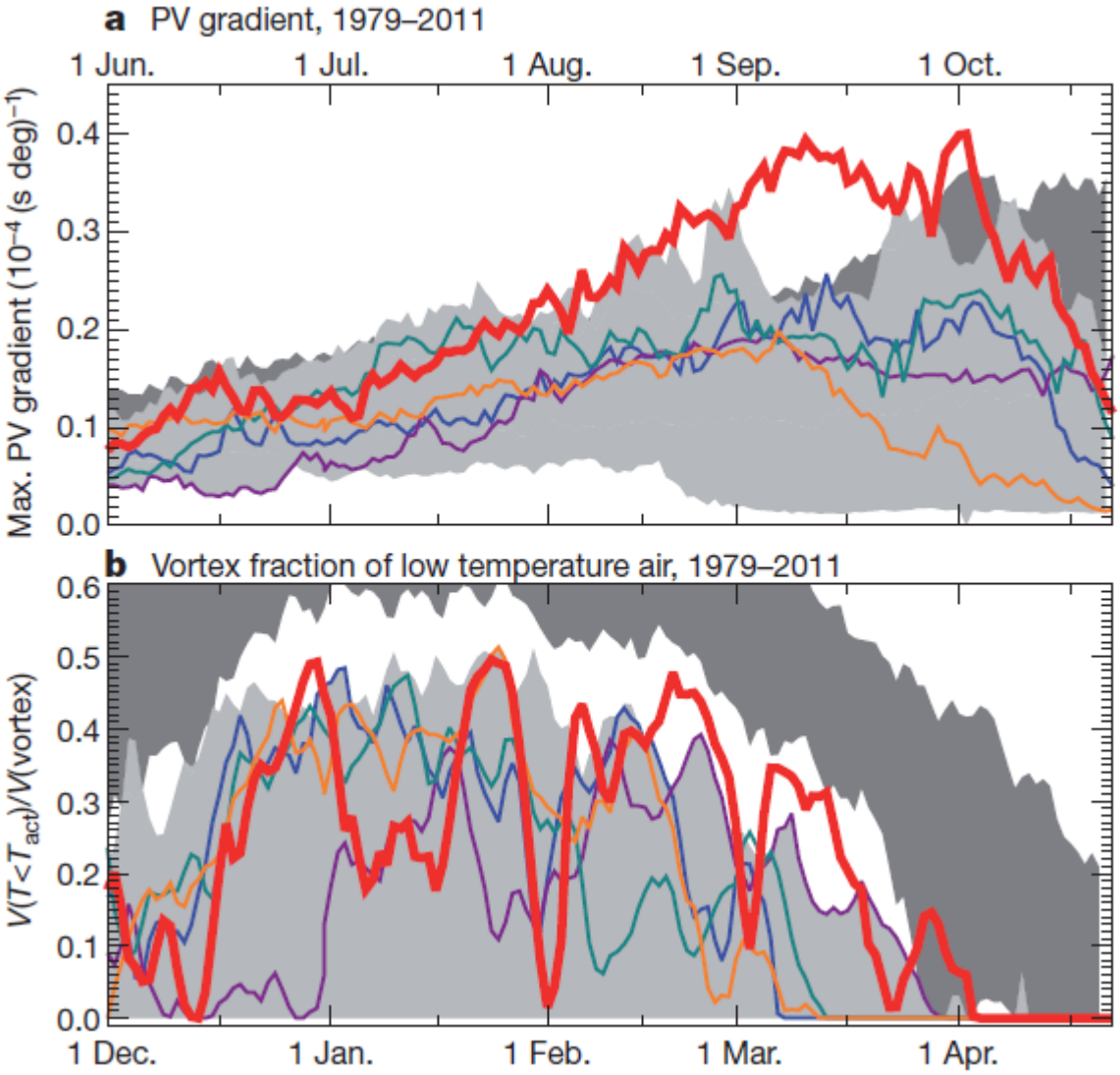

Figure 1.5: Winter/spring conditions in the Arctic lower stratosphere for 1979-2011. (a) Maximum potential vorticity (PV – see Appendix A) gradient at 460 K potential temperature (measure of vortex strength) and (b) fraction of vortex volume which is below the chlorine activation temperature threshold for altitudes 390-550 K for December - April (lower x-axis). Shading shows ranges for 1979-2010 in the Arctic (dark grey) and the Antarctic shifted by six months (light grey, upper x-axis). Winters with large ozone depletion are shown in colour: 2010-2011 (red), 2004-2005 (orange), 1999-2000 (green), 1996-1997 (purple), and 1995-1996 (blue). Figure adapted from *Manney et al.* [2011].

1.2 Tropospheric Ozone

Tropospheric ozone is a toxic greenhouse gas. An overview of tropospheric chemistry is given in *Jacob* [2000]. The majority of tropospheric ozone is created when hydrocarbons are oxidized to form peroxy radicals. The peroxy radicals convert NO to NO_2, which, in turn, produces ozone through photolysis. Hydrocarbons have natural sources, as well as anthropogenic sources, such as combustion, agriculture, and biomass-burning, while NO_x is primarily emitted by fossil fuel combustion. Therefore tropospheric ozone concentrations have increased, with higher concentrations near urban and industrial sources, leading to an estimated radiative forcing of $+0.35\pm0.15$ W/m^2 [*IPCC*, 2007].

1.2.1 The Arctic Boundary Layer

Micrometeorology can have a large impact on boundary layer composition through mixing, transport, and temperature. A review of the Arctic boundary layer is given in *Anderson and Neff* [2008]. The boundary layer is the region of the atmosphere that is directly influenced by the surface. A convective boundary layer can occur when the potential temperature at the surface is larger than the potential temperature higher in the atmosphere. Over polar night, a strong "temperature inversion" forms in the Arctic lower troposphere. This occurs because the surface cools due to lack of sunlight, as well as long-wave emissions. Furthermore, sunlight is reflected away from the surface by snow and ice. Therefore, the temperature at the surface becomes colder than at ~1-2 km altitude, leading to a stable boundary layer and a temperature inversion. Note that although a temperature inversion leads to a stable boundary layer, the inversion altitude does not necessarily represent the top of the boundary layer.

Above Eureka, a strong temperature inversion forms from January to March [*Lesins et al.*, 2010], with weaker inversions also observed in the fall and spring. Since stratified boundary layers prevent surface heat from being transported throughout the tropospheric column, warming is enhanced at the surface. Therefore, the temperature inversion gradient observed in the Eureka boundary layer has weakened since 1980 [*Lesins et al.*, 2010].

1.2.2 Bromine Explosions

Around the same time as the discovery of the Antarctic ozone hole, scientists became aware of severe ozone depletion episodes in the Arctic troposphere [*Bottenheim et al.*, 1986; *Barrie et al.*, 1988]. These events have since been linked to extremely high concentrations of bromine and are reviewed by *Simpson et al.* [2007b]. "Bromine explosions" proceed via the following sequence of reactions

$$HOBr + Br^- + H^+ \xrightarrow{mp} H_2O + Br_2 \quad (1.19)$$

$$Br_2 + h\nu \rightarrow 2Br \quad (1.20)$$

$$2(Br + O_3 \rightarrow BrO + O_2) \quad (1.21)$$

$$2(BrO + HO_2 \rightarrow HOBr + O_2) \quad (1.22)$$

$$net: H^+ + Br^- + 2HO_2 + 2O_3 \xrightarrow{mp,h\nu} HOBr + H_2O + 2O_2 . \quad (1.23)$$

Note that *mp* stands for multiphase. This is an autocatalytic cycle, meaning that the end product, HOBr, acts as a catalyst. This leads to exponential conversion of inactive bromine (Br^-) to active bromine (HOBr). As bromine concentrations increase, ozone is depleted rapidly. These reactions only proceed when sunlight is available. The surface on which Equation 1.19 proceeds is unknown. Studies have suggested sea-salt deposited on the snow-pack [*McConnell et al.*, 1992], acidified sea salt aerosol [*Vogt et al.*, 1996], brines concentrated on frost flowers which form on young sea-ice [*Rankin et al.*, 2002; *Kaleschke et al.*, 2004], snow and ice contaminated with sea salts [*Simpson et al.*, 2007a], sea-salt aerosol [*Yang et al.*, 2008], and bromine within blowing snow [*Jones et al.*, 2009].

Other halogens have also been observed in polar boundary layers. Elevated IO is linked to iodine deposits in coastal Antarctica [e.g., *Saiz-Lopez et al.*, 2007a; *Schonhardt et al.*, 2008; *Friess et al.*, 2010]. In the Arctic, boundary layer iodine has never been detected, but chlorine species have been measured during ozone depletion episodes [*Pohler et al.*, 2010].

High bromine concentrations are typically measured in airmasses which have had recent contact with young sea-ice [e.g., *Friess et al.*, 2004; *Simpson et al.*, 2007a; *Gilman et al.*, 2010; *Pohler et al.*, 2010], suggesting that sea-ice processes play a role in Equation 1.19. Generally ozone depletion episodes occur when the boundary layer is stable [e.g., *Wagner et al.*, 2001; *Friess et al.*, 2004], but have also been observed during blizzard conditions [e.g., *Jones et al.*, 2009]. Furthermore, elevated bromine has been observed at higher altitudes and inland, likely through advection [*Hausmann and Platt*, 1994; *Honninger and Platt*, 2002]. Ozone depletion episodes typically occur in spring, due to temperature, snow, and ice cycles.

Tarasick and Bottenheim [2002] studied ozonesonde records at various stations in the Arctic and Antarctica in order to identify ozone depletion episodes. When temperatures were below -20°C, these episodes occurred frequently at Eureka and other High Arctic locations. Furthermore, they found that the frequency of these events has increased since the 1960s. This may be due to increases in young sea-ice coverage, due to climate change. If the Arctic becomes ice-free in spring and summer, *Voulgarakis et al.* [2009] suggest that tropospheric ozone will increase by up to 50-60% in the Arctic and 20% at mid-latitudes due to the elimination of bromine chemistry.

Bromine explosions are connected to the stratospheric bromine budget as a possible measurement background. Satellite measurements of elevated total column BrO, or "BrO hotspots", have typically been attributed to ozone depletion episodes [e.g., *Chance*, 1998]. Recently, *Salawitch et al.* [2010] found that satellite "BrO hotspots" can also be caused by stratospheric bromine enhancements when the tropopause is low (~5 km). Therefore, ground-based measurements of stratospheric and tropospheric BrO are necessary for the interpretation of satellite total columns.

1.3 Methodology

Differential optical absorption spectroscopy (DOAS) is a technique for studying atmospheric composition using UV-visible spectroscopy. DOAS was developed in the 1970s [*Noxon*, 1975; *Platt et al.*, 1979] and is described in detail by *Platt and Stutz* [2008]. This section explains DOAS methodology for zenith-scattered sunlight, which is primarily sensitive to the stratosphere. Alternative viewing geometries for enhanced tropospheric sensitivity are also presented.

1.3.1 Radiation in the Atmosphere

Sunlight incident at the top of the atmosphere has a spectrum which is determined by the temperature and composition of the sun. The bulk of this sunlight is at visible wavelengths (~380-760 nm). As sunlight travels through the atmosphere, it can be absorbed and scattered by molecules and aerosols. The DOAS technique relies on both of these processes. Sunlight takes a path through the atmosphere that is determined by scattering processes. Along this path, sunlight is absorbed by trace gases, which modify the incident solar spectrum. Therefore, the amount of a trace gas along the path the sunlight takes to the instrument, or a slant column density (SCD), can be determined.

Molecules absorb light at specific wavelengths, determined by quantized electronic, rotational, and vibrational states. An absorption cross-section is the unique "fingerprint" of a molecule. It quantifies a molecule's propensity to absorb light versus wavelength and can be measured in controlled laboratory experiments. Cross-sections can be then be applied to solar absorption measurements in order to determine the SCD.

For measurements of scattered sunlight, the route that light takes through the atmosphere depends on the scattering particles. Elastic scattering processes, for which wavelength does not change, dominate in the atmosphere and include Rayleigh, Lorenz-Mie, and geometrical scattering [*Liou*, 2002]. Rayleigh scattering occurs when the wavelength is much larger than the particle size. After Rayleigh scattering, light which is perpendicular to the incident beam is polarized, while light scattering forward and backward is partly polarized. Lorenz-Mie scattering occurs when the wavelength and the particle size are approximately the same, and, involves preferential forward scattering. Finally, geometrical scattering occurs when the particle radius is much larger than the wavelength. This type of scattering is also preferentially in the forward direction, with lobes caused by reflection, refraction, and diffraction of light around the particle. Raman scattering, or inelastic scattering, occurs when sunlight is absorbed by molecules in the atmosphere, primarily N_2 and O_2. These molecules become excited and then re-emit the sunlight at a different wavelength. While this type of scattering is uncommon compared with elastic scattering, it impacts sensitive DOAS measurements by filling in the lines of the incident solar spectrum via the Ring effect [*Grainger and Ring*, 1962].

1.3.2 Differential Slant Columns Densities

Two sample spectra from one of the UV-visible spectrometers deployed at PEARL are shown in Figure 1.6a. These spectra are primarily made up of the solar spectrum that is measured at the instrument resolution and modified by the instrument function, which includes detector and grating efficiencies, among other effects. Furthermore, the broad varying features of these spectra can be attributed to Rayleigh and Lorenz-Mie scattering. Therefore, in order to identify tiny atmospheric absorption features, this large background must be removed. The DOAS technique makes this process relatively simple by comparing spectra taken at different SZA.

Figure 1.7 is a schematic of the zenith-sky viewing geometry. Sunlight at midday (small SZA) travels a different average path to the instrument than sunlight at twilight (large SZA). Meanwhile, the instrument function (for a stable instrument) and the solar spectrum do not normally change significantly during this time period*. Therefore, a differential SCD (DSCD) can be retrieved by taking the ratio of twilight and noon spectra, cancelling out the instrument function and solar spectrum. The DSCD, the primary product of DOAS retrievals, is therefore the amount of a trace gas along the path followed by light to the instrument at twilight minus the amount at noon. The theory behind the DOAS technique is described below.

The Beer-Bouguer-Lambert Law [*Perrin*, 1948], or Beer's law, describes the change in the intensity of radiation at a particular wavelength $I(\lambda)$ due to an absorber with cross-section σ and density ρ over the path distance z,

$$dI(\lambda) = -\sigma(\lambda)\rho(z)I(\lambda)dz\,. \tag{1.24}$$

For cross-sections that do not depend on temperature and pressure, and therefore z, this equation can be integrated to get

$$I(\lambda) = I_o(\lambda)\exp\left(-\sigma(\lambda)u\right), \tag{1.25}$$

* Note that this is not always the case. This is treated for a changing solar spectrum in Chapter 6 and a changing instrument function in Appendix B.

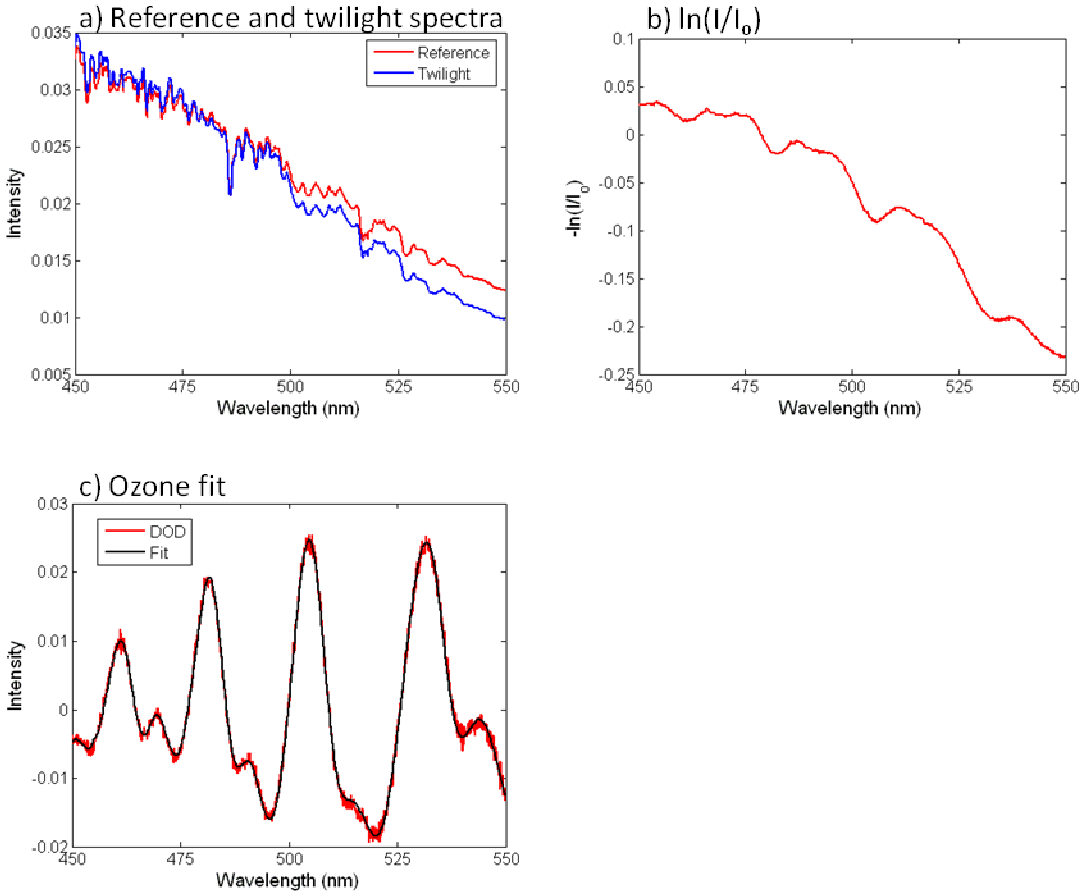

Figure 1.6: DOAS DSCD retrieval applied to spectra taken at SZA 90° during the morning twilight on 5 March 2008 at Eureka. (a) Reference and twilight spectra, which contain the solar spectrum and instrument function. (b) Negative logarithm of the ratio between twilight and reference spectra. (c) Ozone differential optical depth (DOD) from measurements (red) and cross-section fit (black).

where I_o is the incident intensity of light and u is the SCD.

Beer's law can be generalized for multiple absorbers in the atmosphere to

$$I(\lambda) = I_o(\lambda)\exp\left(-\sum_i\left(\sigma_i(\lambda)u_i\right)+\varepsilon_R(\lambda)+\varepsilon_M(\lambda)\right), \tag{1.26}$$

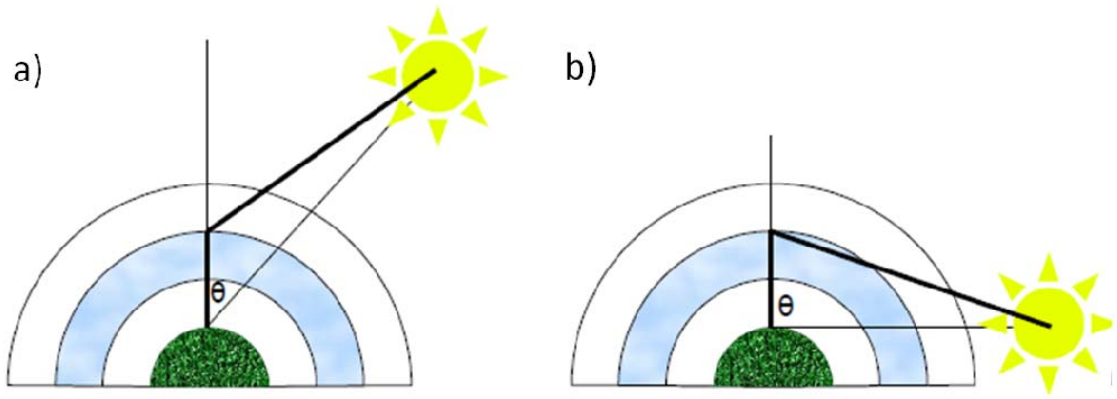

Figure 1.7: Schematic of zenith-sky viewing geometry. Average path of zenith-scattered sunlight through the atmosphere for (a) small SZA, high sun and (b) large SZA, low sun. θ = SZA. Figure adapted from *Fish* [1994].

where ε_R is the optical depth due to Rayleigh scattering and ε_M is the optical depth due to Mie scattering.

For DOAS measurements at twilight and noon, this can be written as,

$$C(\lambda)I_T(\lambda) = I_R(\lambda)C(\lambda)\exp\left(-\sum_i\left(\sigma_i(\lambda)(u_{T,i}-u_{R,i})\right)+\varepsilon_R(\lambda)+\varepsilon_M(\lambda)\right) \tag{1.27}$$

where I_T is the spectrum at twilight, I_R is the reference spectrum (typically taken midday), and $(u_T\text{-}u_R)$ is the DSCD. $C(\lambda)$ represents the instrument function, which describes instrument effects, such as grating and detector efficiencies and cancels out, yielding,

$$I_T(\lambda) = I_R(\lambda)\exp\left(-\sum_i\left(\sigma_i(\lambda)(u_{T,i}-u_{R,i})\right)+\varepsilon_R(\lambda)+\varepsilon_M(\lambda)\right). \tag{1.28}$$

For the direct-fit DSCD retrieval technique, non-linear Equation 1.28 is fit directly. For a DOAS analysis, this equation is rewritten as,

$$-\ln\left(\frac{I_T(\lambda)}{I_R(\lambda)}\right) = -\sum_i\left(\sigma_i(\lambda)(u_{T,i}-u_{R,i})\right)+\varepsilon_R(\lambda)+\varepsilon_M(\lambda). \tag{1.29}$$

By taking the ratio of the spectrum at twilight and noon, the solar spectrum and instrument functions cancel. This can be seen in Figure 1.6b.

The optical depth due to Rayleigh and Mie scattering changes throughout the day depending on SZA, clouds, etc. Fortunately, scattering effects vary slowly with wavelength, while absorption cross-sections contain some quickly varying features. Therefore, in the DOAS technique, the right hand side of Equation 1.29 is divided into slowly and rapidly varying components. When a low-order polynomial is subtracted from both sides of Equation 1.29, the following remains,

$$-\ln\left(\frac{I_T(\lambda)}{I_R(\lambda)}\right) - polynomial = -\sum_i \left(\sigma_{D,i}(\lambda)(u_{R,i} - u_{N,i}\right), \tag{1.30}$$

where σ_D is the rapidly varying component of the cross-section, called the differential cross-section. The left-hand side of Equation 1.30 is called the differential optical depth (DOD). Using known laboratory-measured cross-sections and measurements at twilight and noon, DSCDs can be retrieved from Equation 1.30 using a non-linear least squares fitting technique. The result of a DOAS fit for ozone is shown Figure 1.6c. The data (red) are what remain of the ratio of the twilight and reference spectra after the DOAS process has been completed and contributions from interfering trace gases have been removed. The fit (black) is the differential ozone cross-section multiplied by the calculated DSCD of ozone.

In practical terms, in order to employ the DOAS technique, the trace gas of interest is identified. A fitting wavelength window is determined based on the absorption cross-sections of the target gas and interfering species. Absorption cross-sections are convolved to the resolution of the instrument prior to analysis. This introduces a source of error called the I_o effect, which arises primarily because the spectra have been convolved to the resolution of the spectrum and not the logarithm of the spectrum [*Aliwell et al.*, 2002]. A correction can be applied to the cross-section to account for this. A Ring pseudo-cross-section is also typically included to account for the filling in of absorption lines by Raman scattering [e.g., *Chance and Spurr*, 1997]. Finally an offset correction can be applied during the DOAS fitting procedure in order to account for stray light and dark current in the instrument.

QDOAS [*Fayt et al.*, 2011] is a new version of WinDOAS [*Fayt and Roozendael*, 2001], a DSCD retrieval software that was developed at IASB-BIRA. A schematic of the

QDOAS/WinDOAS software is given in Figure 1.8. First, spectra are calibrated in wavelength against the solar spectrum. During this calibration, the slit function (resolution versus wavelength) of the instrument is calculated. This slit function is then used to smooth the cross-sections to the resolution of the instrument. Next, DSCDs are retrieved using the DOAS technique. Finally, DSCDs are converted to vertical column densities (VCDs)*, as described in Section 1.3.3.

1.3.3 Vertical Column Densities

The VCD is the amount of a trace gas that is in a column above the instrument. In order to convert SCDs to VCDs, the average path that light takes through the atmosphere is calculated using a radiative transfer model, which outputs airmass factors (AMFs). AMFs are a measure of the optical path enhancement through scattering and are defined as AMF=SCD/VCD.

For DOAS retrievals, the DSCD is equal to the SCD minus the reference column density (RCD), the amount of the absorber in the reference spectrum. DSCDs of ozone as a function of SZA are shown in Figure 1.9a. DSCDs increase with SZA because the path of light to the instrument also increases with SZA. The DSCDs can be written as,

$$DSCD(SZA) = VCD(SZA) \times AMF(SZA) - RCD. \tag{1.31}$$

For each twilight, a Langley plot of DSCDs versus AMFs over a range of SZAs can be plotted. A sample Langley plot is shown in Figure 1.9b. The VCD can simply be taken as the slope of the Langley plot. However, better results are obtained if the RCD is characterized over two or more twilights. Therefore, the RCD can be obtained from the y-intercept of Langley plot for each twilight and an averaged RCD can be calculated.

With this RCD, Equation 1.31 can be rearranged, and the VCD calculated as a function of SZA

$$VCD(SZA) = \left(\frac{DSCD(SZA) + RCD}{AMF(SZA)} \right) \quad . \tag{1.32}$$

---

* Note that for this thesis, VCDs were not retrieved using QDOAS. Instead, they were retrieved with in-house software.

VCDs can then be averaged over a twilight to produce a final DOAS data product. The DOAS analysis and error budget for the GBS ozone and NO_2 measurements are described in Chapter 4.

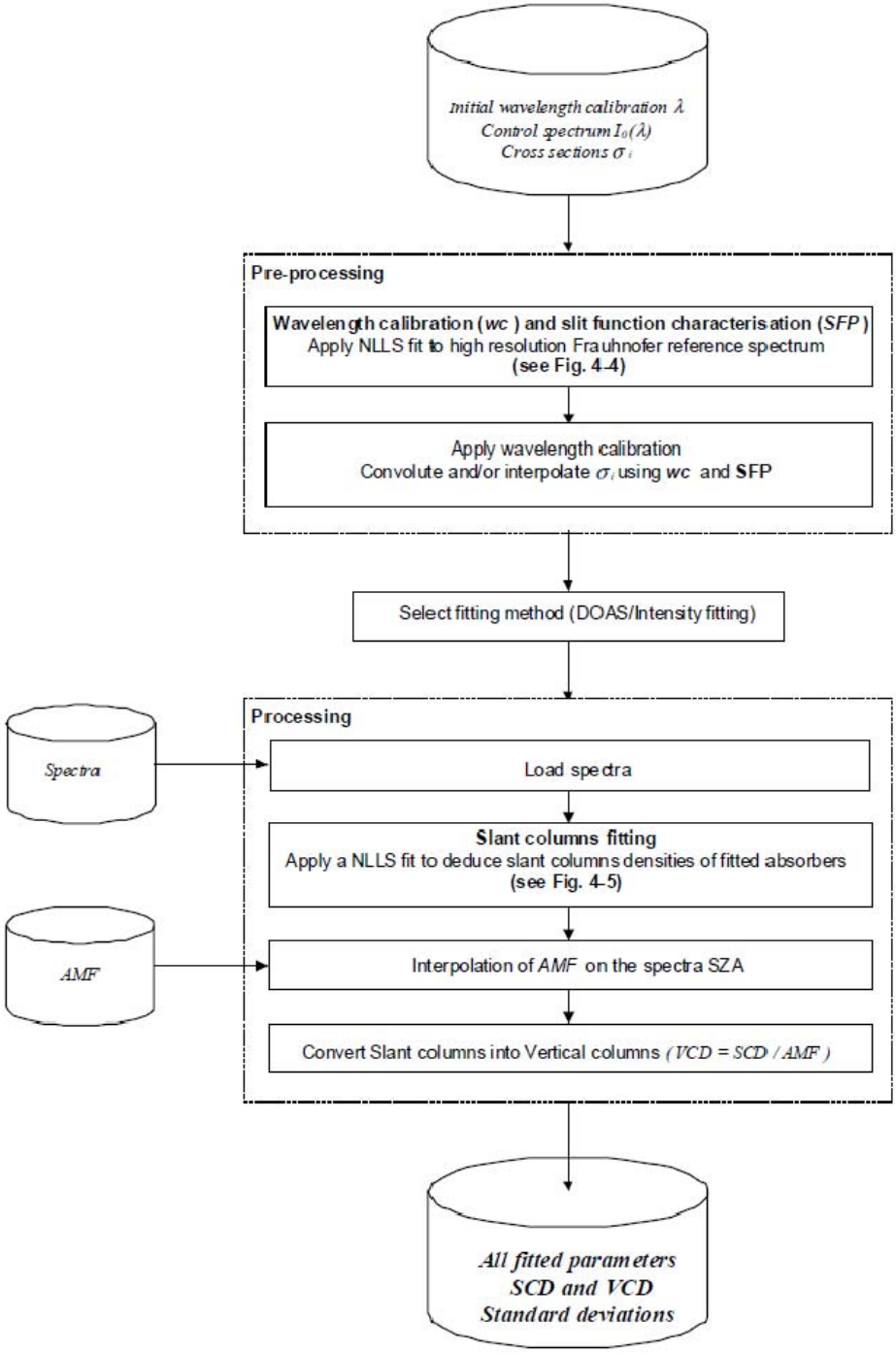

Figure 1.8: Schematic of the QDOAS software. Figure from *Fayt and Van Roozendael* [2011].

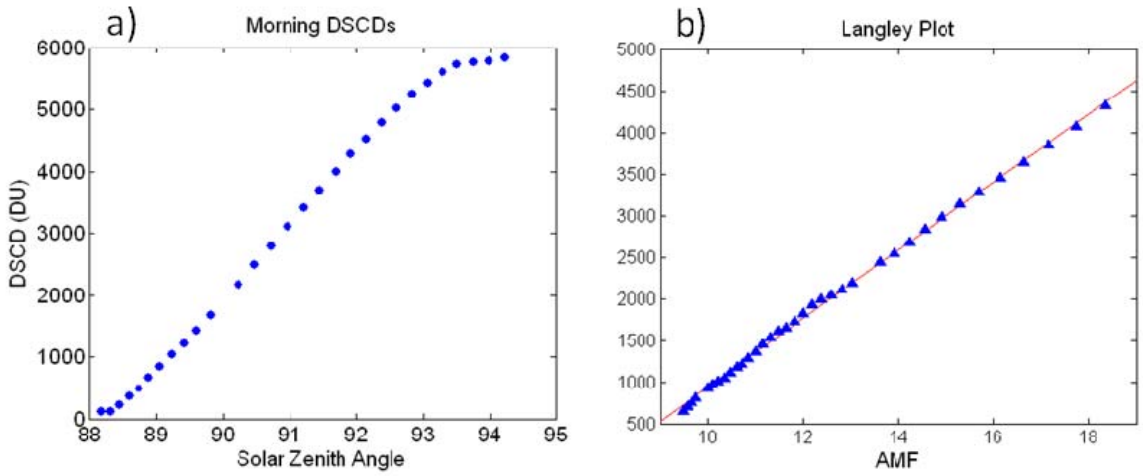

Figure 1.9: DOAS VCD retrieval for 5 March 2008 at Eureka. (a) DSCD versus SZA. (b) Langley plot, DSCD versus AMF.

1.3.4 Viewing Geometries

The viewing geometry of a DOAS instrument can be modified in order to sample different parts of the atmosphere, as shown in Figure 1.10. The zenith-sky measurements, described above, are primarily sensitive to stratospheric trace gases [e.g., *Solomon et al.*, 1987]. Direct-sun measurements are more sensitive to tropospheric trace gases, as the average path taken by sunlight through the troposphere is up to twenty times larger at sunset than at noon [e.g., *Schofield*, 2003]. The combination of direct-sun and zenith-sky measurements can be used to retrieve tropospheric and stratospheric partial columns of BrO [*Schofield et al.*, 2004b]. Furthermore, direct lunar measurements can be used to take measurements over polar night [e.g., *Solomon et al.*, 1988].

The multi-axis DOAS (MAX-DOAS) [e.g., *Honninger et al.*, 2004] viewing geometry is also shown in Figure 1.10. The MAX-DOAS technique involves measuring scattered sunlight at various elevation angles. Sunlight arriving at the instrument from the horizon has typically taken a long path through the lower troposphere. Therefore, MAX-DOAS measurements are sensitive to the boundary layer and can be used to detect bromine explosions [e.g., *Simpson et al.*, 2007b and references therein]. It is easier to acquire MAX-DOAS DSCDs than direct-sun DSCDs because they do not require accurate solar tracking. However, the retrieval of concentrations or

tropospheric partial columns from MAX-DOAS DSCDs is difficult because sunlight undergoes multiple scattering in the troposphere, which depends on SZA, surface albedo and weather conditions [e.g., *Honninger et al.*, 2004].

Long-path DOAS measurements are taken using an artificial light source, instead of the sun or moon. Long-path DOAS systems are more logistically challenging than the passive techniques described above. However, they present the advantages of producing a continuous day and night dataset and having a well-known light path. Boundary layer halogens, BrO, IO, and OClO have been measured using long-path DOAS systems [e.g., *Saiz-Lopez et al.*, 2007b; *Pohler et al.*, 2010].

1.3.5 Clouds, aerosol, and O_4

Clouds and aerosol alter the path taken by scattered sunlight to the surface. Within clouds, multiple scattering can occur, enhancing the path of sunlight through the cloud and, therefore, also enhancing the DSCD. Furthermore, water vapour within clouds has absorption features at

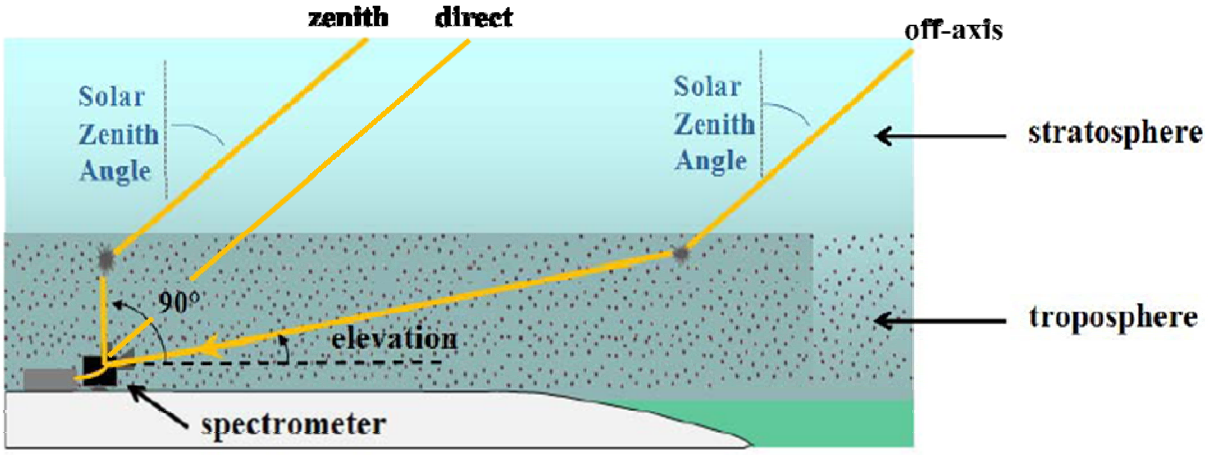

Figure 1.10: Viewing geometries for DOAS measurements. Zenith-scattered sunlight (left beam) scatters high in the atmosphere then straight down to the instrument, maximizing the path through the stratosphere only. Direct-sunlight (middle beam) samples both the stratosphere and the troposphere equally. Off-axis scattered sunlight (right beam) samples the same path through the stratosphere as zenith-scattered sunlight; however the path through the troposphere is much longer, leading to sensitivity to the boundary layer. Figure adapted from *Roscoe et al.* [2010].

visible wavelengths, which can reduce the quality of DOAS fits. For zenith-sky measurements at large SZA, the average scattering height is high (> 15 km) and therefore clouds and aerosol are expected to have little impact on the measurements [*Platt and Stutz*, 2008]. However, for the smaller SZA measurements taken at Eureka during the summer, clouds affect the data (see Sections 4.1.3.1 and 4.2). MAX-DOAS measurements are sensitive to tropospheric aerosol and clouds. Since the O_4 profile is well known and changes little over time, O_4 DSCDs can be used to assess radiative transfer [e.g., *Wagner et al.*, 2002]. Qualitatively, large O_4 DSCDs suggests path enhancement of sunlight reaching the instrument.

1.4 Long-Term Monitoring of the Atmosphere

Continuous and consistent long-term atmospheric datasets are essential for the assessment of climate change. The Global Climate Observing System (GCOS) aims to compile the comprehensive observations that are necessary to characterize the global climate system and its variability [*GCOS*, 2012]. The "Essential Climate Variables" listed by GCOS include ozone measured by the Network for the Detection of Atmospheric Composition Change (NDACC). NDACC (formerly the Network for the Detection of Stratospheric Change - NDSC) was formed in 1991 and currently includes over 70 research stations world-wide [*Kurylo and Zander*, 2000]. NDACC monitors changes in the stratosphere with Brewer and Dobson Spectrometers, Fourier-Transform Infrared (FTIR) spectrometers, lidars, microwave instruments, satellites, sondes, UV-visible spectrometers, and spectral UV instruments.

The NDACC UV-visible working group has developed a set of standards and recommendations to ensure a consistent and homogenous datasets [*NDACC*, 2009]. NDACC requires certification of new instruments through an evaluation of instrument design, performance, and data analysis, as well as validation against other UV-visible instruments during a formal NDACC intercomparison campaign. Once an instrument is accepted by NDACC, the instrument investigator must continually assess data quality by maintaining records of equipment changes; evaluating performance routinely through instrument tests; monitoring DOAS fitting errors and residuals; analysing data using NDACC recommendations; and validating measurements against other available datasets, when available.

1.5 Thesis Outline and Scientific Contributions

This thesis addresses the scientific objectives listed on page 2, using the DOAS technique. This work resulted in the publications that are cited throughout this section. The thesis is organized as follows.

Chapter 2 describes the spectrometers and suntracker used in this study and improvements that were made to them over the course of my PhD. I have been responsible for the University of Toronto Ground-Based Spectrometer (UT-GBS) and PEARL-GBS since 2008. To perform instrument maintenance, testing, and occasionally to install new instrumentation, I traveled to Eureka six times and to Cabauw once. I tested spectrometer performance using the guidelines developed primarily by Matt Bassford, Elham Farahani, and Annemarie Fraser. I also identified light leaks in the instruments and repaired them in 2009. In 2010, I developed a new set of methods to characterize and improve the resolution of the instruments. The University of Toronto (UT) Suntracker was developed in Toronto, primarily by Clive Midwinter, who contributed to all aspects of the suntracker development presented here. I developed the tracking software used in Eureka, based on the early work of summer student Nir Friedman. Furthermore, with intern Suri Like, I developed the testing techniques described in this thesis. Finally, I deployed the suntracker at Eureka in 2008.

Chapter 3 describes the NDACC certification process for the PEARL-GBS. Annemarie Fraser provided the original instrument characterization and intercomparison tests [*Fraser et al.*, 2009], which led to NDACC certification. I was responsible for the deployment of the instruments at the Cabauw Intercomparison of Nitrogen Dioxide measuring Instruments (CINDI) in Cabauw, Netherlands in summer 2009 [*Piters et al.*, 2012]. Intern Maryam Akrami and I designed the housing for the UT Suntracker, organized shipping logistics, and deployed the instruments. During the campaign, I analyzed and submitted O_4 and NO_2 DSCDs daily. I also took MAX-DOAS measurements for the first time in our research group. Following the campaign, I analyzed and submitted a final version of O_4, NO_2, and HCHO DSCDs, which were compared with other instruments by *Roscoe et al.* [2010] and *Pinardi et al.* [2012].

The analysis of the 1999-2011 Eureka dataset is described in Chapter 4. The 1999-2007 data were acquired by Matt Bassford, Elham Farahani, and Annemarie Fraser. I acquired the data for

2008-2010. In 2011, MSc student Xiaoyi Zhao and I acquired the data together. Intern Joseph Mendonca and I wrote spectral preprocessing software. I retrieved DSCDs using QDOAS software, which was developed at IASB-BIRA. I identified and corrected the polarization errors in ozone retrievals and developed automated filtering methods. I also wrote software to automate the VCD retrieval process and calculate errors, which is now being used by Xiaoyi Zhao.

In Chapter 5, an intercomparison between numerous satellite and ground-based instruments is presented. Satellite columns were calculated from profiles by intern Dan Weaver and summer students Boris Pavlovic and David Park. Ozone and NO_2 datasets were provided to me by many different parties. I compared these measurements, using photochemical corrections for NO_2. I identified dynamical variability and rapid photochemical changes across latitudes as possible contributors to spring-time variability. This work has been published [*Adams et al.*, 2012a].

Chapter 6 presents a study on ozone and NO_2 during the August 2008 solar eclipse above Eureka. This work was published in 2010 [*Adams et al.*, 2010]. I analyzed the UV-visible measurements using techniques to account for the changing solar spectrum. I assessed these measurements through comparisons with previous studies and modeling results provided by Chris McLinden.

The unusual spring 2011 ozone, NO_2, and OClO dataset is presented in the context of 11 years of measurements in Chapter 7. In March 2011, severe ozone depletion was observed above Eureka. I quantified this event and compared it with previous years using GBS data and Système d'Analyse par Observations Zenitales (SAOZ) data provided by Florence Goutail and Andrea Pazmino. I used dynamical parameters provided by Gloria Manney and William Daffer in order to identify the dynamical and chemical contributions to these measurements. Ozone loss was estimated using modeled passive ozone columns provided by Martyn Chipperfield and Wuhu Feng. This work has been published [*Adams et al.*, 2012b]. As the vortex moved away from Eureka in April 2011, a large maximum in NO_2 was observed in the ground-based measurements. I investigated this using dynamical parameters, satellite and ozonesonde measurements, and output from the Global Modeling Initiative (GMI), provided by Susan Strahan. OMI data used in this study were provided by Chris McLinden. This work also benefited from discussions with Dylan Jones, Gloria Manney, and Markus Rex. This event

demonstrates the transport of NO_2-rich air to the Arctic via an anticyclone. Following this transport, middle-stratosphere ozone loss occurred inside the anticyclone, which remained directly above Eureka for much of April/May. This work is in preparation for publication [*Adams et al.*, 2012c].

GBS BrO retrievals are described in Chapter 8. I retrieved zenith-sky BrO DSCDs using both WinDOAS and "BOAS", a direct-fit software, provided by Kelly Chance. Using optimal estimation profile retrieval software provided by Robyn Schofield, I retrieved stratospheric partial columns of BrO. I performed retrieval sensitivity tests, using *a priori* profiles constructed from Scanning Imaging Absorption spectroMeter for Atmospheric CartograpHY (SCIAMACHY) satellite data by Sunny Choi. I then compared the GBS columns with OMI satellite data provided by Thomas Kurosu and OSIRIS satellite partial columns, calculated from profiles by David Park. In spring 2010, I took new MAX-DOAS measurements with the UT Suntracker. I performed a preliminary analysis of this data, using QDOAS, which suggests that bromine explosion occur above PEARL.

Overall, this thesis presents a new standardized 11-year dataset of UV-visible measurements in the High Arctic. This dataset was used for long-term satellite validation, the assessment of NO_x photochemistry, and the evaluation of the unusual spring 2011 ozone depletion in the context of previous years. Furthermore, new stratospheric and tropospheric BrO measurements are presented and could be applied to evaluate stratospheric bromine budget and investigate boundary layer bromine explosions.

2 Instrumentation

This chapter describes the UT-GBS and PEARL-GBS DOAS instruments that were used throughout this thesis (see Section 1.3 for an overview of the DOAS methodology). Many small changes have been made to the GBS instruments since the first Arctic deployment of the UT-GBS in 1999. These changes and their effects on performance are documented here, as recommended for long-term monitoring (see Section 0). The UT-GBS and the PEARL-GBS UV-visible spectrometers are described in Section 2.1. Characterization testing techniques and results, as well as some subsequent instrument improvements are described in Sections 2.2-2.6. In order to take new MAX-DOAS and direct-sun measurements, the UT Suntracker was developed and tested, as described in Section 2.7. Finally, the GBS data acquisition software was modified to improve operations at the remote Eureka lab and to incorporate the UT Suntracker, as described in Section 2.8.

2.1 Spectrometers

2.1.1 History of the GBS Instruments

The GBS instruments have been involved in numerous field campaigns and studies, which are summarized in Table 2.1. The UT-GBS was assembled in 1998 and is the travelling GBS instrument. It has been to Eureka, Nunavut for polar sunrise annually since 1999 to study Arctic photochemistry and to validate measurements from the Atmospheric Chemistry Experiment (ACE) satellite mission. In 2002, the instrument was in Resolute Bay instead of Eureka. It also participated in the four Middle Atmosphere Nitrogen TRend Assessment (MANTRA) campaigns in Vanscoy, Saskatchewan and in the 2009 CINDI at Cabauw, Netherlands. When it is not travelling, the UT-GBS takes measurements in the Toronto Atmospheric Observatory at the University of Toronto or stays at PEARL for extended periods. The PEARL-GBS was assembled and permanently installed at PEARL in August 2006 and has been taking measurements during the sunlit part of the year since then.

Table 2.1: Measurement history of the UT-GBS and PEARL-GBS instruments.

Campaign	Location	UT-GBS	PEARL-GBS
MANTRA	Vanscoy, Saskatchewan (52°N, 107°W)	19-26 Aug 1998[a, b, c] 18-26 Aug 2000[d] 20 Aug - 3 Sep 2002[d] 3 Aug - 15 Sep 2004[e, f, g]	N/A
Stratospheric Indicators of Climate Change (spring 2001, 2003), Canadian Arctic Validation Campaign (spring 2004-present), and CANDAC (year-round 2006-present)	Eureka, Nunavut (80°N, 86°W)	22 Mar - 11 Apr 1999[h, i, j] 22 Feb - 23 Mar 2000[d, j] 28 Feb - 23 Mar 2001[d] 18 Mar - 22 Apr 2003[d, j, k] 25 Feb - 14 Apr 2004 [e. j, k, l, m, n] 21 Feb - 30 Mar 2005 [e, j, k, m, n] 20 Feb - 31 Mar 2006[e, j, k, m, n] 21 Feb - 11 May 2007[e, j, k, o] 26 Feb - 17 Oct 2008[j, k] 18 Feb - 31 Mar 2009[j, k] 23 Feb - 17 Oct 2010[j, k] 14 Feb - 31 2011[j, k]	13 Aug - 17 Oct 2006[e, j, o] 14 Feb -17 Oct 2007[e, j, k, o] 14 Feb - 17 Oct 2008[j, k, p] 14 Feb - 17 Oct 2009[j, k] 8 Mar - 17 Oct 2011j[j, k] 16 Mar - 10 Apr 2011[j, k]
CINDI/NDACC Certification	Cabauw, Netherlands (52°N, 56°E)	13 Jun - 17 Jul 2009[q, r, s]	N/A
Stratospheric Indicators of Climate Change	Resolute Bay, Nunavut (75°N, 95°W)	15 Mar - 15 Apr 2002	N/A
Toronto Atmospheric Observatory	Toronto, Ontario (44°N, 79°W)	19 Dec - 31 Dec, 2001 1 Jan - 11 Feb, 2002 12 Dec - 31 Dec, 2002 1 Jan - 3 Feb, 2003 29 Jul - 28 Aug, 2003 7 Jan - 3 Feb 2004 2 May - 14 Dec 2005 18 Apr - 31 Dec 2006[e] 27 Jun - 25 Dec 2007 8 Jan - 14 Jan 2008	N/A

[a] [*Bassford et al.*, 2001]
[b] [*Bassford et al.*, 2005]
[c] [*Melo et al.*, 2005]
[d] [*Farahani*, 2006]
[e] [*Fraser*, 2008]
[f] [*Fraser et al.*, 2007a]
[g] [*Fraser et al.*, 2007b]
[h] [*Bassford et al.*, 2000]
[i] [*Melo et al.*, 2004]
[j] [*Adams et al.*, 2012b]
[k] [*Adams et al.*, 2012a]
[l] [*Kerzenmacher et al.*, 2005]
[m] [*Fraser et al.*, 2008]
[n] [*Kerzenmacher et al.*, 2006]
[o] [*Fraser et al.*, 2009]
[p] [*Adams et al.*, 2010]
[q] [*Roscoe et al.*, 2010]
[r] [*Piters et al.*, 2012]
[s] [*Pinardi et al.*, 2012]

2.1.2 Triax-180 Spectrometer

The UT-GBS and PEARL-GBS are both Triax-180 grating spectrometers, built by Instruments S.A. / Jobin-Yvon / Horiba. The Triax-180 is a crossed Czerny-Turner triple grating imaging spectrometer, meaning that light is directed by a collimating mirror to a grating and is then focused by a focusing mirror onto a CCD. This scheme is advantageous for DOAS applications because the wavelength range can be selected by rotating the grating and stray list is minimized [*Platt and Stutz*, 2008]. A schematic of the Triax-180 spectrometer is shown in Figure 2.1. Focused light enters the slit of the instrument and passes through a mechanical shutter. The light is then collimated by the collimating mirror, dispersed by the diffraction grating, and focused by the focusing mirror onto the detector. The optics of the instrument provide point-to-point imaging, generate a flat-field input, and are aspherical, to correct for astigmatism. The spectrometer has a focal length of 0.190 m (f-number 3.9) and a 12x30 mm focal plane.

Various diffraction grating types are described in *Horiba* [2012]. The most basic equation for a diffraction grating is

$$sin\alpha - sin\beta = kn\lambda \,, \tag{2.1}$$

where α is the angle of incidence, β is the angle of diffraction, k is the diffraction order, n is the groove density of the diffraction grating, and λ is the wavelength of light. Therefore, for larger groove density gratings, light is diffracted at larger angles. This yields a higher resolution, but a narrower wavelength range incident on the detector. Ruled gratings are produced using a ruling engine with a diamond stylus and are more susceptible to imperfections, which can lead to grating ghosts. Holographic gratings are produced using the interference fringes of two lasers and therefore do not have periodic imperfections that can cause ghosts. Both holographic and ruled gratings can be "blazed" at a given wavelength to optimize efficiency for a given wavelength interval.

The Triax-180 spectrometer has three gratings. The rulings, blaze, and wavelength ranges of the gratings used for the UT-GBS and PEARL-GBS are summarized in Table 2.2. The gratings are attached to a motorized turret, so that for a given measurement the grating with the appropriate

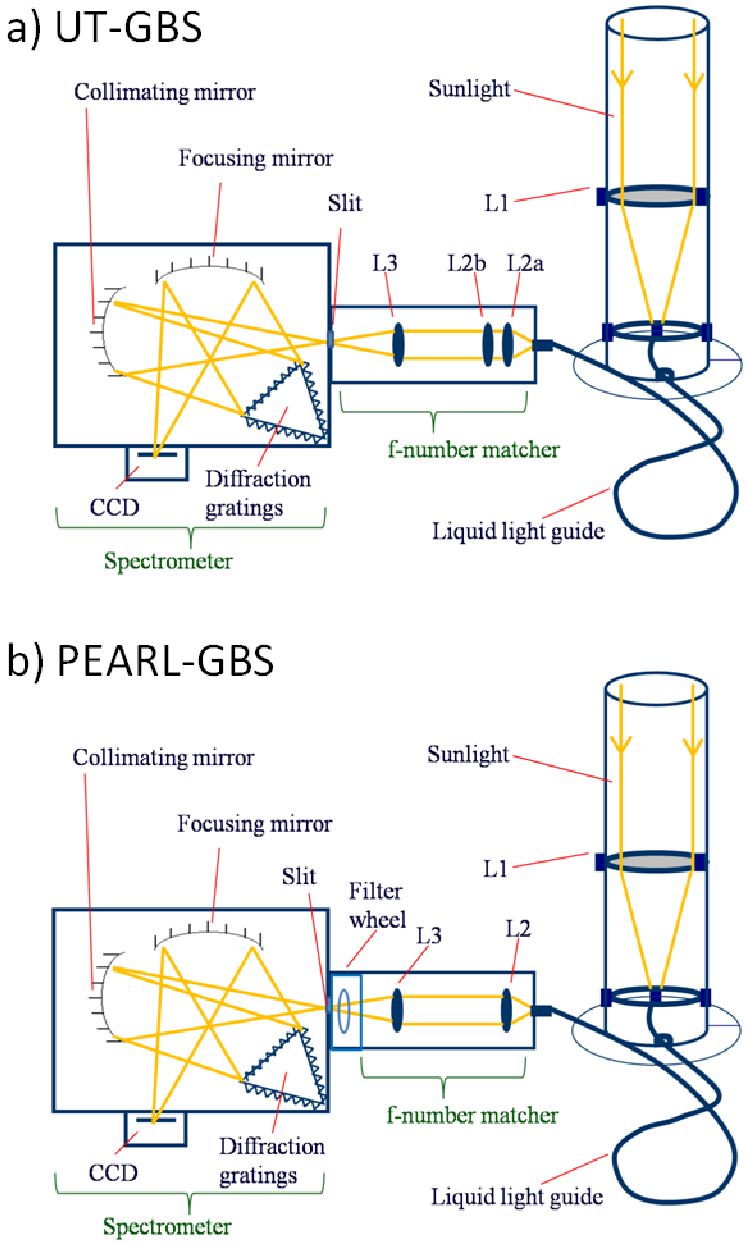

Figure 2.1: Schematics of (a) the UT-GBS and (b) the PEARL-GBS. Figure adapted from *Fraser* [2008].

Table 2.2: UT-GBS and PEARL-GBS gratings.

	Grating (gr/mm)	Grating type	Blaze (nm)	Wavelength window width (nm)
UT-GBS	400	ruled	400	325
	600	holographic	500	210
	1800	holographic	400[a]	60
PEARL-GBS	300	ruled	500	440
	600	holographic	500	210
	1200	holographic	330	100

[a] Note: different 1800 gr/mm grating with 500 nm blaze was used 1998-2002.

wavelength range and resolution can be selected. The position of the grating, which determines the measured wavelength region, can also be controlled by the grating turret. Typically, the 600 gr/mm grating is used to retrieve ozone, NO_2, and O_4, while the 1800 gr/mm or 1200 gr/mm gratings are used to retrieve gases with weaker absorption features such as BrO, OClO, and HCHO. The gratings have varying efficiencies across the spectral region and for different polarizations, as shown in Figure 2.2. More details on the resolutions and wavelength regions can be found in Section 2.2.6.

2.1.3 The UT-GBS

A schematic of the UT-GBS is shown in Figure 2.1a. Sunlight is collected by *L1*, a 40-mm diameter fused silica lens (f-number 2.5). For some measurements and instrument characterization tests, a red (> 575 nm; Andover 590FG05), UV band-pass (250-400 nm) (Edmund Optics), or 25% neutral density filter (Edmund Optics) is placed between *L1* and the liquid light guide. The light is focused onto a 1 m liquid light guide, with a core diameter of 3 mm (f-number 0.85), which depolarizes the light and brings it into the f-number matcher. Note that in March 2011, the liquid light guide was replaced with a 1-m slit-to-spot fibre bundle with a spot of 0.65 mm diameter at the entrance end, with a 2.27 f-number. At the exit, the fibre bundle is rectangular 3.3 mm x 0.1 mm (height x width). This improves coupling of signal to the spectrometer and the resolution as discussed in Section 2.2.5. Both the liquid light guide and the slit-to-spot fibre bundle depolarize light.

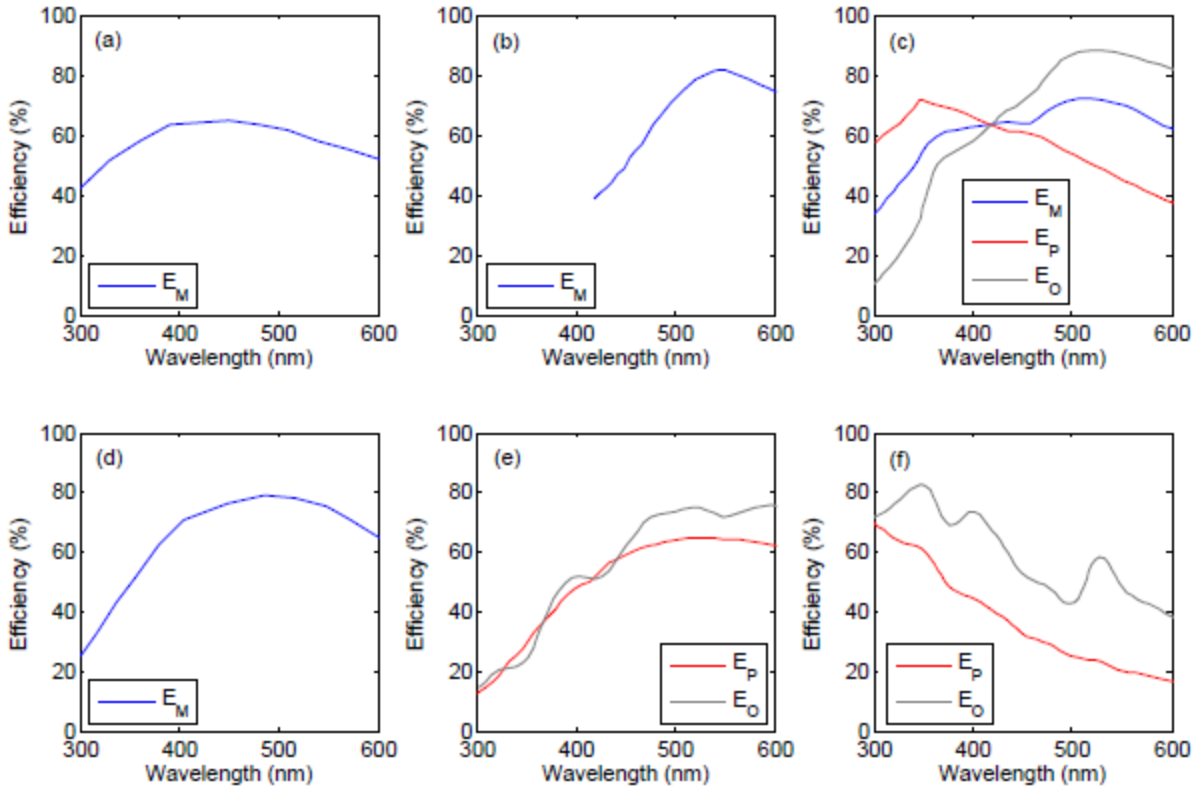

Figure 2.2: Grating efficiencies for the UT-GBS: (a) 400 gr/mm (blazed at 400 nm), (b) 600 gr/mm (blazed at 500 nm), (c) 1800 gr/mm (blazed at 400 nm), and for the PEARL-GBS: (d) 300 gr/mm (blazed at 500 nm), (e) 600 gr/mm (blazed at 500 nm), and (f) 1200 gr/mm (blazed at 330 nm). In all figures, E_M is the efficiency for unpolarized light and E_P is for light polarized parallel to the grooves of the grating, and E_O is for light polarized perpendicular to the grooves of the grating. Figure adapted from ISA documentation from *Fraser* [2008].

The f-number matcher contains three lenses: *L2a* and *L2b* collimate the light and then *L3* refocuses the light to the 3.9 f-number of the spectrometer. The focused light is brought to the adjustable, mechanical slit, which is typically set to 0.1 mm width, and then enters the Triax-180 spectrometer.

Upon exiting the spectrometer, light is recorded using a CCD detector. The UT-GBS has used three CCD detectors since 1998, which are described by *Fraser* [2008]. Since 2004, it has used a

back-illuminated detector with 2048x512 pixels, each of which has the physical size 13.5x13.5 μm. The 2048 horizontal pixels (X-pixels) correspond to different measurement wavelengths, while 512 vertical pixels (Y-pixels) correspond to the height of the light incident on the slit. The detector is thermoelectrically cooled to 201 K, leading to low dark current signal. It is also coated with a UV-enhanced coating, yielding a high quantum efficiency of 50-70% between 300-600 nm.

2.1.4 The PEARL-GBS

A schematic of the PEARL-GBS is shown in Figure 2.1b. Like the UT-GBS, sunlight is collected by *L1*, a 40-mm diameter fused silica lens (f-number 2.5). For some UV measurements, a UV band-pass filter (250-400 nm) is placed below *L1*. From 2006-2009, light was focused onto a 1-m liquid light guide, with a core diameter of 3 mm (f-number 0.85). In March 2010, this was replaced with a 1-m spot-to-fiber bundle, which is identical to fiber-bundle described for the UT-GBS above. The f-number matcher of the PEARL-GBS is identical to the UT-GBS, except *L2a* and *L2b* are combined in a single lens *L2*. Between *L3* and the slit, there is a motorized filter wheel, which holds six filters. Currently, the filter wheel contains an empty slot, a long-wave (>575 nm) filter (Andover 590FG05), and 25%, 1%, 0.1%, and 0.01% neutral density filters (Edmund Optics). Unlike the UT-GBS, the PEARL-GBS slit is fixed, to improve reproducibility of measurements. For 2006-2010, a 0.05-mm slit was used. In 2011, a 0.1-mm slit was installed in order to prevent undersampling, as described in Section 2.2.6. A fixed 0.25-mm slit is also available, but is rarely used. Spectra are recorded using a CCD detector, which is identical to the UT-GBS CCD except that it uses an enhanced broadband CCD coating, improving the quantum efficiency to 50-90% between 300-600 nm. The temperature of the PEARL-GBS CCD oscillates slightly between 201 and 205 K on a timescale of minutes. During summer 2010, CCD temperatures began to rise to ~220 K due to a leak in the vacuum seal. In winter 2010, the CCD was removed from PEARL and technicians at ISA moved the CCD chip to new housing and electronics to repair this problem. The CCD was reinstalled in March 2011, where it operated until it failed in April 2011. Therefore, in summer 2011, the CCD was returned to ISA for further repairs.

2.2 Spectral Resolution

2.2.1 Resolution for the GBS Instruments for 1999-2009

In order to optimize the performance of an instrument, the signal-to-noise ratio, spectral resolution, sampling and desired measurement wavelength range must be considered. The spectral resolution can be increased by using a narrower slit or a finer grating. However, as the slit width is reduced, the instrument loses signal and spectral sampling is reduced. In order to prevent undersampling errors, sampling should exceed 4.5-pixels full width at half maximum (FWHM), but does not need to exceed 6.5 pixels FWHM [*Roscoe et al.*, 1996]. Fine-ruled gratings do not decrease sampling, but reduce the wavelength range, limiting the number of trace gases that can be measured simultaneously.

The focus of the CCD also determines the instrument resolution. Each campaign, the instrument is focused by moving the CCD while measuring the 435.8 nm mercury line with the 600 gr/mm grating centered at 450 nm. The Y-pixels are binned in five regions, to ensure that the mercury line is centered at the same X-pixel in all five regions. This alignment of vertical CCD regions is controlled by rotating the CCD. By moving the CCD closer to and further away from the focusing mirror, the central mercury line comes in and out of focus.

Mercury lines measured by the PEARL-GBS 600 gr/mm grating in spring 2009 at Eureka are shown in Figure 2.3 for the 365.0 nm (panel a), 404.7 nm (panel b), 435.8 nm (panel c) and 546.1 nm (panel d) lines. The 435.8 nm mercury line is at the centre of the CCD and has a small FWHM and a fairly Gaussian shape. The 365.0 and 546.1 nm mercury lines, at edges of the CCD, have larger FWHM and non-Gaussian line-shapes. The changing resolution and line-shapes across the focal plane are present for both GBS instruments and complicate characterization of the instruments in DOAS retrievals. This is discussed further in Sections 2.2.2 and 2.2.3. Note that these lineshapes are not caused by the addition of nearby lines, as with the improved optics a single mercury line was resolved.

Each campaign, the resolution across the CCD is measured for each grating using mercury, neon, and xenon lamps. The resolution of the instruments in spring 2009 at Eureka is plotted in

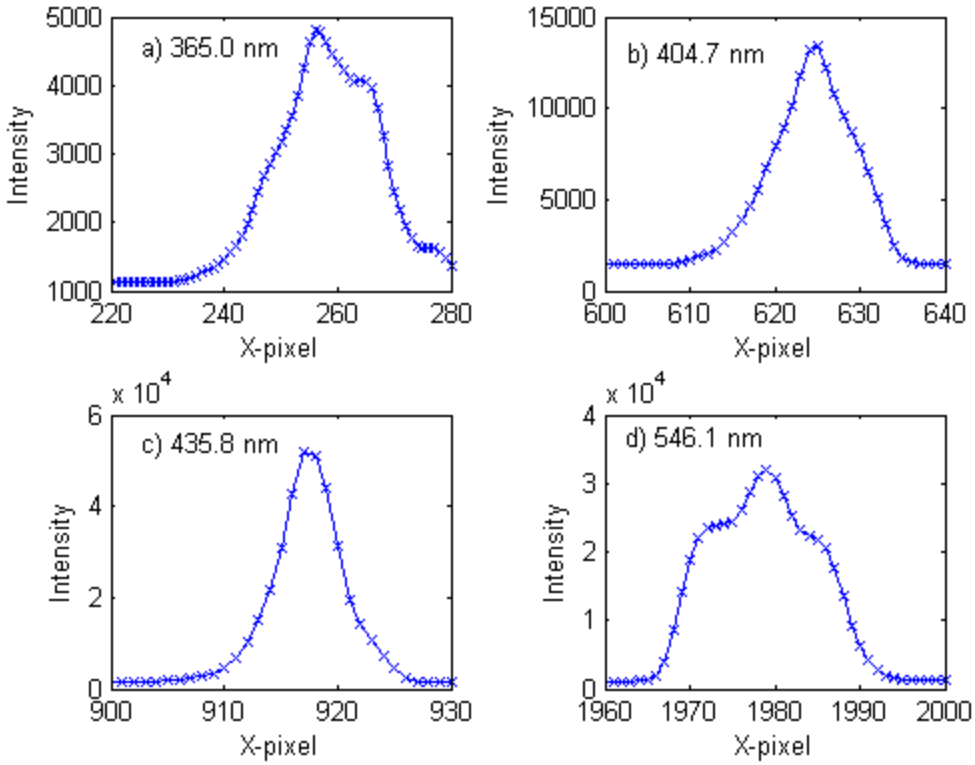

Figure 2.3: The (a) 365.0 nm, (b) 404.7 nm, (c) 435.8 nm, and (d) 546.7 nm mercury lines measured by the PEARL-GBS 600 gr/mm grating centered at 450 nm on February 25, 2009 at Eureka.

Figure 2.4. Resolutions for the PEARL-GBS 300 gr/mm grating centered at 450 nm (panel a), the 600 gr/mm grating centered at 450 nm (panel b), and the 1200 gr/mm grating centered at 380 nm (panel c) and the UT-GBS 400 gr/mm grating centered at 450 nm (panel d), the 600 gr/mm grating centered at 450 nm (panel e), and the 1800 gr/mm grating centered at 368 nm (panel f) are all shown. Resolutions for all gratings in both instruments vary greatly across the CCD, with better resolution at the centre of the CCD. Similar instrument resolutions have been recorded in previous years.

2.2.2 Monochromatic Aberrations

The non-Gaussian line-shapes and resolution variations are caused by monochromatic aberrations in the spectrometer. Monochromatic aberrations occur when light enters a lens, or in

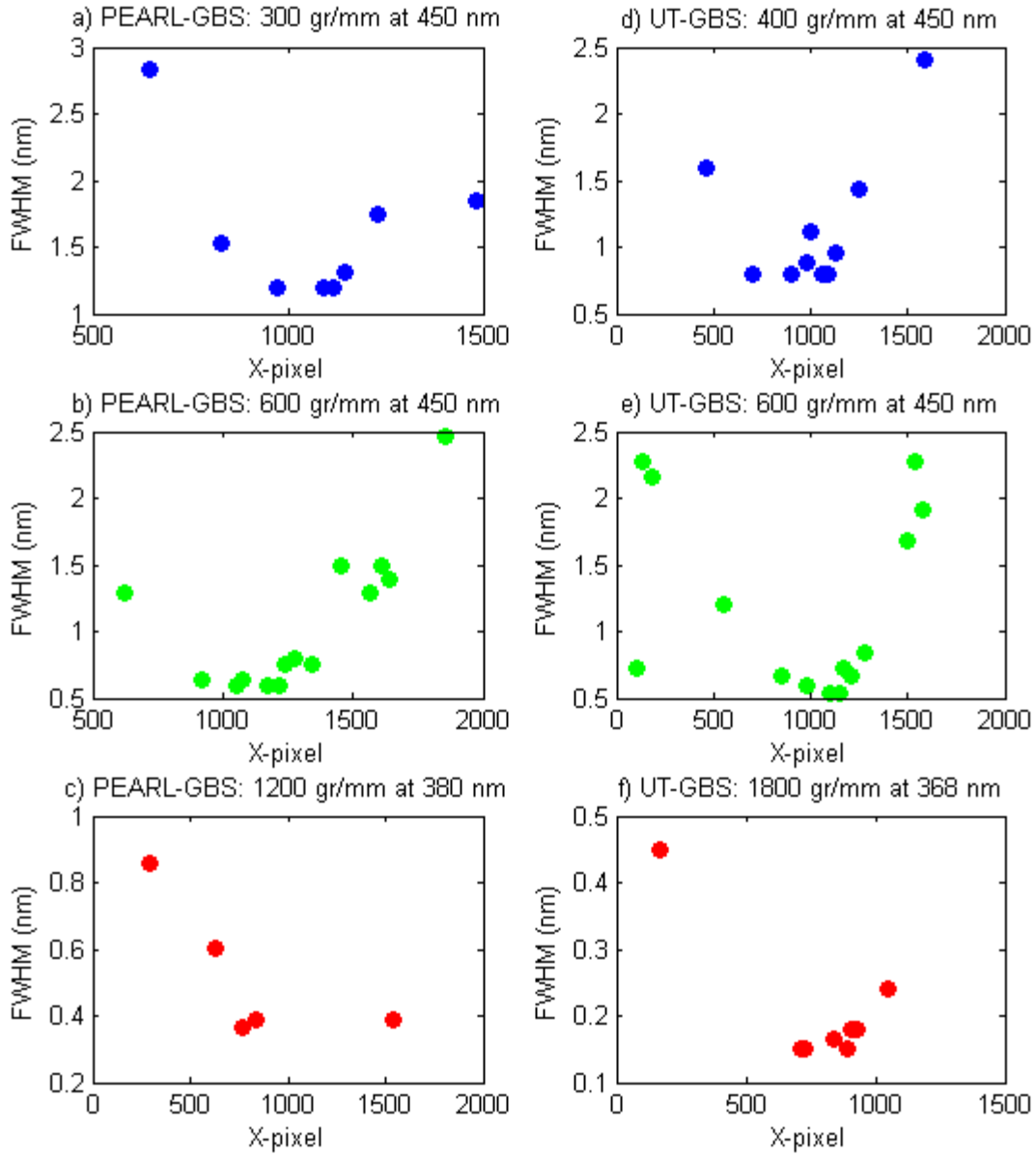

Figure 2.4: Resolution at Eureka in spring 2009 of the PEARL-GBS (a) 300 gr/mm grating centered at 450 nm, (b) 600 gr/mm grating centred at 450 nm, (c) 1200 gr/mm grating centered at 380 nm and of the UT-GBS (d) 400 gr/mm grating centered at 450 nm, (e) 600 gr/mm grating centered at 450 nm, (f) and 1800 gr/mm grating centered at 368 nm.

this case, a spectrometer, at wide angles and is focused at different locations than light entering a lens along the focal plane [e.g., *Hecht*, 1987].

Spherical aberration is a type of monochromatic aberration which causes blurring of the image [e.g., *Hecht*, 1987] and is shown in Figure 2.5. Light incident on the edges of the lens is focused closer to the lens than light incident along the focal plane. The ideal focal point in such a system is called the "circle of least confusion" and is indicated by "LC". The circle of least confusion is different from the focal point of light along the optical axis. Spherical aberration can be reduced by narrowing the aperture of the instrument, but this restricts the amount of light entering the instrument, which reduces the signal-to-noise ratio [e.g., *Hecht*, 1987].

Coma occurs when an object is not centered on the optical axis and light enters a lens at an angle which is not perpendicular to the lens [e.g., *Hecht*, 1987]. This causes the image to have different magnifications across the plane perpendicular to the focal plane as shown in Figure 2.6.

2.2.3 Characterization of Aberrations in the Triax-180 Spectrometers

In order to characterize the aberrations for the Triax-180 spectrometers, tests were performed on the PEARL-GBS in spring 2010 at Eureka*. An approximate point source was shone into the

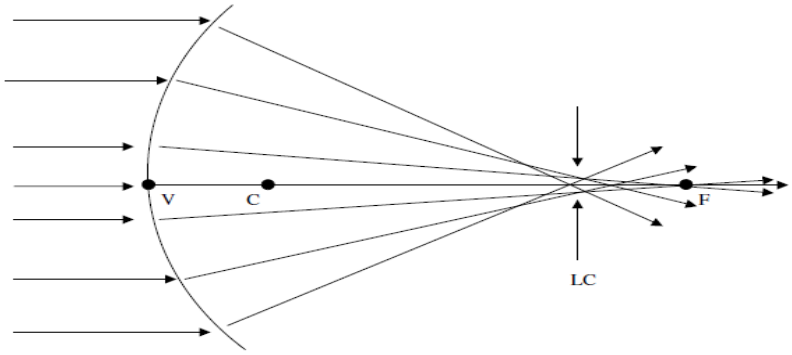

Figure 2.5: Schematic of spherical aberration, from *Farahani* [2006].

* Testing procedures based on advice from T. McElroy.

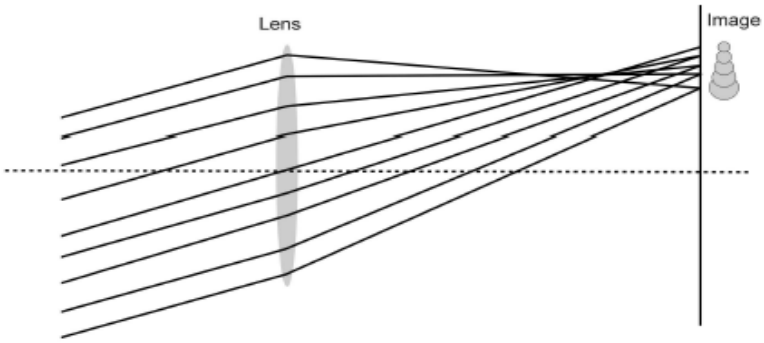

Figure 2.6: Schematic of coma, from *Fraser* [2008].

entrance slit of the PEARL-GBS at different angles so that limited portions of the mirrors and the diffraction grating were illuminated.

A schematic of the aberrations test setup is shown in Figure 2.7. The input optics were removed from the PEARL-GBS. A 0.1% neutral density filter was placed in front of the slit and the 600 gr/mm grating was centered at 450 nm. The CCD of the PEARL-GBS was focused around the 435.8 nm mercury line with the mercury lamp close to the slit so that it illuminated the slit from many angles simultaneously. The mercury lamp was then placed 1 m away from the slit and was centered in the field-of-view of the spectrometer by moving the lamp up, down, left, and right until the maximum signal was obtained. The lamp location of maximum signal is referred to here as the "middle." Then the lamp was then moved up and down until the signal was reduced by approximately 60%. These lamp locations and are referred to as the "top" and "bottom", respectively. The lamp was then moved to left (into the page of Figure 2.7) and right of the slit until the signal was reduced to approximately 60% and these locations are referred to here as "left" and "right" respectively.

The resulting mercury lines are shown in Figure 2.8 for the mercury lamp positioned at various locations for the 365.0 nm (panel a), 404.7 nm (panel b), 435.8 nm (panel c), and 546.1 nm (panel d) mercury lines. All measurements were taken for a 40-ms exposure time. For all mercury lines, moving the lamp from left to right of the slit caused the mercury lines to move in

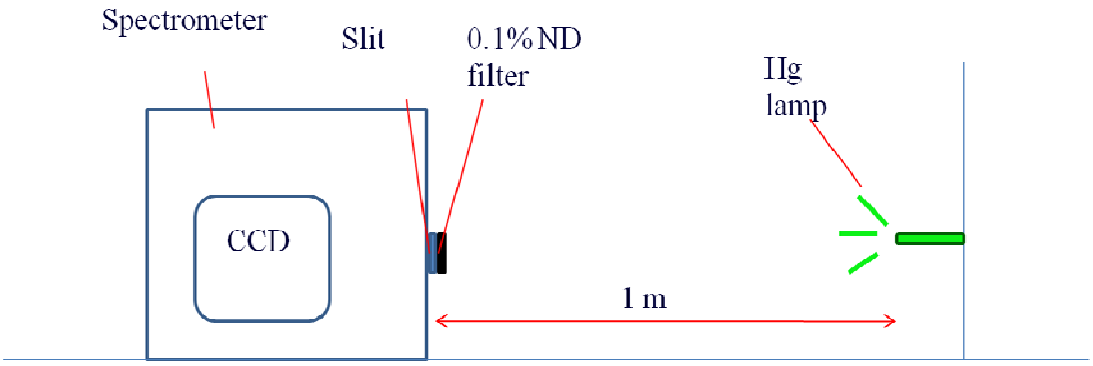

Figure 2.7: Schematic of spectrometer aberrations test.

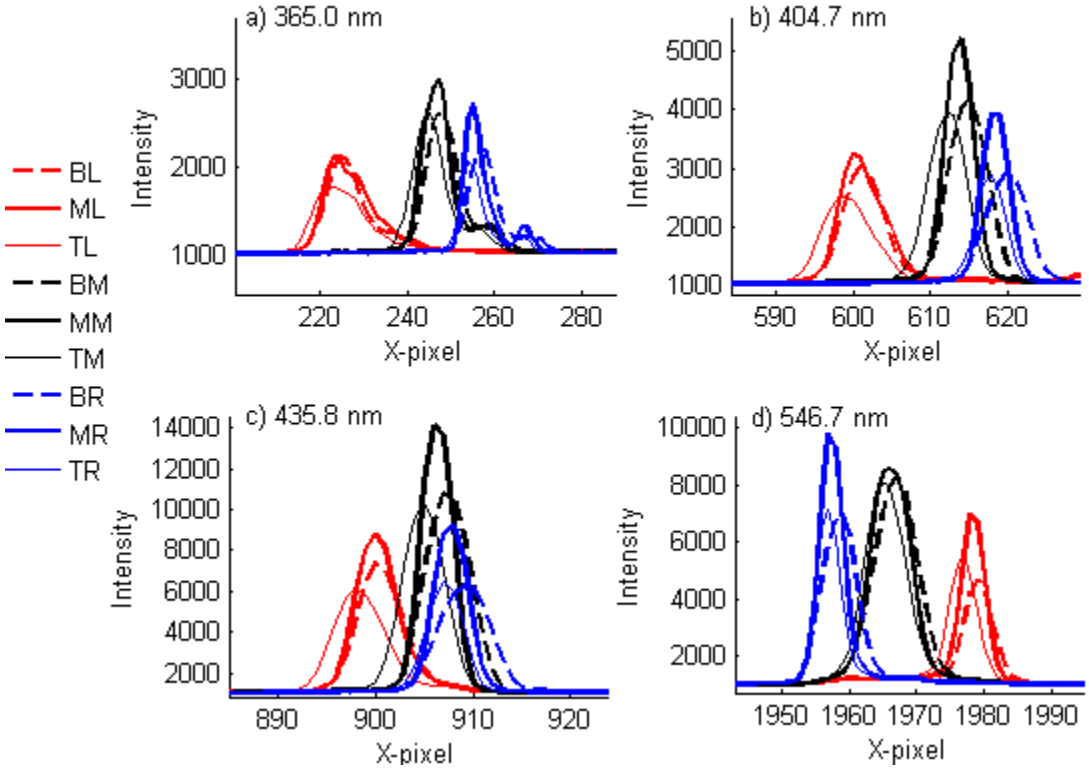

Figure 2.8: Results of spectrometer aberrations test for the PEARL-GBS. The (a) 365.0 nm, (b) 404.7 nm, (c) 435.8 nm, and (d) 546.1 nm mercury lines for source shone on the PEARL-GBS slit from the bottom-left (red dash), middle left (thick red line), top left (thin red line), bottom middle (black dash), middle (thick black line), top middle (thin black line), bottom right (blue dash), middle right (thick blue line), and top right (thin blue line).

X-pixel across the CCD. Since the instrument was focused around the 435.8 nm mercury line, the spread in X-pixel of the 435.8 nm line at the center of the CCD (panel c) is smaller than the spread at the edges of the CCD (panels a, d). This suggests that limiting the angles at which light enters the slit could significantly improve the resolution of the instrument.

When the lamp is moved up and down relative to the slit, small changes in the width and pixel location of the mercury line are observed. This suggests that by limiting the height of the beam (or the Y-pixels of the CCD) small improvements to the resolution of the instrument could be made.

When the input optics are placed in front of the spectrometer, the liquid light-guide scrambles the image of the incoming light. Therefore, the mercury lines do not change in shape or resolution as the mercury lamp is moved across the field-of-view of *L1*. However, the light focused by *L3* enters the spectrometer at various angles. Therefore the spectrum is blurred across X-pixels of the CCD, causing the non-Gaussian line-shapes at the edges of the CCD observed in the lamp tests in Figure 2.3.

In an effort to reduce aberrations, attempts were made to change the focus of the instrument without disassembling the spectrometer. The slit of the spectrometer was moved closer to and further from the collimating mirror, which changed the instrument focus, but did not improve the aberrations. It was observed while focusing the spectrometer that, by moving the CCD closer to the focusing mirror, the mercury lines to the left side of the CCD come into focus. As the CCD is moved further from the focusing mirror, the mercury lines on the right side of the CCD come into focus. This suggests that the CCD or the focusing mirror should be tilted slightly, so that all X-pixels of the CCD are in focus at once. Unfortunately, this cannot be achieved without making significant changes to the spectrometer. Therefore, spring 2010 spectrometer improvement efforts were focused on limiting light entering the slit from wide angles.

2.2.4 Improvement to UT-GBS Resolution in Spring 2010

In spring 2010, steps were taken to improve the resolution of the UT-GBS. First, the input optics were tested qualitatively. The f-number matcher was removed from the instrument and a halogen lamp was shone into the optics tube, approximately 3 m from the instrument. *L1* was

moved relative to the liquid light guide so that light was focused on the liquid light guide (see Figure 2.1). The light was then observed by placing a white card at various locations along the optical axis. Through these tests, it was found that the collimated light between *L2* and *L3* diverged as the white card was placed further from *L2*.

To test this more quantitatively, the input optics were returned to the instrument and a mercury lamp was placed above *L1* so that it roughly filled the field-of-view of the instrument. The spectrometer then took a series of measurements with the 600 gr/mm grating centered at 450 nm and a 25% neutral density filter placed between *L1* and the liquid light guide. A series of measurements were taken with various input optics configurations, as described below. These measurements were taken at various exposure times, so the relative intensities of the spectra are not significant.

The mercury lines from these tests are shown in Figure 2.9 at 365.0 nm (panel a), 404.7 nm (panel b), 435.8 nm (panel c) and 546.1 nm (panel d). The mercury lines for the original measurements (thin black line) are non-Gaussian at the edges of the CCD, like the lines shown in Figure 2.3 for the PEARL-GBS. When *L2* was moved as close to *L3* as the input optics would permit (with the liquid light guide kept at a fixed distance from *L2*), the mercury lines (black dashed line) became slightly more Gaussian, with smaller FWHM. Furthermore, the X-pixels of the mercury line peaks were shifted.

In order to improve resolution further, additional tests were performed. A series of light limiters were placed in the input optics between *L2* and *L3* to prevent the light from entering the slit at large angles from the optical axis. A diagram of the light limiters as viewed facing the slit of the spectrometer is shown in Figure 2.10. The resulting mercury lamp spectra are also plotted in Figure 2.9 for the 8-mm (red), 5-mm (green), 4.5-mm (cyan), and 3.6-mm (blue) light limiters. Narrower light limiters have better resolutions at the edges of the CCD, but less signal. To balance these requirements, the 5-mm light limiter was selected and used for the rest of the campaign.

The CCD was then refocused and the mercury lines for the "optimized" 2010 instrument are also shown in Figure 2.9 (thick black line) and are approximately Gaussian across the full CCD.

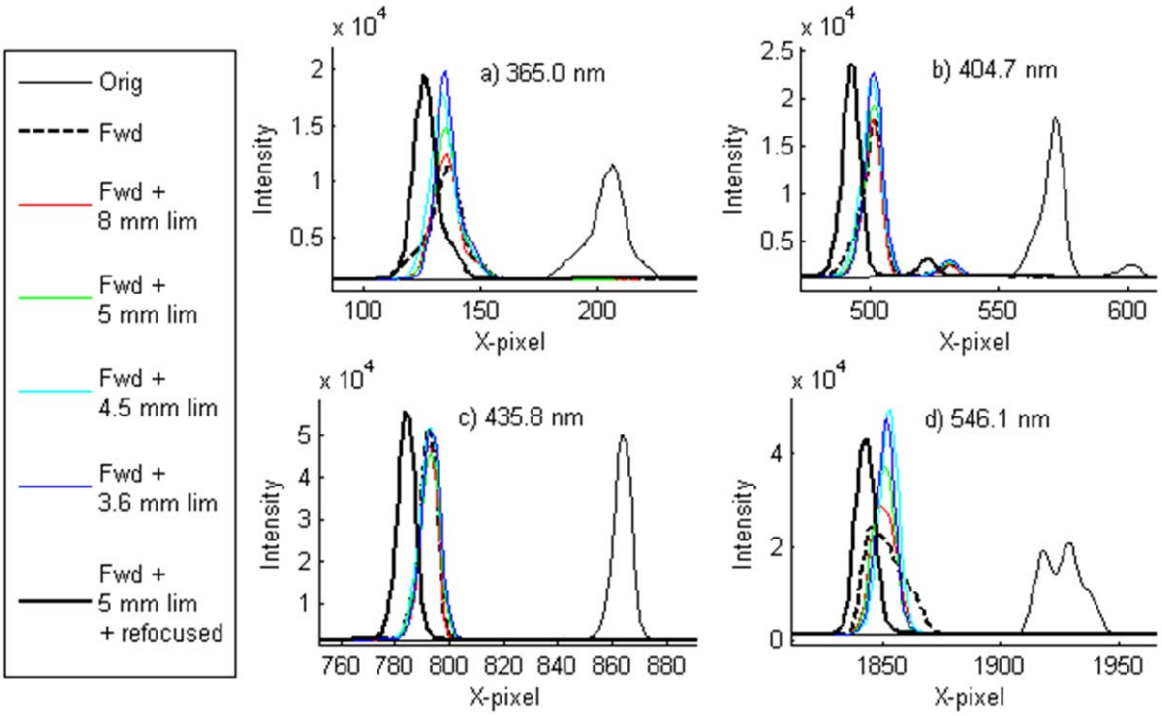

Figure 2.9: The (a) 365.0 nm, (b) 404.7 nm, (c) 435.8 nm, and (d) 546.1 nm mercury lines measured by the UT-GBS with the old input optics (thin black line); L2 moved forward (dashed black line); L2 moved forward with a 8 mm (red) , 5 mm (green), 4.5 mm (cyan), and 3.6 mm (blue) limiters; and L2 moved forward with a 5 mm limiter and the instrument refocused.

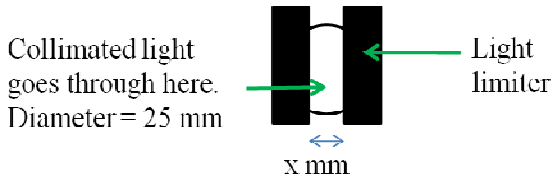

Figure 2.10: Diagram of light limiter placed in collimated beam between *L2* and *L3*.

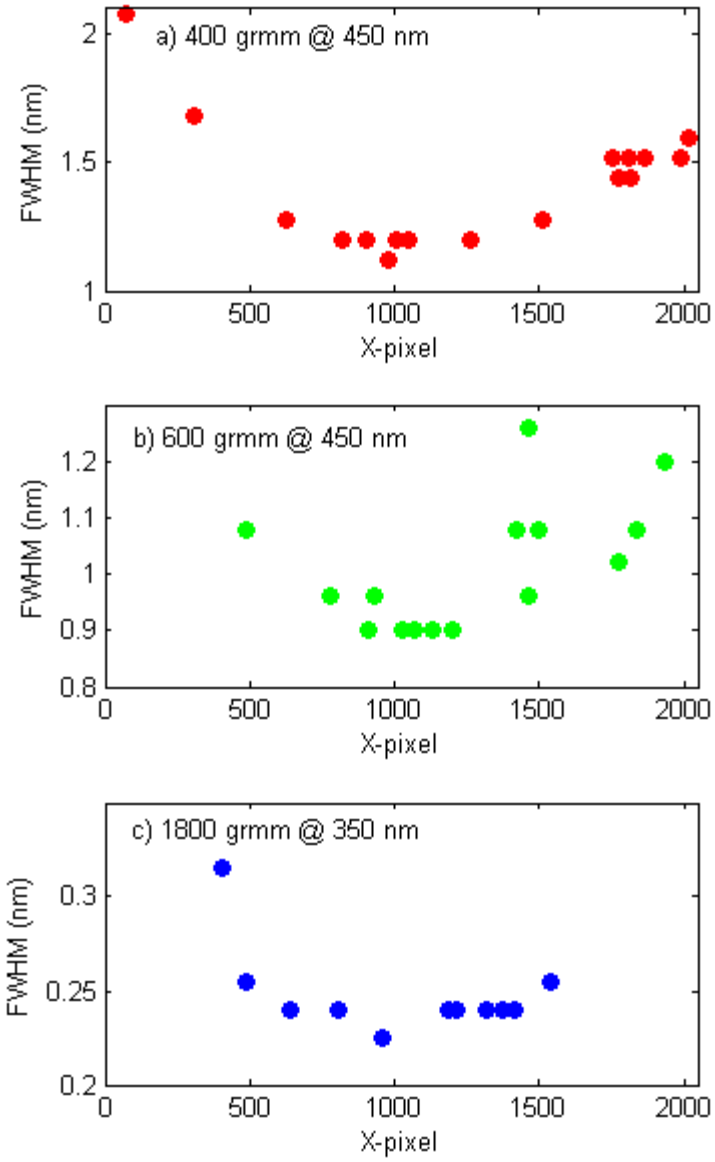

Figure 2.11: UT-GBS resolution in 2010 for (a) the 400 gr/mm grating at 450 nm, (b) the 600 gr/mm grating at 450 nm, and (c) the 1800 gr/mm grating at 350 nm.

Lamp tests with the mercury, xenon, and neon lamps were performed and the resulting resolutions are shown in Figure 2.11 for the 400 gr/mm grating at 450 nm (panel a), the 600 gr/mm grating at 450 nm (panel b), and the 1800 gr/mm grating at 350 nm (panel c). The resolutions are slightly worse than in previous years at the center of the CCD, but, the range ofFWHM values are much smaller than in previous years (Figure 2.4). Due to these improvements, the configuration with the light-limited and adjusted input optics was used for the remainder of 2010.

2.2.5 Improvement to PEARL-GBS Resolution in Spring 2010

In spring 2010, the PEARL-GBS liquid light guide was replaced with a spot-to-slit fibre bundle in order to maximize signal and reduce light entering the spectrometer from the wide angles. This allows the instrument to intercept the circular beam of sunlight at *L1* and transfer most of that light into a narrow rectangular beam at *L2* and eventually at the entrance slit. A schematic of the spot-to-slit fibre bundle is shown in Figure 2.12, with dimensions as indicated. Mercury lines were measured through the input optics with this new fibre bundle and are shown in blue in Figure 2.13 at 365.0 nm (panel a), 404.7 nm (panel b), 435.8 nm (panel c) and 546.1 nm (panel d). The FWHM of the lines and the shape of the lines are improved significantly compared with the lines through the spot-to-spot liquid light guide as shown in Figure 2.3.

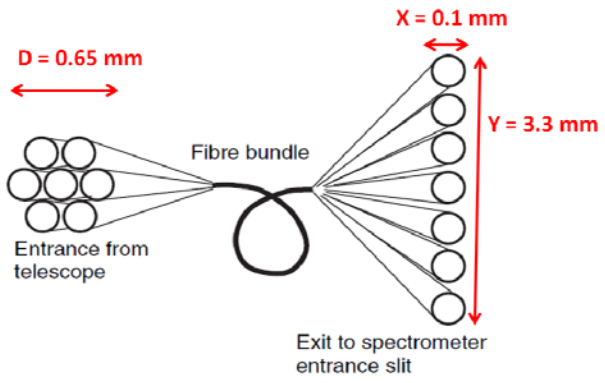

Figure 2.12: Schematic the PEARL-GBS spot-to-slit fibre bundle, adapted from *Platt* [2008].

Unlike the UT-GBS light-limiter system, the slit-to-spot fibre bundle system also maximizes signal to the instrument by transferring light efficiently directly into the slit. Therefore, further improvements could be made to the resolution of the instrument. In order to reduce the blurring of light entering the top and bottom of the slit, the Y-pixel binning in the CCD was reduced to Y-pixels #200-512 instead of the full CCD. Note that due to an alignment problem, the maximum intensity fell around pixel #400. This was corrected by ISA technicians in summer 2011. The resulting mercury lines for this test are also shown in Figure 2.13 in red.

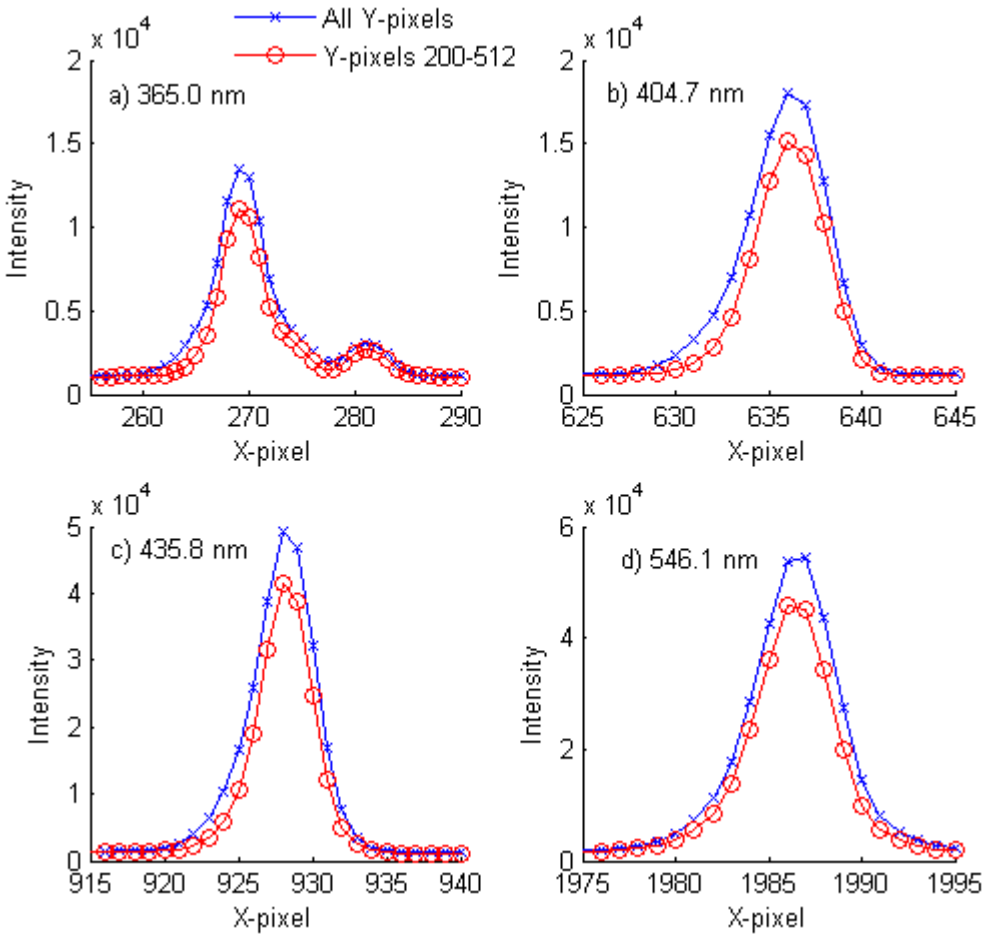

Figure 2.13: The (a) 365.0 nm, (b) 404.7 nm, (c) 435.8 nm, and (d) 546.1 nm mercury lines measured by the PEARL-GBS 600 gr/mm grating with the spot-to-slit fibre bundle in spring 2010 for binning all Y-pixels of the CCD (blue X) and limited binning of the Y-pixels of the CCD (red circles).

With the new setup in place, a series of mercury, neon, and xenon lamp tests were taken with the PEARL-GBS and are shown in Figure 2.14 for full binning of the CCD (black X) and partial binning of the CCD (closed circles) for the 300 gr/mm grating centered at 450 nm (panel a), 600 gr/mm grating centered at 450 nm (panel b), and 1200 gr/mm grating centered at 350 nm (panel c). The resolution is improved vastly over the 2009 resolution for the PEARL-GBS shown in Figure 2.4. Note that there are many more data-points in the 2010 resolution tests than in 2009 because many more lines could be resolved. Due to these improvements, the configuration with the spot-to-slit fibre bundle was used for the remainder of 2010.

2.2.6 Instrument Resolution and Sampling from 1998-2011

Summaries of the sampling and resolution are shown for the UT-GBS in Table 2.3 and the PEARL-GBS in Table 2.4. As both instruments are refocused at the beginning of each campaign and occasionally at other times, the resolution and sampling change slightly campaign-to-campaign. The UT-GBS sampling changed with each CCD because the physical size of the pixels differed. Both the UT-GBS and PEARL-GBS resolutions improved in 2010 due to the modified input optics described in Sections 2.2.4 and 2.2.5 respectively. The PEARL-GBS sampling was below 4.5 pixels/FWHM in 2010, leading to possible undersampling errors [*Roscoe et al.*, 1996]. Therefore, in 2011, the PEARL-GBS 0.05 mm slit was replaced with a 0.1 mm slit in order to resolve this issue. Furthermore, a new spot-to-slit fibre bundle replaced the UT-GBS light-limiter. During the spring 2011 campaign, there were numerous instrument failures. Therefore, there was not time to focus and align the instruments with the same care as in 2010. Therefore, the instrument resolution worsened between 2010 and 2011.

2.3 Dark Signal

Dark signal is the signal measured by the detector when the shutter of the instrument is closed. It comprises the bias, an offset to the CCD count, and the dark current. Dark current is caused by thermal energy from the CCD and therefore increases with CCD temperature (T) and exposure time (t) according to the relationship

$$dark\ current = Ate^{-B/T}, \tag{2.2}$$

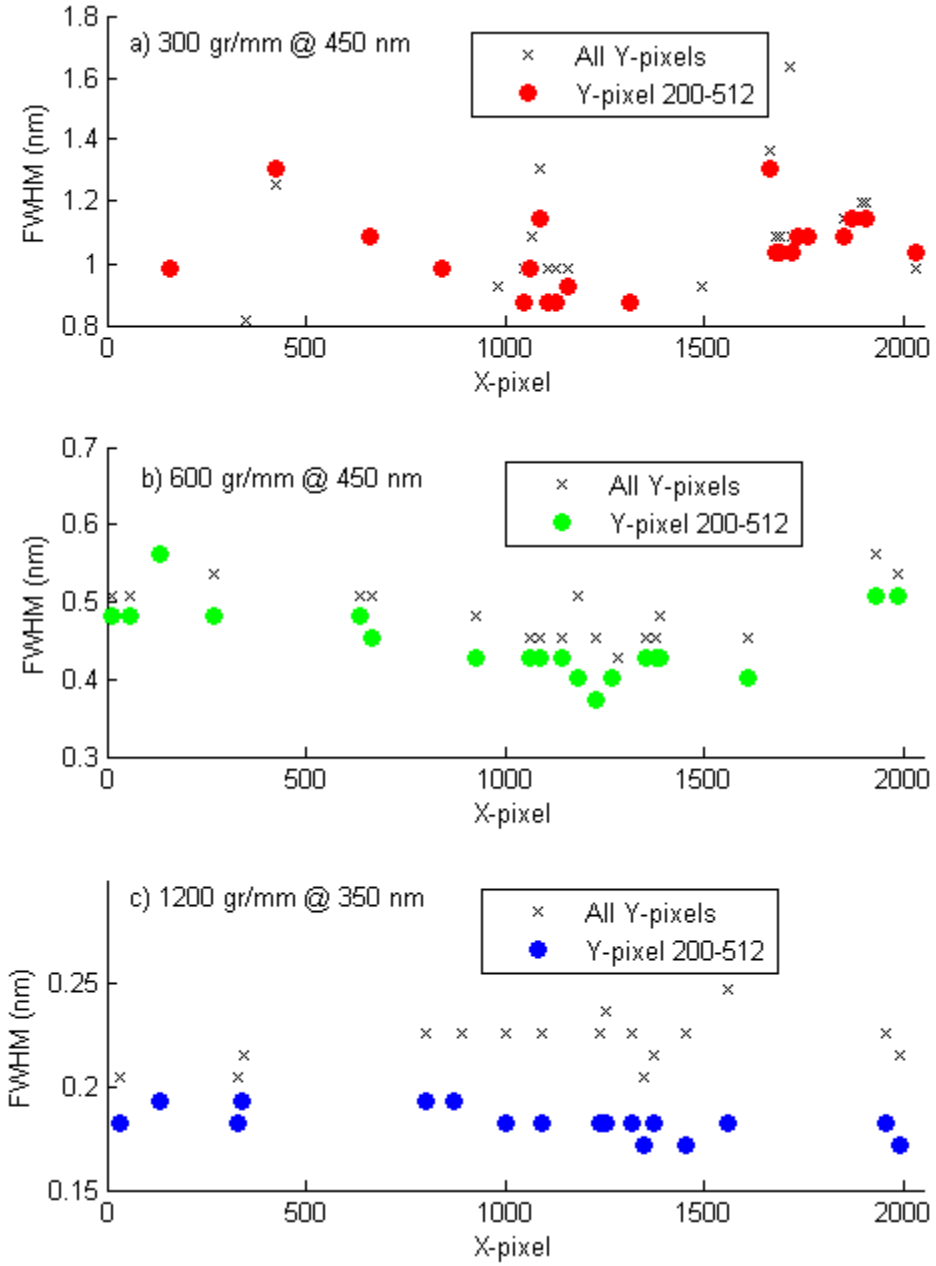

Figure 2.14: PEARL-GBS resolution in spring 2010 for binning the full CCD (black x) and for partial binning of the CCD (circles) for (a) 300 gr/mm grating centered at 450 nm, (b) 600 gr/mm grating centered at 450 nm, and (c) 1200 gr/mm grating centered at 350 nm.

Table 2.3: UT-GBS sampling and resolution 1998-2011.

	Sampling (pixel/FWHM)			Resolution (nm)		
Grating (gr/mm)	400	600	1800	400	600	1800
Original CCD: 1998-Eu2004[a]	7-20	6-20	7-16	0.8-5.4	0.5-2.3	0.2-0.8
Loaner CCD: MANTRA 2004[a]	3-19	3-18	3-12	"	"	"
New CCD: 2005-2009[b]	5-14	5.5-16	7-12	"	"	"
New CCD + input optics: 2010	7-13	7.5-13	7.5-10.5	1.1-2.1	0.9-1.3	0.2-0.3
New CCD + new fibre: 2011	7-13	7.5-13	7.5-10.5	0.9-1.4	0.6-2.0	0.2-0.3

[a] Values combined from [*Fraser*, 2008] and [*Farahani*, 2006].
[b] Values from [*Fraser*, 2008].

Table 2.4: PEARL-GBS sampling and resolution 2006-2010.

	Sampling (pixel/FWHM)			Resolution (nm)		
Grating (gr/mm)	300	600	1200	300	600	1200
Original setup: 2006-2009[a]	5-14	4.5-16	7-12	1.0-3.0	0.5-2.5	0.2-1.8
New spot-to-slit fibre: 2010	4-6	3.5-5	4-4.5	0.9-1.3	0.4-0.6	0.17-0.19
New spot-to-slit fibre + slit: 2011	7-15	7-15	7-12	1.4-3.0	0.7-1.5	0.3-0.5

[a] Values from [*Fraser et al.*, 2009].

where A and B are constants which describe the detector [*Mackay*, 1986]. Since the data acquisition software prevents measurements from being taken for CCD temperatures above 206 K for the UT-GBS and 207 K for the PEARL-GBS, an increase in CCD temperature is not expected to lead to significant dark current.

In order to check the performance of the detectors and the spectrometers, the dark current and bias of the GBS instruments are measured at the beginning each campaign. To do this, a series of dark signal, or closed-shutter measurements, are taken at various exposure times. For each X-pixel, the dark signal is plotted against the exposure time. A linear fit is applied and the dark current is the slope (counts/second) and the bias is the y-intercept (counts). Spring 2009 UT-GBS dark current (panel a) and bias (panel b) and PEARL-GBS dark current (panel c) and bias (panel d) are shown in Figure 2.15. These values are typical and vary only by several counts each year. Dark current and bias information for the previous UT-GBS CCDs are presented by *Fraser* [2008] and *Farahani* [2006]. The dark current from this test multiplied by the exposure time and the bias are both subtracted from each measurement prior to DOAS processing.

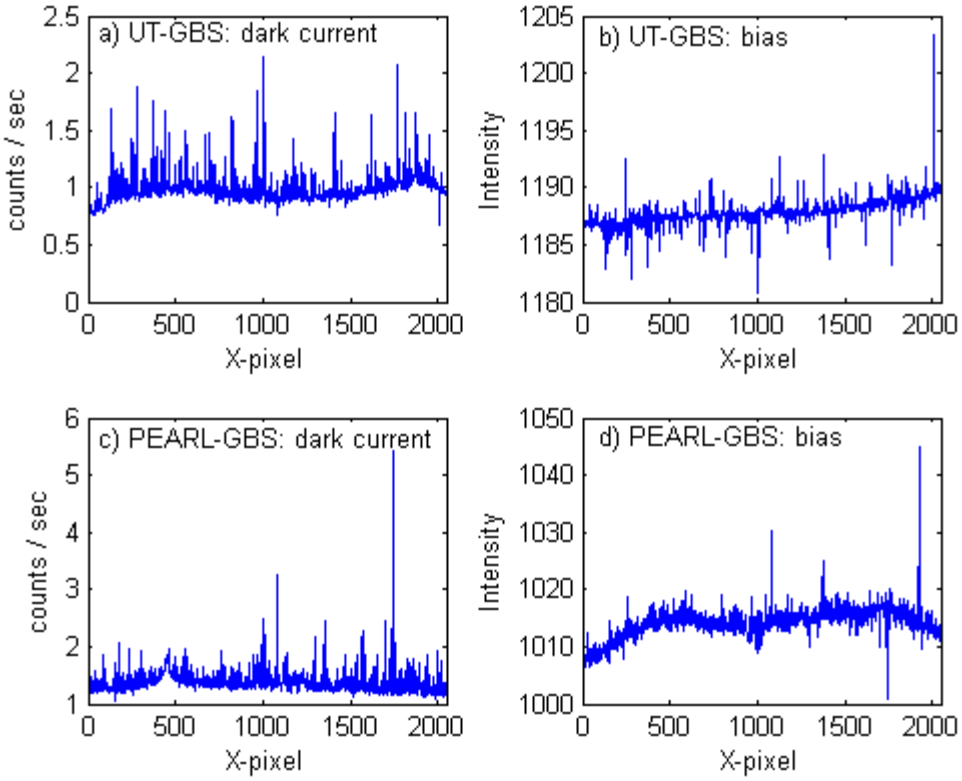

Figure 2.15: UT-GBS (a) dark current and (b) bias and PEARL-GBS (c) dark current and (d) bias.

2.3.1 Light Leaks

In August 2008, during routine testing at Eureka, the dark signal in both instruments was much higher than in previous campaigns. For the UT-GBS, this was caused by light leaks at the top of the CCD head and at the Triax-180 electronics connections. For the PEARL-GBS, light leaks were found at the base of the spectrometer. They were corrected in spring 2009.

In order to understand the effect of these leaks on measurements, the UT-GBS and PEARL-GBS 2006-2008 routine dark signal measurements were analyzed. All dark signal measurements were taken for a one-second exposure time. The average dark signal count across the CCD was calculated and is plotted against Julian day in Figure 2.16 for the UT-GBS at Eureka in blue and Toronto in red (panel a) and the PEARL-GBS (panel b). The large spikes in dark signal (around

day 235 in 2007 and day 2 in 2008 for the UT-GBS and around 235-290 in 2007 for the PEARL-GBS) were caused by shutter failures. Both instruments have larger average counts across the CCD in the summer months than the winter months, because there is more sunlight leaking into the instruments. The PEARL-GBS has larger dark signal counts during summer months than the UT-GBS. Unfortunately, these light leaks cannot be characterized and subtracted from the measurements because they depend on constantly changing light conditions and the instrument setup. Therefore, an offset correction was applied during the DOAS analysis.

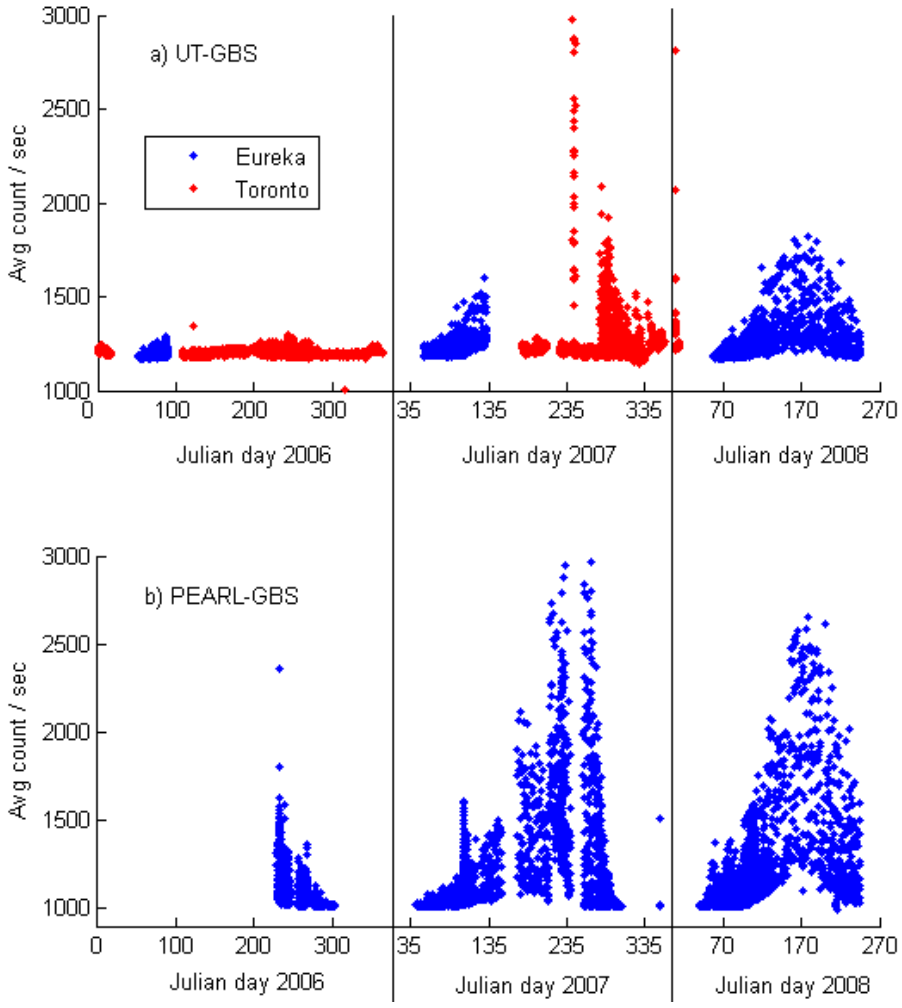

Figure 2.16: Average dark signal across the CCD from 2006-2008 for (a) the UT-GBS in Toronto (red) and Eureka (blue) and (b) the PEARL-GBS in Eureka.

2.3.2 Relationship between CCD Temperature and Dark Signal

In Figure 2.17, the average closed shutter count from 2006-2008 is plotted against CCD temperature for the UT-GBS (panel a) and the PEARL-GBS (panel b). Most measurements are within 200.5-201.5 K for the UT-GBS and 203.5-205.5 K for the PEARL-GBS. There is no clear correlation between CCD temperature and dark signal, likely because light leaks dominate. For the UT-GBS, more high CCD temperatures are observed in Toronto because the instrument housing overheated frequently in summer months. On these occasions, an increase in dark signal is observed as the CCD temperature increases, as suggested by Equation 2.2. This suggests that for most measurements, the CCD temperature does not have a significant impact on dark signal.

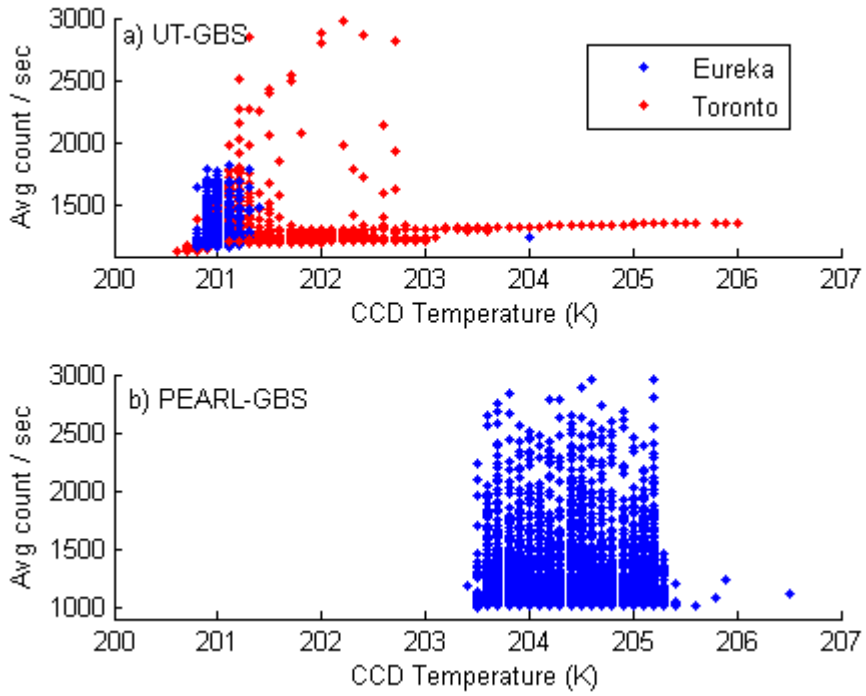

Figure 2.17: Average dark signal versus CCD temperature from 2006-2008 for (a) the UT-GBS in Eureka (blue) and Toronto (red) and (b) the PEARL-GBS in Eureka.

2.4 Stray Light

Stray light is caused by reflection off optical elements, the detector surface, and spectrometer walls, as well as grating effects, such as grating ghosts [*Platt and Stutz*, 2008]. For monochromatic light sources, the fraction of stray light is on the order of 10^{-5} to 10^{-3}, while for broad-band light sources, such as the sun, it increases to the order of 10^{-3} to 10^{-1} [*Zong et al.*, 2006]. Even for a high quality spectrometer, with 10^{-3} stray light, significant errors are introduced in DOAS fits when considering gases with small absorption features <0.1% of the solar spectrum, such as BrO. Therefore, stray light is often the dominant source of error in DOAS measurements [*Zong et al.*, 2006].

In order to characterize the stray light of the GBS instruments, three measurements are taken at a fixed exposure time: one normal open shutter measurement, one open shutter measurement with a red filter (> 575 nm), and one dark spectrum. The red filter is used to limit incoming light to the spectrometer to wavelengths outside of the desired measurement range (350-550 nm for the 600 gr/mm centered grating at 450 nm). If there was no stray light, the red filter measurement would be identical to a dark spectrum. The stray light is then calculated by

$$stray\ light = \left(\frac{red\ -dark}{open-\ dark}\right) \quad . \tag{2.3}$$

In Figure 2.18, the stray light for the 600 gr/mm grating in 2010 using zenith-scattered sunlight as a source is plotted for the UT-GBS (panel a) and the PEARL-GBS (panel b). The stray light for both instruments is less than 10^{-3} over the whole measurement region. These values are lower than those measured by *Fraser* [2008] because the sun, which has more signal in the UV, was used instead of the halogen lamp source. Stray light tests were performed for other gratings and the stray light was found to be similar for wavelengths above 325 nm, where the signal of sunlight becomes very low.

In this work, residual stray light has been partly accounted for using a polynomial offset correction during the DOAS procedure. However, full characterization of stray light is possible with a monochromatic set of laser sources and leads to improvement in stray light error of 1-2 orders of magnitude [*Zong et al.*, 2006].

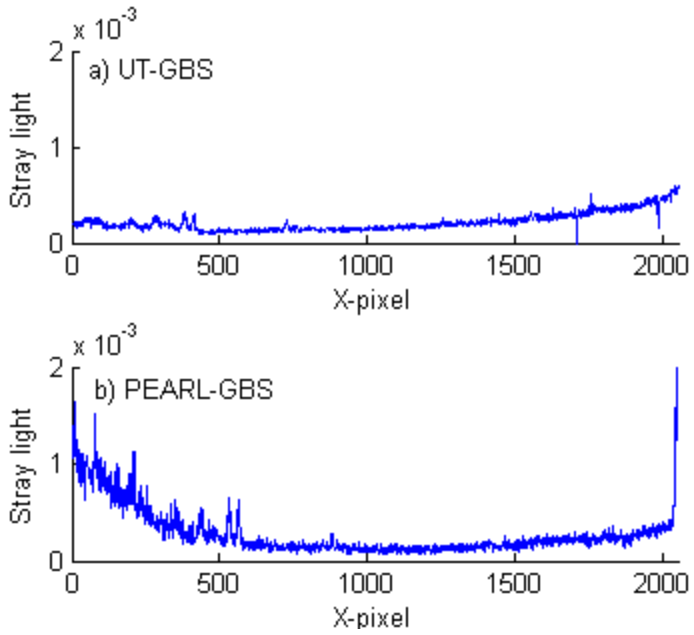

Figure 2.18: Stray light measured with the 600 gr/mm grating of (a) the UT-GBS and (b) the PEARL-GBS.

2.5 Polarization

Due to scattering effects in the atmosphere, the polarization of sunlight varies with SZA. Since the GBS gratings are sensitive to polarization, light must be depolarized to avoid errors in DOAS retrievals. To check that the GBS liquid light guides or fibre bundles are depolarizing light, a polarization test is performed each campaign. The spectrum of a quartz-halogen lamp is measured with a polarizer placed above *L1*. Note that since the halogen lamp is partly polarized, this changes the signal of the incident light; therefore this test needs to be improved in the future*. The polarizer is rotated at intervals of 45° and ratios of lamp spectra are then taken. Sample ratios for 0°/90° are shown in Figure 2.19 for the UT-GBS (panel a) and the PEARL-GBS (panel b). These measurements were taken with the 600 gr/mm grating centered at

* Personal communication with X. Zhao, 28 August 2011

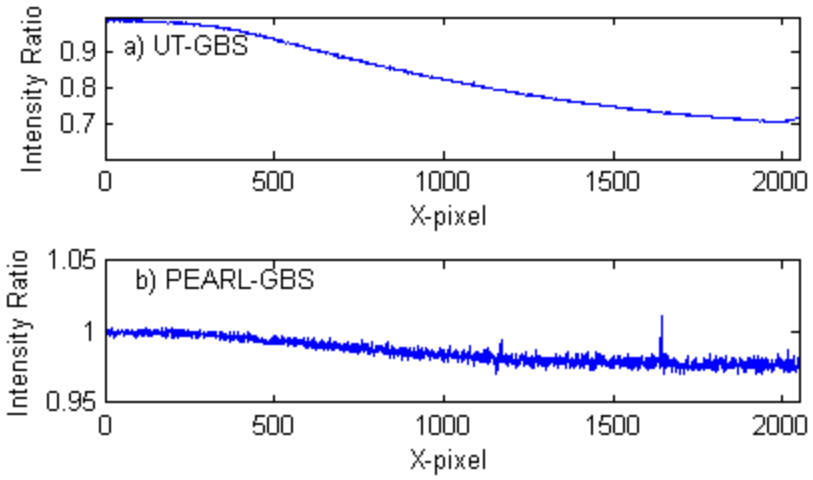

Figure 2.19: Polarization tests measured with the 600 gr/mm grating. Intensity of light from halogen lamp with polarizer at 0° ratioed to that with polarizer at 90° for (a) UT-GBS and (b) PEARL-GBS.

450 nm. The effect of polarization varies smoothly with wavelength and, therefore, should not introduce large errors to DOAS fits.

2.6 Additional Instrument Effects

The tests described above do not account for some of the systematic errors observed in the GBS measurements. SZA-dependent residuals were observed for both UT-GBS and PEARL-GBS measurements in the 450-550 nm fitting region (see Appendix B). This suggests a polarization dependence which is not captured by the tests described above. This may be linked to a strangely-behaved line at 506 nm, measured in the mercury lamp spectrum with the 600 gr/mm grating centred at 450 nm. Note that this line appears in the manufacturer's spectral figures, but is not deemed useful for wavelength calibration [*Newport*, 2011]. The intensities of all other mercury lines in the measurement window (365 nm, 405 nm, 435.8 nm, and 546.1 nm) vary gradually as the mercury lamp is moved across the field-of-view and peak when the mercury lamp is directly above *L1*. However, at 506 nm, the intensity varies sharply with the position of the mercury lamp over *L1* and reaches maximum intensity when the lamp is not directly above *L1*. Furthermore, when a diffuser is placed above the input optics, the 506 nm line disappears

completely. This process is not fully understood and needs to be properly characterized for various gratings and target wavelengths, with polarizers and diffusers.

Temperature dependence of GBS measurements has never been tested directly. However, there is strong evidence that temperature changes throughout the day reduce the measurement quality (see Sections 3.3.4 and 4.1.3.1). These changes are caused by the thermal expansion of materials inside the spectrometer and can be prevented by thermostating the instrument [*Platt and Stutz*, 2008]. Attempts were made to control the temperature in 2010, using heating pads and foam insulation, but the temperature rose quickly above operational guidelines. This was not pursued in 2011 due to time-constraints and instrument problems during the campaign.

Additionally, interpixel variability can play a role for sensitive measurements such as BrO and OClO. GBS spectra shift across CCD X-pixels, due to temperature changes (see Sections 3.3.4 and 4.1.3.1). Therefore, during the DOAS procedure, pixels with slightly different properties are ratioed. A previous attempt to measure GBS inter-pixel variability and correct spectra did not improve DOAS results [*Farahani*, 2006]. However, due to recent improvements to the spectra and analysis techniques, interpixel variability corrections may improve present GBS retrievals.

Finally, measurements taken with filters were found to be of worse quality than measurements taken without filters (see Section 4.1.3.1). This could not be accounted for by signal-to-noise. These uncertainties may be introduced by Fabry-Perot etalon structures, which arise from interference patterns when light encounters two reflecting surfaces [e.g., *Hecht*, 1987]. These structures can be caused by reflective neutral density filters and the surface of CCD detectors [*Stutz and Platt*, 1993].

2.7 UT Suntracker

The UT Suntracker was developed at the University of Toronto for UV-visible and infrared spectrometers. It is made from off-the-shelf parts using open-source software, and, once fully tested, the design and control software will be made publicly available. For DOAS instruments, the UT Suntracker can be used to enhance sensitivity to tropospheric and boundary layer trace gases such as BrO and HCHO, through the direct-sun and MAX-DOAS viewing geometries (see

Section1.3.4). Furthermore, with lunar tracking, DOAS measurements can be extended into polar night.

The UT Suntracker was assembled and tested in Toronto from 2006-2007. In February 2008, it was installed permanently above the PEARL-GBS at Eureka so that the instrument could take zenith-sky, direct-sun (with passive tracking), and MAX-DOAS measurements. In summer of 2009, another UT Suntracker was installed above the UT-GBS during the CINDI campaign to allow for MAX-DOAS measurements [*Roscoe et al.*, 2010]. Additional development on active tracking is currently underway at Dalhousie University.

2.7.1 Design

Figure 2.20 shows a photograph (a) and diagram (b) of the UT Suntracker. Light enters Mirror 1, a 15-mm diameter round mirror, at a 45° angle and is reflected off Mirror 2, a 102x127 mm rectangular mirror, and down into the instrument. Mirror 1 is controlled by an azimuthal step motor (Newport URS150BCC) and an elevation step motor (Newport URS75BCC), so that the mirror is always angled at 45° from the targeted incoming sunlight. Two SMC 100CC Motion Controllers act as an interface between the tracker and the computer. For tracker development, test-grade mirrors were used. For the UV-visible measurements at Eureka and Cabauw, these were replaced with ¼-wave fine annealed pyrex UV-enhanced aluminum mirrors that were custom-ordered from Advanced Optics.

2.7.2 Software

The UT Suntracker is controlled by the Trax2.4 Python program. Trax2.4 interprets commands received over user datagram protocol (UDP) and controls the UT Suntracker motors using the Universal Serial Port Python Library [*Barona*, 2001]. The user can command Trax2.4 to move the motors to fixed positions or to passively track a body (sun or moon) based on the latitude, longitude, and time, using the PyEphem Module [*Rhodes*, 2010]. Trax2.4 is also able to monitor the position of the sun using a NetCamXL 640 camera and the Pythonware Image Library [*Lundh*, 2005]. Active tracking, using the camera, has since been implemented in the system by researchers at Dalhousie University. However, for the PEARL-GBS passive tracking was used for 2008-2011.

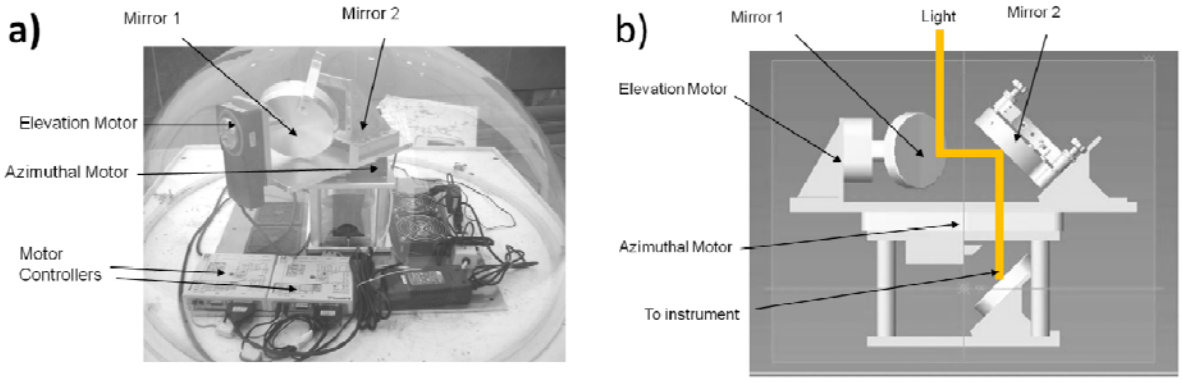

Figure 2.20: The University of Toronto Suntracker. (a) Photo taken by S. Like. (b) Schematic modified from figure by C. Midwinter.

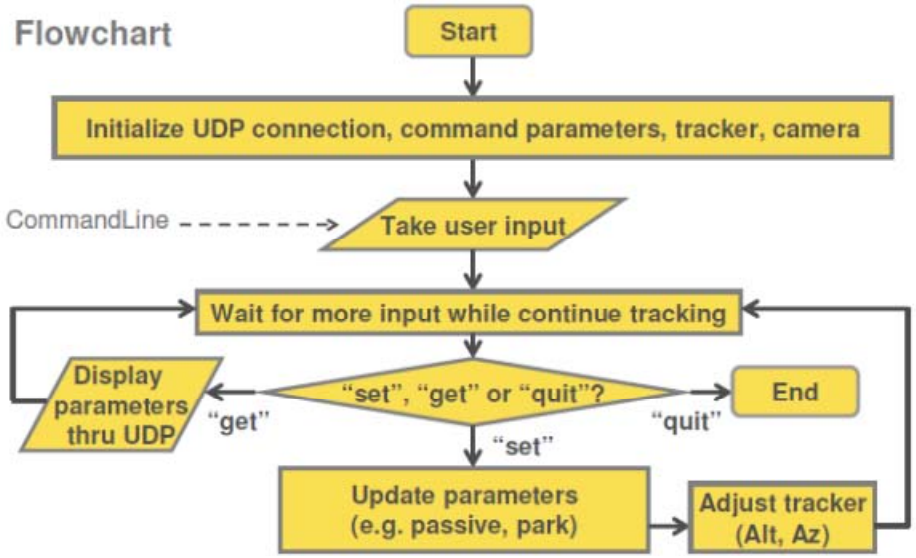

Figure 2.21: Flow-chart of the Trax2.4 software. Figure produced by S. Like.

A flow-chart of Trax2.4 is shown in Figure 2.21. The Trax2.4 program initializes the UDP connection, the tracker, and camera. The software then continually iterates between searching for new UDP input, and updating internal parameters, such as the calculated position of the body. When Trax2.4 receives a "get" command, it returns current parameter values, such as the

coordinates of the sun or the motor error status. "Set" commands are used to change the Trax2.4 parameters, such as motor offsets, latitude, or tracker position.

2.7.3 Testing

In the summer of 2007, the UT Suntracker was installed at the Toronto Atmospheric Observatory for passive tracking testing. It was secured to a table, levelled, and oriented azimuthally. The tracker and motors were covered with a plastic dome that was transparent to visible light. At the base of the tracker, fans and a heater were installed for operation in summer and winter conditions. By observing the tracker pointing with a mechanical sight, motor offsets of -0.9° in azimuth and -0.4° in altitude were found. These corrections account for imperfect levelling and azimuthal orientation*.

In order to monitor the tracking, sunlight was directed from the tracker into a NetCamXL 640 camera. Pixels near the center of the sun were typically saturated or near saturation. Using the Trax2.4 software, the center of the sun was identified at the intersect of the brightest row and brightest column in the camera image. The intensity of the sun was taken to be the average intensity of the nine pixels surrounding the center of the sun. The pixel coordinates of the center of the sun and the average intensity were recorded along with the date, time, and calculated solar coordinates. Low average intensities (< 78% saturation level) corresponded with cloudy weather and therefore were not included in this study.

The results of these tests are shown in Figure 2.22 for 29 September 2007, before the tracker was calibrated using the mechanical sight, and 4 November 2007, after calibration. The intensity of the sun relative to the saturation level (panels a, b) can be used to identify thin clouds. The X-Y pixel coordinates of the center of the sun depend systematically on one another prior to calibration (panel c). This improves after calibration (panel d). The difference between center of the sun at each measurement time and the daily average of the center of the sun was taken. This

* Note that, while this correction method improved tracking to the desired accuracy, it does not account for all degrees of freedom. In order to correct for possible errors in tracker azimuth as well as tilt in the X and Y directions, the tracker pointing should be sighted over the course of a day [e.g., *Merlaud*, 2011]. Corrections can then be applied to the input latitude and longitude in the passive tracking routines.

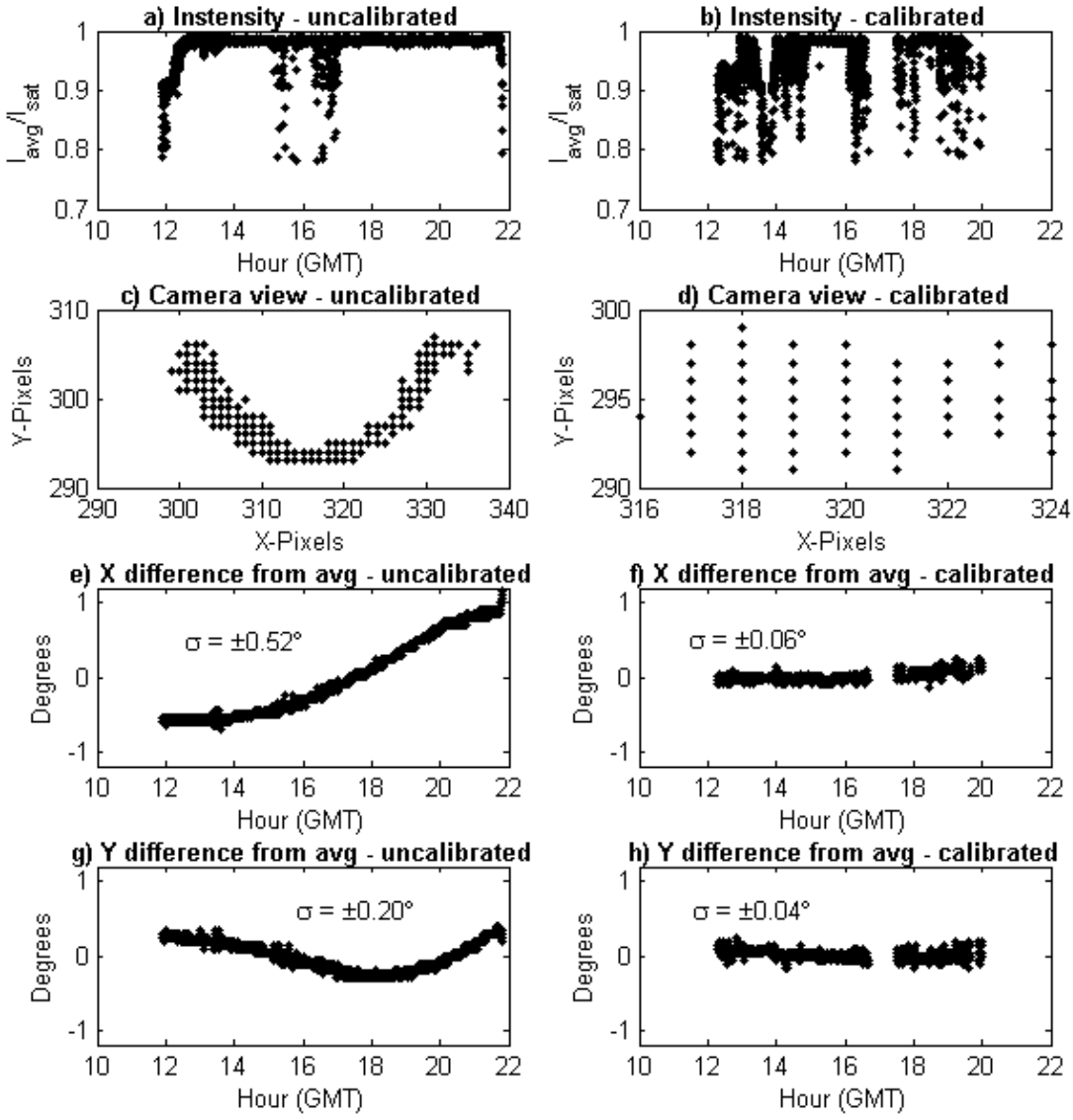

Figure 2.22: Testing output for uncalibrated tracking on 29 September 2007 and calibrated passive tracking on 4 November 2007. (a) Uncalibrated and (b) calibrated solar image intensity (% saturation) versus time for the ten camera pixels at the center of the sun. (c) Uncalibrated and (d) calibrated variation of solar coordinate Y versus X. X versus time for (e) calibrated and (f) uncalibrated. Y versus time for (g) calibrated and (h) uncalibrated. σ indicates the 1σ standard deviation in the measurements over the course of the day.

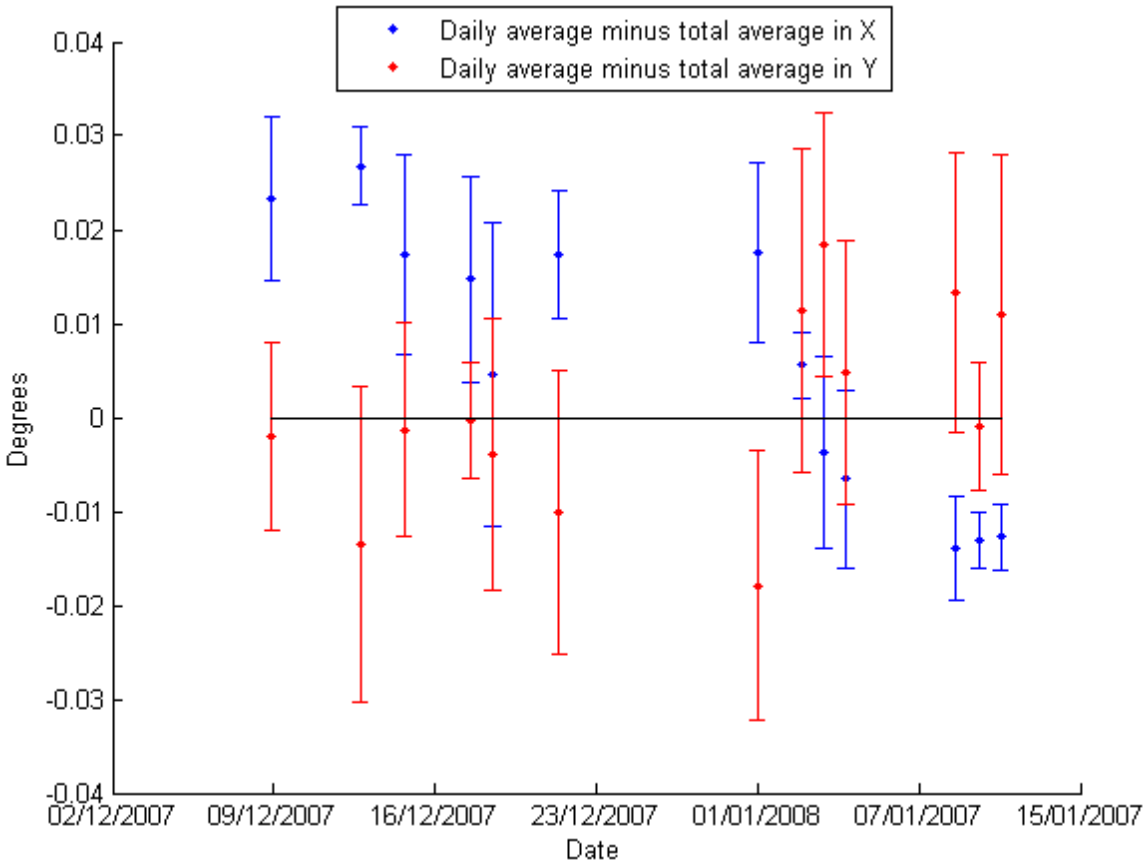

Figure 2.23: Daily average position of the sun in degrees versus date for X-axis of the camera frame (blue) and the Y-axis of the camera frame (red), using passive tracking.

difference was converted to degrees, using the angular size of the sun divided by the pixel size of the sun. The uncalibrated data show a 2° drift in X over the course of the day (panel e) and a minimum in Y around noon (panel g). The calibrated data shows smaller variation and less systematic structure in both X (panel f) and Y (panel h). Similar results were obtained for sunny or partly sunny days from 22 October 2007 to 10 January 2008.

From 7 December 2007 to 10 January 2008, the camera setup was not moved and therefore the daily variation of the center of the sun could be examined. For each sunny or partly sunny day, the average (X, Y) coordinates of the center of the sun and standard deviation were calculated and converted to angular distances. The daily variation is shown in Figure 2.23 for the X (blue)

and Y (red) coordinates of the sun. Good tracking is maintained throughout this period, with a small systematic change around 1 January 2008. This could reflect a small change in the position of the camera.

2.8 Data Acquisition Software

The GBS instruments are operated automatically using in-house Labview data acquisition software. Upon start-up, the software communicates with the grating turret through a general purpose interface bin (GPIB) connection, and moves the turret to the user-specified grating and central wavelength position. For the PEARL-GBS, the software also initializes the filter wheel via serial cable communication and selects a user-specified filter. The software then initializes the CCD, by communicating with the CCD Symphony Controller through a cross-over ethernet cable, and waits for the CCD to cool. Once the CCD has reached operating temperature, the instrument takes a series of snapshots of sunlight and calculates an ideal exposure time for maximum signal without saturation. If there is enough sunlight, it takes a series of measurements, typically up to 300 acquisitions, averages the spectra from the measurement sequence, and saves the averaged spectrum to a data file. Every 20^{th} measurement or when the signal is low, the instrument takes a closed-shutter dark signal measurement. The software also has an option to wait 15 minutes between measurements when the sun is higher than SZA 80° in order to prolong shutter life.

In spring 2010, the software was streamlined and the following features were added:

- Default to prevent the grating turret from spinning at each instrument restart, improving the stability of measurements.
- Manual control of the exposure time, number of acquisitions, and shutter to simplify testing and trouble-shooting procedures.
- Error catching and warnings to help identify instrument problems, such as broken shutters.
- CCD binning options to specify Y-pixels that are averaged during acquisition.
- Automatic identification and removal of saturated spectra from the average over accumulations.

Furthermore, for the PEARL-GBS, suntracker control was added to the Labview software through a UDP connection to the Trax2.4 program. Preset measurement routines that alternate between direct-sun, MAX-DOAS, and zenith-sky viewing geometries with automated filter-changes were then implemented.

2.9 Summary

The UT-GBS and PEARL-GBS are triple grating, UV-visible spectrometers with cooled CCD detectors. The UT-GBS has taken measurements since 1998 on a campaign basis at Eureka, Vanscoy, and Toronto in Canada and at Cabauw in the Netherlands. The PEARL-GBS was installed permanently at Eureka in 2006. Several improvements were made to the GBS instruments from 2008-2011. In 2009, light leaks to both instruments were corrected, while in 2010 the resolutions of both instruments were improved through modifications to the input optics. The UT Suntracker was installed above the PEARL-GBS in 2008, allowing for new direct-sun and MAX-DOAS measurements. Instrument performance and changes were documented in compliance with NDACC recommendations.

3 NDACC Certification and the CINDI Campaign

NDACC is a network of remote-sensing research stations that is committed to the long-term monitoring of tropospheric and stratospheric composition (see Section 0). NDACC instruments and data products are expected to meet a set of standards in order to ensure a homogenous and accurate NDACC dataset. The certification process for NDACC UV-visible instruments is described in Section 3.1 and includes instrument characterization, data analysis, and validation. Section 3.2 summarizes previous validation of GBS measurements. In January 2009, the PEARL-GBS was granted NDACC certification. Therefore a GBS is required to participate in formal intercomparison campaigns, the most recent of which, the Cabauw Intercomparison Campaign of Nitrogen Dioxide Measuring Instruments (CINDI), was held in Cabauw, Netherlands from 8 June to 26 July 2009. During CINDI, NDACC zenith-sky NO_2 DSCDs and new MAX-DOAS NO_2, O_4, and HCHO DSCDs were all acquired and validated, as discussed in Section 3.3.

3.1 NDACC Certification of UV-Visible Instruments

The NDACC UV-visible working group has established a series of criteria to ensure consistency in NDACC-certified UV-visible instruments. These standards are described on the NDACC website [*NDACC*, 2009]. In order to obtain certification, a report on the PEARL-GBS was prepared. This report included a description of the instrument; results from dark current, resolution, stray light and polarization tests; a description of data analysis procedures; sample spectra and fits; and details of previous instrument intercomparisons. Based on this report, the PEARL-GBS was granted NDACC certification in January 2009 and was slated to participate in the next formal NDACC UV-visible intercomparison campaign.

3.1.1 NDACC Intercomparison Criteria

Following the second NDACC intercomparison campaign held in 1996 [*Roscoe et al.*, 1999], a set of DSCD intercomparison criteria were adopted. These standards will be referred to as the "1996 NDACC standards". For Type I intercomparisons, a linear regression is performed between DSCDs measured by two instruments over one twilight. For each linear regression, the

slope, y-intercept, and residual are calculated as described in *Roscoe et al.* [1999] and averages are taken over the campaign. A group of reference instruments for which the slopes are near one and the y-intercept and residual are small is selected. The DSCDs from this "reference group" are then averaged. DSCDs from all campaign instruments are then compared with the reference group, using a linear regression. The slope quantifies agreement between datasets; systematic offsets are reflected by the y-intercept; and random and non-linear systematic errors appear in the residuals. The "1996 NDACC standards" for the slope, y-intercept, and root mean square (RMS) are summarized in Table 3.1. Type II intercomparisons involved taking ratios of DSCDs [e.g., *Vandaele et al.*, 2005]. The 1996 NDACC standards were used in the third NDACC intercomparison campaign in 2003 [*Vandaele et al.*, 2005] and three studies including the GBS instruments by *Fraser et al.* [2007a; 2008; 2009].

In 2009, following the CINDI campaign, the NDACC intercomparison criteria were revised and published on the NDACC webpage [*NDACC*, 2009]. These criteria will be referred to as the "2009 NDACC standards." The Type I linear regression test now includes the smaller targets for NO_2 y-intercept and residuals that are summarized in Table 3.1. The Type II ratio tests are no longer included in the NDACC standards.

3.2 Previous Intercomparisons

Prior to certification, the UT-GBS and PEARL-GBS had never participated in a formal NDACC intercomparison campaign. However, UT-GBS and PEARL-GBS ozone and NO_2 DSCDs and VCDs have been compared with many other instruments, using a variety of comparison methods. A summary of the campaigns and measurement dates for the UT-GBS and PEARL-GBS is given in Section 2.1.1.

Table 3.1: NDACC standards for linear regression of DSCDs.

	NDACC Standards	Slope	y-intercept (mol/cm^2)	RMS (mol/cm^2)
Ozone	1996 and 2009	1.00±0.03	$\pm 0.15 \times 10^{19}$	0.10×10^{19}
NO_2	1996	1.00±0.05	$\pm 0.15 \times 10^{16}$	0.10×10^{16}
	2009	1.00±0.05	$\pm 0.10 \times 10^{16}$	0.05×10^{16}

Fraser et al. [2007a; 2008; 2009] performed 1996 NDACC standard comparisons between the UT-GBS, PEARL-GBS and other DOAS instruments, during MANTRA 2004 and the Canadian Arctic ACE Validation Campaigns for 2004-2007 at Eureka. GBS ozone and NO_2 DSCDs were compared against SAOZ (see Appendix C), Measurements of Aerosol Extinction in the Stratosphere and Troposphere-Ground (MAESTRO-G) [*McElroy et al.*, 2007], and the SunPhotoSpectrometer (SPS) [*McElroy*, 1995]. Details of these instruments are summarized in Table 3.2. The results of the 1996 NDACC Type I intercomparisons are given in Table 3.3 and are discussed in the sections below.

Table 3.2: UV-visible instrumentation participating in past intercomparison campaigns.

Instrument Name	Description	Wavelength range	Resolution	Detector	Field-of-view
UT-GBS	UV-visible triple-grating ground-based spectrometer	350-500 nm (600 gr/mm)	0.5-2 nm (600 gr/mm)	CCD cooled to 201 K	2°
PEARL-GBS	UV-visible triple-grating ground-based spectrometer	350-500 nm (600 gr/mm)	0.5-2 nm (600 gr/mm)	CCD cooled to 203-205 K	2°
SAOZ	UV-visible grating spectrometer	270-620 nm	1.0 nm	Uncooled 1024-pixel linear diode array	10°
MAESTRO-G	Double spectrometer (UV spectrometer and visible spectrometer), with two independent input optics, gratings, and detectors	260-560 nm (UV) 525-1010 nm (visible)	1.0 nm (UV) 2 nm (visible)	Uncooled 1024-pixel linear diode arrays (both UV and Visible)	0.1x6.5°
SPS	UV-visible grating spectrometer	375-775 nm	1.5 nm in NO_2 and ozone regions	Uncooled 1024-pixel linear diode array	0.1x10°

Table 3.3: Results from 1996 NDACC standard Type 1 comparisons with UT-GBS and PEARL-GBS. These are in the form "am-test-result/pm-test-result", where Y (N) means that the standards were (were not) met. UT=UT-GBS, SZ = SAOZ, SP = SPS, MA = MAESTRO-G, PE = PEARL-GBS. NDACC standards are summarized in Table 3.1.

		Ozone			NO_2		
Campaign	Instruments	Slope	Y-int	Res	Slope	Y-int	Res
MANTRA 2004[a]	UT vs SZ	N/N	N/N	N/N	Y/Y	N/N	N/N
	UT vs SP	Y/N	N/N	N/N	----	----	----
	UT vs MA	N/N	N/N	N/N	----	----	----
Eureka 2004[b]	UT vs SP	Y/N	Y/Y	N/N	----	----	----
	UT vs MA	Y/Y	Y/N	N/N	----	----	----
Eureka 2005[a]	UT vs SZ	N/N	Y/Y	N/N	Y/Y	Y/Y	Y/N
	UT vs SP	N/Y	Y/Y	N/N	Y/N	Y/Y	N/N
	UT vs MA	Y/N	Y/Y	N/N	----	----	----
Eureka 2006[b]	UT vs SZ	N/N	Y/Y	N/N	Y/Y	Y/Y	Y/Y
	UT vs SP	Y/Y	Y/Y	N/N	Y/Y	Y/Y	N/N
	UT vs MA	Y/Y	Y/N	N/N	Y/Y	Y/Y	N/N
Eureka 2007[c]	UT vs SZ	N/N	Y/Y	Y/Y	Y/Y	Y/Y	Y/Y
	UT vs PE	Y/Y	Y/Y	Y/Y	Y/Y	Y/Y	Y/Y
	PE vs SZ	Y/Y	Y/Y	Y/Y	N/N	Y/Y	Y/Y

[a] [*Fraser et al.*, 2007a]
[b] [*Fraser et al.*, 2008]
[c] [*Fraser et al.*, 2009]

Additionally, GBS ozone and NO_2 VCDs have been compared with many other instruments. Brewer spectrophotometers (see Appendix C) measure ozone using UV light at discrete wavelengths, with a photomultiplier tube detector. Ozonesondes (see Appendix C) sample the atmosphere *in situ* up to a burst height. A total column is integrated from this value and a correction is made to account for concentrations about the burst height. The University of Toronto Fourier Transform Spectrometer (UT FTS) [*Wunch et al.*, 2006] is an ABB Bomem DA5 FTS that measures with indium antimonide and mercury cadmium telluride (MCT) detectors, and a spectral range spanning 1200-5000 cm^{-1}, which took balloon measurements during MANTRA. The Portable Atmospheric Research Interferometric Spectrometer for the InfraRed (PARIS-IR) [*Fu et al.*, 2007] is a compact, portable FTS built by ABB Bomem with a resolution of 0.02 cm^{-1} and a spectral resolution and spectral coverage of 750-4400 cm^{-1}, which

took balloon measurements during MANTRA and participates in spring campaigns at Eureka. The Meteorological Service of Canada FTS (MSC-FTS) [*Donovan et al.*, 1997] is a Bomem-DA8 which was housed at Eureka from 1993-2009 and records spectra on MCT and InSb detectors with resolution of 0.004 cm^{-1} with wavelength range 715-4000 cm^{-1}. The University of Denver FTS (DU FTS) [*Fogal et al.*, 2005] took balloon measurements during MANTRA in two bandpasses of approximately 718-1438 and 1438-2154 cm^{-1}, with a pair of MCT detectors with a resolution of approximately 0.03 cm^{-1}.

The GBS ozone and NO_2 measurements have also been compared with numerous satellite instruments. ACE (see Appendix D) aboard SCISAT-1 satellite, a solar occultation satellite launched by the Canadian Space Agency in August 2003 [*Bernath et al.*, 2005], has two instruments, the ACE-FTS and ACE-MAESTRO. The ACE-FTS is a high resolution (0.02 cm^{-1}) infrared instrument, operating from 750-4400 cm^{-1}. ACE-MAESTRO is a UV-visible-near-IR double spectrometer, with a resolution of 1.5-2.5 nm, and a wavelength range of 270-1040 nm. The Earth Probe Total Ozone Mapping Spectrometer (TOMS) is a nadir-looking instrument, which derives ozone by comparing the radiance of the Earth with the radiance of a calibrated diffuser plate in the UV region [*Herman et al.*, 1997]. The Global Ozone Monitoring Experiment (GOME) is also a nadir-viewing instrument that measures the solar radiation scattered by the atmosphere in the UV-visible region (240-790 nm) with a resolution of 0.2-0.4 nm [*Burrows et al.*, 1999b].

3.2.1 MANTRA

MANTRA was a series of balloon campaigns held in the late summers of 1998, 2000, 2002, and 2004, designed to measure stratospheric trace gases that impact mid-latitude chemistry [*Strong et al.*, 2005]. These campaigns took place in Vanscoy, Saskatchewan (52°N, 107°W). The UT-GBS took ground-based measurements for all four campaigns.

For MANTRA 1998 [*Bassford et al.*, 2005], 2000 [*Farahani*, 2006] and 2002 [*Farahani*, 2006] UT-GBS ozone and NO_2 VCDs were retrieved using an in-house DOAS software and a Langley plot method [*Fish*, 1994]. In 1998, ozone VCDs were within 5% of ozonesonde and Brewer VCDs, and within 10% of the TOMS and GOME satellite VCDs [*Bassford et al.*, 2005]. In 2000, ozone VCDs agreed within error with Brewer, TOMS, and GOME and in 2002, within

error of the TOMS and GOME measurements [*Farahani*, 2006]. In MANTRA 1998, UT-GBS NO_2 VCDs had similar variability to GOME VCDs, but with a systematic offset, which may be caused by the diurnal variation of NO_2 [*Bassford et al.*, 2005]. The NO_2 DSCDs were also used to retrieve vertical profiles [*Melo et al.*, 2004] with an optimal estimation software [*Preston et al.*, 1997]. These profiles were found to be in good agreement with vertical profiles measured by SPS, which was on board the MANTRA balloon.

Intercomparisons between the UT-GBS, SAOZ, SPS, and MAESTRO-G were made during MANTRA 2004 by *Fraser et al.* [2007a]. Higher-than-usual signal-to-noise was seen for three of the ground-based instruments: the UT-GBS had a loaner front-illuminated CCD and an error in the data acquisition software, while SPS and MAESTRO-G had frosted viewing windows, due to housing inside a commercial freezer. Ozone and NO_2 DSCDs were retrieved for all four instruments, using a common set of fit parameters and cross-sections in the WinDOAS software and a single reference spectrum. NO_2 was below the detection limit for SPS and MAESTRO-G. The DSCDs were compared using the 1996 NDACC standards. The results of the linear regressions are shown in Table 3.3; compared with other campaigns, few of the standards are met, likely due to the instrument problems.

MANTRA 2004 DSCDs were converted to VCDs using the Langley method and compared with other ground-based instruments [*Fraser et al.*, 2007a]. UT-GBS ozone VCDs agreed within error with the other DOAS instruments, the Brewer, sondes, UT FTS, PARIS-IR, and DU-FTS. The UT-GBS and SAOZ NO_2 VCDs also agreed within error bars. Additionally, SAOZ and UT-GBS ozone and NO_2 DSCDs were retrieved during a thunderstorm [*Fraser et al.*, 2007b] and were found to be in good agreement.

3.2.2 Eureka 1999-2007

The UT-GBS has been deployed at Eureka during the spring-time on a yearly basis (except 2002) since 1999. For the first campaign, in 1999, ozone and NO_2 DSCDs were retrieved using the in-house DOAS software and converted to VCDs using a Langley plot technique [*Bassford et al.*, 2000; *Melo et al.*, 2004]. Ozone VCDs were found to be in good agreement with a co-located Brewer, sondes, and TOMS VCDs [*Bassford et al.*, 2000; *Melo et al.*, 2004].

UT-GBS ozone for spring 1999-2001, and 2003 and NO_2 DSCDs for spring 1999-2000 were retrieved using WinDOAS and are presented by *Farahani* [2006]. VCDs were calculated using a Langley plot analysis and were compared against the MSC-FTS, GOME, sondes, and several models. UT-GBS ozone VCDs agree within error of the sondes for most measurements. Good agreement is seen with the MSC-FTS for 1999 and 2000, but for many parts of 2001 and 2003, the MSC-FTS is ~20% higher than the UT-GBS measurements. For 1999 and 2000, NO_2 VCDs agree well with GOME and MSC-FTS for the early parts of the campaigns, but start to diverge around April. This is likely due to the diurnal variation of NO_2.

In 2004, ozone and NO_2 VCDs retrieved using WinDOAS and Langley plots were compared with SPS, MAESTRO-G, PARIS-IR, ACE-FTS, and the MSC-FTS [*Kerzenmacher et al.*, 2005]. Good agreement in ozone VCD was seen for all instruments, although the MSC-FTS recorded systematically low values. For NO_2, most of the data agreed within error bars, despite the fact that no corrections were made for tropospheric NO_2 of satellites and the diurnal variation of NO_2. Similar ozone comparisons were made in 2005, with the addition of SAOZ and showed good agreement [*Kerzenmacher et al.*, 2006].

For 2004-2007, *Fraser et al.* [2008; 2009] compared DSCDs and VCDs measured by the UT-GBS and PEARL-GBS with many other instruments. Ozone and NO_2 DSCDs were retrieved for the UT-GBS, PEARL-GBS, SAOZ, MAESTRO-G, and SPS, using a common set of fit parameters and cross-sections in the WinDOAS software. The 1999 NDACC Type 1 and Type 2 criteria were applied to the measurements. The results of the Type 1 comparisons are shown in Table 3.4. Better agreement is seen during these Arctic campaigns than the MANTRA 2004 campaign [*Fraser et al.*, 2007a]. This may be because during MANTRA 2004, a single reference spectrum was used over the whole campaign, which may lead to systematic errors in the DOAS fits if the instruments are not stable. Furthermore, the instruments suffered from various technical problems during MANTRA 2004.

All ground-based DSCDs were converted to VCDs using the Langley plot method. The percent differences between the VCDs retrieved by the UT-GBS and other instruments are summarized in Table 3.4. The largest deviations were seen in 2005, when the polar vortex was very active. This may because the various instruments have different viewing and therefore might sample

Table 3.4: Comparison of GBS VCDs to various other instruments from 2004-2007, where the 2004-2006 intercomparisons are from *Fraser et al.* [2008] and the 2007 intercomparisons are from *Fraser et al.* [2009].

Comparison	Years	Ozone % difference	NO_2 % difference
UT-GBS minus SAOZ	2005-2007	-6.9 to -2.3%	-12.3% to +1.0%
UT-GBS minus SPS	2004-2006	-2.6 to -0.1%	-12.3 to +20.8%
UT-GBS minus MAESTRO-G	2004-2006	-53.7 to +10.7%	-2.9 to +24.6%
UT-GBS minus sondes	2004-2007	-5.7 to 34.8%	--
UT-GBS minus ACE-FTS	2004-2006	-5.6 to -2.3%	+10.5 to +20%
UT-GBS minus ACE-MAESTRO	2004-2006	+1.2 to +19.4%	-1.3 to 3.3%
UT-GBS minus PEARL-GBS	2007	-3.2%	-5.9%
PEARL-GBS minus SAOZ	2007	-2.4%	8.1%
PEARL-GBS minus sondes	2007	-1.2%	--

different parts of the atmosphere. ACE-FTS and ACE-MAESTRO ozone VCDs were calculated from partial columns between 15 and 40 km. Daily ozonesonde data below 15 km was added to the profiles. ACE-FTS and ACE-MAESTRO NO_2 measurements were calculated from 22-40 km. No corrections were made for NO_2 above and below these heights, but the contribution is expected to range from 7-12%.

3.3 CINDI

In 2009, the UT-GBS participated in CINDI, a formal NDACC intercomparison campaign held in Cabauw, Netherlands. The goals of CINDI were to compare DOAS and MAX-DOAS instruments and to validate nadir tropospheric NO_2 measurements by satellite instruments such as GOME, SCIAMACHY and OMI. Ground-based tropospheric measurements of NO_2 are useful for validating satellite measurements and for determining the altitude sensitivity of nadir satellite tropospheric columns. CINDI met the NDACC formal intercomparison campaign criteria [*Roscoe et al.*, 2010] because the participating instruments took measurements for more than ten days, with sufficient temporal resolution to sample at 1° SZA intervals; Cabauw has adequate concentrations of NO_2 and variable weather conditions; and there was a campaign referee, H.K. Roscoe, who followed a semi-blind comparison protocol.

The CINDI campaign was divided into several phases. Instruments were installed and tested from 10-14 June. From 15-30 June, the formal semi-blind intercomparison campaign for DOAS NO_2 and O_4 took place. Other trace gases, including HCHO and CHOCHO, were studied from 31 June - 5 July. Finally, an investigation of the variability in tropospheric NO_2 across one satellite pixel was performed using MAX-DOAS measurements pointing in various azimuthal directions and mobile DOAS from 6-24 July. The UT-GBS participated in all phases of this campaign, but took zenith-sky measurements only for the first part of the campaign.

3.3.1 Field Site

CINDI took place at KNMI's Cabauw Experimental Site for Atmospheric Research at Cabauw, Netherlands (51.97°N, 4.93°E, at sea level) and is described by *Piters et al.* [2012]. Cabauw has an unobstructed view of the horizon, allowing MAX-DOAS measurements to be taken at a variety of azimuthal angles. Two past campaigns that included MAX-DOAS instruments were hosted at Cabauw [*Brinksma et al.*, 2008; *Hains et al.*, 2010].

Figure 3.1 shows a map of the Netherlands, with the location of Cabauw highlighted (left) and the layout of the Cabauw field-site (right). Instruments were installed at three locations: a 200-m scientific tower; the roof-tops of porto-cabins that housed some CINDI instruments; and the wind-profiler. Permanent instruments characterize the boundary layer, meteorology, wind, pressure, and temperature at various heights along the tower. Furthermore, tropospheric wind speeds at various altitudes and clouds are routinely measured with a wind profiler and cloud lidar. Near the base of the tower, an *in situ* NO_2 instrument is also installed permanently. During CINDI, many additional instruments were deployed, including an aerosol lidar, *in situ* NO_2 instruments, an elevation-scanning NO_2 lidar, and newly-developed NO_2 sondes that were flown on balloons. 22 DOAS instruments from 14 institutes also participated in the campaign.

Cabauw is a rural location with few local pollution sources; however tropospheric NO_2 pollution events can be transported to Cabauw from nearby regions. Figure 3.2 shows the average tropospheric column of NO_2 measured by OMI during the campaign. When the wind at Cabauw came from the west (Rotterdam), the south (Antwerp), and the southeast (German Ruhr area), polluted air was measured, while when the wind came from the North, clean air was measured.

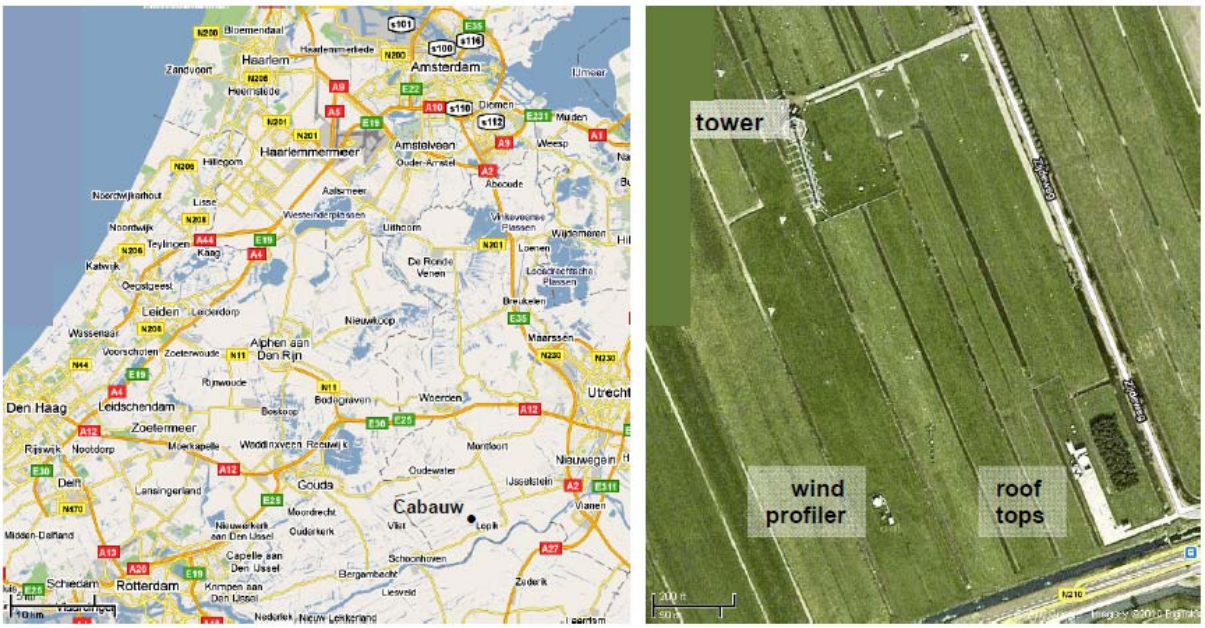

Figure 3.1: Map showing location of Cabauw in Netherlands (left) and layout Cabauw field site (right) from [*Roscoe et al.*, 2010].

Throughout CINDI, the weather varied considerably. Therefore measurements were taken under clear skies, thunderstorms, scattered showers, and rainy conditions. This allowed measurements to be validated under various conditions.

3.3.2 Participating DOAS Instruments

The DOAS instruments that participated in CINDI are summarized in Table 3.5. All instruments took MAX-DOAS measurements except for the three SAOZ instruments, which took only zenith-sky measurements. For the semi-blind intercomparisons, MAX-DOAS instruments took measurements at elevations of 2°, 4°, 8°, 15°, 30° and the zenith within a maximum of 30 minutes and were oriented to an azimuth of 287° (northwest).

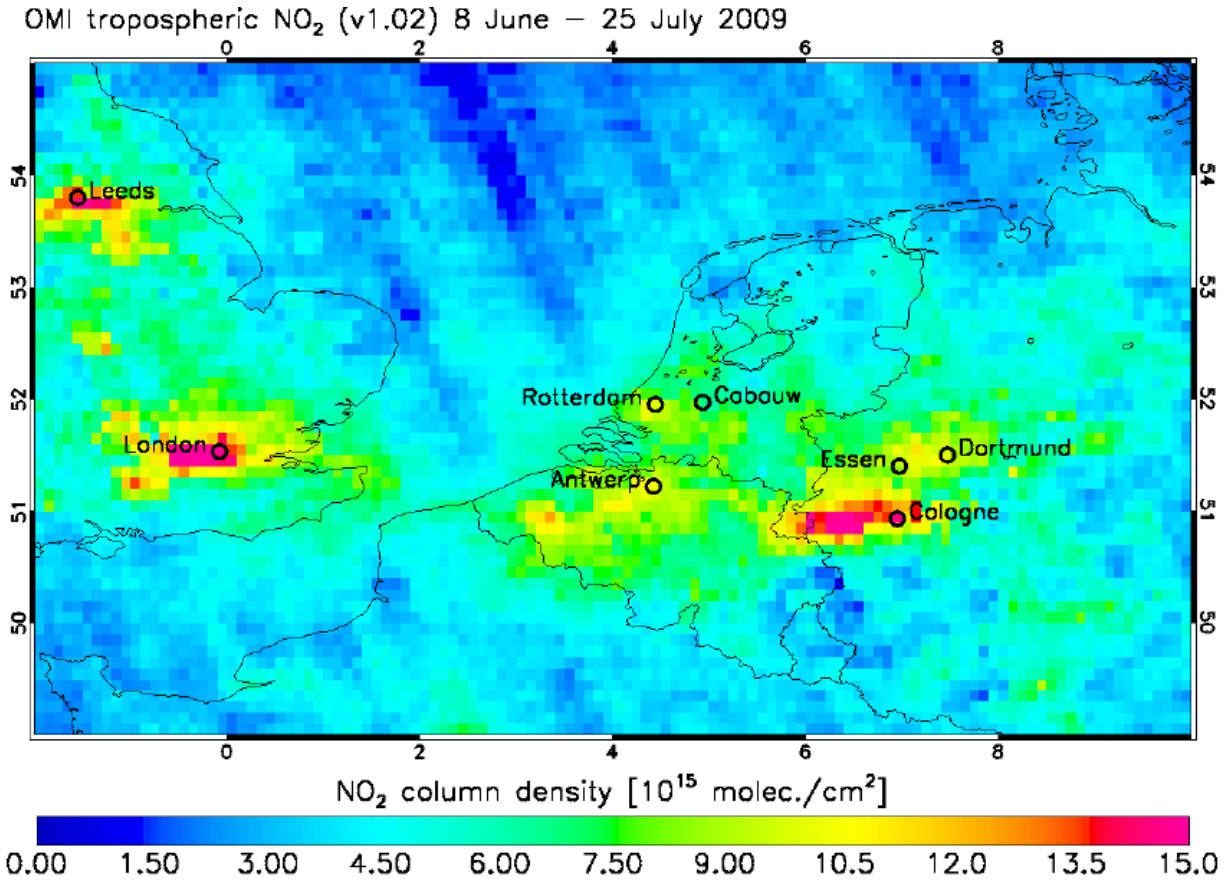

Figure 3.2: Average tropospheric column of NO_2 measured by DOMINO (Derivation of OMI tropospheric NO_2) v1.02 (see Appendix D) during CINDI (8 June to 25 July 2008). Figure from *Piters et al.* [2012].

3.3.3 UT-GBS Instrumentation

The UT-GBS was housed outdoors during the CINDI campaign in a watertight aluminum box manufactured by Cases Unlimited Inc with a Plexiglas UV-grade window. This box had been used to house the instrument previously in Toronto, Vanscoy, and Eureka. The exterior walls are painted white to reduce absorption of sunlight and the box is insulated with 1.24-cm black foam. Prior to this campaign, the box was heated when necessary with a heating circuit [*Farahani*, 2006] and cooled with a TECA 1200XE air-conditioner. The instrument sits on an aluminum frame that was custom-made at the University of Toronto.

Table 3.5: DOAS instruments participating in CINDI intercomparison from *Roscoe et al.* [2010].

Instrument	Wavelengths (nm)	FWHM (nm)	Field-of-view (° FWHM)	Detector type	Detector cooled?	Fibre?
BIRA-Vis	400-700	0.95	0.8	2D CCD	yes	yes
Bremen-Vis	400-573	0.8	1.1	2D CCD	yes	yes
CNRS-SAOZ[a]	270-630	1.2	--	1D NMOS	no	no
CNRS-mobile[a]	270-630	1.2	--	1D NMOS	no	no
CNRS-mini[a]	270-630	0.7	--	2D CCD	no	yes
Heidelberg1	290-789	0.9	0.9	1D CCD	yes	yes
INTA-NEVA2	387-514	0.6	1.0	2D CCD	yes	yes
INTA-RASAS2	393-510	0.45	1.0	2D CCD	yes	yes
JAMSTEC	223-558	0.7	0.9	1D CCD	no	yes
KNMI-2	400-600	0.9	0.4	1D CCD	yes	yes
Leicester	425-490	0.54	1.0	2D CCD	yes	yes
MPI-Mainz	310-461	0.55-0.87	1.2	1D CCD	yes	yes
NASA	269-532	0.6	1.6	2D CCD	no	yes
NIWA	389-510	0.48	0.5	2D CCD	yes	yes
Toronto UT-GBS[b]	340-550[c]	0.5-2.5[d]	2.0	2D CCD	yes	yes
Washington	282-498	0.83	1.0[e]	2D CCD	yes	no[f]
BIRA-UV	315-384	0.37	0.8	2D CCD	yes	yes
BIRA-mini	290-434	0.7	0.6	1D CCD	yes	yes
Bremen-UV	315-384	0.37	1.1	2D CCD	yes	yes
Heidelberg2	320-463	0.45	0.9	2D CCD	yes	yes
GIST-Korea	290-430	0.7	0.5	1D CCD	yes	yes
KNMI-1	290-433	0.7	0.4	1D CCD	yes	yes

[a] Zenith only.
[b] Took zenith only measurement for part of the campaign. Measurement dates and sequences are described in Section 3.3.3.
[c] For UV measurements: 315-380 nm.
[d] For UV measurements: 0.2-0.8 nm.
[e] In the vertical direction, less in the horizontal.
[f] Used wedge depolarizer.

For the Cabauw campaign, several changes were made to the outdoor housing. Due to previous problems with over-heating, an additional air conditioner (ISC CS-020-126-04 with a low ambient package) was installed. Furthermore, temperature data were recorded using a new Omega Four Channel Data Logger (HH309A). The installation of the UT-GBS inside the box during CINDI is shown on the left inset in Figure 3.3. The UT Suntracker was installed above the instrument box, inside a Plexiglas housing that was built at the University of Toronto, which is shown on the right inset of Figure 3.3.

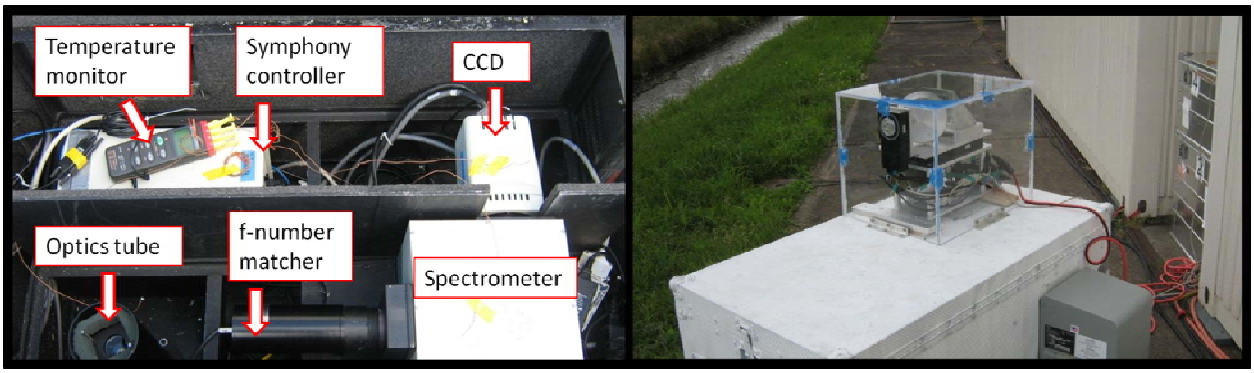

Figure 3.3: UT-GBS layout inside box housing (left) and Plexiglas UT Suntracker housing (right) during CINDI.

For 13-29 June, zenith-sky DOAS measurements were taken with the 600 gr/mm grating and DSCDs were retrieved on site for daily semi-blind intercomparison meetings. From 30 July to 4 July, the instrument operated with the 1800 gr/mm grating, the UT Suntracker was installed above the instrument, and MAX-DOAS measurements were taken. The Plexiglas dome was not used during this part of the campaign and, therefore, the tracker was removed from the instrument overnight and during rainy weather. From 5-11 July, the instrument operated in zenith-sky mode, with the 1800 gr/mm grating. From 11-17 July, the UT Suntracker was reinstalled above the instrument, this time with the Plexiglas dome. During this period, MAX-DOAS measurements with the 600 gr/mm grating were taken. Finally, the instrument took zenith-sky measurements with the 1800 gr/mm grating from 17-26 July, but these measurements were deemed unusable as a neutral density filter in the input optics severely reduced the signal.

Several instrument problems reduced data quality during this campaign. Due to multiple shutter failures, the instrument operated without a shutter for most of the campaign. Therefore short exposure measurements could not be taken and a neutral density filter was used to attenuate the signal. This filter may have added systematic errors to the measurements (see Sections 2.6 and 4.1.3.1). Furthermore, the signal-to-noise ratio and resolution were affected by problems with the mechanical shutter. Finally, large temperature gradients developed inside the box throughout the day, leading to spectral shifts, as described in Section 3.3.4.

3.3.4 UT-GBS O_4 and NO_2 DSCDs

O_4 and NO_2 DSCDs were retrieved simultaneously in the same wavelength window, using the settings described by *Roscoe et al.* [2010]. DSCDs were calculated using the WinDOAS software [*Fayt and Roozendael*, 2001], with a third order polynomial, a daily zenith-sky reference spectrum near noon and wavelength calibration against the Fraunhofer spectrum. NO_2 measured at 295 K [*Vandaele et al.*, 1996], O_4 [*Hermans*, 2004], ozone measured at 223 K [*Bogumil et al.*, 2003], H_2O*, and Ring [*Chance and Spurr*, 1997] cross-sections were fit. DSCDs were retrieved in the 425-490 nm window for the visible measurements (600 gr/mm grating) and the 338-370 nm for the UV measurements (1800 gr/mm grating). The spectrum was allowed to shift and stretch to first order against the reference spectrum during the fitting procedure. During the campaign, one of the pixels was performing poorly, resulting in large spikes in the dataset around 460 nm for the visible grating and around 354 nm for the UV grating. Therefore gaps in the DOAS analysis were introduced at these wavelengths.

Figure 3.4 shows sample DOAS fits (black) and data (magenta) for afternoon twilights at SZA 90°. Figure 3.5 shows the residuals of the sample DOAS fits. On 20 June, when the visible grating was used, the fit RMS is 0.0014, and no systematic errors appear in the O_4 (panel a) and NO_2 (panel c) fits. On 23 June, however, the fit RMS is 0.0029 and NO_2 systematic residuals are larger (panel e). This is likely because on 20 June, the temperature inside the box was fairly stable, with a difference between twilight and noon temperature (ΔT) of 1°C, while on 23 June, ΔT was 2°C. Similar results are seen for the UV measurements. On 7 July, when ΔT was 0.5°C, the fitting RMS is 0.0026 and O_4 (panel b) and NO_2 (panel d) fits have small systematic errors. Contrarily on 5 July, when ΔT was 2.5°C, the fitting RMS is 0.0080 and large spikes are seen in the NO_2 data (panel f). These spectral shifts arise due to thermal expansion of materials (see Section 2.6).

* Converted from line parameters given in Vandaele et al. [2005] and Rothman et al. [2003], but using HITRAN 2004.

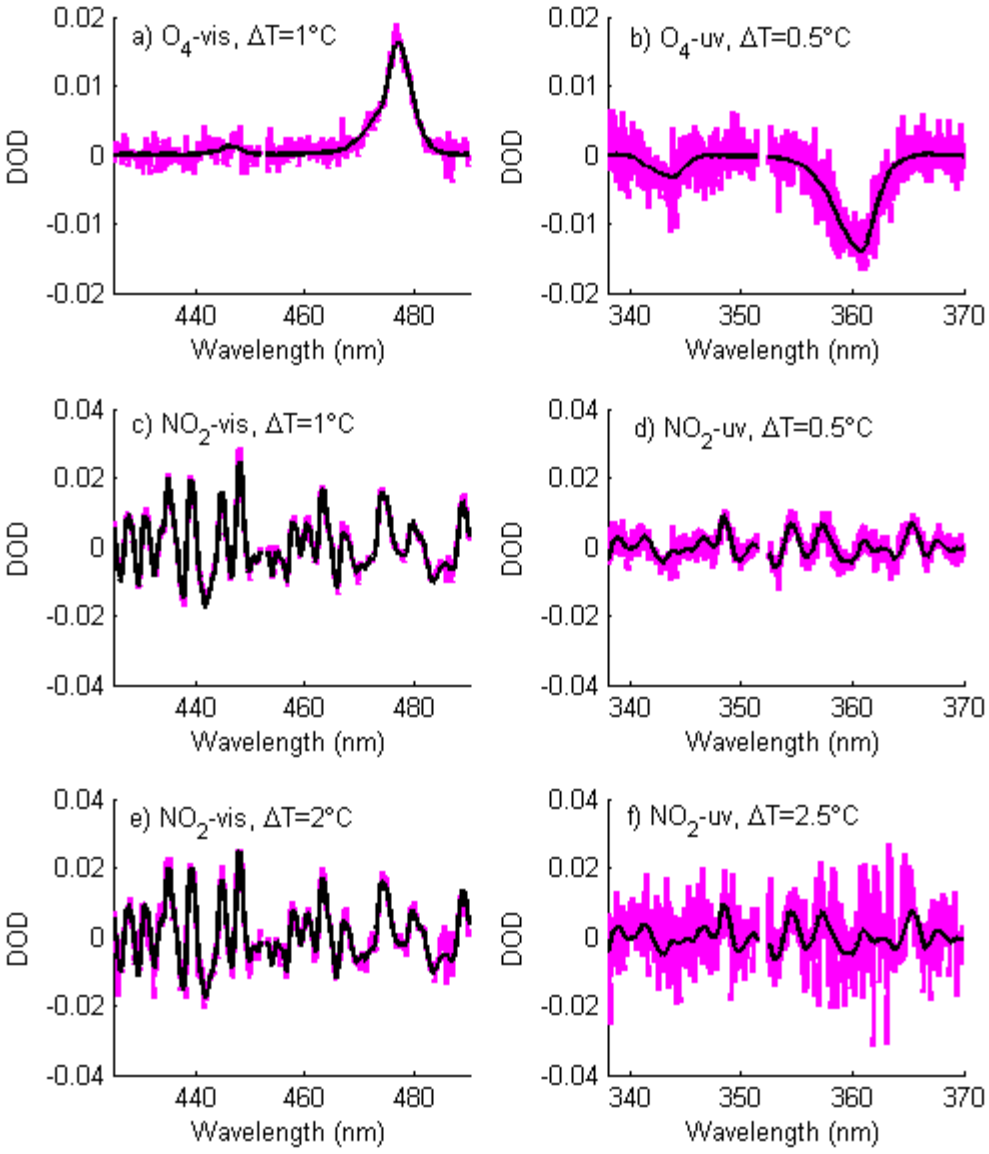

Figure 3.4: Sample twilight UT-GBS DOAS fit (black) and data (magenta) at SZA = 90° on twilights with a small noon-to-twilight temperature gradient (ΔT) for O_4 in the (a) visible and (b) UV wavelength regions and NO_2 in the (c) visible and (d) UV wavelength regions; and on twilight with larger ΔT for NO_2 retrieved in the (a) visible and (b) UV wavelength regions. The shown DOAS fits with the small (large) ΔT were taken on 20 June (23 June) for the visible measurements and on 7 July (5 July) for the UV measurements.

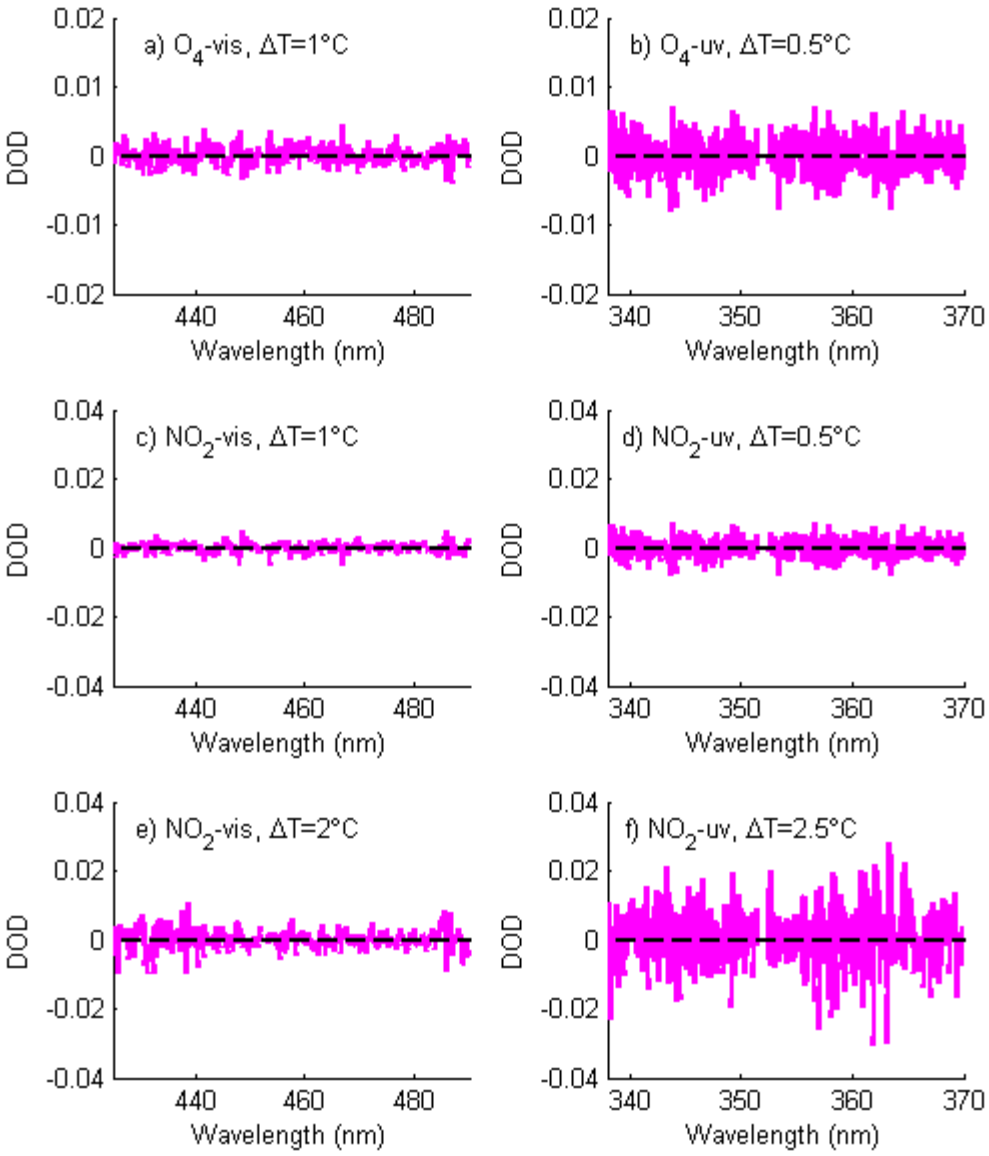

Figure 3.5: Residuals (magenta) for DOAS fits shown in Figure 3.4. Black dashed line indicates zero.

The resulting time-series of NO_2 (panel a) and O_4 (panel b) DSCDs is shown in Figure 3.6. The black dots correspond with zenith-sky measurements, and the coloured points show MAX-DOAS measurements taken at various pointing elevations. The regions in which thevisible (600 gr/mm) and UV (1800 gr/mm) gratings were used are indicated. The fit error is shown in grey and is small compared with the DSCDs for all measurements. NO_2 and O_4 DSCDs increase toward twilight, as SZA increases. O4 can be used identify path enhancement by clouds, as described in Section 1.3.5. Morning NO_2 DSCDs are smaller than evening DSCDs due to the diurnal variation of NO_2. Spectrometer temperature is also shown (panel c). Temperatures in the box systematically increased to a maximum at noon, and decreased at twilight and overnight.

In Figure 3.7, MAX-DOAS NO_2 is shown for the UV (panel a) and visible (panel b) measurements (left y-axis). *In situ* photolytic conversion NO_2 measurements taken by the commercial IUP Bremen nitrogen oxide analyzer [*Piters et al.*, 2012] are also shown in green (right y-axis). When *in situ* boundary layer NO_2 is enhanced, DSCDs for small viewing elevation increase. This illustrates the sensitivity of MAX-DOAS measurements to boundary-layer NO_2.

3.3.5 Zenith-Sky NO_2 Intercomparisons

Semi-blind intercomparisons of NO_2 and O_4 were performed, based on the precedent set by *Roscoe et al.* [1999] and adopted by *Vandaele et al.* [2005] during previous NDACC intercomparison campaigns. For the formal intercomparison phase of CINDI (15-30 June), the UT-GBS took zenith-sky measurements with the 600 gr/mm grating. NO_2 and O_4 DSCDs were retrieved and submitted to the referee, H.K. Roscoe, on a daily basis. Every afternoon, comparisons between all submitted DSCDs were presented by the referee anonymously. Individual groups were notified if large errors were observed in their datasets.

Following the campaign, each group submitted a final dataset to the referee. These datasets were compared and are presented by *Roscoe et al.* [2010]. NDACC Type 1 intercomparisons were performed for zenith-sky measurements from 15-26 June. Since INTA-RASAS2 had good sampling throughout the twilight, the INTA DSCDs were interpolated to the measurement times of the other instruments and correlations were performed. Sample linear regressions are shown

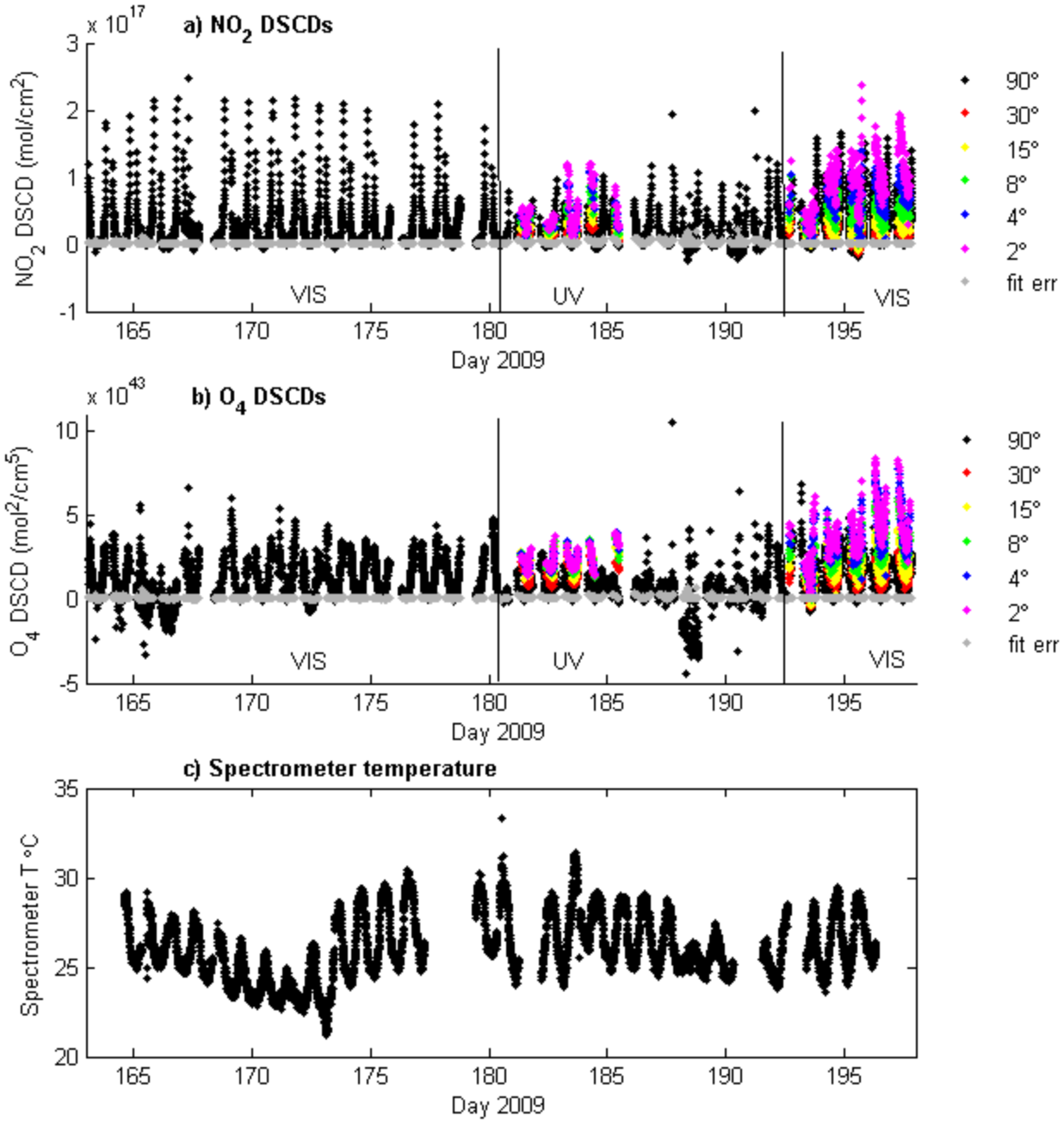

Figure 3.6: UT-GBS (a) NO_2 and (b) O_4 DSCDs retrieved at viewing angles 90° (black), 30° (red), 15° (yellow), 8° (green), 4° (blue), and 2° (magenta), and associated fitting error (grey). Time periods in which the visible and UV gratings were used are indicated. (c) The temperature inside the spectrometer housing.

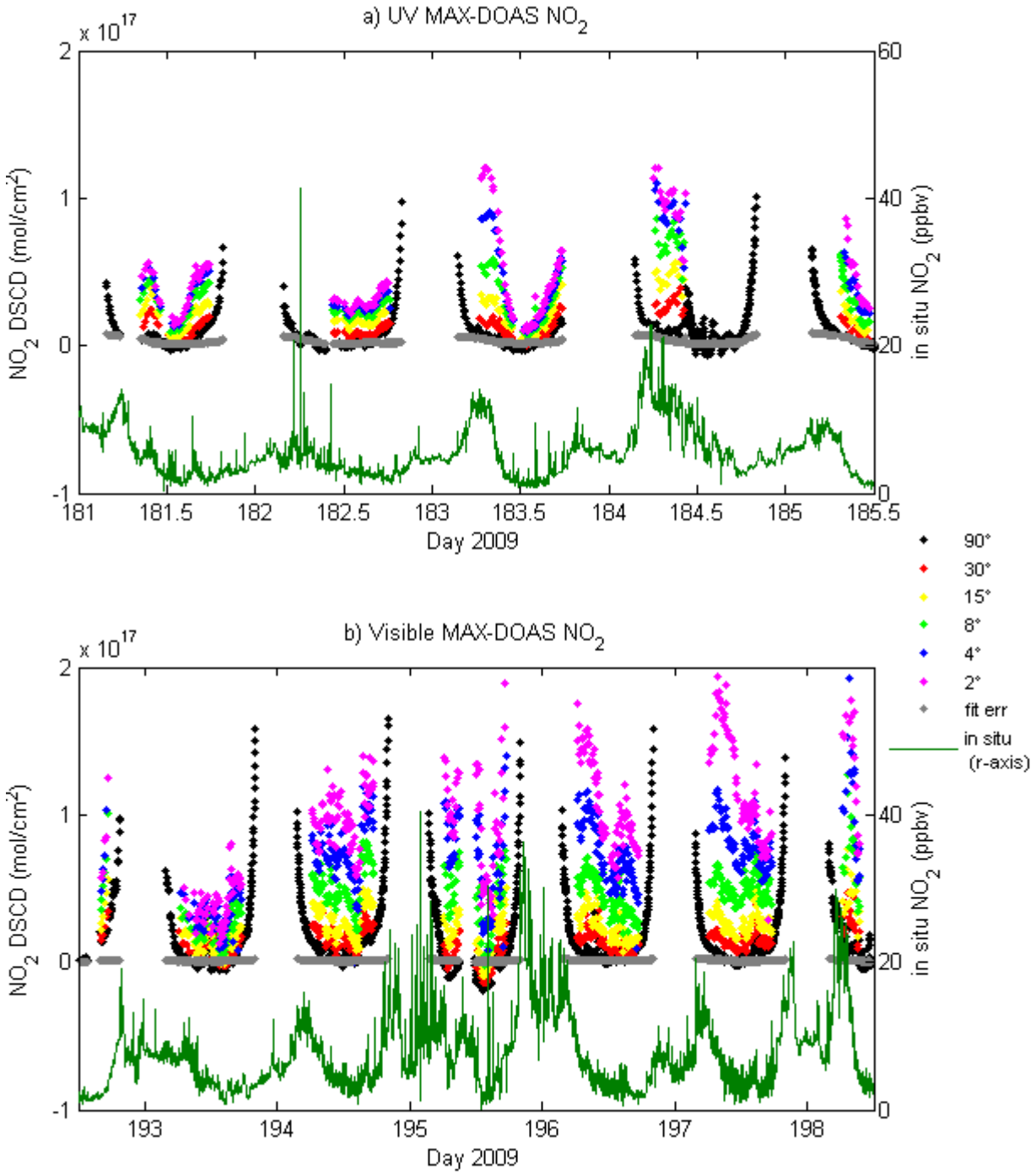

Figure 3.7: UT-GBS (a) UV and (b) visible MAX-DOAS NO_2 DSCDs retrieved at viewing angles 90° (black), 30° (red), 15° (yellow), 8° (green), 4° (blue), 2° (magenta), and associated fitting errors (grey) are plotted on the left Y-axis. On the right Y-axis, *in situ* NO_2 from the Bremen instrument is shown with the dark green line.

in Figure 3.8 for NIWA and UT-GBS versus INTA. The UT-GBS data are well correlated with INTA, but has more scatter in the measurements than NIWA. This is likely due to fitting noise caused by the temperature instability in the box and the instrument problems discussed above. INTA measured systematically more NO_2 than the other instruments, and, therefore, slopes against INTA were calculated for each instrument and were averaged to normalize the slope. A summary of the results from these regressions against INTA-RASAS2 are shown in Table 3.6. The measurements which meet NDACC Type 1 intercomparison criteria are shown in red. All instruments, including the UT-GBS, meet the NDACC slope requirements of 1±0.05, which is the most important criterion [*Roscoe et al.*, 2010]. Furthermore, the UT-GBS has similar error in the slope to other instruments. Both the UT-GBS and SAOZ fall slightly outside the NDACC requirements for intercept of $\pm 0.1 \times 10^{16}$ mol/cm^2, while Heidelburg falls further from the requirement. This may be because the UT-GBS and SAOZ both have a larger field-of-view than the other instruments (see Table 3.2). None of the instruments meet the RMS < 0.05×10^{16} mol/cm^2 NDACC criterion. These results, however, are very good because highly variable tropospheric pollution at Cabauw leads to differences in the instrument reference spectra.

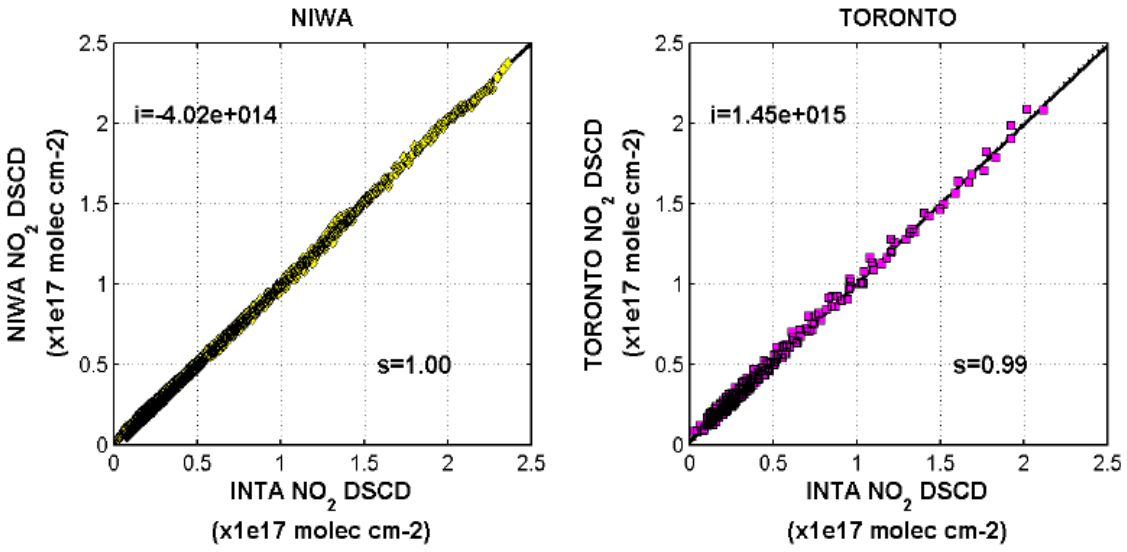

Figure 3.8: NO_2 correlation plots for NIWA versus INTA (left) and Toronto (UT-GBS) versus INTA (right) for the entire campaign. Figure from *Roscoe et al.* [2010].

Table 3.6: Results from NDACC Type 1 intercomparisons of zenith-sky NO_2 DSCDs measured during CINDI, with the values meeting NDACC 2009 standards shown in red [*Roscoe et al.*, 2010]. The NDACC standards are given in Table 3.1.

Instrument	Slope	Intercept ($x10^{16}$ mol/cm^2)	RMS residual ($x10^{16}$ mol/cm^2)	Fitting error ($x10^{16}$ mol/cm^2)
BIRA-Vis	1.030±0.003	0.012	0.282	0.062
Bremen-Vis	1.010±0.002	0.034	0.225	0.027
CNRS-SAOZ	0.933±0.002	0.114	0.348	0.134
Heidelberg1	1.015±0.003	0.231	0.358	0.091
INTA-NEVA2	0.989±0.002	0.086	0.247	0.029
INTA RASAS2	1.043	----	----	0.044
Leicester	1.017±0.006	-0.052	0.964	0.039
NASA	0.973±0.003	0.062	0.298	----[a]
NIWA	1.003±0.002	-0.049	0.250	0.108
Toronto UT-GBS	0.981±0.003	0.139	0.312	0.091
Washington	1.005±0.003	0.025	0.159	0.019

[a] NASA's fitting program did not produce an error.

Therefore, most instruments in the campaign, including the UT-GBS, were deemed to have met the NDACC standards for zenith-sky measurements [*Roscoe et al.*, 2010].

3.3.6 MAX-DOAS NO_2 Intercomparisons

CINDI was the first formal NDACC intercomparison campaign to include MAX-DOAS measurements. UT-GBS NO_2 and O_4 DSCDs were retrieved from the 1800 gr/mm grating MAX-DOAS measurements taken from 30 June to 4 July and with the 600 gr/mm measurements taken later in the campaign. The UT-GBS UV DSCDs were included in the formal intercomparisons presented by *Roscoe et al.* [2010].

Measurements with SZA less than 80° were compared for pointing elevations of 2°, 4°, 8°, 15°, 30° and the zenith. All instruments were oriented to an azimuth of 287° (northwest). NO_2 DSCDs, especially for smaller elevations, can change rapidly due to clouds and tropospheric pollution. Since the instruments measure simultaneously, 30-minute averages of the DSCDs were taken for each instrument at each elevation angle. A reference dataset was constructed by taking the weighted average of the 30-minute DSCDs for all UV-instruments measuring on a

given day. Then a linear regression was performed for each instrument, with the technique described in Section 3.3.5 and shown in Figure 3.4.

The results of these linear regressions are shown in Figure 3.9 for days that the UT-GBS took UV MAX-DOAS measurements. The UT-GBS performed well against the other instruments, with slopes within 5% of unity for all elevations except 15°, which was within 8% of unity (top panel). The error in the slope (middle panel) of the UT-GBS instrument was comparable to the other instruments. The y-intercept of the UT-GBS DSCDs (bottom panel) were within $1x10^{15}$ mol/cm^2 for all measurements.

3.3.7 HCHO

The UT-GBS measured MAX-DOAS HCHO for the first time ever, with the 1800 gr/mm grating from 30 June to 4 July. DSCDs were retrieved in the 336.5-359 nm window using the WinDOAS software [*Fayt and Roozendael*, 2001]. HCHO measured at 297 K [*Meller and Moortgat*, 2000], ozone measured at both 223 and 243 K [*Bogumil et al.*, 2003], NO_2 measured at 295 K [*Vandaele et al.*, 1996], O_4 [*Hermans*, 2004], and Ring [*Chance and Spurr*, 1997] cross-sections were included in the analysis. Furthermore a first order offset correction was used. A sample HCHO fit is shown in Figure 3.10.

The timeseries of UT-GBS HCHO measurements is given in Figure 3.11. Measurements at 2-30° elevation viewing angles are significant above fitting error for much of the time period. On 2 July 2009 (day 183), HCHO is elevated. This corresponds to enhanced boundary layer NO_2 (see Figure 3.7). MAX-DOAS data from 3 July 2009 are not shown because DOAS RMS values were greater than $0.002x10^{-3}$.

Pinardi et al. [2012] compared HCHO DSCDs measured by nine MAX-DOAS instruments. A reference dataset was constructed from DSCDs with good time-resolution and low noise. Then linear regressions were performed against the reference dataset. The resulting slopes, correlation coefficients, and y-intercepts are shown in Figure 3.12. The agreement between the UT-GBS and the reference dataset is acceptable. However UT-GBS data are more scattered than for high-quality measurements. This is expected due to the instrument problems encountered during the campaign. Over the course of CINDI, HCHO DSCDs agreed within 15% on average.

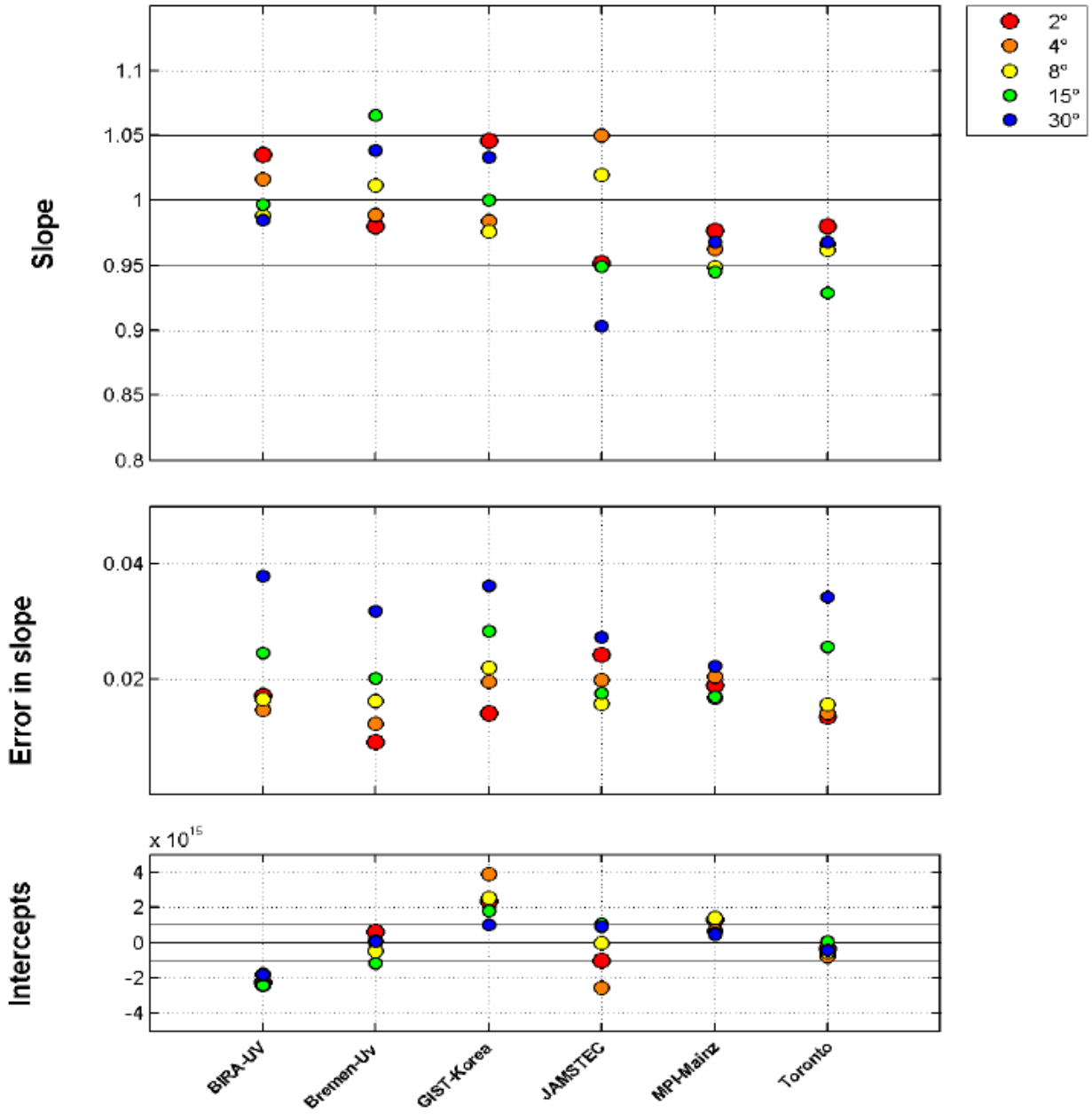

Figure 3.9: Results from intercomparison of NO_2 UV MAX-DOAS DSCDs from 30 June - 4 July 2010. Toronto = UT-GBS. Figure from *Roscoe et al.* [2010].

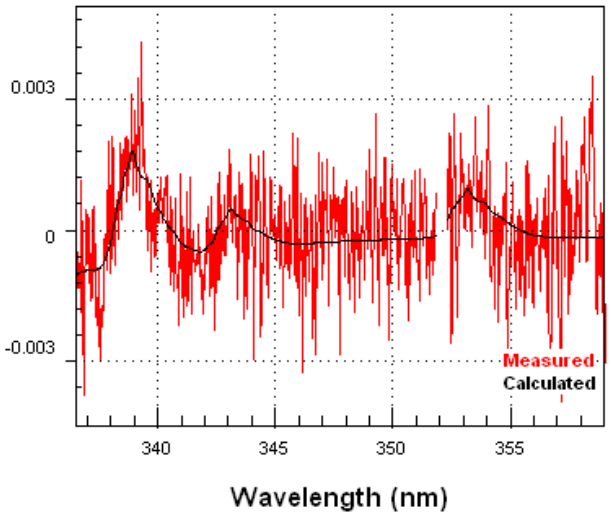

Figure 3.10: Sample UT-GBS HCHO data (red) and fit (black) at 4° elevation on 2 July 2009 around noon (DSCD = 4.29×10^{15} mol/cm^2).

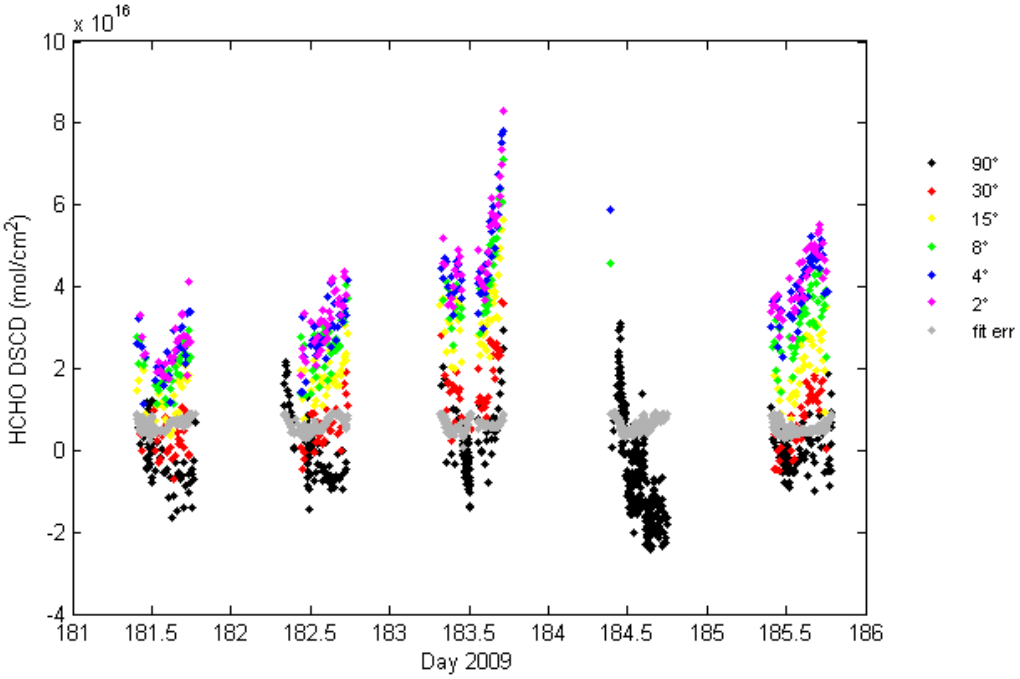

Figure 3.11: UT-GBS HCHO DSCDs retrieved at viewing angles 90° (black), 30° (red), 15° (yellow), 8° (green), 4° (blue), 2° (magenta) and associated fitting error (grey).

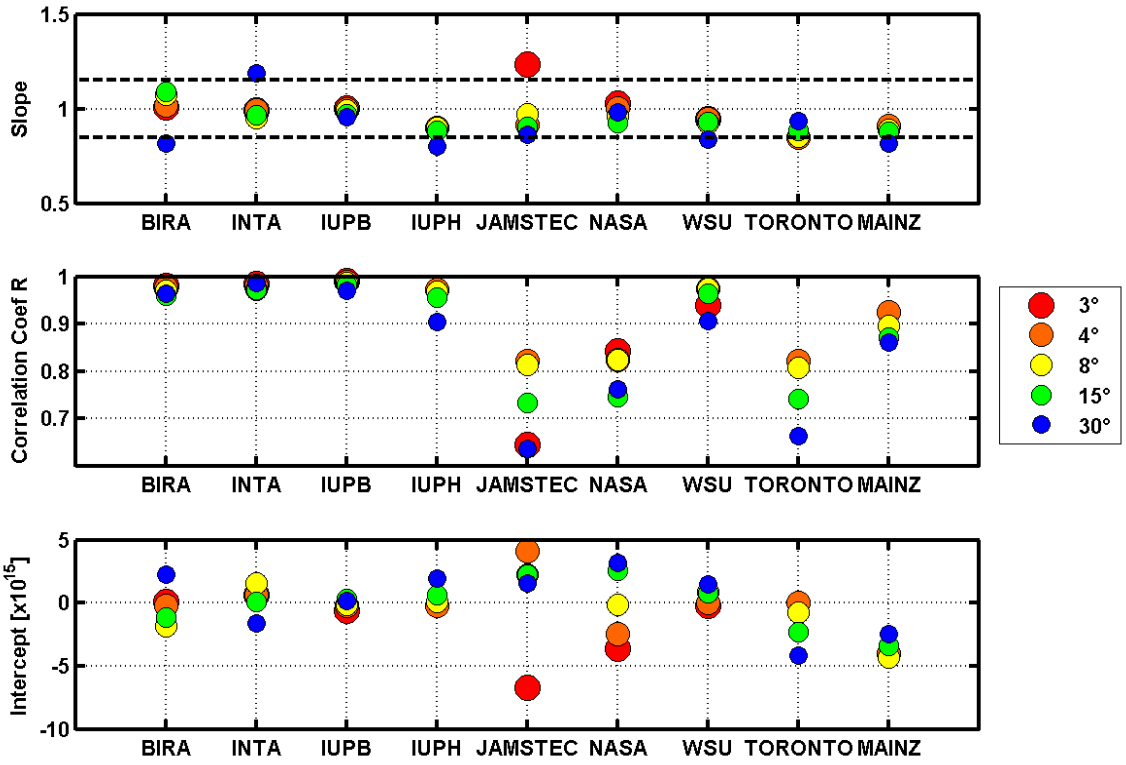

Figure 3.12: Straight-line slopes, correlation coefficients and intercepts of HCHO slant columns against those of the reference dataset, for each instrument and all off-axis elevation angles. The dotted lines in the first subplot correspond to values of 1.15 and 0.85. Toronto = UT-GBS. Figure from *Pinardi et al.* [2012].

3.4 Summary

GBS measurements have been validated against numerous ground-based and satellite instruments since the UT-GBS was assembled in 1998. In 2009, the PEARL-GBS was granted NDACC certification and therefore was required to participate in CINDI, a formal NDACC intercomparison campaign. The UT-GBS is nearly identical to the PEARL-GBS and therefore participated in the campaign in place of the PEARL-GBS. Therefore the PEARL-GBS, the permanent PEARL instrument, was not removed from Eureka. During the first two weeks of CINDI, the UT-GBS took zenith-sky measurements of NO_2. The zenith-sky NO_2 DSCDs met the NDACC standards and were on average within 2% of the reference dataset. Afterward, the

UT-GBS took its first-ever MAX-DOAS measurements, and resulting NO_2 and HCHO DSCDs were found to agree well with other instruments. Therefore, GBS measurements are consistent with other NDACC UV-visible instruments, suggesting that they could be useful for multi-station studies.

4 Ozone and NO_2 above Eureka

This chapter describes the retrieval of 11 years of ozone and NO_2 columns measured at Eureka using a consistent processing approach to ensure usefulness for long-term monitoring (see Section 0). Retrievals were performed using the DOAS technique (see Section 1.3), with the retrieval parameters given in Table 4.1. These retrieval parameters are discussed throughout this chapter. Data quality was monitored closely through analysis of the fitting parameters and the establishment of data filtering techniques. NDACC guidelines for ozone retrievals [*Hendrick et al.*, 2011] were followed . NDACC recommendations for NO_2 are currently under development [*Van Roozendael and Hendrick*, 2012], but were not available at the time of this analysis.

Table 4.1: Summary of DOAS retrieval parameters.

	Ozone	NO_2-vis	NO_2-UV
DOAS fitting interval	UT-GBS: 450-545 nm P-GBS: 450-540 nm	UT-GBS: 425-450 nm P-GBS: 425-450 nm	UT-GBS: 350-380 nm P-GBS: 350-380 nm
Cross-sections			
Ozone	*Bogumil et al.* [2003] at 223 K	*Bogumil et al.* [2003] at 223 K	*Bogumil et al.* [2003] at 223 K
NO_2	*Vandaele et al.* [1998] at 220 K	*Vandaele et al.* [1998] at 220 K	*Vandaele et al.* [1998] at 220 K
H_2O	Hitran 2004 [*Rothman et al.*, 2005b]	Hitran 2004 [*Rothman et al.*, 2005b]	--
O_4	*Greenblatt et al.* [1990] with corrected wavelengths	*Greenblatt et al.* [1990] with corrected wavelengths	*Greenblatt et al.* [1990] with corrected wavelengths
BrO	--	--	*Fleischmann et al.* [2004] at 223 K
OClO	--	--	*Wahner et al.* [1987] at 203 K
Polarization correction	Based on residuals (see Appendix B)	--	--
Ring	*Chance and Spurr* [1997]	*Chance and Spurr* [1997]	*Chance and Spurr* [1997]
Offset correction	--	1st order	1st order
Polynomial	3rd order	3rd order	3rd order
AMF	IASB-BIRA ozone AMF LUTs [*Hendrick et al.*, 2011]	IASB-BIRA NO_2 AMF LUTs [Appendix A of *Adams et al.*, 2012a]	IASB-BIRA NO_2 AMF LUTs [Appendix A of *Adams et al.*, 2012a]

The evolution of available SZA ranges above Eureka is shown Figure 4.1. This prevents the standard SZA 86-91° DOAS retrieval windows from being used for most of the year. At the summer solstice, the maximum SZA above Eureka is 76°, which leads to challenges in the DOAS procedure that are discussed throughout this chapter.

This chapter is organized as follows. DSCD and VCD retrievals are described in Sections 4.2 and 4.3. A new GBS error budget, which reflects year-to-year and seasonal changes in data is outlined in Section 4.4. The resulting 1999-2011 GBS ozone and NO_2 datasets are presented in Section 4.5. These datasets are then used to validate satellite measurements in Chapter 5 and to assess the unusual spring 2011 in the context of previous years in Chapter 7.

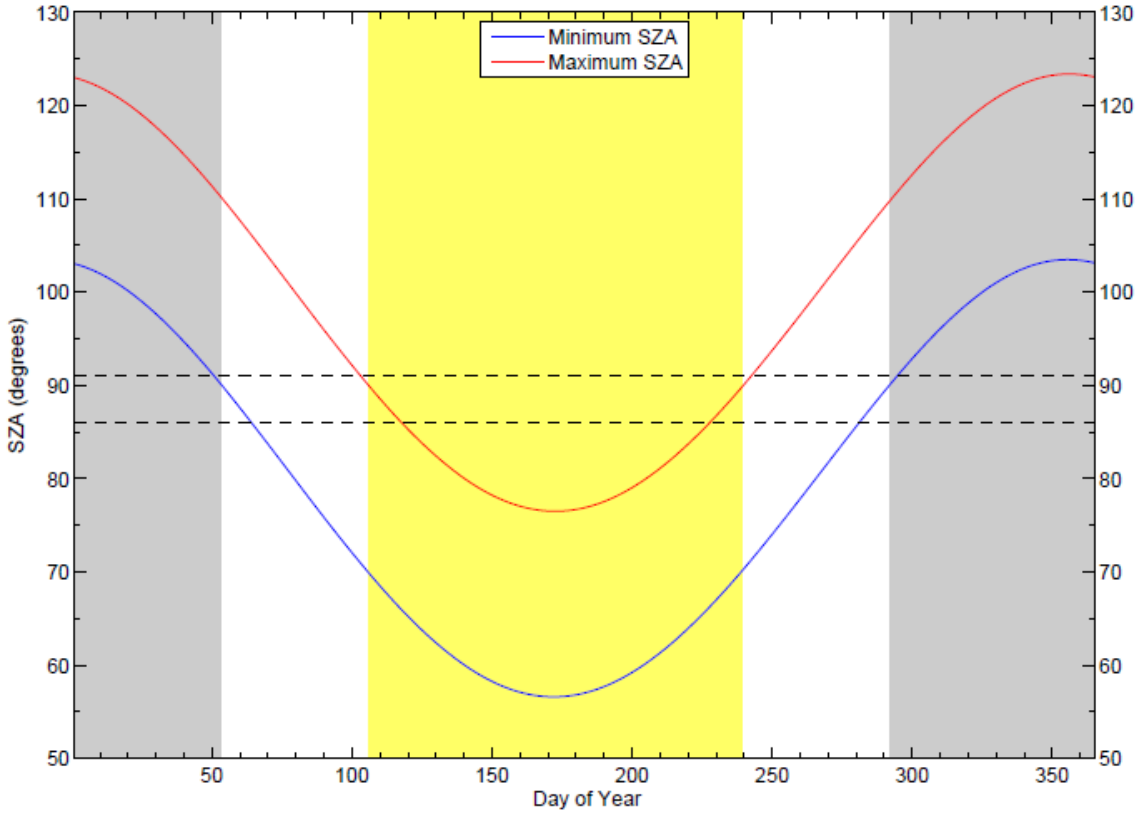

Figure 4.1: Maximum (red) and minimum (blue) SZAs in Eureka throughout the year, calculated for 2007. The grey shaded region indicates polar night, when the sun does not rise above the horizon, while the yellow shaded area indicates the time of year when the sun is continuously above the horizon. The horizontal dotted lines indicate 86° and 91°, the preferred range of SZAs used in the calculation of VCDs. Figure from *Fraser* [2008].

4.1 DSCD Retrievals

4.1.1 Ozone and NO_2-vis

Ozone and NO_2 DSCDs were retrieved for all 600 gr/mm PEARL-GBS measurements and 600 gr/mm and 400 gr/mm UT-GBS measurements taken at Eureka. These analyses were performed in QDOAS [*Fayt et al.*, 2011], with the settings summarized in Table 4.1.

Ozone DSCDs were retrieved using the settings recommended by the NDACC UV-visible working group [*Hendrick et al.*, 2011]. DSCDs were retrieved in QDOAS in the 450-545 nm window for the UT-GBS and in the 450-540 nm window for the PEARL-GBS. Neither window was extended to 550 nm, as recommended by NDACC, because this was at the edge of the CCD and the quality of the spectra decreased for these wavelengths. For the UT-GBS, a 1 nm gap in the fitting window was introduced at around 461 nm (and 468 nm after 22 August 2010) in order to exclude a bad pixel. Daily reference spectra were selected because the grating turrets spun upon instrument restarts prior to 2010, leading to large wavelength shifts in the datasets[*]. Wavelengths were calibrated against the solar spectrum [*Kurucz et al.*, 1984] daily based on the reference solar atlas. Ozone measured at 223 K [*Bogumil et al.*, 2003], NO_2 measured at 295 K [*Vandaele et al.*, 1998], O_4 [*Greenblatt et al.*, 1990] with corrected wavelengths, H_2O [*Rothman et al.*, 2005b], and Ring [*Chance and Spurr*, 1997] cross-sections were all fit. A third order polynomial was used in the analysis. Correction cross-sections were applied to all 600 gr/mm grating datasets due to large systematic errors in the ozone fitting window (see Appendix B).

NO_2 DSCDs were retrieved in the 425-450-nm window with the same daily references, calibration scheme and cross-sections as for ozone. A first order offset was also applied to correct for dark current and stray light. These NO_2 measurements, taken in the visible part of the spectrum, are referred to as NO_2-vis.

Sample DOAS fits for ozone and NO_2-vis are shown in Figure 4.2, for several for measurement dates. The magnitudes of the DSCDs vary significantly over the course of the year. This is

[*] This was particularly significant when the UT-GBS turret motor was degrading in 2009. The UT-GBS turret was replaced in winter 2009.

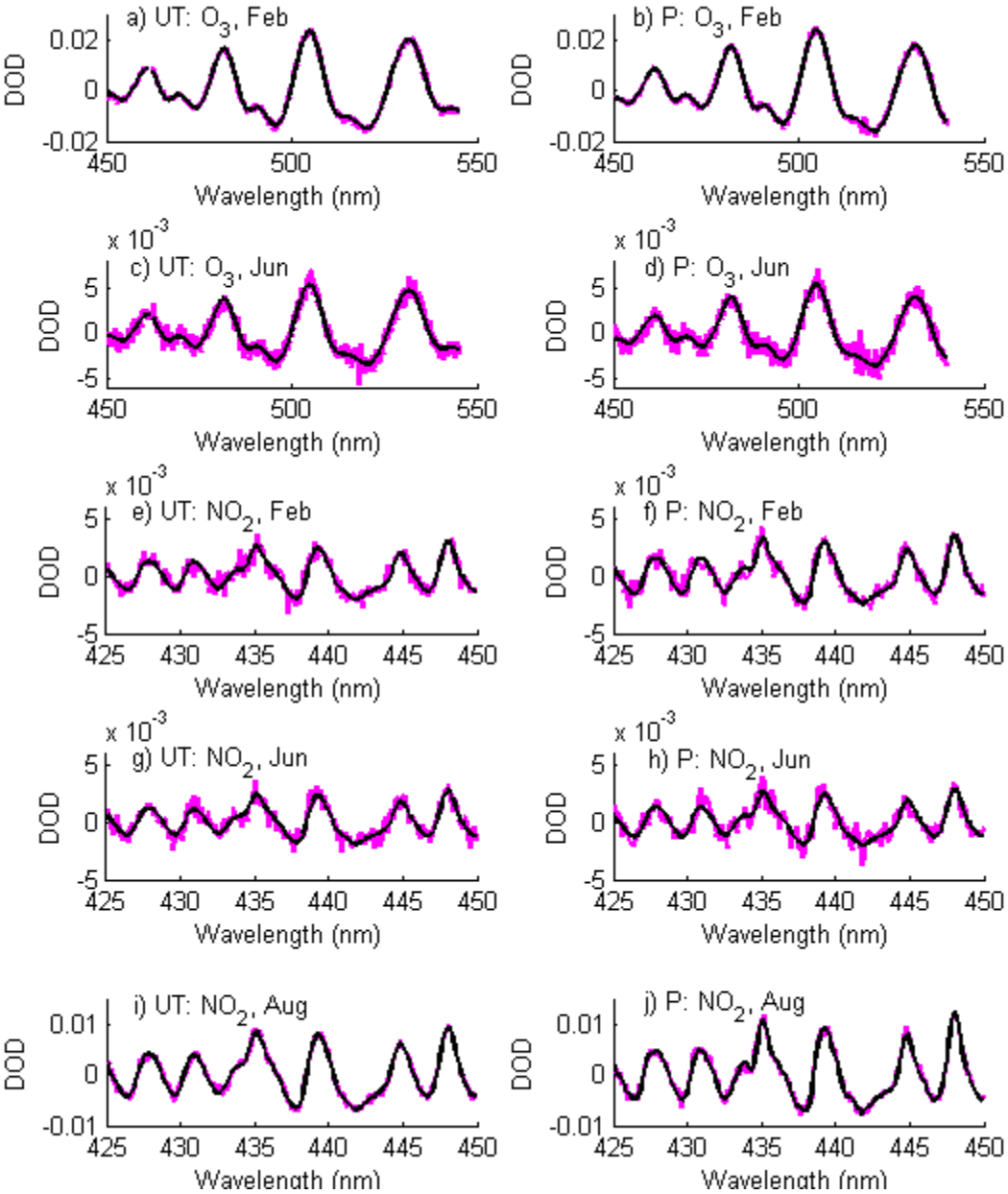

Figure 4.2: Sample ozone and NO_2 DOAS fit (black) and data (magenta), with instrument and date given in captions. (UT = UT-GBS, P = PEARL-GBS; Feb = 27 February 2008 at SZA = 91°; Jun = 20 June 2008 at SZA = 76°; Aug = 20 August 2010 at SZA = 88°).

primarily because of the varying SZA range at Eureka, shown in Figure 4.1. In the summer, when the twilight measurement SZA is small, the DSCD is also small. Furthermore, the Brewer-Dobson circulation leads to a minimum in ozone in the summer. Contrarily, photochemistry leads to a maximum in NO_2 in the summer.

4.1.2 NO_2-UV

When the UT-GBS and PEARL-GBS were taking dedicated BrO measurements with the high-resolution 1800 gr/mm and 1200 gr/mm gratings respectively, NO_2 could not be retrieved in the 425-450 nm range. Therefore, NO_2 was retrieved in the 350-380 nm window, and is referred to as NO_2-UV. This DOAS fit parameters used for NO_2-UV are also given in Table 4.1. Wavelengths were calibrated against the solar spectrum daily based on the reference solar atlas [*Kurucz et al.*, 1984]. Ozone measured at 223 K [*Bogumil et al.*, 2003], NO_2 measured at 295 K [*Vandaele et al.*, 1998], O_4 [*Greenblatt et al.*, 1990] with corrected wavelengths, BrO measured at 223 K [*Fleischmann et al.*, 2004] and OClO measured at 204 K [*Wahner et al.*, 1987], and Ring [*Chance and Spurr*, 1997] cross-sections were all fit using QDOAS, with a third order polynomial. A first order offset correction was also applied to correct for dark current and stray light. Sample DOAS fits are shown in Figure 4.3.

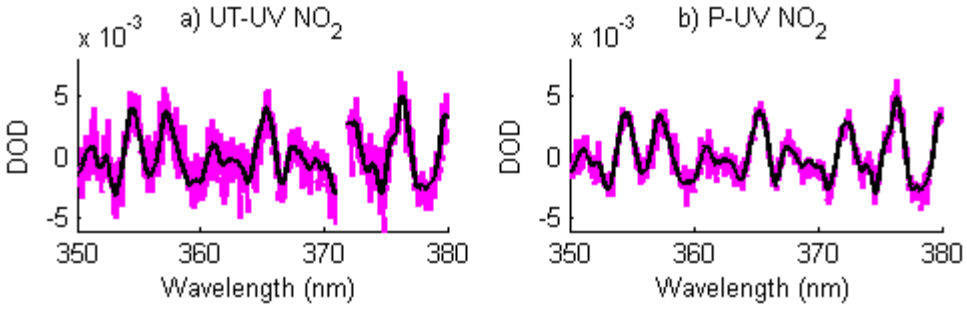

Figure 4.3: Sample twilight DOAS fit (black) and data (magenta) for NO_2 at SZA 90° in the UV range on (a) 30 March 2008 for the UT-GBS and (b) 30 March 2007 for the PEARL-GBS.

4.1.3 Data Quality

The quality of the UT-GBS and PEARL-GBS spectra vary from year-to-year and season-to-season. This can be due to instrument problems, errors in the data acquisition software, available SZA ranges, and weather. Furthermore, spectra can be saturated when sunlight conditions are changing rapidly or when an instrument shutter is not working correctly. Saturated spectra are averaged with up to hundreds of normal spectra and therefore can be difficult to identify via intensity thresholds in preprocessing software and visual inspection*. This section assesses year-to-year and seasonal changes in GBS spectral quality and presents data selection criteria.

4.1.3.1 Seasonal Variation

The Eureka fall 2006 - fall 2010 datasets were used in order to investigate the seasonal variability in UT-GBS and PEARL-GBS ozone and NO_2 data quality. In order to remove low-quality data, such as partly saturated spectra, RMS filters were applied to residuals. For ozone and NO_2-vis, RMS thresholds of 0.002 for SZA < 90° and 0.003 for SZA > 90° were selected to remove most extreme outlying DSCDs and DSCDs retrieved from spectra that were visually identified as saturated. For SZA < 94°, more than 95% of the data passed this RMS threshold, as shown in Table 4.2. For NO_2-UV, weaker RMS thresholds of 0.002 for SZA < 87° and 0.003 for SZA < 91° were used. Spectra taken for SZA > 91° were noisy due to reduced signal at twilight and therefore were not included.

Table 4.2: Percentage of DSCDs that remain for SZA < 94° after RMS and wavelength shift thresholds.

	Ozone		NO_2-vis	
	RMS cuts	RMS and shift	RMS cuts	RMS and shift
UT-GBS	99.3%	97.2%	99.1%	97.1%
PEARL-GBS	95.7%	94.6%	96.4%	95.5%

* This was solved in 2010, with data acquisition software that excluded saturated spectra from the recorded average.

Measurement quality is also very sensitive to wavelength shifts caused by temperature variability (see Section 3.3.4) and spinning of the grating turret. For both ozone and NO_2 DSCD retrievals, the twilight spectrum was allowed to shift and stretch in order to match the reference spectrum. Some large wavelength shifts were observed, particularly when the grating spun after instrument restarts[*]. When the wavelength shift was larger than 0.1 nm, systematic changes in the NO_2 DSCDs were observed. Therefore all measurements were filtered for wavelength shifts larger than 0.1 nm. The percentage of data that passed both thresholds is also shown in Table 4.2.

A timeseries of average daily RMS, wavelength shift, and wavelength stretch calculated in QDOAS is shown Figure 4.4 for the UT-GBS and PEARL-GBS DSCDs that passed the RMS and shift thresholds described above. The average daily average RMS tends to be lower in the winter than in the summer. The average wavelength shift between the reference and twilight spectra is larger for the UT-GBS than the PEARL-GBS. However, the average stretch parameter is larger for the PEARL-GBS than the UT-GBS. This suggests slight differences between the instruments.

Both instruments show a seasonal variation, with lower RMS, shift, and stretch parameters in the spring and fall than in the summer. This is likely due to a combination of reasons, listed below.

- Reflective neutral density filters can decrease measurement quality due to the Fabry-Perot etalon effect [*Platt and Stutz*, 2008] (see Section 2.6). There is evidence of this as the RMS in the PEARL-GBS measurements peaks in August 2007 and June-August 2008, when neutral density filters were used during shutter breakages.

- Due to the 24-hour sunlight, the time between the reference spectrum and the twilight spectrum can reach 12 hours in summer, increasing the likelihood of a temperature gradient (and therefore wavelength shift) between these spectra.

- Light-leaks in both spectrometers prior to 2009 led to increased dark spectrum signals in the summer (see Section 2.3.1).

[*] This was also solved in 2010, with data acquisition software that prevented the turret from spinning upon restart.

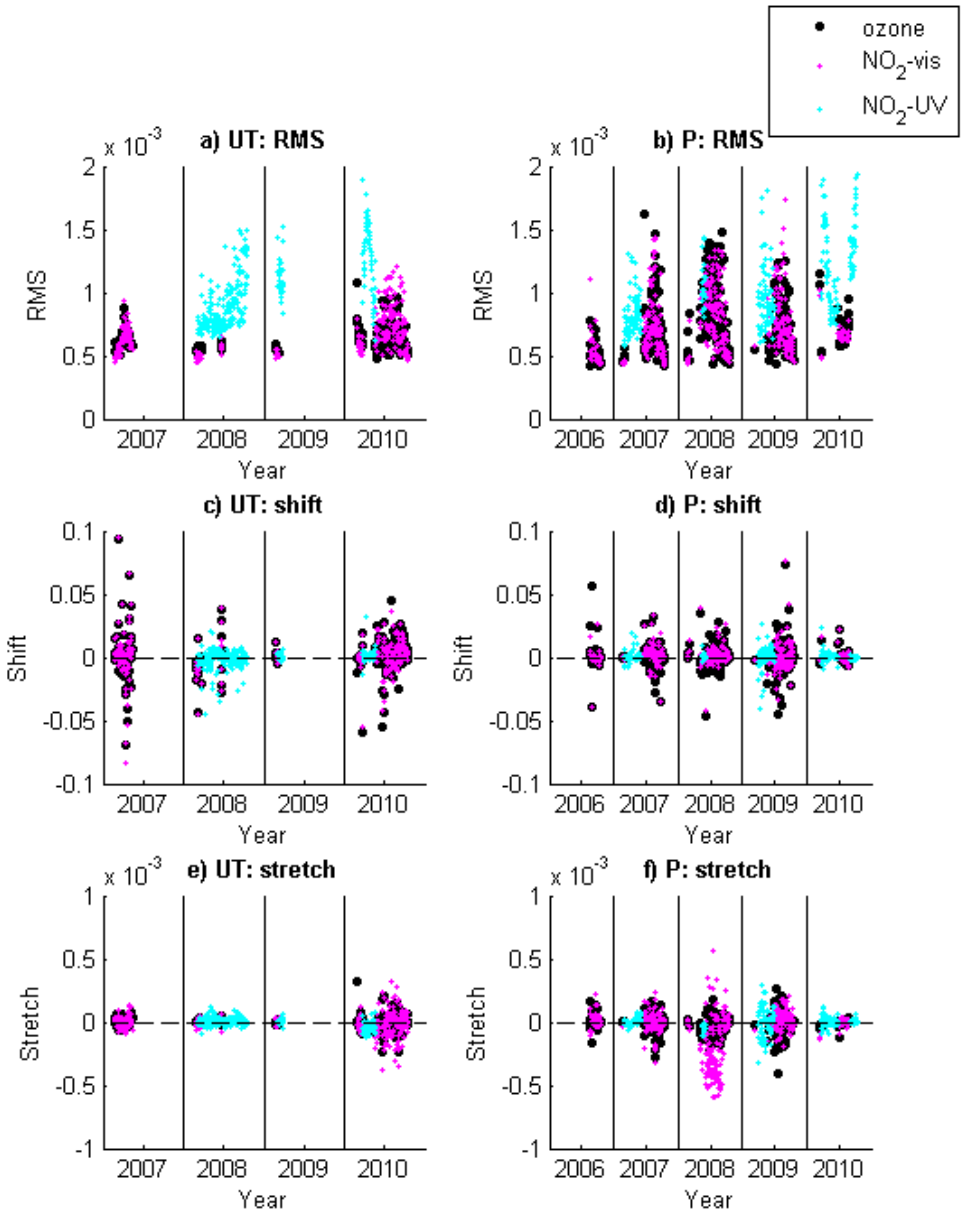

Figure 4.4: Daily average fit parameters for ozone (black), NO_2-vis (magenta), and NO_2-UV for SZA < 90°. (a) UT-GBS and (b) PEARL-GBS RMS; (c) UT-GBS and (d) PEARL-GBS wavelength shift; and (e) UT-GBS and (f) PEARL-GBS wavelength stretch. The black vertical lines indicate 1 January. The horizontal dashed line indicates the zero-line.

- The altitude sensitivity of DOAS measurements changes with SZA. The approximate averaging kernels for DOAS measurements at SZA 90° in March and SZA 76° in June at 75°N are shown in Figure 4.5. The averaging kernels indicate that for the large SZA, corresponding to spring and fall measurements at Eureka, sensitivity peaks in the stratosphere, with very little sensitivity to the troposphere. This is expected, as strong scattering occurs in the stratosphere for these SZA. In the summer, at smaller SZA, photons are scattered throughout the atmosphere, leading to enhanced sensitivity to the troposphere and clouds. This reduces the quality of the DOAS fits, particularly in the ozone retrieval window, as O_4 and water vapour interfere with the measurements.

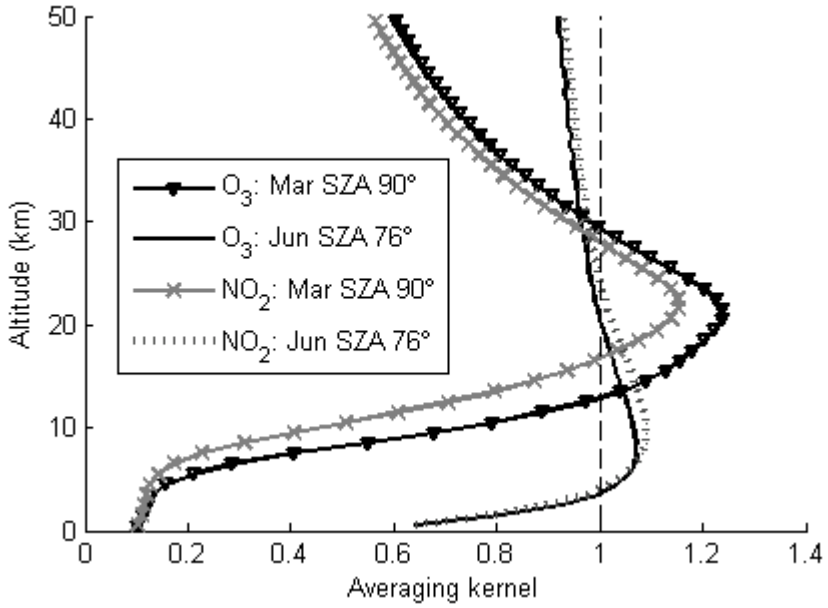

Figure 4.5: Approximate averaging kernels at 75°N for DOAS measurements of ozone and NO_2 in March at SZA 90° and June at SZA 76°, calculated by F. Hendrick at IASB-BIRA, using the method of *Eskes and Boersma* [2003]. For ozone, the AMFs were calculated with TOMS v8 climatology for 375 DU of ozone [*Hendrick et al.*, 2011]. For NO_2, the sunrise NO_2 profiles from the *Lambert et al.* [1999; 2000] climatology AMFs [Appendix A of *Adams et al.*, 2012a], were used. Note that for NO_2, measurements do not extend below 17 km, as AMFs are set to zero below 17 km.

The PEARL-GBS wavelength shifts reach a maximum in 2009, likely because it was housed in the penthouse at PEARL, which underwent large temperature oscillations. In 2010, the PEARL-GBS measurements are more stable than in other years, likely due to improvements made to the instrument resolution in spring 2010 (Section 2.2.5). The PEARL-GBS minimum RMS is higher in 2010 than in other years, likely because fewer spectra were averaged per measurement, in order to increase the sampling in MAX-DOAS and direct-sun measurements. Furthermore, the increased RMS could reflect undersampling errors (see Section 2.2.6).

4.1.3.2 Spring 1999-2011

Summaries of the UT-GBS and PEARL-GBS spring-time measurement settings and data quality are given in Table 4.3 and Table 4.4. Measurement dates at Eureka for 1999-2011 are given in Table 2.1. For most campaigns, the data quality was good. However, in 2001 the UT-GBS mechanical slit jammed open, leading to a reduced resolution*, which was calculated in QDOAS at 4-5 nm FWHM. Therefore, data from this campaign were not analyzed. During the 2003-2004 campaigns, there was an error in the data acquisition software such that only one spectrum was averaged per acquisition, instead of the typical seven to 300 spectra per acquisition [*Fraser et al.*, 2007a]. This reduced signal-to-noise in the spectra. Therefore, averages of two spectra were calculated prior to analysis. More spectra could not be averaged because this reduced time resolution and introduced errors in the Langley plot VCD retrievals. In 2010, the UT-GBS resolution and signal-to-noise were compromised slightly, due to problems with the mechanical slit. The PEARL-GBS measurements were of good quality for all campaigns. In 2008, the UT Suntracker was installed above the PEARL-GBS, allowing for direct-sun measurements. In 2010, MAX-DOAS measurement routines were also introduced.

In order to remove saturated and other low-quality spectra, filters were applied to these datasets, as described in Section 4.1.3.1. All data were filtered with the requirement that the wavelength shift between the twilight and reference spectrum be less than 0.1 nm. During the years with good spectral quality, the ozone, NO_2-vis data were filtered by RMS less than 0.002 for

* Personal communication with E.E. Farahani, 18 April 2011.

Table 4.3: Summary of UT-GBS springtime measurements at Eureka.

Year	Grating (gr/mm)	Spectral quality
1999	400	Good
2000	600 and 1800	Good
2001	600	Poor - slit jammed open (resolution ~ 4-5 nm)
2003	400 and 600	Fair - error in acquisition software (reduced signal)
2004	400	Fair - error in acquisition software (reduced signal)
2005	600	Good
2006	600	Good
2007	600	Good
2008	600 and 1800	Good
2009	600 and 1800	Good
2010	600 and 1800	Fair - slit jammed open (slightly reduced signal/resolution)
2011	600	Good, with improved resolution

Table 4.4: Summary of PEARL-GBS springtime measurements at Eureka.

Year	Grating (gr/mm)	Viewing	Spectral quality
2007	600 and 1200	Zenith-sky	Good
2008	600 and 1200	Zenith-sky and direct-sun	Good
2009	600 and 1200	Zenith-sky and direct-sun	Good
2010	600 and 1200	Zenith-sky, direct-sun and MAX-DOAS	Good with improved resolution
2011	1200	Zenith-sky, direct-sun and MAX-DOAS	Good with improved resolution

SZA < 90° and RMS less than 0.003 for SZA < 94°. In 2003 and 2004, when the UT-GBS signal-to-noise was compromised, the RMS threshold was increased to 0.004 for SZA < 90° and 0.006 for SZA < 94°. For NO_2-UV, RMS thresholds of 0.002 for SZA < 87° and 0.003 for SZA < 91° were used.

The average and standard deviation of the DOAS RMS, shift, and stretch are shown in Figure 4.6 for ozone and NO_2-vis DSCDs retrieved from February to May for SZA < 90°. Larger RMS and more variability in shift and stretch values are observed in the 2003-2004 UT-GBS measurements, as expected. Furthermore, year-to-year variability is evident in all measurements, pointing to small changes in performance.

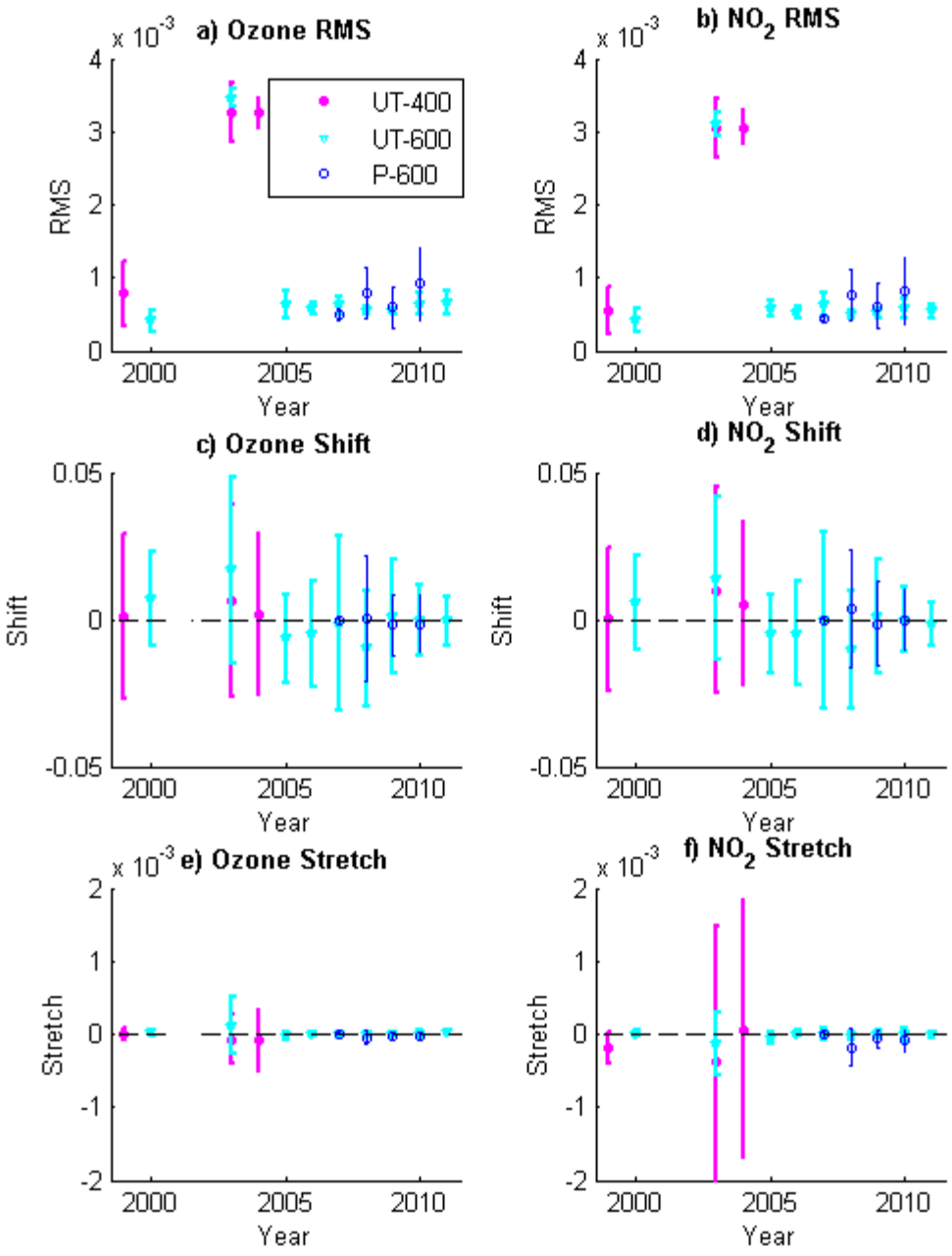

Figure 4.6: Average and standard deviation in DOAS parameters for DSCDs retrieved from February to May at SZA < 90° for the UT-GBS 400 gr/mm grating (magenta), UT-GBS 600 gr/mm grating (cyan), and the PEARL-GBS 600 gr/mm grating (blue). The ozone (panel a) and NO_2 (panel b) RMS; the ozone (panel c) and NO_2 (panel d) twilight to reference spectrum wavelength shift; and the ozone (panel e) and NO_2 (panel f) twilight to reference spectrum stretch are all shown. Black dashed lines indicate zero.

4.1.4 Intercomparisons of UT-GBS and PEARL-GBS DSCDs

In order to validate the corrected PEARL-GBS ozone DSCDs beyond spring 2007, Type I intercomparisons (see Section 3.1.1) were performed between the UT-GBS and PEARL-GBS DSCDs for 2008-2010. PEARL-GBS and UT-GBS measurement were interpolated to an SZA grid with 0.1° intervals for SZA > 80° and a reduced grid of 1° intervals for SZA < 80°. The reduced grid was used because the GBS instruments take fewer measurements for SZA < 80° in order to prolong shutter lifetime. DSCDs with SZA < 92° were compared with a linear regression. The comparisons were restricted to days on which the reference spectra of the two instruments were within 0.2° SZA; coincident measurements ranged over at least 2° SZA; each instruments had at least ten DSCDs; and at least one measurement was for SZA > 70°. Linear regressions were performed and the slope, y-intercept, and RMS residual were calculated. The mean slope, y-intercept, and RMS were calculated for both summer and spring. The standard error, the standard deviation divided by the square root of the number of measurements, was also calculated.

These results are shown in Table 4.5 for ozone, Table 4.6 for NO_2-vis, and Table 4.7 for NO_2-UV. Most values meet the 2009 NDACC standards within error (see Table 3.1). The spring-time ozone and NO_2-vis values are comparable to the intercomparison results from *Fraser et al.* [2009]. The NO_2-UV RMSs do not meet NDACC standards (see Table 4.7) , likely due to lower signal-to-noise ratio at these wavelengths.

Table 4.5: Type-1 NDACC intercomparisons of UT-GBS and PEARL-GBS ozone DSCDs from 2008-2010. All values meet the NDACC standards, which are given in Table 3.1.

	Spring (Feb 28- March 7)		Summer (June 19 - Aug 26)	
	AM	PM	AM	PM
Number twilights	3	3	27	29
Slope	1.009±0.003	1.010±0.001	1.00±0.01	0.983±0.008
Intercept ($x10^{19}$ mol/cm^2)	0.057±0.070	-0.054±0.023	0.087±0.023	0.057±0.018
RMS residual ($x10^{19}$ mol/cm^2)	0.023±0.004	0.026±0.004	0.045±0.004	0.044±0.003

Table 4.6: Same as Table 4.5 but for NO_2 DSCDs measured in the 425-450 nm range. All values meet the NDACC standards.

	Spring (Feb 27 - March 6)		Summer (June 19 - Aug 26)	
	AM	AM	AM	PM
Number twilights	3	3	27	29
Slope	0.96±0.03	1.02±0.01	1.00±0.01	0.985±0.006
Intercept ($x10^{16}$ mol/cm^2)	-0.013±0.016	0.028±0.011	-0.025±0.014	0.010±0.014
RMS residual ($x10^{16}$ mol/cm^2)	0.030±0.033	0.031±0.032	0.040±0.002	0.037±0.001

Table 4.7: Same as Table 4.5 but for NO_2 DSCDs measured in the 350-380 nm range. Values that do not meet the NDACC standards are given in red.

	Spring (29 March - 1 June)	
	AM	PM
Number twilights	22	21
Slope	0.98±0.02	0.99±0.02
Intercept ($x10^{16}$ mol/cm^2)	-0.05±0.03	-0.06±0.02
RMS residual ($x10^{16}$ mol/cm^2)	0.010±0.012	0.093±0.008

4.2 VCD Retrievals

Ozone and NO_2 total columns were retrieved using the Langley method with the settings described in *Hendrick et al.* [2011]. For each twilight, DSCDs in the SZA 86-91° window were selected, when those SZAs were available. Otherwise, the nearest available 5° SZA window was used. A daily average RCD was calculated from the morning and evening twilights because a daily reference spectrum was used. Twilights without measurements for SZA > 70° or for which the SZA span was smaller than 2° were not analyzed. Furthermore, a minimum of eight DSCDs was required.

DOAS VCD retrievals in the summer at 80°N are particularly challenging. The evolution of available SZA ranges above Eureka is shown in Figure 4.1. At the summer solstice, the maximum SZA above Eureka is 76°. This yields AMFs of ~4 for both ozone and NO_2, which is approximately four times smaller than the typical AMF at SZA 90°. Furthermore, the range in AMFs for SZAs 86-91° is greater than 10, while for SZAs 71-76°, the range in AMFs is smaller

than 1. This leads to larger uncertainties in the summertime RCD calculations from the Langley plots. Furthermore, the altitude sensitivity of DOAS measurements changes significantly between the spring and summer (see Figure 4.5), with more sensitivity to the troposphere in the summer. This enhanced sensitivity to clouds yields uncertainties in the AMFs that are discussed in Section 1.3.5 and in the sections below.

4.2.1 Ozone

For DOAS ozone retrievals, the inclusion of daily ozone data in the AMF calculations improves results, especially under vortex conditions [*Bassford et al.*, 2001]. Ozone total columns were retrieved using the NDACC-recommended AMF look-up tables (LUTs) [*Hendrick et al.*, 2011]. Daily AMFs are extracted from these LUTs based on the latitude and elevation of PEARL, day of year, sunrise or sunset conditions, wavelength, SZA, surface albedo, and ozone column. For the GBS, daily ozone total columns interpolated from ozonesonde data were input to the AMF LUTs. RCDs from the 2007 ozone DOAS analysis are shown in panel a of Figure 4.7. RCDs calculated from morning and evening twilight Langley plots agree well. RCDs are larger in the spring and fall as the noon-time SZA is larger.

For ozone, cumulus clouds can have up to 80% impact at SZA 86° [*Bassford et al.*, 2001]. This can introduce errors in the ozone retrievals in the summertime, when the instruments are sensitive to the troposphere. Therefore, twilights with $R^2 < 0.9$ in the Langley plot were rejected. Furthermore, after analysis, measurements with > 60 DU error were removed (see Section 4.3 for a description of the error budget). This removed less than 0.1% of the data.

4.2.2 NO_2

For NO_2, the input ozone profile has a small impact on DOAS AMFs [*Bassford et al.*, 2001] and therefore daily ozonesonde data are not necessary for the interpolation of AMFs. For the GBS measurements, the AMFs were extracted from a new set of LUTs, developed by BIRA-IASB [Appendix A of *Adams et al.*, 2012a]. The NO_2 concentration below 17 km was set to zero, so these AMFs produce partial columns from 17 km upward.

RCD determination is a large source of error in NO_2 VCDs [*Vaughan et al.*, 1997]. Figure 4.7 shows the NO_2 RCDs calculated for the UT-GBS and PEARL-GBS in 2007. In the early spring and late fall, there is a bias between the morning and afternoon RCD calculations, with much less NO_2 measured in the morning Langley plots than the afternoon. This is likely due to the rapidly changing concentrations, as NO_2 is released from night-time reservoirs throughout the day. Therefore, to prevent biases in the dataset, NO_2 was only retrieved on days with both morning and afternoon RCD calculations, with $R^2 > 0.6$ in the Langley plots. VCDs were also filtered for error < $2x10^{15}$ mol/cm^2 and < 200% (see Section 4.3 for a description of the error budget).

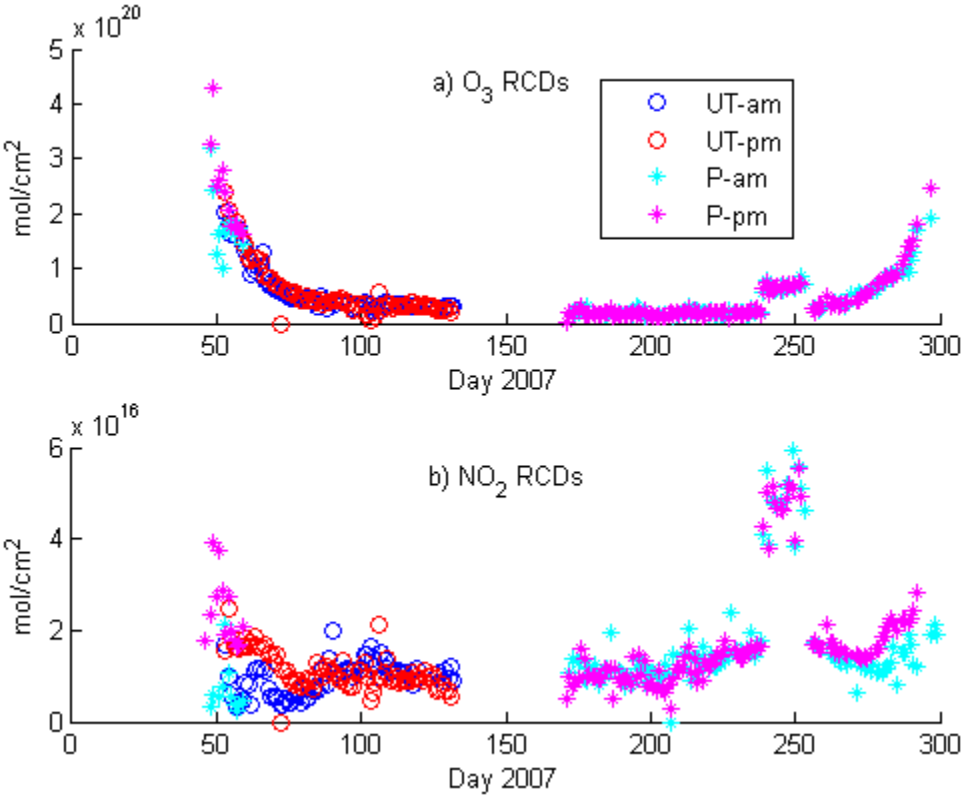

Figure 4.7: (a) ozone and (b) NO_2 RCDs versus day of 2007 for the UT-GBS morning (blue circles) and evening (red circles) and PEARL-GBS morning (cyan stars) and evening (magenta stars) twilight measurements. Note that the large RCD values around day 250 are due higher SZA reference spectra, which were selected because a shutter problem saturated noon spectra.

4.3 Error Estimates

Since the DOAS fit quality, RCDs, and SZA range vary systematically throughout the year, a new error budget was developed. Systematic errors are calculated for each VCD(SZA) and are averaged within the Langley plot SZA range for each twilight. Random error is calculated from the standard deviation of VCDs over the twilight. The systematic and random error is added in quadrature to produce a total error for a twilight measurement.

The systematic errors included in this budget are summarized in Table 4.8. Each error source listed in the table is estimated for a given twilight by multiplying a parameter of the DOAS retrieval by a multiplication factor. Systematic error contributions to the VCD are broken into four components: SCD (DSCD+RCD), DSCD only, RCD, and AMF errors. Each of these main error components is calculated by adding the subset of individual error contributions in quadrature. These four error components are described below and were propagated through Equation 1.32 using error analysis formulae to calculate the error in each VCD(SZA).

The SCD error is made up of systematic errors that scale as a fixed percentage of the DSCD in the DOAS analysis. These systematic errors in the DSCD affect the y-intercept, or RCD, by the same percentage. Therefore, these errors are applied equally to the entire SCD=DSCD+RCD. The SCD error includes uncertainties in the instrument, cross-section, temperature-dependence of the cross-section, and improper correction for the Ring effect.

Systematic errors caused by structure in the DOAS residuals do not necessarily vary as fixed percentage of the DSCD and, therefore, do not propagate directly to the RCD. Therefore, these errors are only applied as DSCD errors. DSCD errors were estimated by comparing UT-GBS and PEARL-GBS DSCDs for various fitting errors. When the fitting error for both instruments was small, good agreement was observed, as expected. For larger fitting errors, typically caused by systematic errors in the residual due to poor temperature control or polarization errors, poorer agreement was observed. The impact of structure in the residuals on agreement between the UT-GBS and PEARL-GBS was estimated at three times the DOAS fitting error for both ozone and NO_2. For ozone, a polarization error, which scales with the polarization DSCD (see Appendix B) is also included.

Table 4.8: Systematic error budget for ozone and NO_2 VCDs.

Value	Error	Multiply by	Multiplication factor ozone	NO_2
SCD	Instrument error	SCD	0.01[a]	0.01[a]
	Absolute cross-section	SCD	0.031[b]	0.05[c]
	Temperature dependence of cross-section	SCD	--	0.08[d]
	Filling in of absorption by Raman scattering	SCD	0.01[e]	0.05[f]
DSCD	QDOAS fitting errors and structure in residual	QDOAS fitting error	3[g]	3[g]
	Polarization systematic error	Polarization residual DSCD	$1x10^{17}$ mol/cm^{2} [h]	--
RCD	Baseline error	--	$1x10^{17}$ mol/cm^{2}	$2x10^{15}$ mol/cm^{2}
	Variation in RCD	Difference between am/pm RCD	0.5	0.5
AMF	Shape of profile, aerosol loading, ozone VCD, and radiative transfer model	AMF	0.04[i]	0.05[j]

[a] [*Fraser et al.*, 2009]
[b] [*Bogumil et al.*, 2003]
[c] [*Vandaele et al.*, 1998]
[d] Estimated from Figure 2 in Pfeilsticker et al. [1999], using one-sigma standard deviation of stratospheric temperature at 30 km from the NDACC automailer 2006-2010 during measurements period (day 50 - 300)
[e] [*Fish and Jones*, 1995]
[f] For multiple Mie-scattering at 5.4 nm resolution [*Pfeilsticker et al.*, 1999]
[g] Estimate based on comparisons between UT-GBS and PEARL-GBS DSCDs
[h] 2σ error on slope used for polarization residual corrections shown in Appendix B
[i] [*Hendrick et al.*, 2011]
[j] [*Bassford et al.*, 2005]

The RCD and AMF errors account for additional systematic errors in the Langley analysis. The RCD baseline error was estimated by varying the SZA interval of the Langley analysis and observing its effect on the RCD. The variation in RCD error was estimated by taking half of the difference between the morning and afternoon RCDs. This error is particularly important for characterization of NO_2, as morning and twilight RCDs differ in the early spring and late fall. The AMF error accounts for the shape of the ozone and NO_2 profiles and uncertainties in the radiative transfer model.

Figure 4.8 shows measurements and errors for the UT-GBS and PEARL-GBS in 2007 and 2008. The uncertainty in ozone has three maxima. The early spring and late fall maxima are attributed

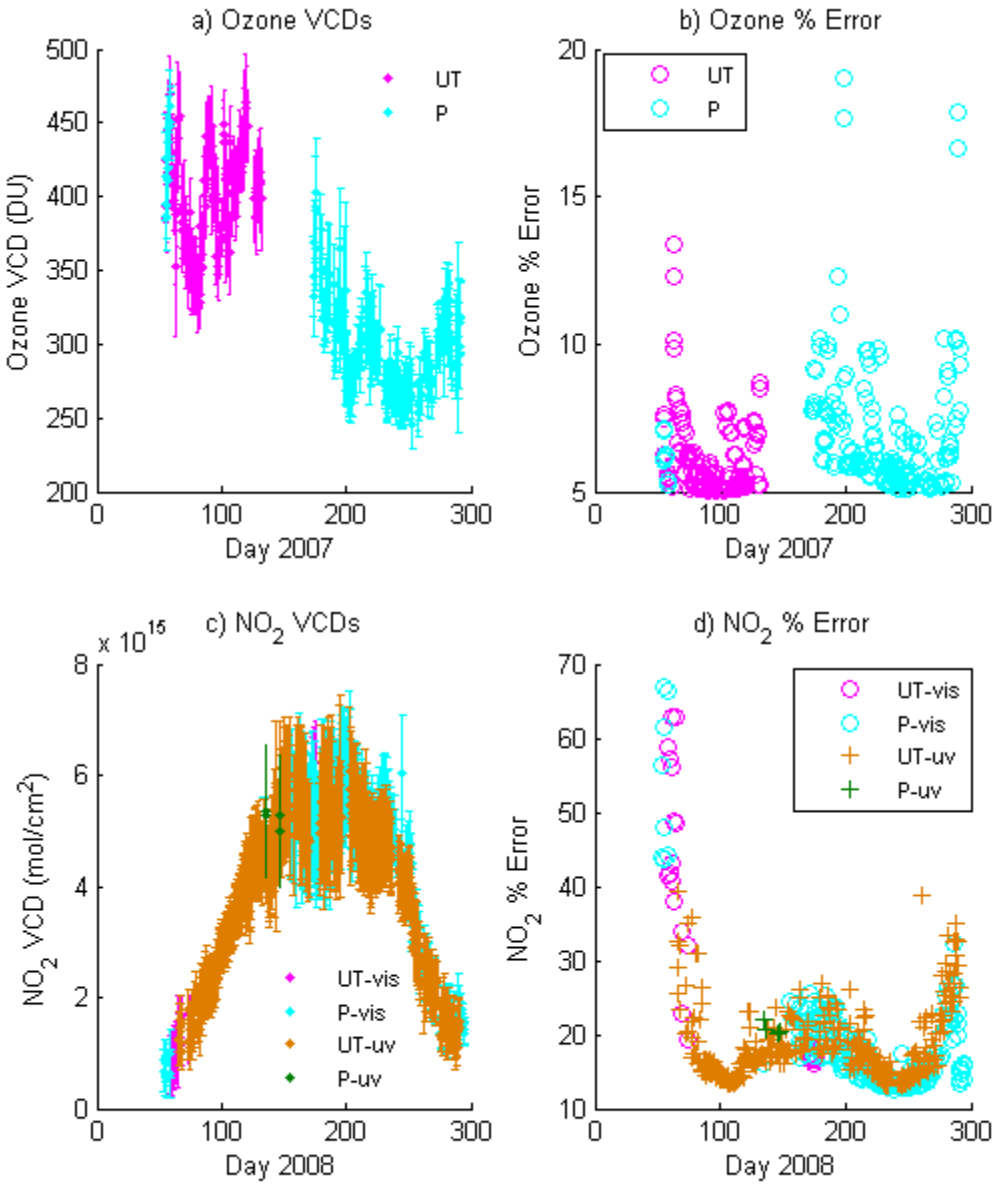

Figure 4.8: UT-GBS (UT) and PEARL-GBS (P) measurements and errors. Ozone (a) VCDs and (b) total percent error shown for 2007. NO_2 (c) VCDs and (d) total percent error for NO_2-vis and NO_2-UV measurements shown for 2008. 2007 data are shown for ozone because more visible measurements were taken in spring 2007 than in other years. 2008 data are shown for NO_2 because NO_2-UV measurements were taken for most of that year.

to the small range of SZAs available at twilight. This limits the range over which the Langley plot analysis can be performed. The summer maximum reflects the small AMFs and larger uncertainties in DSCDs. For NO_2, similar maxima are observed. In early spring, the percent error in NO_2 is very high because concentrations of NO_2 are low.

The mean total ozone error for 2003-2011 was 6.2%. This is slightly larger than the 5.9% total error reported for NDACC ozone column measurements [*Hendrick et al.*, 2011], but is consistent with the challenges of taking DOAS measurements at high latitudes, particularly during seasons when the 86-91° SZA range is not available (see Figure 4.1). Mean total errors for 2003-2011 of 23% for NO_2-vis and 22% for NO_2-UV were calculated. These errors are heavily weighted by uncertainties of up to 100% in the early spring when concentrations of NO_2 are low and daylight SZA ranges are limited. For measurements taken between days 80-260, the mean total error is 18% for NO_2-vis and 20% for NO_2-UV.

4.4 Ozone and NO_2 Datasets

Year-round ozone and NO_2 measurements for 2006-2011 are shown in Figure 4.9. Good qualitative agreement is observed between the various GBS datasets. The ozone measurements are high in the spring and decrease over summer, due to the Brewer-Dobson circulation. NO_2 measurements are dominated by photochemistry, with a maximum in the summer, when NO_x is released from night-time reservoirs. Spring-time ozone and NO_2 measurements are shown in Figure 4.10 and Figure 4.11, respectively, for 1999-2011. Note that the error bars for the 2003 and 2004 data are larger due to the instrument problems described in Section 4.1.3.2. There is large year-to-year variability, which depends on the position and strength of the polar vortex. Low ozone columns are observed in 2001, 2005, 2007, and 2011, years in which the polar vortex was above Eureka [*Lindenmaier et al.*, 2012]. This is explored further in Chapter 7.

4.5 Summary

Ozone and NO_2 were retrieved using consistent retrieval settings for measurements made at Eureka by the UT-GBS for 1999-2011 and the PEARL-GBS for 2006-2011. Ozone was retrieved using the new NDACC guidelines and AMF LUTs [*Hendrick et al.*, 2011], while NO_2 was retrieved using a new set of AMF LUTs developed at IASB-BIRA. DOAS fit quality was

characterized through RMS, spectral shift, and spectra stretch and was found to have improved in 2010, following modifications to the input optics. This new, consistent long-term dataset was used for the validation and ozone depletion studies in Chapters 5 and 7 of this thesis.

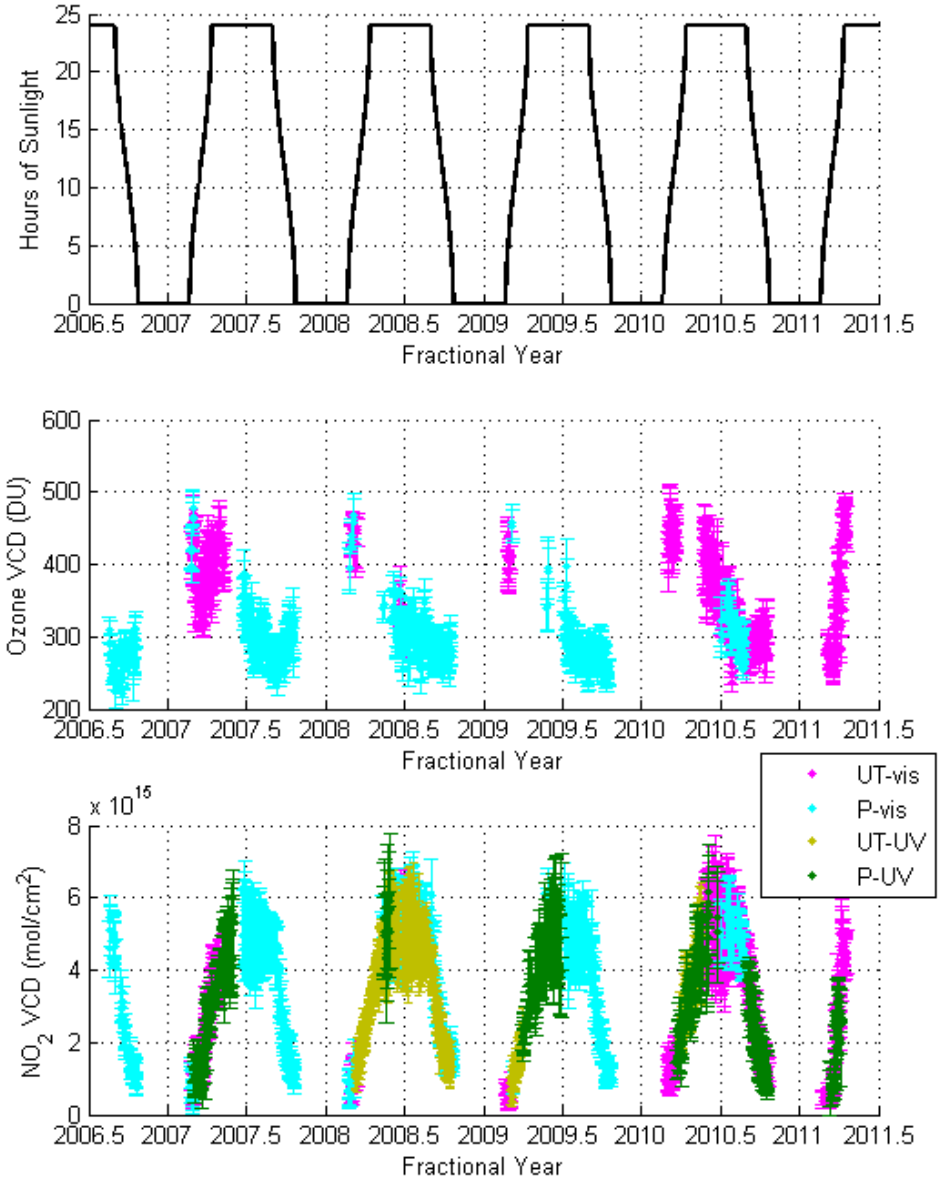

Figure 4.9: Year-round measurements at PEARL. (a) Hours of sunlight. (b) Ozone measured by the UT-GBS (magenta), and PEARL-GBS (cyan). (c) NO_2-vis measured by the UT-GBS (magenta) and PEARL-GBS (cyan) and NO_2-UV measured by the UT-GBS (gold) and PEARL-GBS (green).

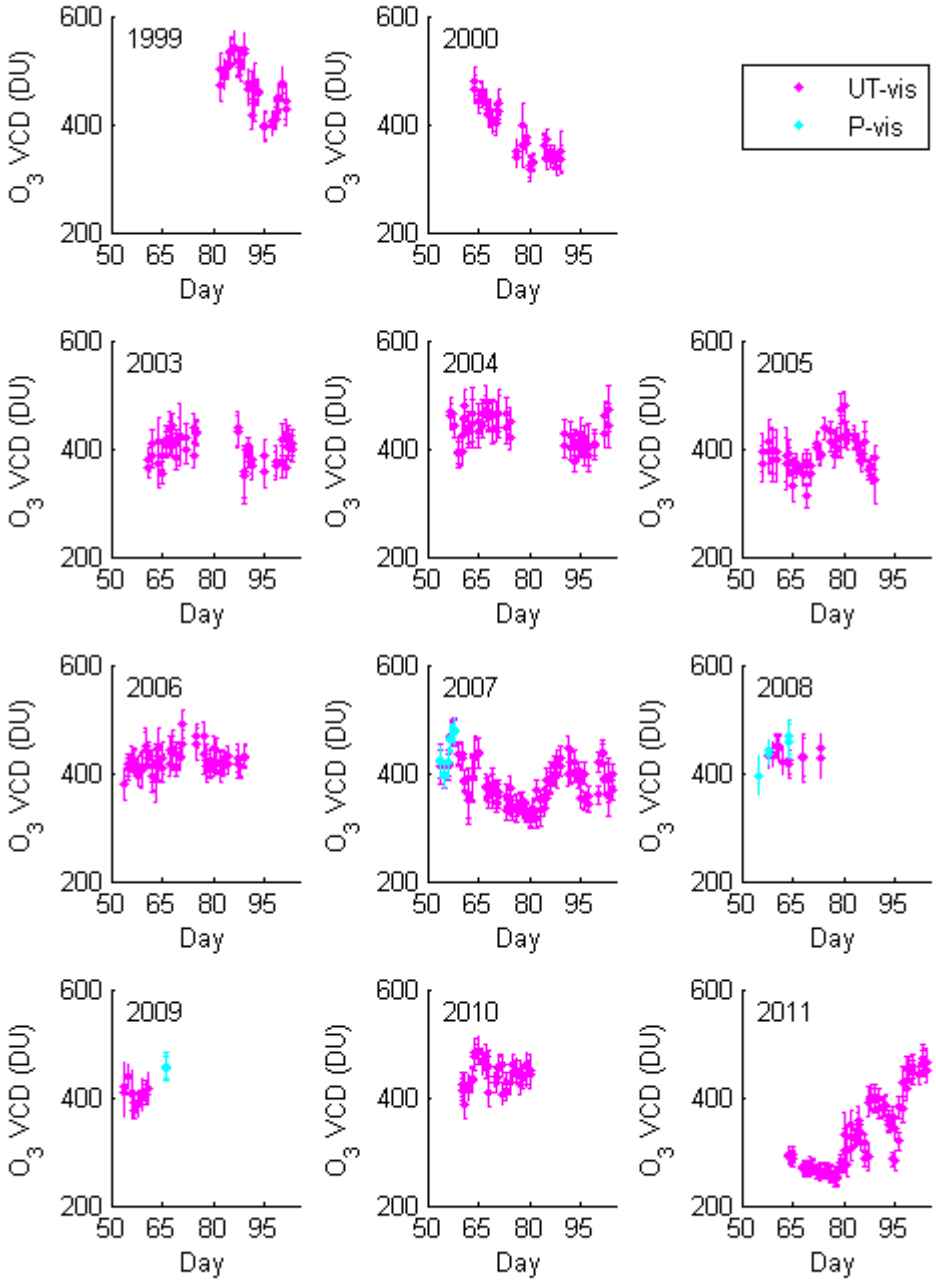

Figure 4.10: Spring 1999-2011 ozone VCDs measured by the UT-GBS (blue) and PEARL-GBS (cyan).

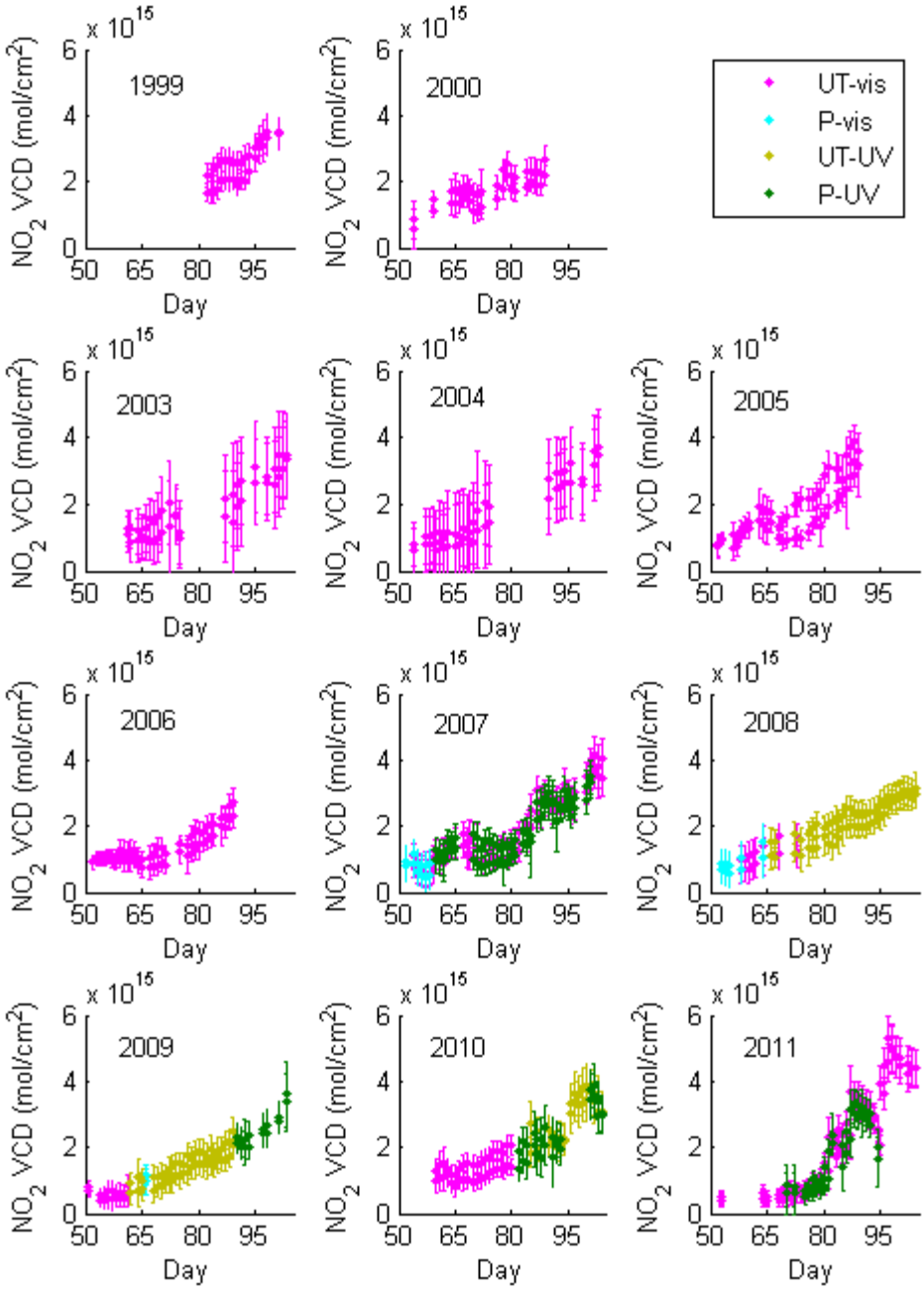

Figure 4.11: Spring 1999-2011 NO_2-vis measured by the UT-GBS (magenta) and PEARL-GBS (cyan) and NO_2-UV measured by the UT-GBS (gold) and PEARL-GBS (green).

5 Validation of Ground-Based and Satellite Measurements

Consistent long-term measurements of ozone and NO_2 are essential for the characterization of ozone depletion and recovery. GCOS (see Section 0) also designates ozone as an Essential Climate Variable that can be complemented by simultaneous measurements of NO_2, among other trace gases [*WMO*, 2011b]. Since instrument performance can change in time, long-term evaluation of satellite measurements is necessary.

The OSIRIS and the ACE satellite instruments have been taking measurements since 2001 and 2003, respectively. While ozone and NO_2 data products from both satellites have been validated [e.g., *Brohede et al.*, 2008; *Kerzenmacher et al.*, 2008; *Degenstein et al.*, 2009; *Dupuy et al.*, 2009], continued assessment assures long-term consistency within the datasets. Furthermore, the new ACE FTS v3.0 ozone and NO_2 data have not yet been validated.

Measurements and validation in the High Arctic present a unique set of challenges. There is reduced spatial coverage by ground-based measurements due to the logistical challenges of operating in a cold, remote, and largely unpopulated environment. Intercomparisons between measurements in the Arctic are complicated by the polar vortex, which isolates an airmass over the pole during the winter and spring. When the polar vortex is present, two instruments can sample airmasses which are near each other spatially, but are isolated from one another. Therefore, coincident measurement pairs can include one measurement inside the vortex, with e.g., low ozone and NO_2, and one measurement outside the vortex. This reduces the apparent agreement between two datasets. In some validation studies, additional coincidence criteria based on dynamical parameters have been adopted in order to match similar airmasses [e.g., *Manney et al.*, 2007; *Batchelor et al.*, 2010; *Fu et al.*, 2011].

PEARL is an excellent location for Arctic satellite validation. Measurements taken at PEARL have been included in numerous validation studies [e.g., *Kerzenmacher et al.*, 2005; *Fu et al.*, 2007; *Sung et al.*, 2007; *Fraser et al.*, 2008; *Sica et al.*, 2008; *Dupuy et al.*, 2009; *Batchelor et al.*, 2010; *Fu et al.*, 2011]. Measurements included in this study were taken at the PEARL Ridge Lab (80.05°N, 86.42°W) and the Eureka Weather Station (79.98°N, 85.93°W), which is located

15 km from the Ridge Lab. Since August 2006, CANDAC instruments have recorded measurements of ozone and NO_2, using ground-based zenith-sky DOAS instruments and a FTIR, when sunlight and weather permitted. Additional spring-time measurements were taken on a campaign basis as a part of the 2003 Stratospheric Indicators of Climate Change Campaign and the 2004-2011 Canadian Arctic ACE Validation Campaigns [e.g., *Kerzenmacher et al.*, 2005]. Brewer spectrophotometer measurements were also taken year-round for 2004-2011 by Environment Canada, with support from the Canadian Arctic ACE Validation Campaigns and CANDAC. This yields a multi-year dataset that can be used for long-term validation of satellite measurements.

The DOAS and Bruker FTIR instruments at PEARL are part of NDACC. Therefore, intercomparisons between the measurements can be used to assess consistency between NDACC datasets. Furthermore, the new NDACC guidelines and AMF LUTs for DOAS ozone retrievals [*Hendrick et al.*, 2011] can be validated for several DOAS instruments at a High Arctic location.

5.1 Instrumentation

The names and measurement periods of the datasets included in this intercomparison are summarized in Table 5.1. Abbreviations for datasets, used in the figures throughout this paper, are also included in Table 5.1. Error estimates for the various data products are summarized in Table 5.2. The GBS instruments, data analysis and error estimates are described in Chapters 2 and 4, respectively. The Eureka SAOZ, Brewer and Bruker instruments, datasets and error estimates are described in Appendix C, while descriptions of the satellite data products and error estimates are given in Appendix D.

5.1.1 Differences between GBS and SAOZ DOAS Retrievals

The PEARL-GBS and SAOZ are both NDACC-certified instruments and, therefore, data retrieved from these instruments and submitted to the NDACC database are expected to agree well. Furthermore, the UT-GBS and SAOZ both met NDACC standards during the 2009 CINDI campaign [*Roscoe et al.*, 2010]. GBS and SAOZ ozone and NO_2 measurements have been compared during several Arctic and mid-latitude campaigns using the same analysis settings and the same retrieval software [*Fraser et al.*, 2007a; 2008; 2009].

Table 5.1. Measurement dates for data included in this intercomparison. (Abbr. = abbreviation used in figure and table captions throughout this paper; S = spring only, F= fall only, Y = year-round excluding polar night.)

Data product	Abbr.	Ozone	NO_2
GBS-vis	GV	S: 2003-2006 Y: Aug 2006 - Apr 2011	S: 2003-2006 Y: Aug 2006 - Apr 2011
GBS-UV	GU	N/A	S: 2007, 2009-2011 Y: 2008
SAOZ	SA	S: 2005-2011	S: 2005-2011
Bruker FTIR	FT	Y: Aug 2006 - Apr 2011	Y: Aug 2006 - Apr 2011
Brewer	BW	Y: Mar 2004 - Oct 2010	N/A
OSIRIS[a]	OS	Y: Mar 2003 - Apr 2011	Y: Mar 2003 - Jun 2010
ACE-FTS v2.2+updates	A2	S/F: Mar 2004 - Mar 2010	S/F: Mar 2004 - Mar 2010
ACE-FTS v3.0	A3	S/F: Mar 2004 - Mar 2011	S/F: Mar 2004 - Mar 2011
ACE-MAESTRO v2.1	MA	S/F: Mar 2004 - Oct 2010	S/F: Mar 2004 - Oct 2010

[a] For ozone, used SaskMART v5.0x. For NO_2, used Optimal Estimation v3.0.

Table 5.2: Mean percent error of various measurements. Square brackets indicate errors in partial columns. Instrument abbreviations are summarized in Table 5.1. Note that for some instruments, error estimates include systematic and random errors, while for others, only random errors are calculated.

Instrument	Ozone (%)	NO_2 (%)
GV	5.9	[23]
GU	--	[22]
SA	5.9	13.2
FT	4.3 [3.8]	[15.0]
BW	1 [a]	--
OS	[3.7] [a]	[6.8] [a]
A2	[1.4] [a]	[3.7] [a]
A3	[1.6] [a]	[2.7] [a]
MA	[1.3] [a]	[2.3] [a]

[a] Random error only.

In this study, GBS and SAOZ ozone total columns were retrieved independently, following the new NDACC guidelines [*Hendrick et al.*, 2011], with different analysis software and small differences in retrieval settings, which are summarized in Table 5.3. Therefore, this is a good example of the practical implementation of the new settings and the resulting homogeneity of the NDACC dataset. The NDACC UV-Visible Working Group is currently developing similar guidelines for NO_2 [*Van Roozendael and Hendrick*, 2012] and they will be made available in the near future. Therefore, for the present study, the GBS and SAOZ NO_2 datasets were analyzed with their own preferred settings and AMFs, as summarized in Table 5.4.

5.2 Methodology

Coincident measurements for this validation study were selected using the criteria described in Section 5.2.1. Satellite ozone partial columns were calculated and combined with ozonesonde data to create total columns as described in Section 5.2.2. Using the method described in Section 5.2.3, all NO_2 measurements were scaled to local solar noon prior to comparison.

Table 5.3: Differences between ozone analyses for the UT-GBS, PEARL-GBS, and SAOZ.

	UT-GBS	PEARL-GBS	SAOZ
DOAS fitting window	450-545 nm	450-540 nm	450-550 nm
Reference spectrum	Daily noon	Daily noon	Yearly
O_4 cross-section[a]	*Greenblatt et al.* [1990]	*Greenblatt et al.* [1990]	*Hermans et al.* [2004]
Additional cross-sections?	Polarization correction	Polarization correction	--
Ozone input to AMF LUTs	Ozonesonde VCD above Eureka interpolated to the measurement date	Ozonesonde VCD above Eureka interpolated to the measurement date	SAOZ SCDs from the analysis twilight

[a] The difference between the O_4 cross-sections is expected to have less than a 1% impact on the DSCDs, based on sensitivity tests by X. Zhao at the University of Toronto, using UT-GBS data.

Table 5.4: Differences between NO_2 analyses for the UT-GBS, PEARL-GBS, and SAOZ.

	UT-GBS	PEARL-GBS	SAOZ
DOAS fitting window	425-450 nm	425-450 nm	410-530 nm (gap: 427-433 nm)
Reference spectrum	Daily noon	Daily noon	Yearly
O_4 cross-section[a]	*Greenblatt et al.* [1990]	*Greenblatt et al.* [1990]	*Hermans et al.* [2004]
AMFs	IASB-BIRA AMF LUTs	IASB-BIRA AMF LUTs	SAOZ Arctic AMFs
Column altitude range	17 km to top of atmosphere	17 km to top of atmosphere	0 km to top of atmosphere

[a] The difference between the O_4 cross-sections is expected to have less than a 1% impact on the DSCDs, based on sensitivity tests by X. Zhao at the University of Toronto, using UT-GBS data.

Agreement between these datasets was evaluated using several methods. The mean absolute difference Δ_{abs} between sets of coincident measurements (M_1 and M_2) is defined as

$$\Delta_{abs} = \frac{1}{N}\sum_{i=1}^{N}(M_{1i} - M_{2i}), \tag{5.1}$$

where N is the number of measurements. The mean relative difference Δ_{rel} between M_1 and M_2 is defined as

$$\Delta_{rel} = 100\% \times \frac{1}{N}\sum_{i=1}^{N}\frac{(M_{1i} - M_{2i})}{(M_{1i} + M_{2i})/2}. \tag{5.2}$$

The standard deviation (σ) and the standard error ($\sigma/\sqrt{N}$) of the mean absolute and relative differences were also calculated. The standard error is the reported error throughout this chapter. To assess correlation between the datasets, correlation plots were also produced. Measurement errors were not included in the linear regressions.

The OSIRIS, ACE-FTS, and ACE-MAESTRO satellite instruments have better vertical resolution than the ground-based ozone and NO_2 instruments included in this study. Some studies [e.g., *Kerzenmacher et al.*, 2008; *Dupuy et al.*, 2009; *Batchelor et al.*, 2010] account for this by smoothing the higher-resolution measurements by the averaging kernel of the lower-resolution measurements [*Rodgers and Connor*, 2003]. Data were not smoothed in the present study because averaging kernel matrices were not available for some ground-based instruments and we preferred to treat all datasets in a consistent manner. In previous studies, ACE-FTS data have been smoothed to the resolution of the Bruker FTIR [*Batchelor et al.*, 2010; *Lindenmaier et al.*, 2011]. Smoothing is expected to have a small impact on ozone intercomparisons, since the Bruker FTIR has good sensitivity for most of the ozone column [*Batchelor et al.*, 2009]. A subset of ACE-FTS NO_2 measurements was smoothed to the resolution of the Bruker FTIR by Lindenmaier et al. [2011]. ACE partial columns for 17-40 km changed on average by 1%, with a 4% standard deviation, when smoothing was perfomed. This is small compared with the agreement between NO_2 measurements in this study. The impact of smoothing on OSIRIS measurements is expected to be comparable.

5.2.1 Coincidence Criteria

Temporal coincidence criteria were selected to maximize the number of coincident data points while minimizing the reliance on the photochemical model corrections for the diurnal variation of NO_2, described in Section 5.2.3. For comparisons between the ACE-FTS v3.0, ACE-FTS v2.2, and ACE-MAESTRO v1.2 measurements, coincidences were restricted to the same occultation. For the twilight-measuring instruments (ACE and the DOAS instruments), measurements were compared from the same twilight. This prevents morning twilight measurements from being scaled to the evening by the photochemical model and vice versa. For intercomparisons between all remaining instruments, a ±12 hour coincidence criterion was used.

Satellite ozone and NO_2 measurements taken within a 500-km radius of the PEARL Ridge Lab were selected for intercomparisons with the ground-based measurements. Note that the satellite geolocations are given at the geometric tangent heights of 25 km for OSIRIS ozone, 35 km for OSIRIS NO_2, and 30 km for ACE ozone and NO_2. ACE solar occultations typically have ground

tracks of 300-600 km [*Dupuy et al.*, 2009], while OSIRIS limb measurements have ground tracks of ~500 km.

None of the instruments included in this study measures airmasses directly above PEARL. Instead they sample airmasses along their lines-of-sight. Figure 5.1 shows the longitude and latitude of the sampled airmasses in the stratosphere at 25 km for OSIRIS and 30 km for ACE, the Bruker FTIR, and the GBS. The OSIRIS measurements (panel a) do not reach latitudes above 82.2°N. The ACE measurements (panel b) are distributed approximately evenly within 500 km of PEARL. The Bruker FTIR spring-time measurements (panel c) follow the location of the sun during typical operational hours (e.g. ~9:00-16:00 local time), with larger SZA measurements sampling airmasses further from PEARL. The Brewer instruments, which also measure direct-sunlight, would have similar sampling to the Bruker FTIR in the spring. The DOAS instruments' approximate sampling (panel d) depends on the location of the sun, as described in Appendix F. Like the Bruker FTIR, the DOAS measurements get closer to PEARL as the sun gets higher. Furthermore, as sunrises and sunsets shift northward in azimuth, the DOAS measurements shift north of PEARL.

5.2.2 Ozone

For comparison against ground-based total column ozone measurements, an altitude range of 14-52 km was chosen for satellite partial columns. This was the maximum altitude range for which the majority of OSIRIS, ACE-FTS, and ACE-MAESTRO profiles within 500 km of PEARL had available data. Ozonesonde data from the nearest day were added to the satellite profiles from 0-14 km, in a similar approach to *Fraser et al.* [2008]. The resulting satellite-plus-sonde profile was smoothed from 12-16 km using a moving average filter in order to avoid discontinuities where the two profiles joined. No correction was applied above 52 km, since according to the United States 1976 Standard Atmosphere [*Krueger and Minzner*, 1976], there is less than 1 DU of ozone above 52 km. This is much smaller than the measurement errors of the various instruments (see Table 5.2). The satellite-plus-sonde columns are denoted with * in the figures and tables throughout this text.

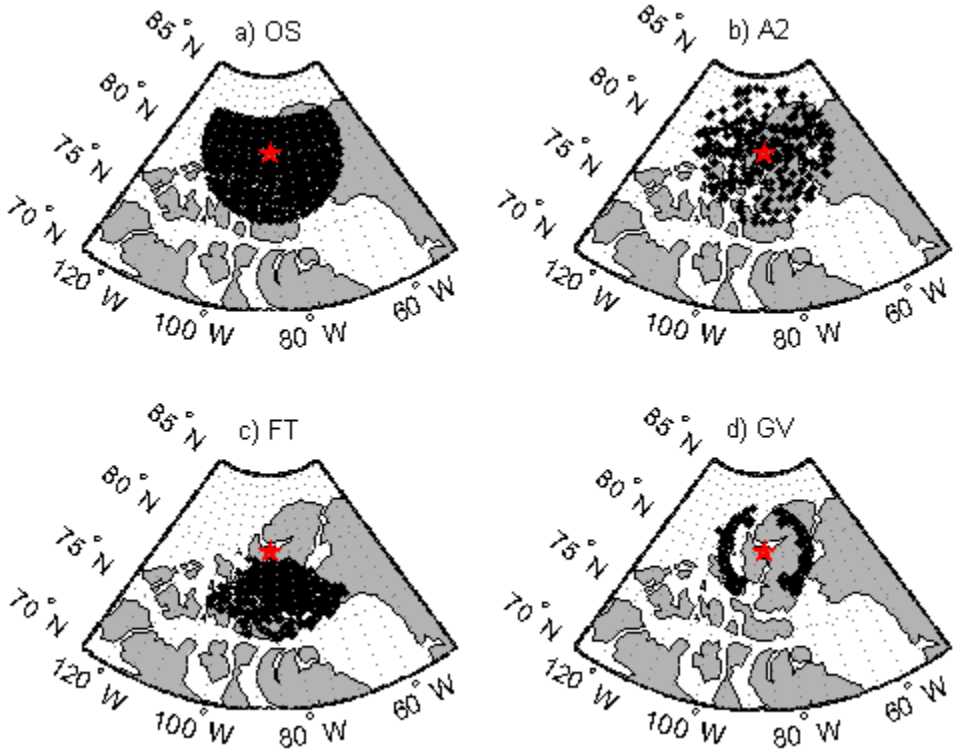

Figure 5.1: Location of ozone airmass sampled by (a) all OSIRIS scans and (b) ACE-FTS v2.2 occultations used in this study; and (c) Bruker FTIR and (d) GBS spring-time measurements. PEARL is indicated by the red star. Locations of the OSIRIS scans are shown for the 25-km airmass, while all other measurements are shown for the 30-km airmass.

5.2.3 NO_2

NO_2 partial columns for satellite and Bruker FTIR measurements were calculated for 17-40 km. The lower limit of this range was determined by GBS partial columns, which range from 17 km to the top of the atmosphere. The upper value of this altitude range was determined by the availability of OSIRIS, ACE-FTS, and ACE-MAESTRO data. For comparison between the satellite and GBS partial columns, no correction was applied above 40 km, because less than 1% of the NO_2 column resides at these altitudes, which is much smaller than the measurement error (see Table 5.2). For comparison against the partial columns, the SAOZ total column

measurements were scaled down by 30%, corresponding to the fraction of NO_2 below 17 km in the profiles used to construct the SAOZ AMFs. These scaled SAOZ measurements are indicated by a * in the figures and tables throughout this text.

NO_2 has a strong diurnal variation and therefore corrections must be applied when comparing measurements taken at different times [e.g., *Brohede et al.*, 2008; *Kerzenmacher et al.*, 2008; *Lindenmaier et al.*, 2011]. A photochemical model (see Appendix E) was used to simulate the evolution of NO_2 at Eureka (80°N) for each measurement day. Ozone profiles and temperatures from the ozonesonde launched closest to the measurement day were used to constrain the model.

The seasonal variation of NO_2 17-40 km partial columns, calculated by the photochemical model using ozonesondes launched in 2009, is shown in Figure 5.2a. NO_2 at solar noon (black) increases throughout the spring as PEARL exits polar night. It reaches a maximum during the summer period of 24-hour sunlight and then decreases again in the fall. Throughout the year, the diurnal variation of NO_2 also changes, as can be seen by the morning (blue) and evening (red) twilight partial columns, where twilight is defined as SZA 90° or the closest available SZA. In the spring and fall, NO_2 increases from morning to evening as NO_x ($NO_x = NO_2 + NO$) is released from its night-time reservoirs. In the summer 24-hour sunlight, NO_2 decreases at noon as it is photolyzed to NO.

The ratios of NO_2 in the evening and morning twilights retrieved by the GBS instruments and calculated with the photochemical model are shown in Figure 5.3 for 2007-2010. The measurements and model show good agreement. In spring 2007, when the vortex passed back and forth over PEARL, there is more scatter in the values than in the less dynamically active 2008-2010 years. Similar scatter is observed in 2011 (not shown here). This may be because the GBSs are sampling different airmasses between the morning and evening twilights. Systematic discrepancies appear in the late fall (days 280-300), as PEARL enters polar night. This may be caused by measurement error since NO_2 concentrations become very low as NO_2 is converted to its night-time reservoirs.

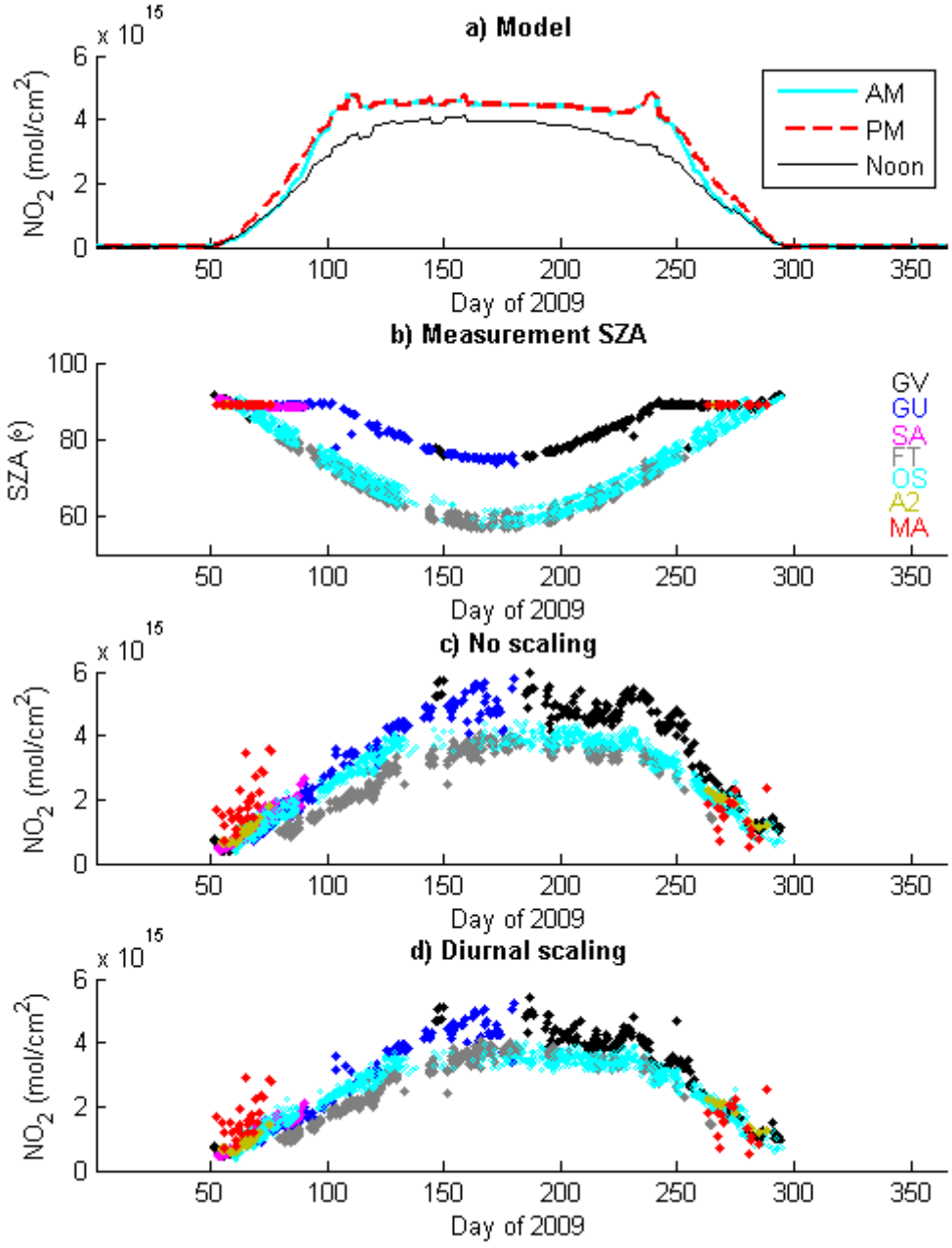

Figure 5.2: Seasonal evolution of NO_2 in 2009. (a) 17-40 km partial columns calculated by the photochemical model initialized with ozonesondes for morning twilight (thick cyan line), evening twilight (red dashed line), and solar noon (thin black line). (b) NO_2 partial columns measured by ground-based and satellite instruments. (c) Same as (b) except all measurements scaled to solar noon using the photochemical model.

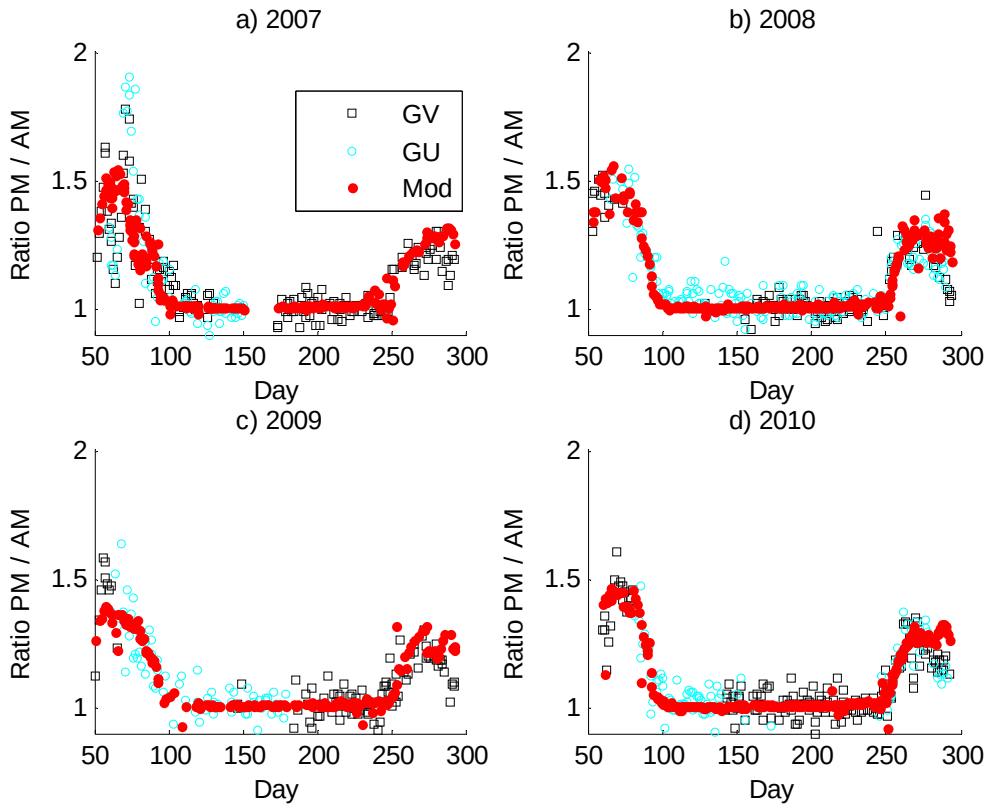

Figure 5.3: Ratio of evening twilight to morning twilight NO_2 as measured by the GBS-vis (black squares) and GBS-UV (blue circles) and as calculated using a photochemical model (red dots). Ratios are plotted against day of year for (a) 2007, (b) 2008, (c) 2009, and (d) 2010. Based on the error analysis described in Section 4.3, the uncertainty in the ratio of VCDs is expected to be ~10%.

The instruments compared in this study sample NO_2 at different times of day, or different times during the diurnal cycle. as shown in Figure 5.2b. Instruments that measure columns at larger SZAs (GBS, SAOZ, and ACE) tend to measure more NO_2 than instruments that measure columns at smaller SZAs (OSIRIS and Bruker FTIR), as can be seen in Figure 5.2c. In order to correct for this, ratios of NO_2 partial columns at noon and at the measurement times were calculated using the photochemical model. These ratios were multiplied by the measurements to produce an NO_2 partial column at noon. The resulting noon-time measurements are shown in Figure 5.2d and were used in all NO_2 intercomparisons. The model profiles were not degraded to the resolution of the ground-based instruments prior to the scale-factor calculations. The modeled ratio of twilight to noon NO_2 does not vary greatly for 15-35 km, where the bulk of the

NO_2 column resides. Therefore, the error that this introduces is expected to be small. *Lindenmaier et al.* [2011] estimate the error in NO_2 scale factors from the same photochemical model at 7.7-16.4% above PEARL, with the maximum values around days 90 and 240, when the ratio of twilight-to-noon NO_2 is largest.

In addition to affecting measurements taken at different times, the diurnal variation of NO_2 can introduce errors in individual measurements through the "diurnal effect", which is also referred to as "chemical enhancement" [e.g., *Fish et al.*, 1995; *Newchurch et al.*, 1996; *Hendrick et al.*, 2006; *McLinden et al.*, 2006]. The diurnal effect is a result of sunlight passing through a range of SZAs, and hence sampling NO_2 at different points in its diurnal cycle, on its way through the atmosphere to the instrument. An error is introduced when this variation is not accounted for in the analysis, and the SZA assigned to a retrieved profile or column corresponds to the location of the instrument (for a ground-based observation) or to the location of the tangent height (for a limb observation). This effect is largest when the range of SZAs encountered includes twilight, when NO_2 varies rapidly.

For OSIRIS, these errors are relevant to measurements taken at SZAs greater than 85° (during the spring and fall, for measurements near PEARL) and can introduce errors up to 40% below 25 km [*McLinden et al.*, 2006; *Brohede et al.*, 2007]. The 60°N error profiles shown in Figure 9 of *Brohede et al.* [2007] were applied to the OSIRIS profiles used in this study and yielded less than 10% error in the 17-40 km NO_2 partial columns. For ACE-FTS and ACE-MAESTRO, measurements of NO_2 can be biased high below 25 km by up to 50% [*Kerzenmacher et al.*, 2008]. When the ACE profiles included in this study were increased by 50% below 25 km, the 17-40 kmNO_2 partial columns increased by up to ~20%. Based on the viewing geometry described in Appendix F, DOAS instruments sample a 30-km layer of the atmosphere with a SZA that is as much as 3° smaller than the SZA at the instrument. This causes the underestimation of NO_2 concentrations, particularly for measurements taken at large SZA in the spring and fall. The Bruker FTIR NO_2 measurements were restricted to SZAs less than 80°. Since NO_2 varies slowly for those SZAs, the diurnal effect for the Bruker FTIR is small.

The instruments also sample the NO_2 maximum at different latitudes, as shown in Figure 5.1. This is of particular concern at high latitudes during polar sunrise and sunset, as NO_x is released

from and returns to its night-time reservoirs, leading to a strong gradient in NO_2, with lower concentrations at higher latitudes [*Noxon et al.*, 1979]. Using the photochemical model initialized with climatological ozone and temperature profiles [*McPeters et al.*, 2007], 17-40 km NO_2 partial columns were calculated at various latitudes for the evening twilight (SZA=90° or nearest available SZA). Ratios of NO_2 partial columns calculated at 78°N to those at 82°N are shown in grey in Figure 5.4. This represents a typical latitude difference between measurements.

On days 55 and 290, which are near the first and last measurement days of the season, NO_2 partial columns at 78°N are ~7 times larger than at 82°N. The difference between the columns decreases throughout the spring until approximately days 80-85. Throughout the summer, no strong latitudinal gradient is observed in NO_2 until approximately days 265-270, as polar night

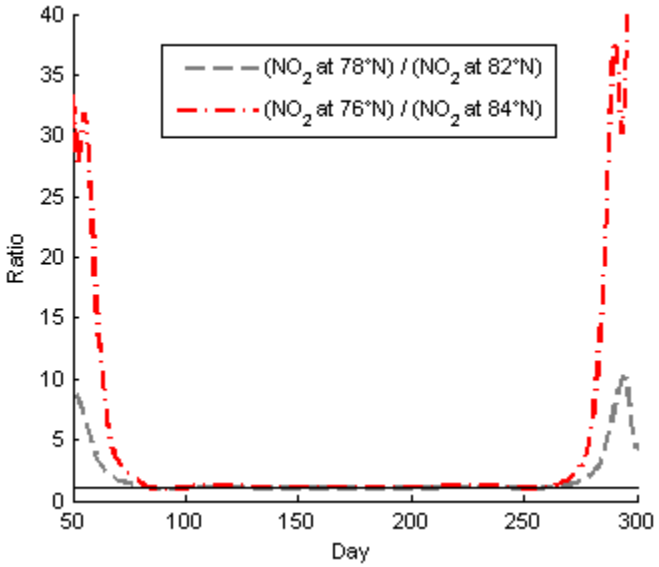

Figure 5.4: Ratios of 17-40 km NO_2 partial columns at various latitudes during the evening twilight, calculated with photochemical model initialized with climatological ozone and temperatures. Evening twilight is defined as SZA = 90° or the nearest available SZA for the given time of year. 76°N to 84°N is the maximum range over which coincident measurements were selected (see Figure 5.1). The thin black line indicates a ratio of one.

begins. Ratios of NO_2 partial columns calculated at 76°N to those at 84°N, representing the maximum latitude difference between coincident measurements, are also shown in Figure 5.4 in red. ACE measures above PEARL during the spring and fall periods for which this effect is significant. The impact of the latitudinal gradient in NO_2 on the spring-time intercomparisons is assessed in Section 5.5.

5.3 Ozone Intercomparisons

Ozone partial and total column measurements made by the ground-based and satellite instruments were compared using the methods described in Section 5.2. The resulting mean absolute and relative differences are summarized in Table 5.5 and are discussed below. Available coincident measurements from all time periods are included in the intercomparisons.

5.3.1 Satellite versus Satellite Partial Columns

The 14-52 km ozone partial columns measured by the satellite instruments were compared and are shown in the first section of Table 5.5. Partial columns from all four satellite instruments agree very well, with mean relative differences of 3% or lower. Correlation plots between the satellite measurements, shown in Figure 5.5, have R^2 values of 0.821 or greater.

The mean relative difference between ACE-FTS v3.0 and v2.2 ozone partial columns is 0.0±0.2%. Furthermore, the two datasets are extremely well correlated, with an R^2 value of 0.973. Note that the ACE-FTS v2.2 and v3.0 datasets have slightly different results when compared with the other instruments in this study because data were compared for different time periods, based on data availability. Therefore, fall 2010 and spring 2011 are included for v3.0, but not for v2.2.

ACE-FTS v2.2, ACE MAESTRO v1.2, and OSIRIS SaskMART v5.0.x measurements have been compared inprevious studies. *Fraser et al.* [2008] found a mean relative difference of +5.5% to +22.5% between ACE-FTS v2.2 and ACE-MAESTRO v1.2 ozone 16-44 km partial columns from 2004-2006, which is larger than the +2.7% mean relative difference found in the present study. *Dupuy et al.* [2009] compared profiles from ACE-FTS v2.2, ACE-MAESTRO v1.2, and OSIRIS SaskMART v2.1 data. They found ACE-MAESTRO profiles agreed with OSIRIS to

Table 5.5. Number of coincidences (N), mean absolute difference (Δ_{abs}) and mean relative difference (Δ_{rel}) between ozone measurements with respective standard deviation (σ) and standard error (err). Instrument abbreviations are summarized in Table 5.1. * indicates 0-52 km satellite-plus-sonde partial columns.

	N	Δ_{abs} (DU)	σ_{abs} (DU)	err_{abs} (DU)	Δ_{rel} (%)	σ_{rel} (%)	err_{rel} (%)
Satellite versus satellite 14-52 km partial columns							
OS - A2	800	9.8	22.9	0.8	3.0	7.4	0.3
OS - A3	754	3.8	18.1	0.7	1.2	5.8	0.2
OS - MA	559	7.4	28.3	1.2	2.8	9.6	0.4
A2 - A3	210	-0.3	9.9	0.7	0.0	3.1	0.2
A2 - MA	198	7.5	23.3	1.7	2.7	7.8	0.6
A3 - MA	162	7.8	22.4	1.8	2.8	7.5	0.6
Satellite-plus-sonde 0-52 km partial columns versus ground-based total columns							
OS* - GV	4727	19.9	27.4	0.4	5.7	7.8	0.1
OS* - SA	2065	32.2	29.3	0.6	7.3	6.7	0.1
OS* - FT	11388	-0.4	25.4	0.2	0.1	6.2	0.1
OS* - BW	4115	10.3	21.5	0.3	2.8	5.8	0.1
A2* - GV	147	28.0	29.2	2.4	6.5	6.6	0.5
A2* - SA	122	14.4	26.6	2.4	3.2	6.1	0.6
A2* - FT	371	-33.0	33.5	1.7	-6.7	7.6	0.4
A2* - BW	6	9.0	13.9	5.7	3.4	5.2	2.1
A3* - GV	141	28.4	27.7	2.3	6.5	6.1	0.5
A3* - SA	146	19.2	25.5	2.1	4.8	6.0	0.5
A3* - FT	481	-21.6	28.6	1.3	-4.7	6.6	0.3
A3* - BW	5	5.8	15.3	6.9	2.3	5.7	2.6
MA* - GV	117	21.7	32.8	3.0	5.0	7.6	0.7
MA* - SA	79	8.7	39.4	4.4	1.6	8.8	1.0
MA* - FT	204	-29.8	35.0	2.4	-6.1	7.9	0.6
MA* - BW	6	-2.8	18.3	7.5	-1.1	6.7	2.7
Ground-based versus ground-based total columns							
GV - SA	296	-14.2	22.0	1.3	-3.2	5.6	0.3
GV - FT	1894	-25.9	30.5	0.7	-6.9	7.8	0.2
GV - BW	658	-4.0	22.7	0.9	-1.4	6.9	0.3
SA – FT	1474	-39.1	23.3	0.6	-9.2	5.2	0.1
SA – BW	107	1.9	21.1	2.0	0.4	5.3	0.5
FT – BW	1491	9.7	10.3	0.3	2.6	2.5	0.1
Satellite versus ground-based 14-52 km partial columns							
OS – FT	11388	-11.1	20.4	0.2	-3.3	6.3	0.1
A2 – FT	371	-45.9	37.3	1.9	-12.2	10.6	0.5
A3 – FT	481	-32.1	31.2	1.4	-9.2	8.8	0.4
MA - FT	204	-40.3	37.9	2.7	-11.2	11.2	0.8

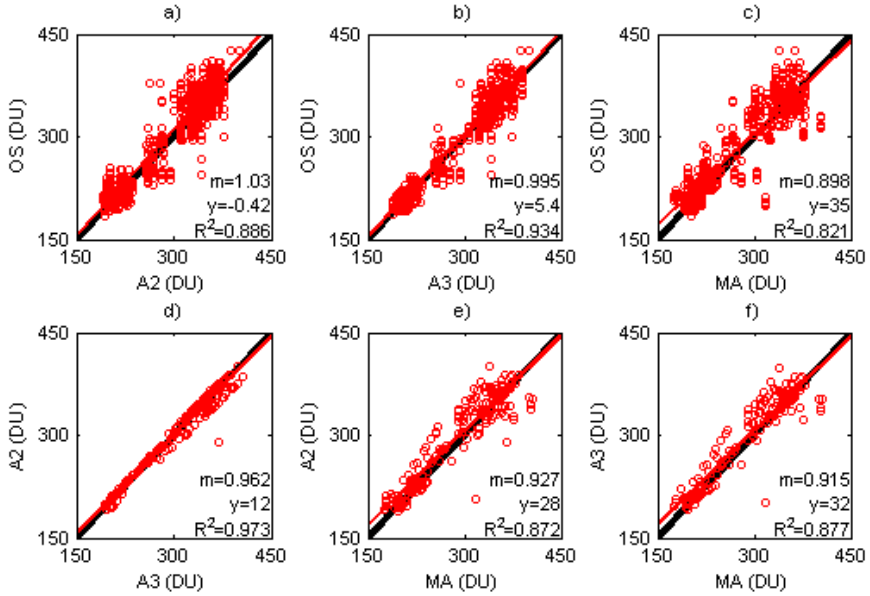

Figure 5.5: Correlations between satellite 14-52 km ozone partial columns. Red lines indicate linear fit (m = fitted slope, y = fitted y-intercept). Black lines indicate 1-1. Instrument abbreviations are given in Table 5.1.

±7% for 18-53 km. ACE-FTS profiles were typically +4% to +11% larger than OSIRIS profiles above 12 km. This is opposite to the findings of this study, in which ACE-FTS partial columns are lower than OSIRIS partial columns. Since OSIRIS SaskMART v2.1 and v5.0x are very similar for the 14-52 km altitude range, this difference is likely because the present study included only measurements taken in the Arctic, while *Dupuy et al.* [2009] considered measurements at all latitudes.

5.3.2 Satellite versus Ground-Based Columns

Mean absolute and relative differences between satellite-plus-sonde 0-52 km columns and ground-based total columns are included in the second section of Table 5.5. The satellite-plus-sonde measurements are consistently larger than the DOAS measurements and smaller than the Bruker FTIR measurements. The Brewer columns fall between the satellite-plus-sonde and other ground-based measurements. All ground-based measurements are within 7.3% of the satellite-plus-sonde columns. Comparisons are not shown between ACE and

the Brewer instruments because there are few coincident measurements as ACE measures above PEARL in the early spring and late fall during periods when the SZA is too large for Brewer direct-sun measurements.

The timeseries of absolute differences between the four satellite-plus-sonde data products and the ground-based measurements are plotted in Figures 5.6 and 5.7. The largest discrepancies occur in the spring-time for all measurements, with the Bruker FTIR measuring more ozone and the DOAS and Brewer instruments measuring less ozone than the satellite-plus-sondes. Although there is some year-to-year variability in the absolute differences, there is no apparent systematic change between the satellite and ground-based measurements in time. The year-to-year variability has no obvious relation to vortex activity above Eureka, such as sudden stratospheric warmings. This suggests that the performance of OSIRIS, ACE-FTS, and ACE-MAESTRO has not changed and their measurements of ozone within 500 km of PEARL are suitable for multi-year analyses. Figure 5.8 shows correlation plots between the satellite-plus-sonde and ground-based total ozone columns. R^2 coefficients range from 0.518-0.910. Note that ACE-FTS v3.0 data were retrieved for spring 2011, which had abnormally low ozone values [*Manney et al.*, 2011], and therefore has higher correlation coefficients than v2.2.

5.3.3 Comparisons with NDACC DOAS Measurements

Intercomparison results between SAOZ and GBS ozone total columns retrieved from 2005-2011 using the NDACC settings (described in Section 5.1.1) are shown in Figure 5.9. The absolute difference between the SAOZ and GBS ozone total columns (panel a) shows good agreement for most years. SAOZ measures more ozone than the GBS in 2005 and 2007, two years in which the polar vortex passed over Eureka. This may be due in part to the different fields-of-view of the two instruments, leading to sampling of different airmasses. The correlation plot between SAOZ and GBS ozone (panel b) shows a strong correlation between measurements, with an R^2 value of 0.898. For large ozone total columns, the GBS measures systematically lower than SAOZ. The mean relative difference for GBS minus SAOZ ozone is -3.2±0.3% (see third section of Table 5.5). This is well within the combined error of the two instruments and is comparable to the values of -6.9% to -2.3% found by *Fraser et al.* [2008; 2009] for 2005-2007, when SAOZ and GBS data were retrieved by the same analysis group, using the same analysis software. This

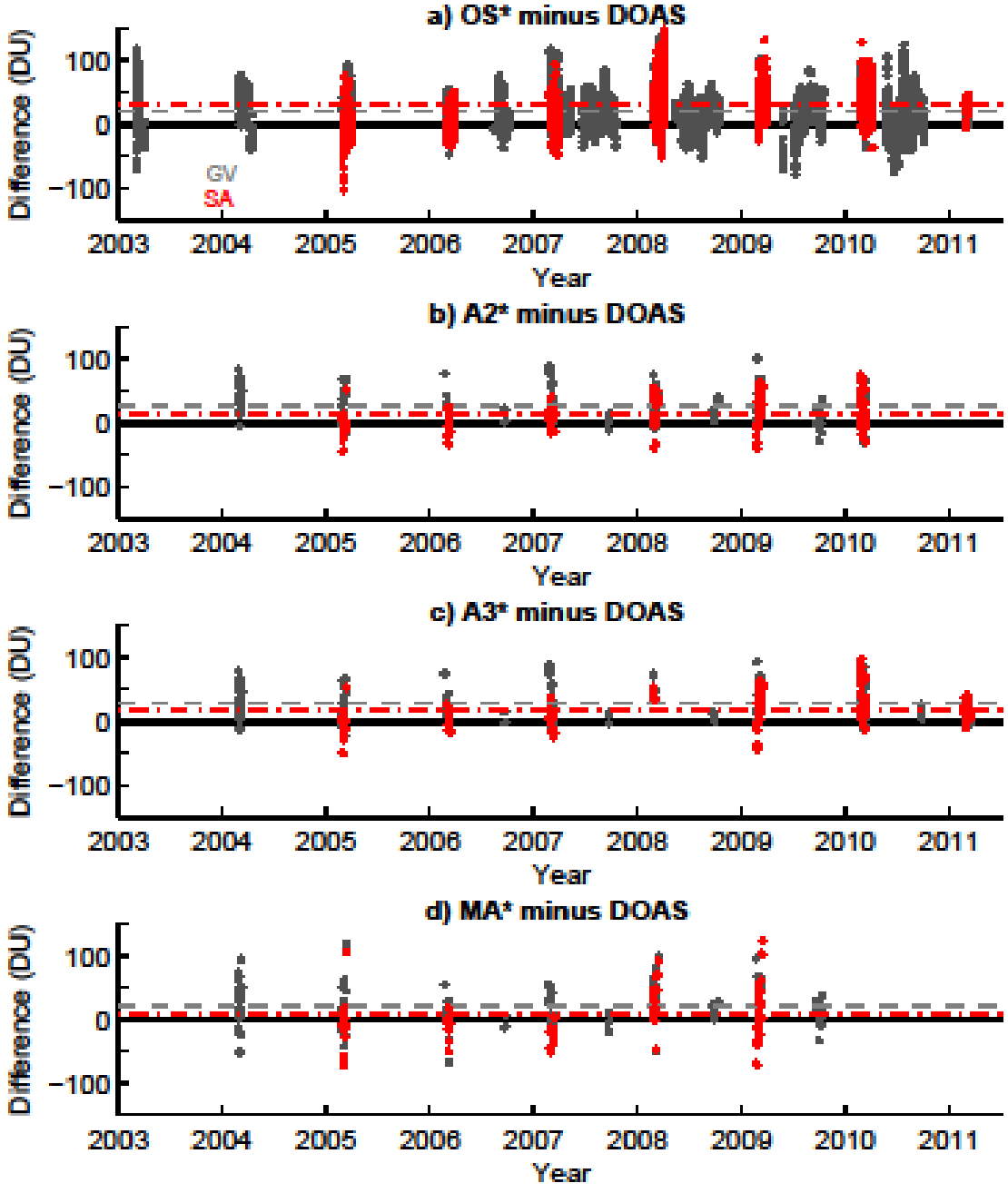

Figure 5.6: Absolute differences (circles) and mean absolute differences (dashed lines) between satellite-plus-ozonesonde and GBS (grey) and SAOZ (red). The solid black lines indicate zero.

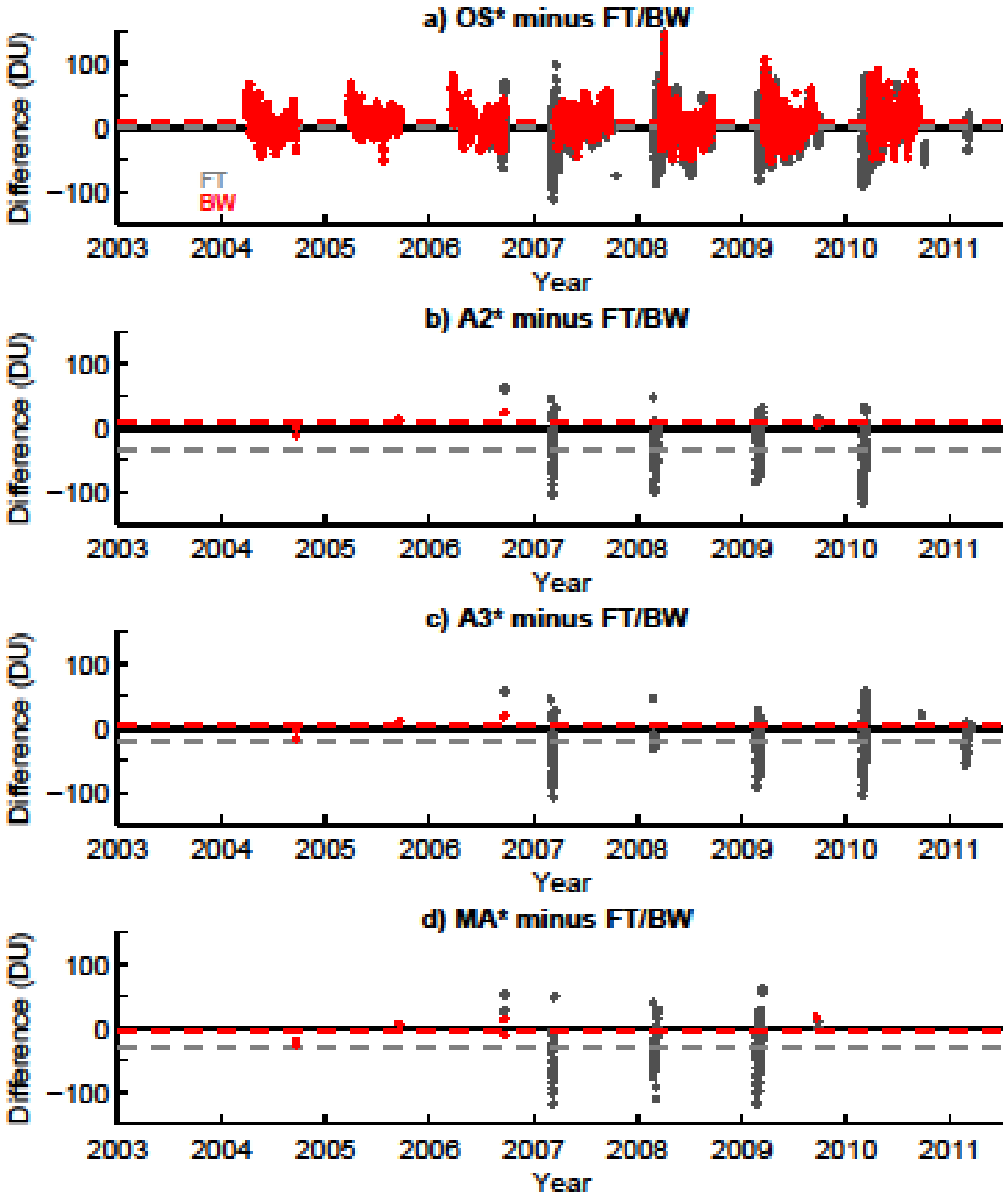

Figure 5.7: Absolute differences (circles) and mean absolute differences (dashed lines) between satellite-plus-ozonesonde and Bruker FTIR (grey) and Brewer (red). The solid black lines indicate zero.

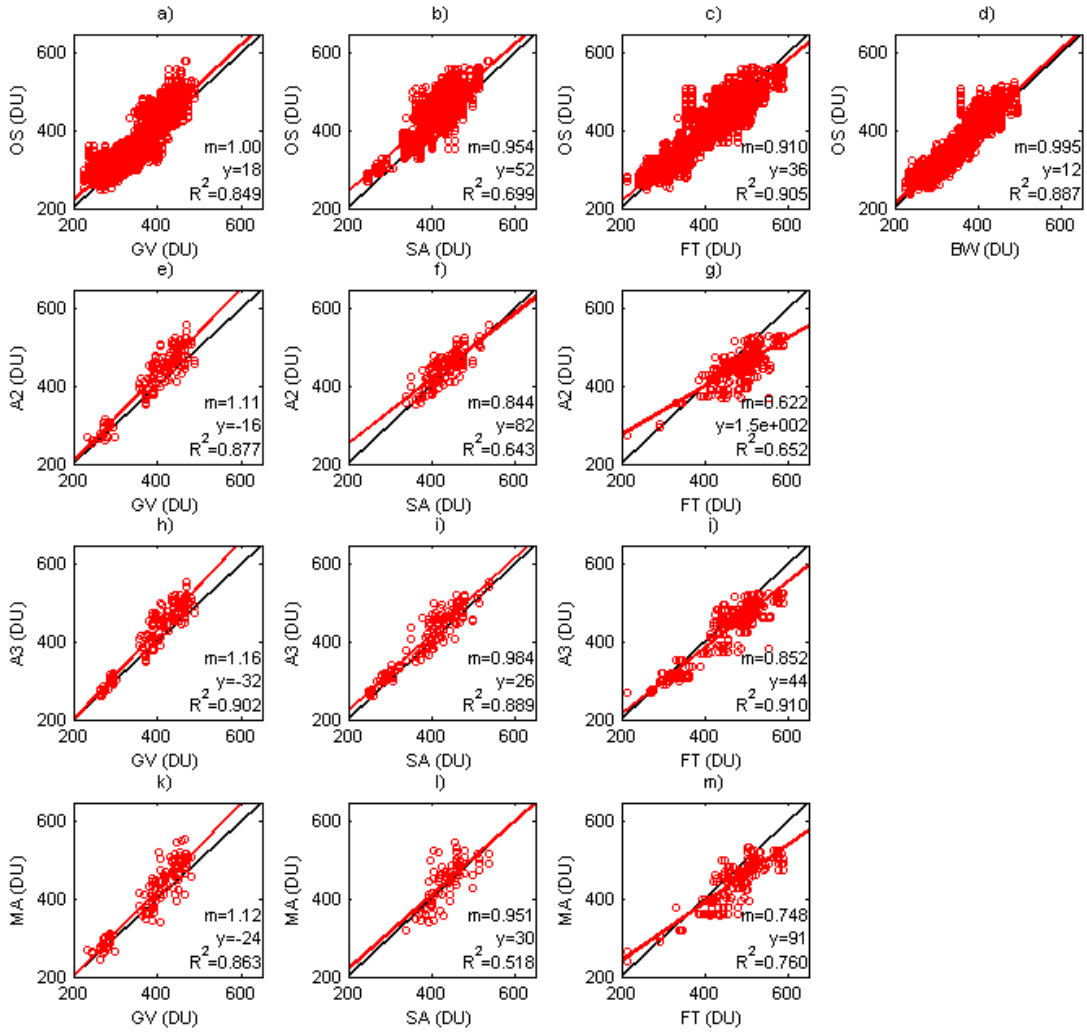

Figure 5.8: As for Figure 5.5, satellite-plus-ozonesonde versus ground-based total ozone columns. Note that comparisons between ACE and Brewer measurements are not shown because there are few coincidences between these instruments.

demonstrates that, even when implemented independently with slight differences in the analysis settings and software, the new NDACC data standards are sufficient to produce a homogeneous ozone dataset.

Absolute differences (panel c) and correlations (panel d) between the DOAS (GBS and SAOZ) and Brewer data are also shown in Figure 5.9. Good agreement between the instruments is

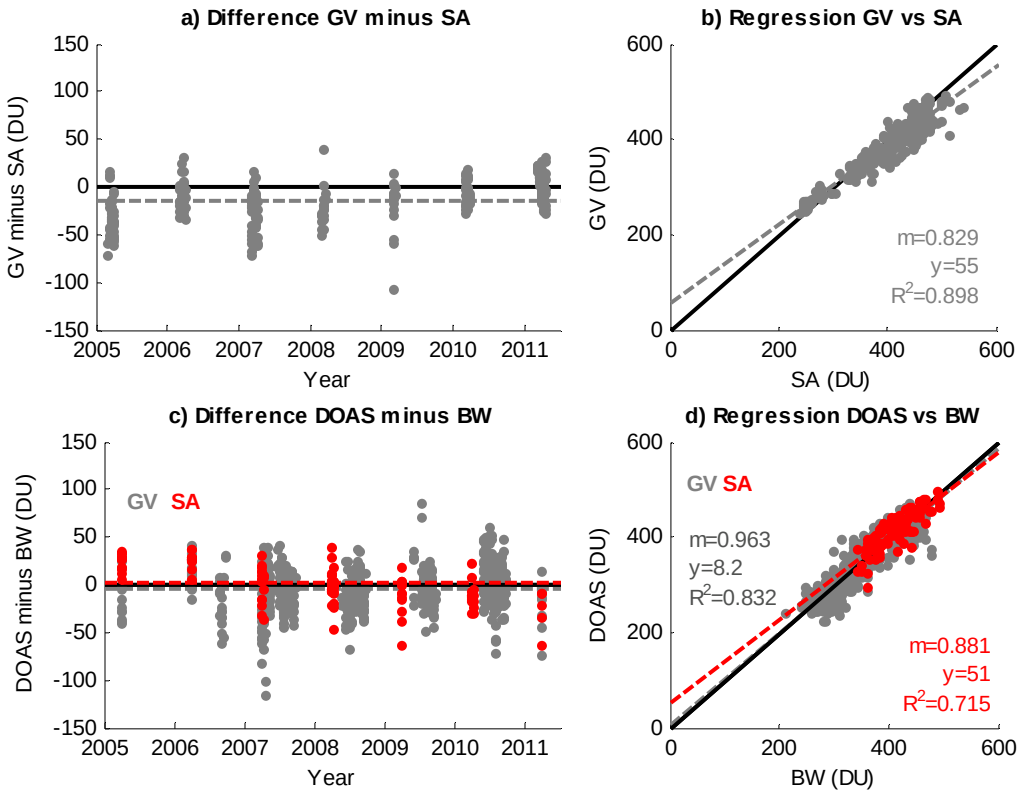

Figure 5.9: (a) Absolute difference (circles) between GBS and SAOZ ozone total columns. (b) Correlation between GBS and SAOZ ozone total columns. (c) Absolute difference (circles) between GBS (grey) and SAOZ (red) minus Brewer ozone total column measurements. (d) Correlation for GBS (grey) and SAOZ (red) versus Brewer ozone measurements. In (a) and (c), the solid black lines indicate the zero line and the dashed lines indicate mean absolute differences. In (b) and (d), the solid black lines indicate the 1-1 line and the dashed lines indicate linear fit (m = fitted slope, y = fitted y-intercept).

evident throughout the year. The mean relative difference between the GBS [SAOZ] and Brewer total ozone column measurements is -1.4% [+0.4%]. This is better than the high-latitude agreement reported by *Hendrick et al.* [2011], who found that SAOZ ozone total columns were systematically lower than Brewer measurements at Sodankyla (67°N, 27°E) by 3-4%, with the largest discrepancies in the spring and fall. *Hendrick et al.* [2011] accounted for this bias with the temperature dependence and uncertainty in the UV ozone cross-section used in Brewer measurements. The agreement between the GBS, SAOZ, and Brewer in the present study is

remarkable given the challenges of taking DOAS measurements at 80°N, particularly in the summer (see Chapter 4).

The DOAS measurements are systematically lower than the Bruker FTIR total column and satellite-plus-sonde measurements by 1.6-9.2% (see Table 5.5). Discrepancies between the satellite-plus-sonde and DOAS measurements, shown in Figure 5.6, are particularly large in the spring. Correlation plots, shown in Figure 5.8, indicate that the the satellite-plus-sonde measurements are systematically higher than the GBS measurements for high ozone columns. R^2 correlation coefficients for the satellite-plus-sonde versus GBS [SAOZ] ozone columns are greater than 0.85 [0.52].

Fraser et al. [2008] compared 15-40 km ACE partial columns with ozonesonde measurements added to the columns below 15 km against GBS and SAOZ measurements. The GBS and SAOZ measurements had been retrieved by the same analysis group with identical settings, including the *Burrows et al.* [1999a] ozone cross-section and the AMFs described in *McLinden et al.* [2002]. They found mean relative differences between ACE-FTS v2.2 satellite-plus-sonde and GBS [SAOZ] measurements of +3.2 to +6.3 % [+0.1 to +4.3%]. This is similar to the values of +6.5% [+3.2%] found in the present study. *Fraser et al.* [2008] found that the mean relative difference between ACE-MAESTRO v1.2 plus updates and the GBS [SAOZ] was -19.4% to -1.2% [-12.9% to -1.9%]. In this study, the mean relative difference for ACE-MAESTRO minus GBS [SAOZ] was +5.0% [+1.6%].

The differences between satellite and DOAS measurements in this study are larger than the values reported for comparisons between SAOZ and satellite ozone total column measurements in Table 10 of *Hendrick et al.* [2011]. The satellite data products compared by *Hendrick et al.* [2011] were TOMS v8, GOME-GDP4 (Global OMI GDP4 retrieval), OMI-DOAS (OMI data retrieved with DOAS algorithm), OMI-TOMS (OMI data retrieved with TOMS algorithm), and two SCIAMACHY products, SCI-TOSOMI (SCIAMACHY with TOSOMI algorithm developed at the Royal Netherlands Meteorological Institute - KNMI) and SCIA-OL3 (SCIAMACHY offline v3). For various stations, *Hendrick et al.* [2011] found that agreement between SAOZ total ozone columns and satellite total ozone columns ranged from -4.1% to +3.1%. The agreement in *Hendrick et al.* [2011] is better than the present study for several possible reasons.

Hendrick et al. [2011] corrected satellite columns for temperature and SZA dependence using comparisons with the SAOZ measurements. Furthermore, DOAS retrievals are particularly challenging for higher latitudes (see Chapter 4). The present study compares different satellite instruments at 80°N, which is higher than the maximum latitude of 71°N considered by *Hendrick et al.* [2011]. Furthermore, the satellite instruments compared by *Hendrick et al.* [2011] are all nadir sounders, which take dedicated ozone column measurements, while in the present study, limb-viewing satellite profiles and ozonesonde are combined to calculate a total column.

5.3.4 Comparisons with Bruker FTIR Measurements

On average, the Bruker FTIR measures more ozone than most other instruments (see Table 5.5), with the largest differences observed in the spring (see Figure 5.7). A mean relative difference of +0.1% is calculated for OSIRIS-plus-sonde minus Bruker FTIR total columns, reflecting particularly good agreement in the summer and fall (seeFigure 5.7). The mean relative difference for the ACE-FTS v2.2 [v3.0] minus the Bruker FTIR is -6.7% [-4.7%]. A similar mean relative difference of -6.1% is observed between ACE-MAESTRO and the Bruker FTIR. The comparisons worsen for the 14-52 km partial columns, to -3.3% for OSIRIS minus Bruker FTIR, -12.2% [-9.6%] for ACE-FTS v2.2 [v3.0] minus Bruker FTIR, and -11.2% for ACE-MAESTRO minus Bruker FTIR. This may be due in part to the altitude resolution of the Bruker FTIR, which is lower than that of the satellite instruments (see Section 5.2). Bruker FTIR 10-50 km partial columns of ozone have on average 4.4 degrees of freedom for signal. Therefore, there is sufficient information to calculate partial columns in the 14-52 km range.

Batchelor et al. [2010] reported mean relative difference between ACE-FTS v2.2 and Bruker FTIR measurements of -7.45% in spring 2007 and -4.26% in spring 2008, for an average coincident partial column range of 6-43 km. This is similar to the resultsfor total column intercomparisons in the present study. *Batchelor et al.* [2010] found that agreement improved with the addition of vortex coincidence criteria. This is discussed further in Section 5.5.

Dupuy et al. [2009] compared ACE-FTS v2.2 with ground-based FTIR measurements at four locations north of 60°N latitude from 2004-2006. They applied the same smoothing and altitude selection scheme as *Batchelor et al.* [2010]. No vortex filtering was performed. This yielded various partial column altitude ranges with minimum values of 10 km and maximum values of

46.9 km. Mean relative differences for satellite minus ground-based FTS of -9.1% to +3.2% for the ACE-FTS and -8.7% to -0.5% for ACE-MAESTRO were obtained. This is similar to the level of agreement found in the present study.

5.4 NO_2 Intercomparisons

NO_2 partial column measurements made by the ground-based and satellite instruments were compared using the methods described in in Section 5.2. ACE, OSIRIS, and Bruker FTIR partial columns were calculated for 17-40 km; GBS-UV and GBS-vis partial columns were retrieved for 17 km to the top of the atmosphere; and SAOZ total column measurements were scaled to partial column amounts (see Section 5.2.3). The resulting mean absolute and relative differences are summarized in Table 5.6 and are discussed below. Available coincident measurements from all time periods are included in the intercomparisons.

5.4.1 Satellite versus Satellite Partial Columns

Mean absolute and relative differences between 17-40 km NO_2 partial columns measured by the satellite instruments are included in the first section of Table 5.6, with correlation plots shown in Figure 5.10. R^2 correlation coefficients between all satellite measurements are greater than 0.61, except for ACE-MAESTRO versus OSIRIS, which has an R^2 value of 0.352.

ACE-FTS v2.2 and v3.0 partial columns are nearly identical, with a mean relative difference of -0.2±0.1% and a correlation coefficient of 0.999. Note that the ACE-FTS v2.2 and v3.0 datasets have slightly different results when compared with the other instruments in this study because data were compared for different time periods, based on data availability. Therefore, fall 2010 and spring 2011 are included for v3.0, but not for v2.2.

The ACE-FTS v2.2 [v3.0] data are systematically higher than the OSIRIS dataset, with mean relative differences of 6.4% [7.4%]. These values are outside the combined random errors of the instruments (see Table 5.2) suggesting that the discrepancies originate from systematic errors in the measurements, the photochemical model scale factors, or the diurnal effect. See Section 5.2.3 for a discussion of errors associated with scale factors and the diurnal effect. This is

Table 5.6. As for Table 5.5, NO_2 partial columns. All measurements were scaled to local solar noon using the photochemical model. Instrument abbreviations are summarized in Table 5.1. ACE, OSIRIS, and Bruker columns are for 17-40 km. GBS columns are for 17 km to top of atmosphere. * indicates SAOZ total columns scaled to 17 km to top of atmosphere.

	N	Δ_{abs} (10^{15} mol/cm^2)	σ_{abs} (10^{15} mol/cm^2)	err_{abs} (10^{15} mol/cm^2)	Δ_{rel} (%)	σ_{rel} (%)	err_{rel} (%)
Satellite versus satellite partial columns							
OS - A2	632	-0.8	3.1	0.1	-6.4	26.8	1.1
OS - A3	595	-0.9	3.2	0.1	-7.4	30.0	1.2
OS - MA	583	-5.9	5.9	0.2	-34.2	39.2	1.6
A2 - A3	187	0.0	0.2	0.0	-0.2	0.9	0.1
A2 - MA	163	-4.2	4.3	0.3	-24.5	26.4	2.1
A3 - MA	157	-4.4	3.2	0.3	-26.9	19.6	1.6
Satellite versus ground-based partial columns							
OS - GV	3186	-3.0	5.7	0.1	-7.8	25.3	0.4
OS - GU	2885	-2.0	5.0	0.1	-3.3	18.5	0.3
OS - SA*	1510	2.0	4.0	0.1	10.2	33.9	0.9
OS - FT	4958	2.2	3.6	0.1	12.2	17.4	0.2
A2 - GV	143	1.7	1.7	0.1	15.0	15.6	1.3
A2 - GU	29	1.4	1.4	0.3	10.3	11.6	2.2
A2 - SA*	107	2.2	2.6	0.2	18.4	21.7	2.1
A3 - GV	151	1.6	1.7	0.1	15.2	16.3	1.3
A3 - GU	38	1.7	1.5	0.3	13.6	13.4	2.2
A3 - SA*	147	1.7	2.8	0.2	12.7	25.5	2.1
MA - GV	118	5.6	4.6	0.4	39.1	31.0	2.8
MA - GU	31	9.1	4.4	0.8	52.1	23.6	4.2
MA - SA*	74	7.2	4.4	0.5	48.5	22.8	2.7
Ground-based versus ground-based partial columns							
GV - GU	388	1.5	2.5	0.1	6.1	7.9	0.4
GV - SA*	295	1.1	2.8	0.2	3.8	18.8	1.1
GV – FT	1503	5.5	3.5	0.1	16.3	10.5	0.3
GU - SA*	208	-0.7	2.6	0.2	-6.4	16.2	1.1
GU – FT	1498	5.4	4.2	0.1	19.2	13.5	0.3
SA* - FT	518	1.7	4.2	0.2	12.0	23.0	1.0

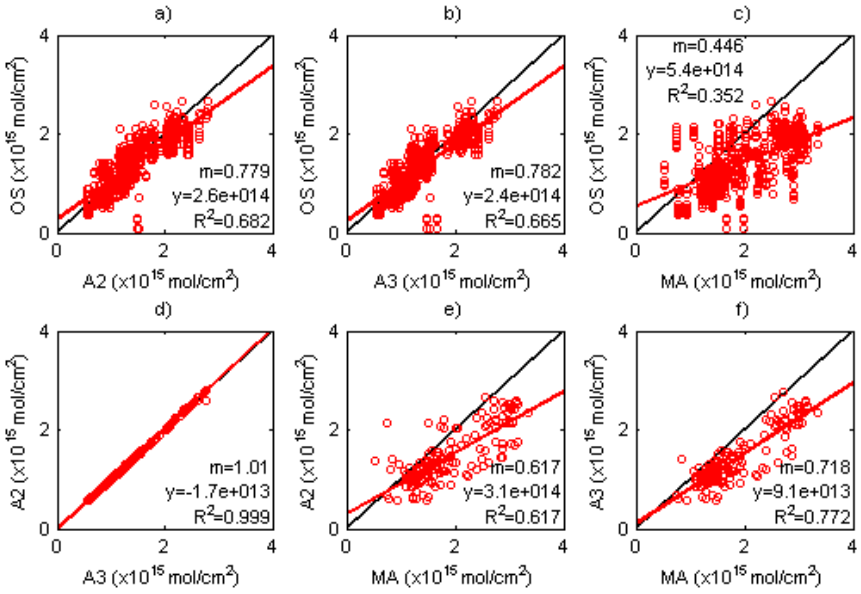

Figure 5.10: As for Figure 5.5, satellite 17-40 km NO_2 partial columns.

opposite to the results for globally coincident measurements in *Kerzenmacher et al.* [2008], who found that on average OSIRIS measurements were 17% larger than ACE-FTS v2.2 measurements at the NO_2 maximum, with better agreement below the NO_2 maximum. This may be because *Kerzenmacher et al.* [2008] compared coincident measurements at all latitudes. Furthermore, they corrected for the diurnal effect in the ACE and OSIRIS measurements prior to comparison, eliminating a high-bias in the ACE measurements below 25 km (see Section 5.2.3).

The OSIRIS, ACE-FTS v2.2, and ACE-FTS v3.0 datasets are 24.5-34.2% lower than the ACE-MAESTRO measurements. Since the ACE-FTS and ACE-MAESTRO instruments take measurements at the same time and location, this bias cannot be attributed to coincidence criteria, photochemical model scaling, or the diurnal effect. The mean relative difference for ACE-FTS v2.2 minus ACE-MAESTRO of -24.5% is comparable to the range of -5.7% to -35% found by *Fraser et al.* [2008] for 22-40 km partial columns from 2004-2006 within 500 km of PEARL. This offset may be due in part to an error of up to a few kilometres in the ACE-MAESTRO tangent heights, which can lead to a high bias in ACE-MAESTRO NO_2 data at high latitudes [*Kerzenmacher et al.*, 2008].

5.4.2 Satellite versus Ground-Based Partial Columns

The comparisons between the ground-based and satellite measurements are summarized in the second section of Table 5.6. The GBS measures partial columns from 17 km to the top of the atmosphere. SAOZ measures total columns, which were scaled down to 17 km to the top of the atmosphere, as described in Section 5.2.3. 17-40 km partial columns were calculated from satellite and Bruker FTIR profiles. The amount of NO_2 above 40 km is negligible compared with the error in the NO_2 partial columns. Therefore no correction was applied above 40 km. No coincidences were available between the Bruker FTIR and ACE instruments because only Bruker FTIR data for SZAs smaller than 80° were included in this study.

On average, OSIRIS NO_2 measurements fall in the middle of the ground-based measurements, with mean relative differences of -7.8% to +12.2%. ACE-FTS measures larger values of NO_2 than the DOAS instruments, with mean relative differences of +10.3% to +18.4%, while ACE-MAESTRO has mean relative differences of +39.1 to +52.1%, compared with the DOAS instruments.

The timeseries of the absolute differences between the various satellite and ground-based measurements is shown in Figure 5.11. Good agreement is observed between the DOAS and OSIRIS measurements in the spring and fall (panel a). In the summer, the GBS-vis and GBS-UV measure significantly larger NO_2 columns than OSIRIS. A similar seasonal variation is observed between OSIRIS and Bruker FTIR measurements (panel b). There is also a slight seasonality observed in differences between the Bruker FTIR and DOAS measurements (not shown here). This suggests that there are seasonal systematic errors in one or more of the datasets or in the diurnal correction scale factors. The differences between the ACE-FTS and the GBS partial columns (panels c, d) are more scattered in the spring than the fall, likely due to increased spatial variability of NO_2 when the polar vortex is changing structure and position rapidly in spring. The ACE-MAESTRO measurements are systematically higher than the DOAS measurements except in fall 2009 (panel e). Differences between the satellite and ground-based measurements do not change year-to-year, indicating that the satellite measurements have not changed systematically over time.

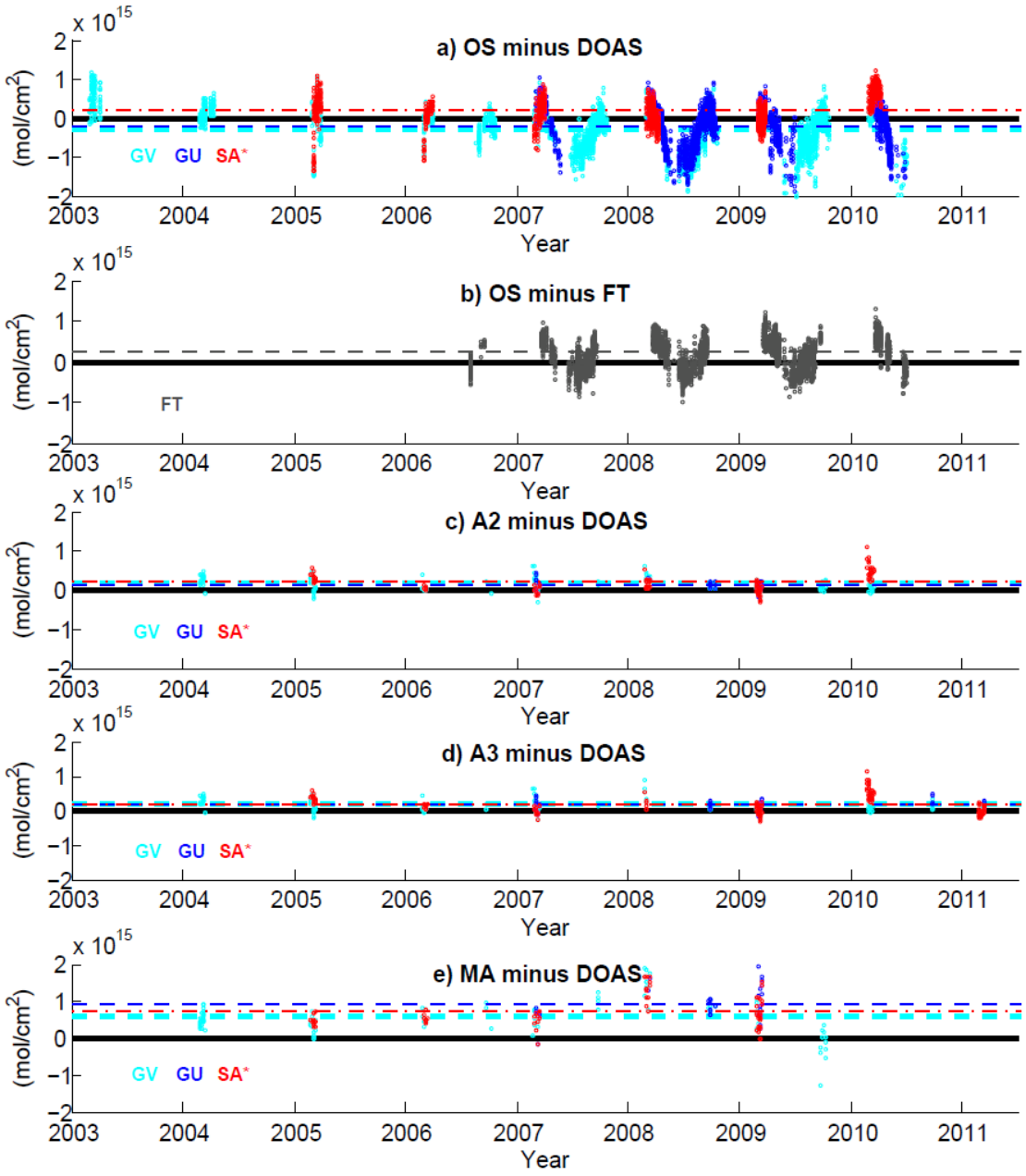

Figure 5.11: Absolute difference between satellite and GBS-vis (cyan), GBS-UV (blue), SAOZ (red), and Bruker FTIR (grey) partial columns of NO_2. Dashed lines indicate mean absolute difference. The black line indicates the zero line.

Correlations between the satellite and ground-based measurements are shown in Figure 5.12. The Bruker FTIR and GBS measure more NO_2 than OSIRIS for larger NO_2 columns. This corresponds with seasonal variation in the discrepancies discussed above. ACE-MAESTRO measurements are not as well correlated with the ground-based measurements as OSIRIS and ACE-FTS.

5.4.3 Comparisons with DOAS Measurements

The mean relative difference for GBS-vis minus GBS-UV NO_2 is +6.1±0.4%. This demonstrates good agreement, despite the shorter paths through the stratosphere taken by zenith-scattered light at UV wavelengths. Furthermore, it indicates that the new AMFs used for the GBS retrievals produce similar NO_2 columns for both UV and visible wavelengths.

The GBS-UV, GBS-vis, and SAOZ partial columns for 17 km to the top of the atmosphere all agree to within 6.4%. *Fraser et al.* [2008; 2009] found a comparable agreement of 2.2-12.3% for 2005-2007, when SAOZ and GBS NO_2 total columns were retrieved using the same analysis settings. In Figure 5.13, the absolute difference (panel a) and correlation plot (panel b) between SAOZ and GBS-vis (grey) and GBS-UV (red) NO_2 are shown. The offset between the GBS minus SAOZ measurements appears to vary year-to-year, with positive offsets in 2005, 2006, 2010 and 2011 and negative offsets in 2007, 2008 and 2009. Similar year-to-year variation is observed in the differences between the satellite and SAOZ measurements (see Figure 5.11).

This may be because the SAOZ instrument measures total columns of NO_2, which have been scaled down to 17-km to the top of the atmosphere by a fixed value. Therefore, year-to-year differences in lower stratospheric NO_2 may be a factor. Furthermore, this may reflect year-to-year differences in the SAOZ RCD, which is averaged on a campaign basis. These reasons may also explain why the GBSs are more strongly correlated with the satellites than SAOZ for NO_2 (see Figure 5.12). The DOAS NO_2 measurements are systematically lower than the satellite NO_2 measurements in the spring. This may be due to the diurnal effect, which causes the GBS partial columns to be lower and the ACE partial columns to be higher (see Section 5.2.3).

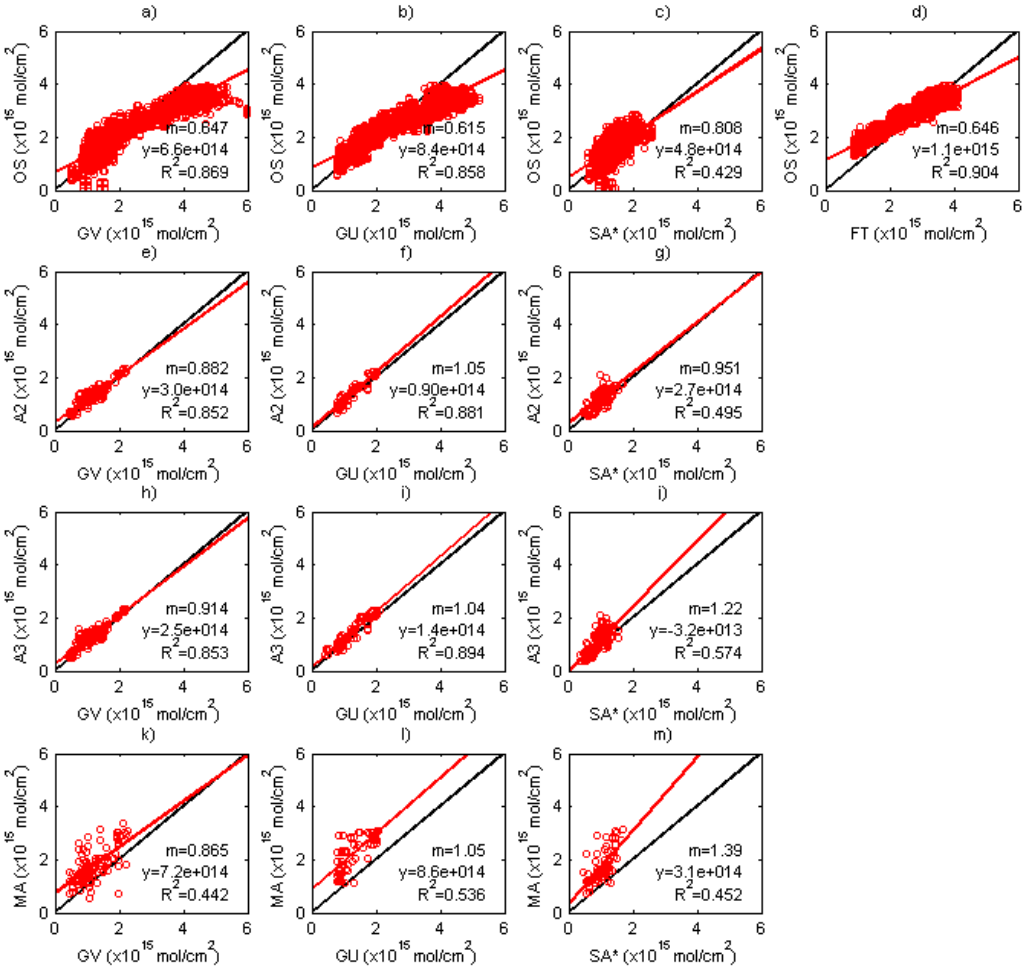

Figure 5.12: As for Figure 5.5, satellite versus ground-based NO_2 partial columns. Comparisons are not shown for ACE versus the Bruker FTIR because the Bruker FTIR NO_2 was measured at SZA > 80° when ACE measured above PEARL.

5.4.4 Comparisons with Bruker FTIR Measurements

The Bruker FTIR measures less NO_2 than the other instruments by 12.2-19.2%. This is similar to the results of *Lindenmaier et al.* [2011] who found that Bruker FTIR NO_2 15-40 km partial columns were systematically lower than GEM-BACH (Global Environmental Multiscale stratospheric model with the online Belgium Atmospheric CHemistry package), CMAM-DAS

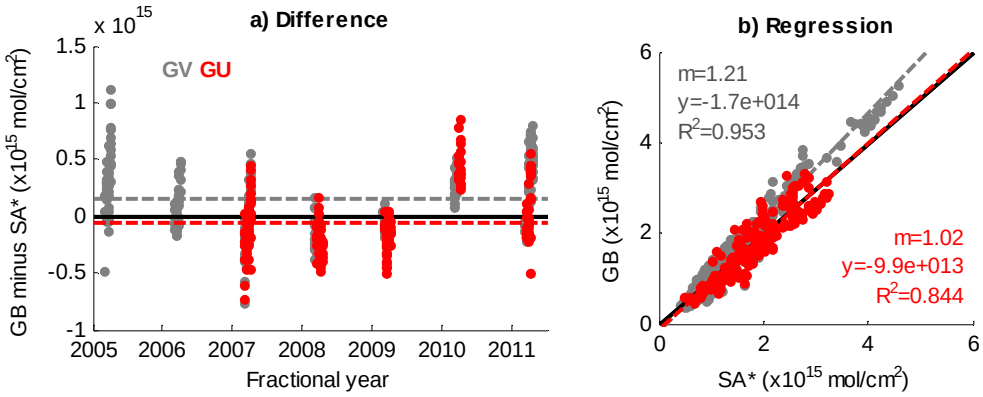

Figure 5.13: Comparison between GBS-vis (grey), GBS-UV (red) and SAOZ. (a) Absolute difference (circles) between GBS and SAOZ NO_2 columns. The solid black lines indicate the zero line and the dashed lines indicate mean absolute differences. (b) Correlation between GBS and SAOZ NO_2 columns. The solid black lines indicate the 1-1 line and the dashed lines indicate linear fit (m = fitted slope, y = fitted y-intercept).

(Canadian Middle Atmosphere Model Data Assimilation System), and SLIMCAT (Single-Layer Isentropic Model of Chemistry and Transport) models for 2007-2009. Aside from these model comparisons, the PEARL Bruker FTIR NO_2 has not previously been validated.

Kerzenmacher et al. [2008] compared ground-based FTIR NO_2 measurements from other stations with ACE-FTS v2.2 and ACE-MAESTRO v1.2 partial columns. For that study, the ACE data were smoothed to the resolution of the FTIRs and partial columns were calculated in ranges determined by the instrument sensitivities. Mean relative differences for satellite minus ground-based FTIR 14.8-32.9 km partial columns measured at Ny Ålesund, Svalbard (78.9°N, 11.9°E) were +20.9% for the ACE-FTS and +25.6% for ACE-MAESTRO. This is consistent with the results of the present study.

5.5 Spring-Time Coincidence Criteria

In this study, it was found that agreement between the various instruments was worse for both ozone and NO_2 in the spring. This may be attributed to the different lines-of-sight described in

Section 5.2.1, which can result in instruments sampling very different airmasses. This is especially relevant during spring when airmasses inside and outside the vortex can be close spatially but isolated from one another. Ozone and NO_2 columns tend to be lower when the lower stratosphere (~18-20 km) is inside the polar vortex. Furthermore, the latitudinal distribution of NO_2 has a strong gradient in the spring (see Section 5.2.3). Therefore, additional coincidence criteria were tested for the 2004-2009 GBS, SAOZ, Bruker FTIR, OSIRIS, and ACE-FTS v2.2 datasets. Spring-time data for days 50-78 (19 February to 18/19 March) were selected, as this is the approximate period of spring-time ACE measurements within 500 km of PEARL.

In order to identify similar airmasses, derived meteorological products (DMPs) [*Manney et al.*, 2007] from the GEOS-5 [*Reinecker et al.*, 2008] analysis were calculated along the line-of-sight of the ACE-FTS, the Bruker FTIR, and the DOAS (GBS and SAOZ) instruments, and at the longitude and latitude of the OSIRIS 25-km tangent height. To determine whether measurements were sampling similar airmasses, scaled PV (sPV), a dynamical parameter used to estimate the location of the vortex edge (see Appendix A), and temperature profiles were considered. *Lindenmaier et al.* [2012] present the evolution of sPV in the lower stratosphere above Eureka for springs 1997-2011.

The selection criteria of *Batchelor et al.* [2010] were applied to comparisons between ACE-FTS v2.2 and the Bruker FTIR. The difference in sPV was restricted to $< 0.3 \times 10^{-4} s^{-1}$ and the difference in stratospheric temperature was restricted to < 10 K at each altitude level from 14-36 km. Note that the present study did not include selection criteria at the 46-km level because this significantly reduced the number of coincident measurements and is unlikely to affect the ozone partial columns as number densities are very small at such high altitudes. *Batchelor et al.* [2010] also included a 1000-km distance criterion at each altitude level. This criterion was not included here due to the narrower 500-km coincidence criterion already imposed on the measurements. These selection criteria improved ozone comparisons between the ACE-FTS and the Bruker FTIR from -5.1±1.3% to +2.1±2.2% in spring 2007, a year in which the vortex was above Eureka for much of the campaign. This is slightly weaker than the improvement reported by *Batchelor et al.* [2010] of -7.5±1.6% to +1.1±2.1%. This may due to the narrower 500-km distance criterion used in the present study. Furthermore, the partial column ranges may play a role.

When averaged over springs 2007-2009, the mean relative difference between the Bruker FTIR and ACE-FTS is -5.0±0.4% without the dynamical selection criteria and -4.0±0.5% with the dynamical selection criteria. The improvement is weaker, likely because in 2008 and 2009, the polar vortex was not near Eureka for much of the campaign.

The selection criteria of *Batchelor et al.* [2010] could not be applied directly to the DOAS (GBS and SAOZ) and OSIRIS datasets because only pressure levels were available for these DMPs. Furthermore, the imposition of dynamical coincidence criteria at altitudes up to 46 km reduced the comparison statistics. The best results were obtained when dynamical coincidence criteria were imposed only in the lower stratosphere, where the bulk of the ozone column resides, at 131 hPa (~14 km), 72.5 hPa (~18 km), and 53.9 hPa (~20 km). The difference in temperature between measurements at each of these layers was restricted to < 10 K. Furthermore, coincident measurements were selected only if they were both inside (sPV > 1.6×10^{-4} s^{-1}) or both outside (sPV < 1.2×10^{-4} s^{-1}) the polar vortex at the selected pressure levels. All measurements on the vortex edge (sPV between 1.2×10^{-4} s^{-1} and 1.6×10^{-4} s^{-1}) at 131 hPa, 72.5 hPa, and 53.9 hPa were rejected. With these additional selection criteria, four out of nine instrument intercomparisons improved within standard error (see Section 5.2 for definition of standard error). For the remaining five intercomparisons, changes were not significant. The largest improvement was observed for ACE-FTS minus Bruker FTIR, which had a mean relative difference of -5.0±0.4% without the dynamical selection criteria and -3.1±0.8% with the dynamical selection criteria.

These modest improvements may be limited by the narrow 500-km coincidence criterion already in place and the approximate line-of-sight calculations used in this study. The DOAS and OSIRIS instruments measure scattered sunlight, for which photons travel various paths through the atmosphere to the instrument. Therefore, precise line-of-sight calculations cannot be performed. The DOAS DMPs were calculated along the approximate line-of-sight (see Appendix B) and the OSIRIS DMPs were calculated at the fixed latitude and longitude of the 25-km tangent height. This weakens the dynamical selection criteria.

For NO_2, dynamical coincidence criteria did not improve comparison results. The uncertainties in the measurements, the diurnal scale factors, and the diurnal effect likely overwhelm the impact of the polar vortex on these intercomparisons (see Section 5.2.3). This is consistent with the

results of *Kerzenmacher et al.* [2008], who found that scatter in the differences between ACE and high-latitude ground-based FTIR measurements could not be attributed to the polar vortex.

Due to the latitudinal gradient of NO_2 in the early spring (see Section 5.2.3), a narrower ±1° latitude coincidence criterion was applied to the 30-km tangent height of the ACE measurements, the 35-km tangent height of OSIRIS measurements, and the location of the 30-km layer along the calculated line-of-sight of the DOAS measurements. Dynamical coincidence criteria were not included. The Bruker FTIR was not included in this comparison because NO_2 measurements for this time period were removed by the SZA < 80° filter.

The resulting mean relative differences with (red circles) and without (grey stars) the additional latitude coincidence criterion are shown in Figure 5.14 for comparisons with twenty or more measurement points. The impact of the additional criterion suggests that the latitudinal gradient of NO_2 plays a role in the intercomparisons. During the time period considered, the average latitude was 77.9°N for GBS-vis, 80.2°N for GBS-UV, 78.1°N for SAOZ, 80.2°N for OSIRIS, and 79.6°N for ACE-FTS. Therefore, with the new criterion, the GBS-vis, SAOZ, and ACE-FTS measurements (taken on average at lower latitudes) decrease relative to the OSIRIS measurements (taken on average at higher latitudes). Mean relative differences between OSIRIS and ACE improve from -6.7±2.4% to -1.1±2.1%. Furthermore, mean relative differences between OSIRIS and SAOZ improve from -5.1±1.6% to +2.3±1.7% with the latitude filter. Agreement between OSIRIS and GBS-vis also improves, but is not significant within standard error. The mean relative difference between the GBS-UV and OSIRIS NO_2 (which measure at the approximately the same average latitude) changes only by a small amount. While some of these improvements may be due in part to the isolation of similar dynamical airmasses, this suggests that the latitudinal distribution of NO_2 plays a significant role in validation exercises at high latitudes.

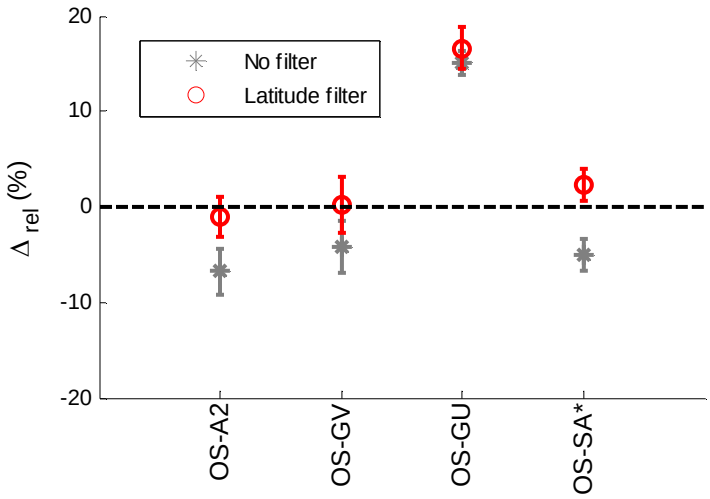

Figure 5.14: Mean relative difference for spring-time OSIRIS minus ACE-FTS v2.2, GBS-vis, GBS-UV, and SAOZ NO_2 without (grey stars) and with (red circles) additional ±1° latitude selection criteria. Error bars indicate standard error.

5.6 Summary

Ground-based and satellite ozone and NO_2 columns were compared for satellite measurements within 500 km of the PEARL Ridge Lab. Satellite ozone and NO_2 partial columns were calculated from 14-52 km and 17-40 km respectively. For comparison with ground-based measurements, satellite-plus-sonde 0-52 km columns were calculated by adding ozonesonde data to the satellite partial columns from 0-14 km. For NO_2 intercomparisons, the satellite data were compared directly to the ground-based data, as all ground-based instruments except SAOZ measured partial columns above 17 km. For SAOZ, the total column measurements were scaled down to 17 km to the top of the atmosphere. All satellite and ground-based NO_2 measurements were scaled to solar noon with the same photochemical model prior to comparison to account for the diurnal variation of NO_2.

DOAS ozone total columns were retrieved for the GBS and SAOZ by independent analysis groups using the new NDACC guidelines [*Hendrick et al.*, 2011]. The mean relative difference between the GBS and SAOZ ozone total columns was -3.2%. The DOAS instruments agreed

with the Brewer to 0.4-1.4%, indicating that the NDACC settings perform well, even in the summer months at PEARL, when the maximum SZA of 76° makes DOAS measurements challenging. Therefore, the NDACC settings and AMFs for DOAS ozone are successful in producing a homogeneous and accurate dataset at 80°N.

For DOAS NO_2, NDACC-recommended settings are currently being developed [*Van Roozendael and Hendrick*, 2012]. GBS NO_2 partial columns for 17 km to the top of the atmosphere were calculated in the 425-450 nm window (GBS-vis) and the 350-380 nm window (GBS-UV), using new AMF LUTs (see Appendix A of *Adams et al.* [2012a]). The mean relative difference for GBS-vis minus GBS-UV measurements was +6.1%, indicating that, despite the challenges of retrieving stratospheric columns at UV wavelengths, the GBS-UV measurements perform well. The GBS NO_2 partial columns agreed to within 6.5% of the SAOZ measurements, which had been calculated using SAOZ Arctic AMFs scaled down to partial columns by a fixed scale-factor.

Partial columns measured by the various satellite instruments showed good agreement for measurements within 500 km of PEARL. For ozone, all satellite instruments agreed with each other within 3%. For NO_2, all satellite instruments except for ACE-MAESTRO agreed within 7.4%. ACE-MAESTRO NO_2 measurements were systematically higher than the others by 24.5-34.2%, perhaps due to a problem with tangent height gridding [*Manney et al.*, 2007; *Kerzenmacher et al.*, 2008]. ACE-FTS NO_2 is systematically larger than OSIRIS by 6.4-7.4%, perhaps due to the diurnal effect on the ACE-FTS measurements [*Kerzenmacher et al.*, 2008]. ACE-FTS v2.2 and v3.0 ozone and NO_2 partial columns were found to be strongly correlated, with mean relative differences of 0.0±0.1% and -0.2±0.1%. This indicates that ACE-FTS v2.2 and v3.0 partial columns of ozone and NO_2 within 500 km of PEARL are nearly identical.

Satellite measurements were validated against ground-based ozone and NO_2 datasets from PEARL. Satellite-plus-sonde measurements agree with ground-based total ozone columns with a maximum mean relative difference of 7.8%. The Bruker FTIR and satellite instruments measure larger ozone total columns than the DOAS and Brewer instruments, with the largest discrepancies in the spring.

For NO_2, OSIRIS, ACE-FTS v2.2 and ACE-FTS v3.0 data agreed with all ground-based measurements to within 20%. ACE-MAESTRO measured systematically larger NO_2 than the ground-based instruments, with mean relative differences of 39.1-52.1%. The Bruker FTIR measured systematically lower NO_2 than the other instruments, which is similar to the comparison results of *Kerzenmacher et al.* [2008] for other Arctic ground-based FTIR instruments. In the spring, the GBS and SAOZ also measured lower NO_2 partial columns than the satellite instruments, perhaps in part due to the diurnal effect (see Section 5.2.3). Large seasonal variation in the differences between satellite and ground-based NO_2 measurements was observed, with more scatter in the differences in the spring than in the fall. The differences between OSIRIS and the ground-based measurements varied systematically throughout the year, reaching minima in the summertime. This could point to seasonal systematic errors in the measurements or in the diurnal scaling applied prior to intercomparison.

Since intercomparison results for both ozone and NO_2 columns were worse in the spring, several filtering tests were applied to the datasets. The addition of dynamical coincidence criteria in the lower stratosphere improved the agreement between some of the datasets by 1-3%. This improvement is likely limited because the 500-km distance coincidence criterion was already narrow and the line-of-sight calculations for the DOAS and OSIRIS instruments are approximate. Furthermore, an additional latitude-filtering criterion was tested on the NO_2 measurements in order to account for the strong latitudinal gradient in NO_2 at high latitudes in the spring and fall. The addition of latitudinal filtering improved mean relative differences between OSIRIS and ACE-FTS v2.2 from -5.1% to +2.3% and between OSIRIS and SAOZ from -6.7% to +1.1%.

For both ozone and NO_2, the OSIRIS, ACE-FTS and ACE-MAESTRO satellite measurements do not change systematically relative to ground-based measurements taken from 2003 to 2011. This indicates that these satellite instruments continue to perform. Furthermore, this demonstrates the usefulness of long-term ground-based datasets at PEARL for the validation of satellite measurements. As the PEARL datasets grow, they could be used in the future to bridge gaps between satellite missions.

6 Solar Eclipse above Eureka

Solar eclipses provide a rare opportunity to study atmospheric photochemistry: during an eclipse, the moon extinguishes sunlight to all layers of the atmosphere in a short time compared to sunset, during which the sunlight is gradually extinguished layer-by-layer. However, the brightness of the sun and the solar spectrum as seen from Earth also change rapidly during solar eclipses. Therefore accurate remote sensing of the atmosphere during a solar eclipse remains a challenge.

Below 30 km, where the bulk of the ozone column resides, ozone has a lifetime of at least a month. Therefore, a two-hour solar eclipse should not lead to significant photochemical changes in the total ozone column. Ozone measurements during eclipses have yielded a variety of results. Brewer and Dobson spectrophotometers have measured both significant increases and decreases in ozone during solar eclipses [e.g., *Bojkov*, 1968; *Chakrabarty et al.*, 2001]. Many of these studies account for the effect of the changing solar spectrum (limb-darkening), which is only of the order of 0.01% [*Blumthaler et al.*, 2006], but they do not account for the effects of diffuse radiation during eclipses, which can cause artificial decreases in Brewer and Dobson vertical column densities of up to 30 DU [*Zerefos et al.*, 2000]. While the Brewer and Dobson spectrophotometer measurements are compromised during eclipses, other instruments have also yielded a variety of results during eclipses, including a 30% decrease in ozone measured by a radiometer [*Dani and Devara*, 2002] and no changes in concentration measured *in situ* at 19.8 km [*Starr et al.*, 1980]. With a visible spectrometer, *Gil et al.* [2000] found a decrease of approximately 5% in ozone VCD, which was not significant due to measurement uncertainties.

While photochemical changes in ozone are not predicted, reduced sunlight during eclipses cools the atmosphere, which could lead gravity waves to form a bow wave with periods ranging from 20 minutes to 4 hours, depending on the distance from the eclipse maximum [*Chimonas and Hines*, 1971]. *Fritts and Luo* [1993] modeled eclipse-induced gravity waves and found that variability in the ozone total column would be difficult to detect above background gravity waves, but recently *Eckermann et al.* [2007] found that this effect may be larger than previously thought. Several studies have found evidence of waves in ozone measurements, but with varying amplitudes and periods. *Mims and Mims* [1993] smoothed Total Ozone Portable Spectrometer

measurements by 30% using a fast Fourier transform routine and found an oscillation of 0.1% of the total ozone column with a period of about 7 minutes, shortly after the eclipse maximum. With a Dobson spectrophotometer, *Chakrabarty et al.* [1997] measured ozone oscillations with an amplitude of about 5% of the total ozone column and a 15-minute period, but did not correct for limb-darkening or increased diffuse radiation. *Dani and Devara* [2002], using a radiometer, measured ozone total column oscillations with amplitudes of ~10% with periods of ~30 minutes. During a 1999 solar eclipse, *Zerefos et al.* [2000] found evidence of ozone oscillations with periods of about 20 minutes in erythemal UV-B solar irradiance. In a later study on a 2006 eclipse, *Zerefos et al.* [2007] corrected Brewer data for diffuse radiation and, using spectral Fourier analysis, found total ozone column oscillations with amplitudes of 2.5-3% and periods of 30-40 minutes in two Brewer datasets.

Unlike ozone, NO_2 is photochemically active on a timescale of minutes, due to the rapid cycling between NO and NO_2. Theoretically, NO_2 should increase (and NO should decrease) as the sun is blocked by the moon until the eclipse maximum, after which both NO_2 and NO should recover to approximately their pre-eclipse values [*Herman*, 1979; *Wuebbles and Chang*, 1979]. *Pommereau et al.* [1976] first measured an increase in NO_2 during an eclipse using a spectrophotometric technique. *Starr et al.* [1980] measured a decrease of *in situ* NO at 19.8 km, which agreed well with modeled NO to NO_2 conversion. During an 82% totality eclipse, *Elansky and Arabov* [1983] measured an NO_2 VCD increase of 60±20%, with a direct-sun UV-band instrument. During another eclipse of 87% totality, *Elansky and Elokhov* [1993] measured a 55±6% increase in NO_2 VCD using zenith-sky visible spectroscopy. *Chakrabarty et al.* [2001] found that NO_2 SCDs measured by a visible spectrometer approximately doubled and identified a wavelike structure in the NO_2 measurements. They suggested that the latter effect was related to eclipse-induced gravity waves. *Gil et al.* [2000] used a zenith-sky visible spectrometer and corrected for the changing visible solar spectrum during the eclipse to find a 155±9% NO_2 SCD increase.

6.1 Measurements and Retrievals

On 1 August 2008, a solar eclipse passed from the Canadian Arctic, over Greenland, and into Asia [*Espenak and Anderson*, 2007]. The path of the eclipse is shown in Figure 6.1. Above

Eureka, Nunavut, the eclipse began at 08:36 UT (03:36 LT), reached a maximum of 98% at 09:30 UT (04:30 LT), and finished at 10:26 UT (05:26 LT). On the morning before the eclipse, 31 July 2008, Environment Canada's Eureka Weather Station recorded mostly cloudy skies, clearing in the afternoon*. On the day of the eclipse, the weather was mostly cloudy and rain started to fall around 12 UT (7 LT).

The PEARL-GBS took measurements during the eclipse in the zenith-sky viewing geometry, with a 600 gr/mm grating yielding a 0.5-2 nm resolution. To better capture the behaviour of ozone and NO_2 during the solar eclipse, the PEARL-GBS measurement frequency was increased

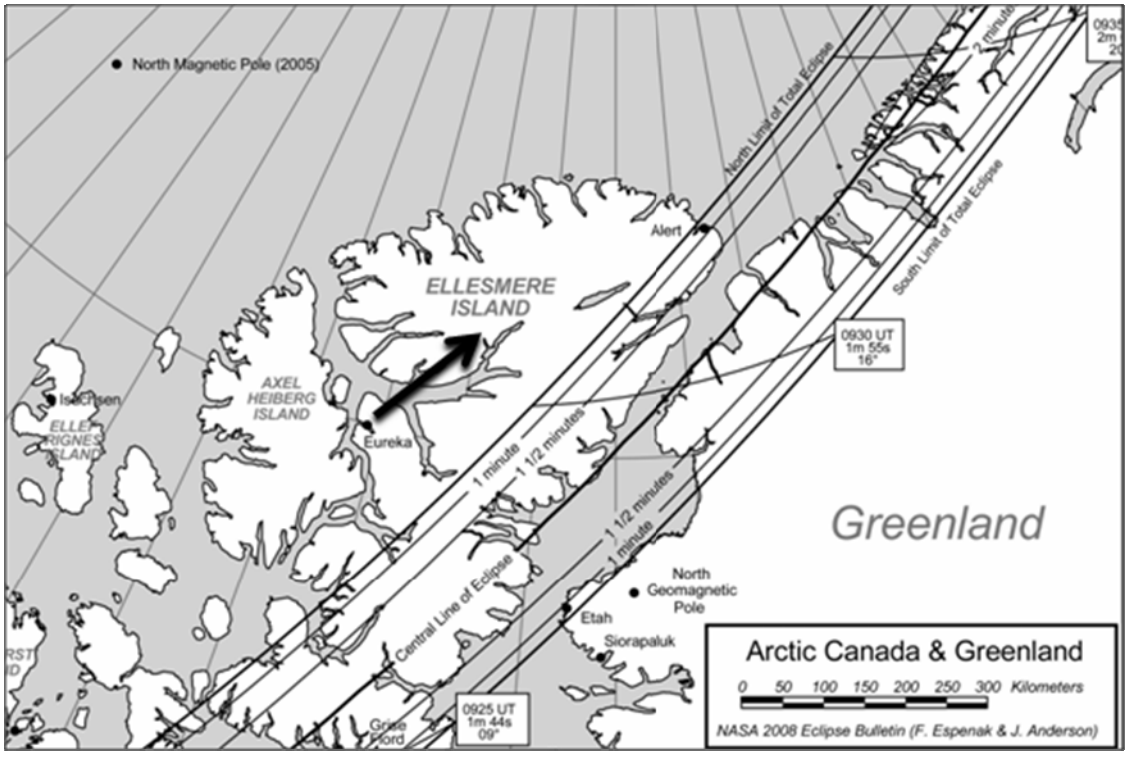

Figure 6.1: Path of eclipse totality in the Canadian Arctic, courtesy of F. Espenak and J. Anderson at NASA [*Espenak and Anderson*, 2007]. The black arrow marks the line-of-sight of the PEARL-GBS at the 98% occultation eclipse maximum with SZA 78°.

* Weather data obtained from http://climate.weatheroffice.gc.ca.

from approximately one measurement every 17 minutes to one measurement every 3 minutes on the day of the eclipse.

The line-of-sight of the PEARL-GBS was calculated using the method described in Appendix F and is marked by the black arrow on Figure 6.1. The totality of the eclipse versus time for locations along the line-of-sight was calculated using the formulae in the constant part of the Astronomical calendar [*Abalakin*, 1981]. The angular distances between the sun and moon and other necessary data were computed from the topocentric coordinates of the sun and of the moon, calculated with the CERES software [*Chernetenko et al.*, 1992][*]. Differences in eclipse timing and occultation between the four locations along the line-of-sight were very small compared with instrument time resolution and other measurement uncertainties. Therefore eclipse circumstances calculated for the airmass directly above the PEARL-GBS are used in this work.

6.1.1 Retrieval of SCDs and VCDs under a Changing Solar Spectrum

The eclipse caused the solar spectrum to change, complicating DOAS retrievals. Figure 6.2 shows the DOD before the eclipse (black) and at 96% occultation (red). DOD is defined in Equation 1.30 and was calculated in WinDOAS [*Fayt and Roozendael*, 2001] by performing a DOAS analysis with a third order polynomial subtracted, but without fitting any absorption cross-sections. The structure of the DOD before the eclipse is small, and can be attributed to absorption of trace gases including ozone and NO_2, while the structure of the DOD at 96% totality has strong H, Fe, Mg, and Ca lines corresponding to the spectrum of the solar corona, as the central part of the solar disk is extinguished [*Pierce*, 1968]. The H_β line in this structure has approximately twice the DOD shown in the residuals of *Gil et al.* [2000] for 96% occultation, which makes these retrievals more challenging.

Ozone and NO_2 DSCDs were retrieved in WinDOAS [*Fayt and Roozendael*, 2001] with ozone [*Burrows et al.*, 1999a], O_4 [*Greenblatt et al.*, 1990], NO_2 [*Vandaele et al.*, 1998], H_2O [converted from line parameters given in *Rothman et al.*, 2003], and Ring pseudo-absorber

[*] Eclipse totality calculations were performed by V. Umlenski at the Bulgarian Academy of Sciences, Institute of Astronomy, Sofia, Bulgaria.

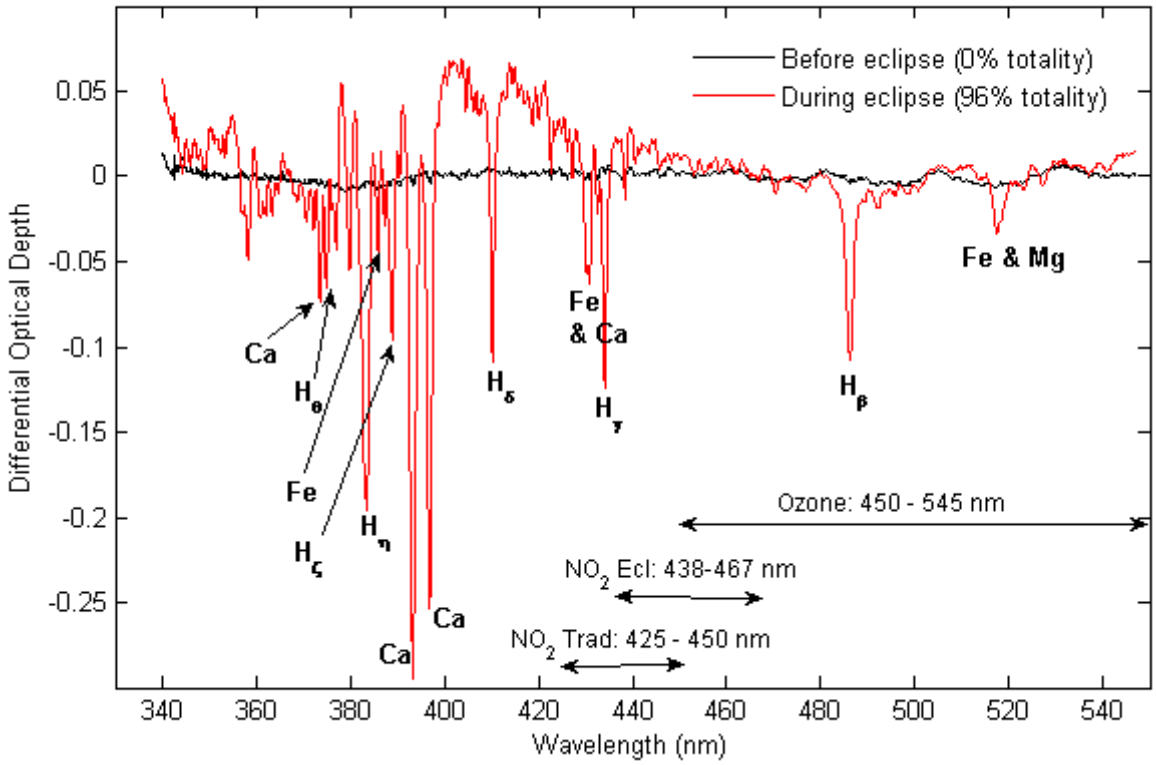

Figure 6.2: Measured DODs, with no fitting of absorption cross-sections, before the eclipse at SZA 80° (black) and at 96% totality at SZA 78° (red). The DOAS fitting windows for ozone and NO_2 are indicated (black arrows).

[*Chance and Spurr*, 1997] cross-sections. A reference spectrum from 17 July 2008 with a 59° SZA under cloudy skies was used, because it yielded the best DOAS fits over the course of the measurement period.

In order to quantify the depths of the coronal features over the course of the solar eclipse, H_β (486.1 nm) and H_γ (434.0 nm) Balmer hydrogen line cross-sections were constructed from the eclipse DOD in Figure 6.2 and added to the WinDOAS analyses for ozone and NO_2 in the usual fitting ranges of 450-545 nm and 425-450 nm respectively. Figure 6.3 shows the DSCDs of the Balmer lines in arbitrary units. On the day before the eclipse, both the H_γ line DSCDs (blue

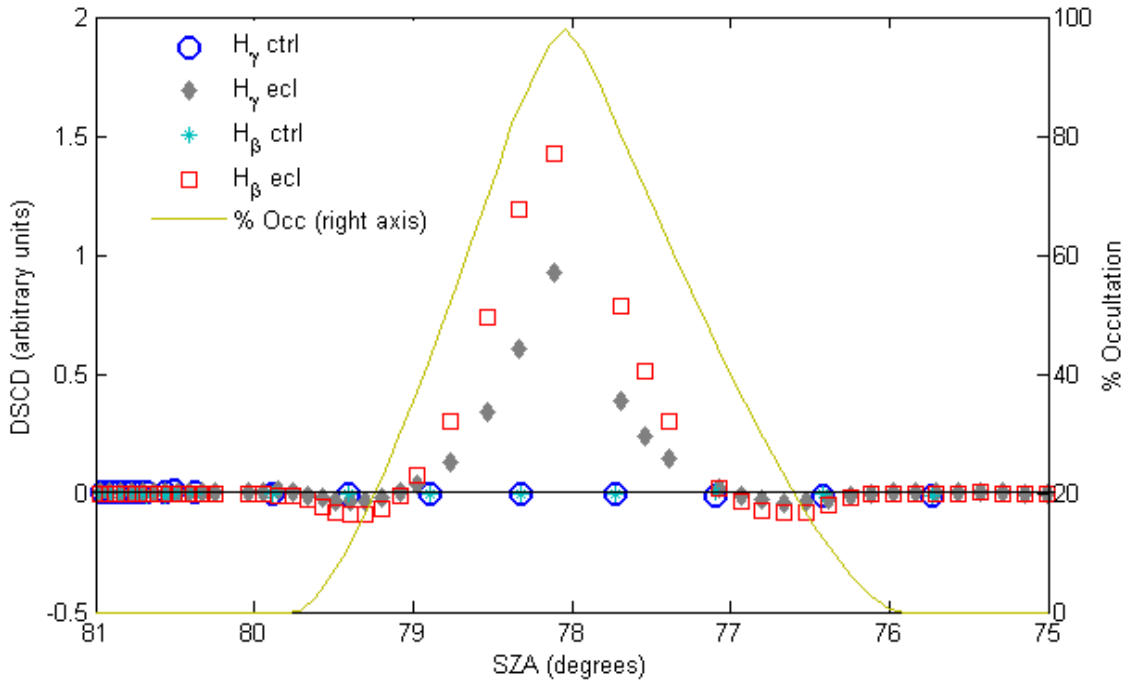

Figure 6.3: On the left axis, DSCDs in arbitrary units for H_γ on the morning before the eclipse (blue open circles), and the morning of the eclipse (grey diamonds) and H_β on the morning before the eclipse (cyan stars) and the morning of the eclipse (red open squares). On the right axis, eclipse % occultation (yellow line).

open circles) and H_β line DSCDs (cyan stars) are negligible, which demonstrates that the Balmer line cross-sections do not interfere with the regular DOAS fits. On the morning of the eclipse, the H_γ line DSCDs (grey diamonds) and H_β line DSCDs (red open squares) follow similar shapes. When the outer region of the solar disk is covered by the moon (occultation less than 20-30%), Balmer line DSCDs become negative. As more of the inner region of the solar disk is covered and the contribution from the chromosphere increases (occultation greater than 20-30%), the Balmer line DSCDs become strongly positive. This agrees with *Gil et al.* [2000], who found that the transition between positive and negative Balmer line DSCDs occurred at ~20% occultation.

In order to avoid the coronal lines, a number of DOAS fitting regions were tested. Ozone DSCDs were retrieved in a variety of fitting windows, including 450-545 nm (traditional fit

window for the PEARL-GBS), 445-480 nm, 445-515 nm, and 445-550 nm with gaps from 480-490 nm and 515-520 nm. Only DSCDs retrieved in the traditional ozone fitting region were stable on the day before the eclipse, likely because the DOD of ozone at the SZA of the eclipse (75-80°) is small and affected by water absorption due to cloudy weather. Furthermore, due to the broad interfering structure of the other coronal lines in the 450-545 nm range, only the H_β correction cross-section was used.

The resulting DOAS cross-section fits for ozone at SZA=78-79° are shown in Figure 6.4, with the DOAS fit in black and the data in red. Ozone fits on the morning before the eclipse (panel a) have random residuals. At 52% totality, the ozone fits (panel b) still have fairly random residuals, showing only a small impact of the changed coronal spectrum. At 82% totality, the ozone fits (panel c) show some systematic residuals around the wings of the H_β line and around the 517 nm Fe & Mg lines. When the Balmer line cross-section is not fit in the ozone retrieval at 82% totality (panel d), large systematic residuals dominate. Ozone DSCDs could not be retrieved for 96% totality because the coronal structure overwhelmed the residuals for this spectrum.

NO_2 was also retrieved in a variety of fitting windows. The best RMS residual before and during the eclipse was obtained for the 438-467 nm window, where there is less coronal structure, as is evident in Figure 6.2. Note that in the 438-467 nm window, no correction cross-sections were necessary. The resulting fits for the traditional 425-450 nm range with H_γ correction cross-section and this new fitting window are also shown in Figure 6.4. NO_2 DSCD fits are good on the day before the eclipse for both windows (panels e, i). At 52% occultation, the advantages of the 438-467 nm window (panel j) over the traditional window (panel f) are apparent. At 82% occultation, the 438-467 nm window (panel k) has some systematic errors, but is much better than the traditional window (panel g). The 425-450 nm fit is overwhelmed by the H_γ line when an H_γ correction cross-section is not included (panel h). Due to the reduced coronal interference in the 438-467 nm range, NO_2 could be retrieved for 96% occultation (panel l).

Ozone and NO_2 RCDs were obtained using a Langley analysis [e.g., *Fraser et al.*, 2009] for the four twilights of 30 and 31 July 2008 in the 76-81° SZA range, which was the maximum available SZA range for this time of year at Eureka. Eclipse day DSCDs were not included in

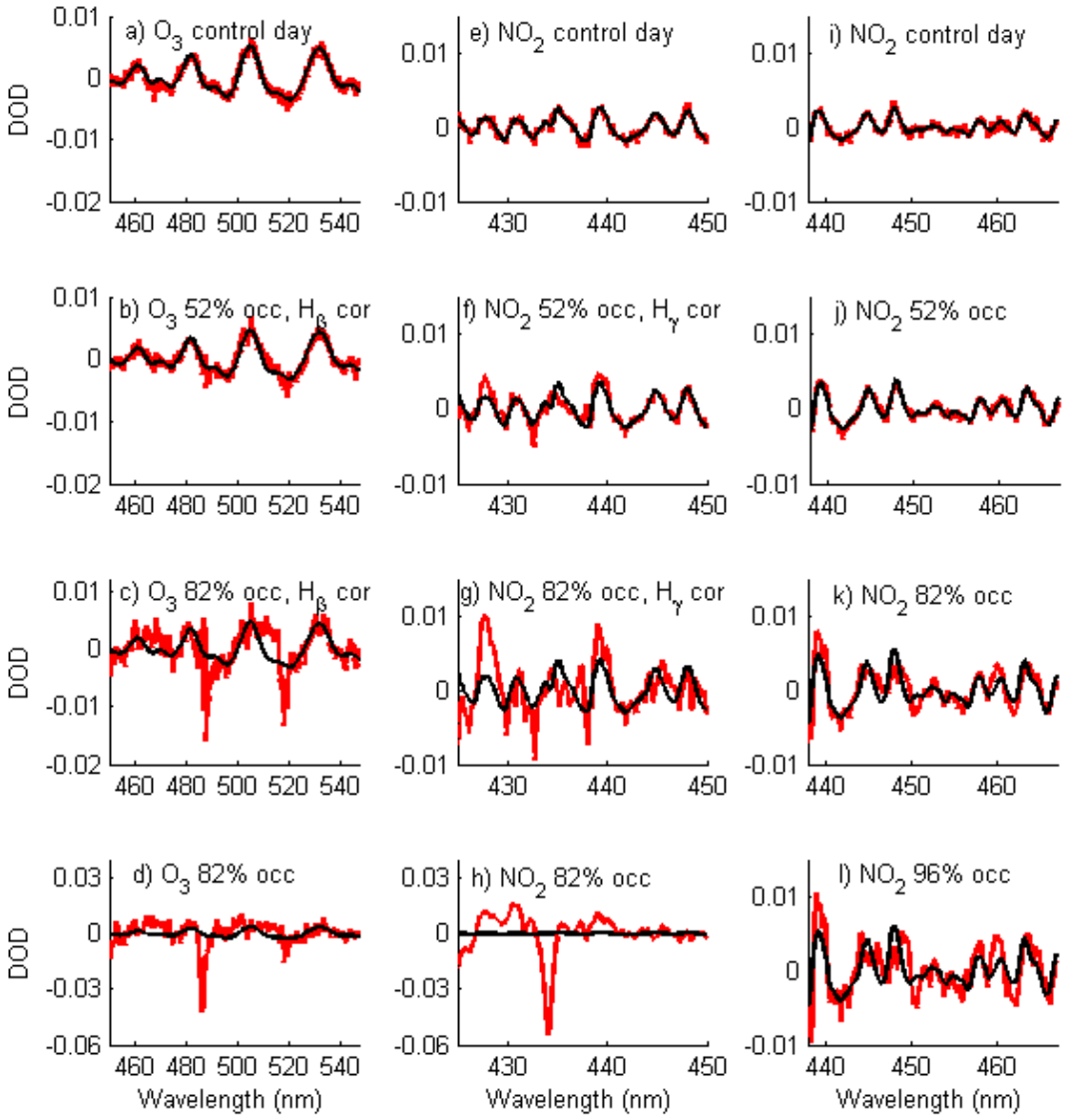

Figure 6.4: DOAS fits (black) and data (red). For ozone in the 450-545 nm window (a) on the afternoon before the eclipse, (b) at 52% occultation (c) at 82% occultation, and (d) at 82% occultation with no correction for H_β. For NO_2 in the 425-450 nm window (e) on the afternoon before the eclipse, (f) at 52% occultation (g) at 82% occultation, and (h) at 82% occultation with no correction for H_β. For NO_2 in the 438-467 nm window (i) on the afternoon before the eclipse, (j) at 52% occultation (k) at 82% occultation, and (l) at 96% occultation.

the calculation of the RCD. AMFs were obtained from a one-dimensional radiative transfer model described in Section 6.2.2. To interpret the PEARL-GBS measurements, the SCDs (DSCD+RCD) from the morning before the eclipse were interpolated in SZA to the eclipse day measurement grid and SCD ratios were taken. For ozone, VCDs throughout the twilight were also calculated with the formula,

$$VCD(\theta_0) = (DSCD(\theta_0) + RCD) / AMF(\theta_0), \quad (6.1)$$

where θ_0 is the SZA.

6.1.2 Estimates of Eclipse Systematic Errors

Previous DOAS studies during eclipses have not quantified the systematic changes in the fit residuals over the course of an eclipse. The error estimates used in this study are summarized in Table 6.1 for the measurements at 82% totality and on the previous morning, both at 78° SZA.

Random, non-eclipse systematic, and eclipse systematic errors all affect the DSCDs. Random fitting errors were calculated for each DSCD in WinDOAS and vary over the twilight. Systematic instrument, pseudo random, absolute cross-section, temperature dependence of cross-section and Raman scattering were estimated by *Fraser et al.* [2009] at 3.3% for ozone and 11.8% for NO_2 and are assumed to be consistent for all DSCDs.

In order to estimate DSCD eclipse systematic errors, two tests were performed on the 82% occultation spectrum. In the first test, the residuals for the DOAS analysis of the 82% occultation spectrum were added to a spectrum from the previous day, which was then re-analyzed for ozone and NO_2. Ozone and NO_2 DSCDs changed by -6.4 % and -3.7% respectively with the added residual. In the second test, the DSCDs of ozone and NO_2 at 82% occultation were retrieved for a variety of DOAS fit parameters, including modified Balmer line cross-sections, wavelength calibration parameters, and offset corrections. Analyses in which these parameters significantly changed the DSCDs on the day before the eclipse or increased the DOAS RMS residual values were omitted. For ozone, the largest variation was a 16% decrease in ozone DSCD, when a quadratic offset correction was added to the analysis. This was added in quadrature with the change observed in the first test. For NO_2, the 82% totality DSCD decreased

Table 6.1: Error estimates for ozone and NO_2 DSCDs, RCDs, and AMFs at 82% occultation. Square brackets indicate error estimate on morning before eclipse at same SZA as the eclipse. Error estimate calculated separately for each measurement.

	O_3 percent error at 82% occultation [same SZA on non-eclipse morning]	NO_2 percent error at 82% occultation [same SZA on non-eclipse morning]
Random fitting error on DSCD: calculated in WinDOAS for each DSCD.	4.6 [1.2] [a]	4.9 [3.2] [a]
Non-eclipse systematic: same for all DSCDs, estimated by *Fraser et al.* [2009].	3.3 [3.3]	11.8 [11.8]
Eclipse DSCD systematic: calculated for 82% occultation by adding the following two tests in quadrature and scaled to other DSCDs by strength of Balmer lines.	17.9 [0] [a]	-31.6, +4.64 [0] [a]
1. Residual addition test.	6.4 [0] [a]	3.7 [0] [a]
2. Analysis variation test.	16.7 [0] [a]	$^{+2.8}_{-31.4}$ [0] [a]
RCD systematic error #1: due to non-eclipse systematic error on DSCD.	3.3 [3.3]	11.8 [11.8]
RCD systematic error #2: from uncertainties in Langley plot. This is independent of other DSCD systematic errors.	10.6 [10.6]	8.2 [8.2]
AMF random error: same for all spectra, estimated by *Bassford et al.* [2005].	2 [2]	5 [5]

[a] Error estimate calculated separately for each measurement.

by 31.4% and increased by 2.8%, when the fitting window was changed to 440-466 nm and 438-471 nm respectively. These two values were each added in quadrature with 3.7% from the first test and taken as upper and lower NO_2 eclipse systematic DSCD errors. The eclipse

systematic errors calculated for the 82% totality spectrum were scaled to the other measurements by the Balmer line DSCD strengths shown in Figure 6.3.

There are two RCD errors, both of which have a systematic effect on the data. The first RCD error is caused by the non-eclipse systematic DSCD errors, which alter the slope of the Langley plot and thus the RCD by the same percentage. The second RCD error is from uncertainty in Langley plots and was taken as the standard deviation of the RCD values calculated from the four twilights. This second RCD error is independent of DSCD systematic errors.

The errors in DSCD, RCD, and AMF were propagated through the SCD ratio calculation and the VCD calculation in Equation 6.1. The random errors were propagated using random error analysis formulae, with an AMF random error for ozone VCD calculations estimated at 2% by *Bassford et al.* [2005]. The systematic errors were each applied as upper and lower limits to the RCDs and DSCDs, and the resulting percent change in SCD ratio and VCD were calculated. For the SCD ratio, the 3.3% and 11.8% systematic errors apply equally to all DSCDs and RCDs and therefore cancel. The total errors for each measurement were calculated by adding all random and systematic errors in quadrature.

6.2 Modeling Ozone and NO_2 SCDs during an Eclipse

6.2.1 Ozone and NO_2 Profiles

Since ozone displays no diurnal variation below the uppermost stratosphere, a single ozone profile was used for all modeling studies[*]. It was derived from an ozonesonde launched on the day of the eclipse and supplemented with an ozone climatology above 35 km [*McPeters et al.*, 2007]. Reaction rates and absorption cross-sections were primarily taken from the JPL compendium [*Sander et al.*, 2009]. This profile was held constant throughout the eclipse in the photochemical model calculations.

A photochemical model [*McLinden et al.*, 2000; *Brohede et al.*, 2008] was used to simulate the evolution of NO_2 during the day of 1 August 2008 at Eureka (80°N). See Appendix E for a

[*] Modeling studies were performed by C.A. McLinden at Environment Canada.

description of the photochemical model. The model was constrained with measured ozone and temperature profiles from the ozonesonde described above, and NO_y from a climatology [*Brohede et al.*, 2008]. Profiles of NO and NO_2 were obtained from the model simulation between 10 and 52 km. Mixing ratios of NO and NO_2 below 10 km were set to the 10 km value at each time step. In this work, modeling of the NO_2 profile through an eclipse is based on the variation in the photolysis rate of NO_2 with the fraction of eclipse totality. This is outlined below.

To a good approximation throughout most of the stratosphere, the ratio of NO_2 to NO_x can be obtained by considering Equations 1.1 and 1.2. Assuming a near steady-state,

$$\frac{[NO_2]}{[NO_x]} = \frac{1}{1 + J/(k[O_3])} = \frac{1}{1+r}, \tag{6.2}$$

where J is the NO_2 photodissociation rate constant, a function of available sunlight in the NO_2 photolysis region (~340-420 nm), and k is the $NO+O_3$ rate constant, where $[NO_2]$ and $[NO_x]$ are the number densities of NO_2 and NO_x respectively. The quantity $r=J/(k[O_3])$ is the ratio of the first-order rate constants assuming ozone remains constant. The desired quantity, r, can be calculated from model calculations of NO_2 and NO_x,

$$r = \frac{1}{[NO_2]/[NO_x]} - 1. \tag{6.3}$$

For this study, r was calculated using full chemistry instead of simply using the model-calculated $J/k[O_3]$ directly. This allowed for slower photochemistry such as the conversion between N_2O_5 and NO_x (see Section 5.2.3 for a description of the diurnal and seasonal cycles of NO_2).

In this work, r is a measure of the NO_x partitioning in the absence of an eclipse. The impact of the eclipse on photochemistry can be taken into account by altering the rate of NO_2 photolysis in a manner consistent with the varying sunlight. To a first approximation, this amounts to scaling J by the fraction of eclipse totality, or eclipse fraction. In this case, NO_2 through an eclipse can be expressed as:

$$[NO_2] = \frac{[NO_x]}{1 + r(1-\gamma)}, \tag{6.4}$$

where γ represents the eclipse fraction, as shown in Figure 6.6 and r was calculated using Equation 6.3. Equation 6.4 is simply Equation 6.2 with a scaling applied to the rate of NO_2 photolysis. When $\gamma = 0$, or no eclipse, NO_2 is at its normal level, but for a total eclipse, $\gamma = 1$, then $[NO_2] = [NO_x]$.

The brightness of the sun, and thus the available sunlight for photolysis, varies across the solar disk. Therefore, an additional limb-darkening correction is applied, based on the calculations of *Koepke et al.* [2001], using their values at 390 nm to represent the NO_2 photolysis region.

6.2.2 SCDs

Slant column densities of ozone and NO_2 are modeled using the general expression,

$$SCD(\theta_0) = \Sigma\, AMF(z, \theta_0)\, [X](z, \theta_0)\, \Delta z, \tag{6.5}$$

where z is altitude, θ_0 is SZA, [X] is the number density of ozone [O_3] or NO_2 [NO_2], Δz is layer thickness, and the summation is over altitude layers. The AMF describes the enhancement in absorption due to light traversing a slant path through a layer and is calculated using the multiple-scattering radiative transfer model of *McLinden et al.* [2002; 2006]. This expression is similar to Equation 1.31, except that it is resolved for vertical layers of the atmosphere. Calculations are performed using a surface albedo of 0.1 and a wavelength of 500 nm for ozone and 452 nm for NO_2 to correspond with the wavelengths regions in which ozone and NO_2 were retrieved. Using these AMFs, ozone SCDs were calculated using the sonde-measured ozone profile and NO_2 SCDs from the model-calculated profile described above.

During an eclipse, the fraction of multiple-scattered light should increase [*Shaw*, 1978; *Emde and Mayer*, 2007]. This is due to a larger relative contribution of diffuse light from neighbouring airmasses that are experiencing a smaller (or zero) eclipse fraction. To assess how this might impact the overall AMF, a total eclipse AMF is calculated considering only multiple-scattered light. An eclipse AMF can then be defined as,

$$AMF_e = (1-\gamma)\, AMF_{std} + \gamma\, AMF_{ms}\,, \qquad (6.6)$$

where AMF_{std} is the standard AMF and AMF_{ms} is the AMF calculated considering only multiple-scattered light. The assumed linear combination implies that during a total eclipse, only multiple-scattered light is measured.

6.3 Results and Discussion

6.3.1 Radiative Transfer during the Eclipse

To aid in the interpretation of the PEARL-GBS measurements during the eclipse, the SCDs from the previous morning were interpolated in SZA to the eclipse day measurement grid; these measurements will be called the control data. Ozone SCD measurements derived from the 450-545 nm window are shown in Figure 6.5. Figure 6.5a shows the eclipse % occultation versus SZA. In Figure 6.5b, the ratio between the eclipse and control ozone SCDs is plotted with the random fitting error only (red with error bars) and for combined fitting and eclipse systematic errors caused by the changing solar spectrum (grey shading) and show no significant changes in ozone caused by the eclipse.

Theoretically, toward an eclipse maximum, contributions from multiple-scattered light dominate in the zenith-viewing direction [*Shaw*, 1978; *Emde and Mayer*, 2007]. Therefore the AMFs were derived for both the standard atmosphere and for increased multiple scattering toward eclipse maximum, as discussed in Section 6.2.2, then applied to modeled ozone profiles to calculate SCDs, and are shown in Figure 6.5b. The modeled difference in ozone SCDs calculated with the standard AMFs (dotted line) is a constant value of one as there are no photochemical changes in ozone over the short time period of the eclipse. The SCD ratio for the multiple scattering AMFs (blue dashed line) is positive, as the multiple-scattering AMFs tend to be about 20% larger than the standard AMFs at eclipse maximum. The multiple scattering AMFs are outside the uncertainty range of the SCD difference, suggesting that this has a small effect up to 82% occultation.

O_4 SCDs can also be used as a proxy for changing radiative transfer(see Section 1.3.5). In Figure 6.5c, the difference between eclipse and control O_4 DSCDs measured in the 450-545 nm

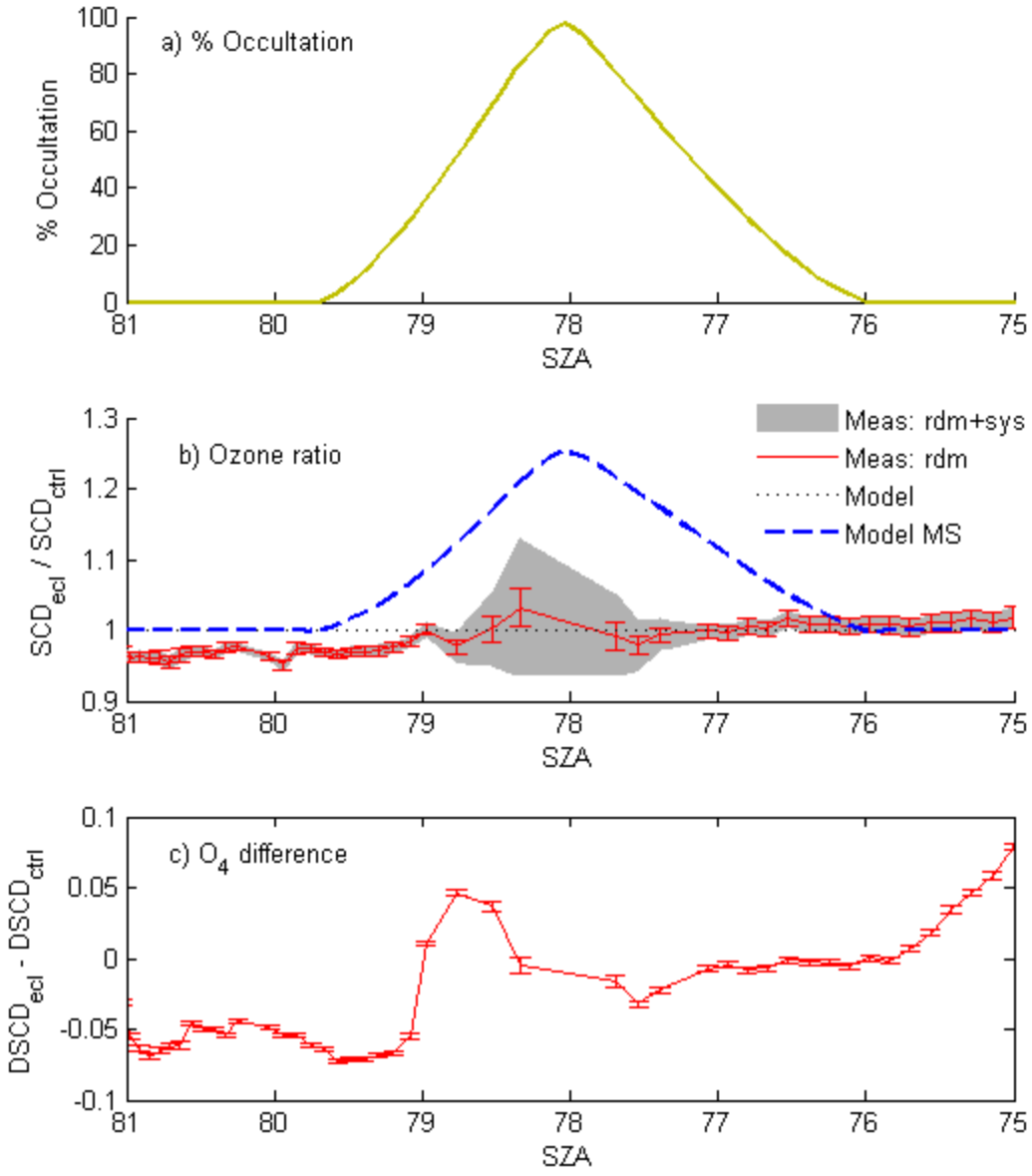

Figure 6.5: (a) Eclipse % occultation versus SZA. (b) Ozone eclipse SCD divided by control SCD with DOAS random fitting error (red with error bars) and combined fitting and eclipse systematic errors (grey shading), and modeled SCD difference for the regular atmosphere (dotted zero-line) and enhanced multiple scattering (blue dashed line). (c) O_4 eclipse DSCD minus control DSCD, with random fitting error.

range are shown with fitting error. The DSCD ratio was not plotted due to near-zero O_4 DSCDs in the denominator. O_4 increases over the morning of the eclipse, likely due to the incoming rain clouds, but does not appear to be correlated with the eclipse occultation, suggesting that the eclipse is not significantly affecting the path of light to the instrument. Since there is no evidence of enhanced multiple-scattering in the O_4 or ozone measurements, standard radiative transfer AMFs were used for this study.

6.3.2 Ozone during the Eclipse

In Figure 6.6a, PEARL-GBS ozone VCDs are plotted against the fractional day (grey with error bars) for the day before and the morning of the eclipse. Ozone VCDs at Eureka from direct-sun Brewer #021 and #069 measurements are shown in black open circles and blue stars respectively. A description of the Eureka Brewer dataset is given in Appendix C. Good agreement between the PEARL-GBS and Brewers is evident. In Figure 6.6b, the VCDs during the eclipse measured by the PEARL-GBS are shown in more detail with random error (red with error bars) and combined eclipse systematic and random errors (grey shading) and are plotted against fractional day (bottom x-axis) and SZA (top x-axis). On the right y-axis, the percent occultation of the eclipse is plotted (thick yellow line). Ozone VCDs from the Brewer spectrometers during the eclipse are not shown as they have not been corrected for the change in the solar spectrum and hence are unreliable.

Over the two hours of the eclipse, ozone VCDs measured with the PEARL-GBS rose at a rate of 7.0±0.5 DU/hour. The gradual increase in ozone over the course of the eclipse could be due to natural variability, as a 10.3±1.2 DU/hour drop in ozone was measured over a two-hour period on the previous afternoon. Two possible ozone oscillations occur between approximately 30-80% occultation on either side of eclipse totality, with ~2-3% amplitudes and ~20-minute periods. These are consistent with ozone oscillations measured by *Zerefos et al.* [2007], who found 2.5-3% amplitude oscillations with periods of 30-40 minutes and *Chakrabarty et al.* [1997], who found ~5% amplitude oscillations with periods of ~15 minutes. However, the oscillations are not significant above the combined random and systematic errors, which run from 3.3-6.8% over the eclipse. Also, only four measurements make up each oscillation and the

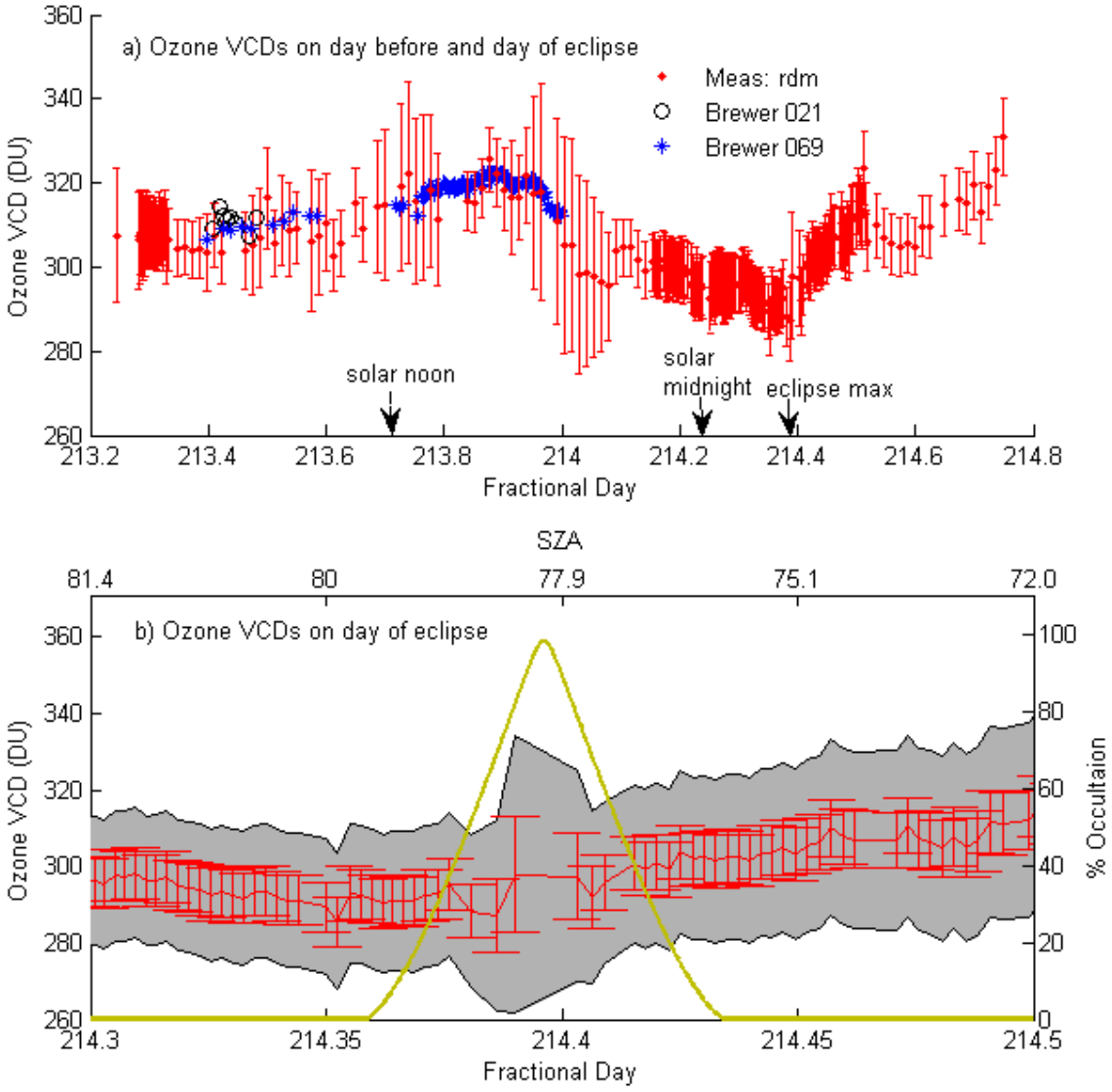

Figure 6.6: (a) Ozone VCDs for the day preceding the eclipse and the eclipse morning versus fractional day measured by the PEARL-GBS with random error (red with error bars), Brewer #021 (black open circles), and Brewer #069 (blue stars). (b) PEARL-GBS ozone VCDs during eclipse versus fractional day (bottom axis) and SZA (top axis) during eclipse with random error (red with error bars) and combined eclipse systematic and random errors (grey shading) plotted with the eclipse % occultation on the right axis (thick yellow line).

19-minute time period around maximum eclipse occultation was not sampled. Therefore, this study is inconclusive regarding ozone oscillations.

6.3.3 NO_2 during the Eclipse

NO_2 shows a much stronger variability during the eclipse. Before the eclipse, the control SCDs were 1.07 times larger than the eclipse SCDs due to the day-to-day variability in NO_2. Therefore, the eclipse SCDs were multiplied by 1.07 to account for this. The measured ratios between eclipse and control NO_2 SCDs are shown on the left y-axis of Figure 6.7, with combined fitting error and eclipse systematic error (grey error bars) and fitting only (red error bars) and indicated. The measurements increase and decrease with eclipse occultation (thick yellow line on right y axis). The ratio of the maximum measured SCD, at 96% occultation, to the SCD measured at the same SZA on the previous morning was $1.84^{+0.12}_{-0.43}$.

NO_2 profiles were modeled for 09:30 UT (04:30 LT), the time of the eclipse maximum, for normal levels of sunlight and for reduced sunlight during the eclipse. For normal sunlight, the corresponding VCD was 4.75×10^{15} mol/cm^2, while at eclipse maximum, it was 9.18×10^{15} mol/cm^2. Modeled VCDs were converted to SCDs and a ratio of eclipse to non-eclipse SCDs was taken.

This ratio is shown in Figure 6.7 for the eclipse under cloud-free conditions (blue dotted line). The modeled ratio agrees well with the data up until the eclipse maximum. For the second half of the eclipse, the measurements follow the same shape as the model, but are systematically lower than the model. This asymmetry may be introduced by multiple scattering in clouds [*Pfeilsticker et al.*, 1998] as cloudy conditions varied over the course of the eclipse. AMFs were also calculated for optical depth 10 and the resulting SCD ratio is shown in Figure 6.7 (cyan dashed line). These cloudy-weather AMFs were found to change the modeled SCD ratio by 6-7%, which could account for the discrepancies between the model and measurements. The model suggests an SCD ratio of 1.91 at 96% occultation for cloud-free conditions.

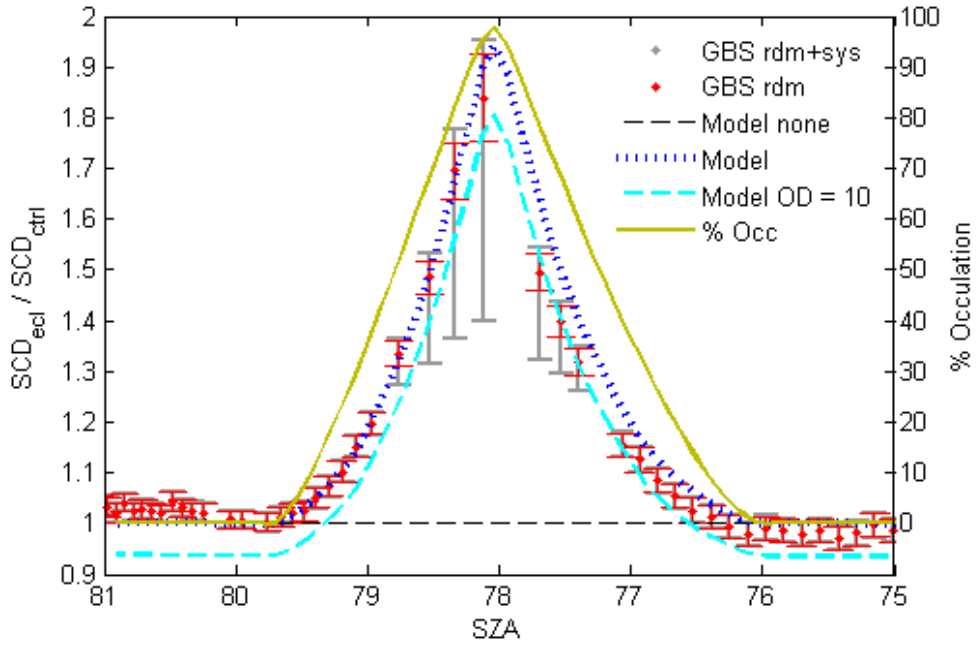

Figure 6.7: On the left y-axis, ratio of eclipse NO_2 SCD to control SCD measured with the PEARL-GBS with systematic and random errors (grey error bars) and random errors only (red error bars), and the modeled SCD ratio for no eclipse (black dashed zero line), eclipse with no clouds (blue dotted line), and eclipse with optical depth 10 (cyan dashed line). On the right axis, the eclipse % occultation is shown (thick yellow line).

In an effort to compare these results to eclipse NO_2 ratios from previous studies, the eclipse model was applied to the dates, eclipse totalities, locations, and SZAs of the previous studies and the results are summarized in Table 6.2. These simulations were carried out in an identical manner to this study except that climatologies were used for the ozone [*McPeters et al.*, 2007] and temperature [*Nagatani and Rosenfield*, 1993] in the model. In all cases, the modeled SCD and VCD ratios agree within uncertainty with the studies. This demonstrates a high level of consistency considering the range of latitudes and SZAs at which the eclipses occurred. It was found that aside from eclipse totality, the main factor affecting the ratio was the SZA. At large SZA, much of the NO_x is already in NO_2, so there is less NO_x available for conversion to NO_2. Therefore, due to the higher-sun SZA of 78°, this study measures a larger increase in NO_2 in than in past studies.

Table 6.2: Measurements NO_2 during eclipses from past studies compared with calculations using the eclipse photochemical model from this study. (Quant = quantity measured, lat = latitude, occ = eclipse occultation, meas = measured ratio, mod = modeled ratio).

	Date	Quant	Lat	Occ	SZA	Meas	Mod
This work	01 Aug 2008	Ratio of eclipse to non-eclipse SCD	80°N	96%	78° am	$1.84^{+0.12}_{-0.43}$	1.91
Gil et al. [2000]	26 Feb 1998	Ratio of eclipse to non-eclipse SCD	28°N	95%	92° pm	1.55±0.09	1.47
Elansky and Elokhov [1993]	22 Jul 1990	Ratio of eclipse to non-eclipse VCD	61°N	99.7%	87° am	1.55±0.06	1.55
Elansky and Arabov [1983], *Elansky and Elokhov* [1993]	31 Jul 1981	Ratio of eclipse to non-eclipse VCD	44°N	92.5%	82° am	1.6±0.2	1.72

6.4 Summary

During the 98% totality solar eclipse on 1 August 2008, ozone and NO_2 were measured using the PEARL-GBS. DSCD retrievals were complicated by the small SZA of the measurements (75-80°) and the changing solar spectrum during the eclipse. The changes in the solar spectrum were explored and fitting parameters were optimized to reduce the impact of the coronal spectrum. Eclipse systematic errors were estimated to account for added structure in the DOAS fitting residuals. With improved DOAS analysis settings, ozone was retrieved up to 82% occultation and NO_2 was retrieved up to 96% occultation.

Radiative transfer up to 82% occultation was studied with O_4 DSCDs and a radiative transfer model with enhanced multiple scattering. It was found that the eclipse had little impact on radiative transfer for zenith-scattered sunlight up to 82% totality.

Ozone VCDs were retrieved and a gradual increase in ozone throughout the eclipse was found to be within the natural variability of ozone at Eureka. Due to measurement errors and the limited

temporal resolution of the data, no conclusion could be drawn about ozone oscillations although there was some evidence of two oscillations with amplitude of 2-3% and a 20-minute period.

Measured eclipse and control day NO_2 SCDs were found to have a peak ratio of $1.84^{+0.12}_{-0.43}$, which agrees with the modeled value of 1.91. The NO_2 eclipse model was applied to the eclipse totalities, locations, and SZA of the measurements of *Gil et al.* [2000], *Elansky and Elokhov* [1993], and *Elansky and Arabov* [1983] and was found to be in good agreement with these studies. Due the large eclipse occultation and the small SZA of this study, the NO_2 SCD ratio from this study was the largest of past measurements.

7 The Unusual Spring 2011 in the Context of 11 Years of Measurements

In spring 2011, chemical ozone loss in the Arctic was comparable to that observed over Antarctica for the first time on record [*Manney et al.*, 2011]. This resulted from an unusually prolonged period with a strong, cold polar vortex. Due to these persistent low temperatures, PSCs were observed until mid-March and activated chlorine was observed until late March, leading to a record ozone loss [*Balis et al.*, 2011; *Manney et al.*, 2011]. An overview of the chemical and dynamical contributions to spring-time heterogeneous ozone loss is given in Section 1.1. Ground-based measurements of ozone, NO_2, and OClO can be combined with stratospheric parameters in order to identify ozone depletion, chlorine activation, and denitrification within the polar vortex [e.g., *Tornkvist et al.*, 2002; *Tétard et al.*, 2009]. OClO is a good qualitative indicator of chlorine activation [*Sessler et al.*, 1995]. However, quantification of ClO from OClO measurements is difficult due to uncertainties in model predictions, particularly under strong chlorine activation (see Section 1.1.1.1; *Oetjen et al.* [2011]).

During the spring-time break-up of the Arctic polar vortex, large variability in stratospheric trace gases can be observed as vortex and lower-latitude air masses mix. Fragments of the polar vortex, containing characteristic values of chemical tracers, such as low N_2O, can become "frozen-in" and be advected throughout the hemisphere [e.g., *Hess*, 1991]. Similarly, lower-latitude air masses, containing, e.g., enhanced N_2O, can be transported northward. In some cases, these low-latitude air masses remain intact through the summer. These so-called frozen-in anticyclones (FrIACs) were observed in 2003 [*Lahoz et al.*, 2007], 2005 [*Manney et al.*, 2006; *Allen et al.*, 2011], and 2007 [*Thieblemont et al.*, 2011]. The 2005 FrIAC formed during the final stratospheric warming and persisted until late May in dynamical fields, and until late summer in chemical tracer fields measured by the Microwave Limb Sounder (MLS) satellite instrument [*Manney et al.*, 2006]. These features were also captured by the GMI chemistry transport model (CTM) [*Allen et al.*, 2011].

Ozone VMRs within frozen-in features depend primarily on middle stratosphere chemistry, as the air masses are isolated. Photochemical production through odd-oxygen reactions depends primarily on SZA, while catalytic loss depends primarily on NO_x concentrations and SZA. For

large SZA (limited sunlight), both the photochemical production and catalytic destruction of ozone are slow. However, production drops off more rapidly with SZA than does destruction. This leads to a maximum ozone loss rate for SZA 80-95° [*Sinnhuber et al.*, 1999].

In the winter, low-ozone pockets have been observed inside anticyclones shortly after the peak of a stratospheric warming [*Manney et al.*, 1995a; *Harvey et al.*, 2002; *Harvey et al.*, 2004; *Harvey et al.*, 2008]. Low-ozone pockets form because the anticyclone isolates the air mass from ozone-rich lower-latitude air and sunlight is limited, repressing the photochemical production of ozone [*Morris et al.*, 1998; *Nair et al.*, 1998]. Low-ozone pockets tend to have 5-30% less ozone than surrounding ambient air [*Harvey et al.*, 2008]. In the summer, lower ozone has also been noted inside anticyclones, but is typically attributed to dynamics instead of chemistry [*Orsolini et al.*, 2003; *Orsolini and Nikulin*, 2006]. Overall, summertime ozone loss is driven by 24-hour sunlight, as NO_x is released from its night-time reservoirs, leading to a ~30% decrease in the ozone column [e.g., *Farman et al.*, 1985b; *Perliski et al.*, 1989; *Fahey and Ravishankara*, 1999].

Spring-time polar ozone loss is typically associated with lower stratospheric heterogeneous chemistry. However, Konopka et al. [2007] found that NO_x-driven middle stratosphere ozone loss during stratospheric warmings can have a greater impact than halogens for some Arctic springs. They studied the transport of subtropical ozone and NO_x-rich air to the Arctic in spring 2003, a year in which the Arctic lower stratosphere was warm. By late April 2003, local ozone loss was up to 50% at the 600-K potential temperature level and was dominated by NO_x chemistry, which accounted for 76% of the loss for the region between 600 and 900 K. Therefore, the ozone loss rates were strongly dependent on the amount of NO_y transported from lower latitudes.

In this chapter, the spring 2011 ozone loss and the break-up of the unprecedentedly strong polar vortex are investigated using the ground-based, satellite, and model datasets described in Section 7.1. GBS and SAOZ ozone, NO_2, and OClO column measurements were used to assess the severity of ozone depletion in 2011 compared to previous years. Dynamical parameters and SLIMCAT modeled passive ozone were used to separate the chemical and dynamical contributions to the low ozone columns. This work is described in Section 7.2. GBS, OMI satellite, and GMI modeled ozone and NO_2 columns above Eureka during the vortex break-up in

2011 were unusual compared with previous years. The evolution of dynamical parameters and trace gases above Eureka in April/May 2011 is presented and discussed in Section 7.3. Conclusions are given in Section 7.4.

7.1 Datasets

In order to produce a complete picture of the vortex break-up in 2011 above Eureka, ground-based, satellite, and model datasets were combined. These datasets are summarized in Table 7.1 and described in the text below.

Ground-based DOAS measurements were used assess ozone depletion within the polar vortex in 2011 and to identify unusual variations in ozone and NO_2 columns above Eureka during the vortex breakup. DOAS ozone, NO_2, and OClO measurements were included in this study. GBS ozone, NO_2-vis and NO_2-UV columns are described in Chapter 4 and SAOZ ozone columns are described in Appendix C. OClO was also retrieved when the GBS high-resolution gratings were used, using the DOAS technique [*Platt and Stutz*, 2008] in the 350-380 nm wavelength range. In 2009 and 2010, instrument problems increased noise, so OClO was not retrieved. Spectra were averaged to a time-resolution of 20-30 minutes prior to data processing in order to improve the signal-to-noise ratio. The following cross-sections were fit during the DOAS procedure: OClO measured at 204 K [*Wahner et al.*, 1987], ozone measured at 223 K [*Bogumil et al.*, 2003], NO_2 measured at 220 K [*Vandaele et al.*, 1998], O_4 [*Greenblatt et al.*, 1990], BrO measured at 223 K [*Fleischmann et al.*, 2004], and Ring [*Chance and Spurr*, 1997]. A sample OClO DOAS fit for 16 March 2011 (day 75) at evening SZA 90° is shown in Figure 7.1. The resulting DSCDs between SZA 89-91° from each twilight were averaged. Based on the average DOAS fitting error and the standard deviation of OClO DSCDs between SZA 89-91°, the detection limit was calculated to be 0.6×10^{14} mol/cm^2. Note that since a daily reference spectrum was used, the OClO reference state is different for each day. However, there is very little OClO during the day, therefore, this is expected to introduce little variability to the DSCDs.

Ozone and NO_2 columns measured during the final stratospheric warming were resolved OSIRIS satellite measurements. OSIRIS aerosol measurements were also used to identify vortex and lower-latitude air masses. The OSIRIS satellite datasets used in this study are described in Appendix D. To investigate air masses above Eureka, OSIRIS ozone, aerosol, and NO_2 profiles

Table 7.1: Summary of data products included in this study.

	Description	Data products used in this study
GBS	Ground-based zenith-sky UV-visible measurements at PEARL	Ozone total columns[a] NO_2-vis and NO_2-UV partial columns (17 km to top of atmosphere)[a] OClO DSCDs at SZA 90°
SAOZ	Ground-based zenith-sky UV-visible measurements at PEARL	Ozone total columns[b]
OMI	Satellite nadir UV-visible measurements	OMI-DOAS ozone total columns[c] DOMINO NO_2 total columns[d]
OSIRIS	Satellite limb-scattered UV-visible measurements	Ozone profiles (SaskMART v5.0.x)[e] Aerosol extinction profiles at 750 nm (SaskMART v5.0.x)[f] NO_2 profiles (Optimal estimation v3.0)[g]
SLIMCAT	3D chemical transport model which uses winds and temperatures from ECMWF[h]	Passive ozone total columns
GMI[i]	3D chemical transport model which uses winds and temperatures from MERRA[j]	Ozone, NO_2, and NO profiles sampled daily at 10:00 LT N_2O, tropopause pressure, PV sampled daily at 12:00 UTC
DMP[k]	Dynamical fields calculated from MetO and GEOS-5[l]	Temperature, EqL, and sPV profiles at 12:00 UTC

[a] [*Fraser et al.*, 2009; *Adams et al.*, 2012a]
[b] [*Hendrick et al.*, 2011]
[c] [*Veefkind et al.*, 2006; *Veefkind and Sneep*, 2009]
[d] [*Dirksen et al.*, 2011]
[e] [*Degenstein et al.*, 2009]
[f] [*Bourassa et al.*, 2007]
[g] [*Brohede et al.*, 2007]
[h] [*Chipperfield*, 2006; *Feng et al.*, 2007]
[i] [*Duncan et al.*, 2007; *Strahan et al.*, 2007]
[j] [*Rienecker et al.*, 2011]
[k] [*Manney et al.*, 2007]
[l] [*Rienecker et al.*, 2008]

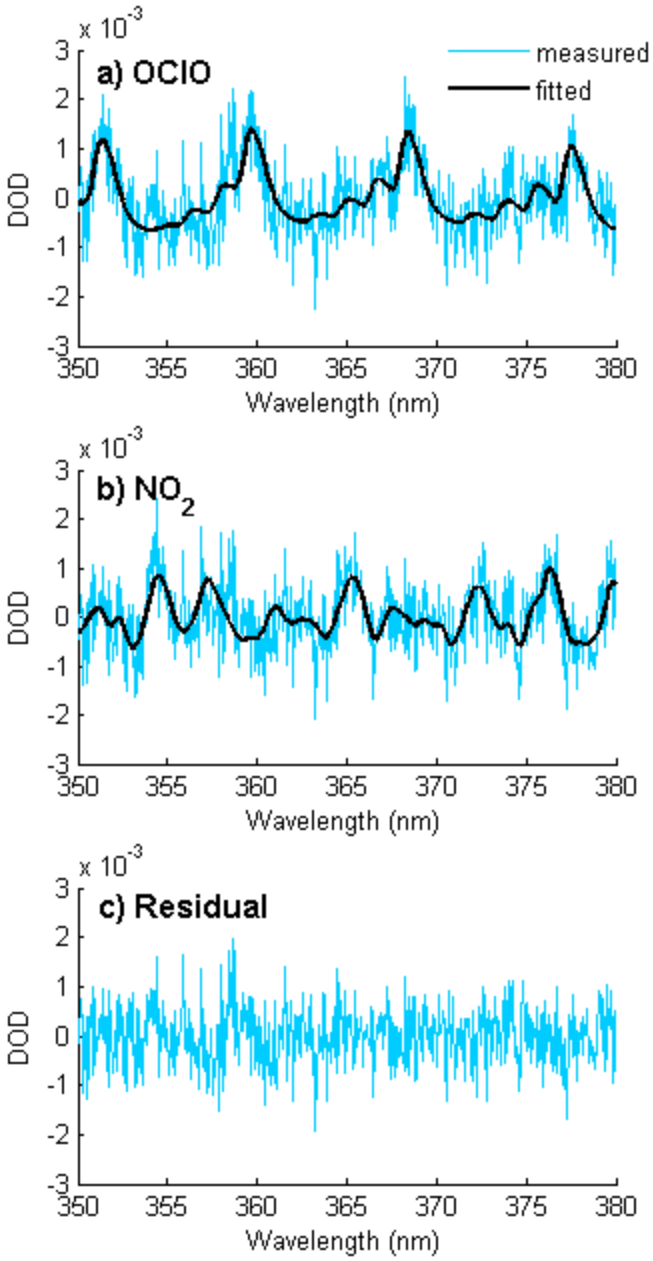

Figure 7.1**:** Example of OClO DOAS measurement for SZA 90° on 16 March (day 75) 2011. Measurement (blue) and fit (black) for (a) OClO and (b) NO_2 and (c) residual are shown. DOD = differential optical depth.

were averaged daily within 500 km of Eureka. To produce polar maps at fixed potential temperature levels, data were passed through a Gaussian filter with a standard deviation of 5° and interpolated onto 2°x2° horizontal grid.

OMI satellite ozone and NO_2 column measurements complemented these datasets, in particular in early April, when OSIRIS was turned off for annual maintenance. OMI satellite datasets are described in Appendix D. To investigate air masses above Eureka, daily OMI ozone and NO_2 columns within 500 km of Eureka were averaged. To produce polar maps at fixed potential temperature levels, data were passed through a Gaussian filter with a standard deviation of 1° and interpolated onto 1°x1° horizontal grid. Note that a smaller grid and standard deviation were used for OMI than for OSIRIS because OMI has better horizontal resolution.

The evolution of these datasets was investigated using meteorological fields from DMPs. DMPs [*Manney et al.*, 2007] were calculated directly above Eureka and along the lines-of-sight of the DOAS instruments (see Appendix F) for 1999-2003 using the MetO analysis and for 2004-2011 using the GEOS-5.0.1/GEOS-5.2.0 analysis [*Rienecker et al.*, 2008]. Stratospheric temperatures and sPV were interpolated to the 490-K potential temperature level (~lower stratosphere ozone maximum, ~19 km) and are referred to here as T_{490K} and sPV_{490K}. The inner and outer vortex edges are identified at sPV_{490K} values of $1.6x10^{-4}$ s^{-1} and $1.2x10^{-4}$ s^{-1}, respectively [*Manney et al.*, 2007]. Equivalent latitude (EqL), temperature, and sPV for DMP calculated daily at 12:00 UTC directly above PEARL were also considered. See Appendix A for definitions of sPV and EqL.

The model datasets used in this study are described in Appendix D. In order to estimate ozone loss due to heterogeneous chemistry, passive ozone columns above Eureka were calculated using the SLIMCAT 3-dimensional offline chemical transport model [*Chipperfield*, 2006]. GMI, a 3-D chemistry and transport model [*Strahan et al.*, 2007], was used to understand the evolution of trace gases during the break-up of the polar vortex. GMI profiles were interpolated to the latitude and longitude of Eureka. Polar maps at various potential temperature levels were also produced. Since passive ozone was not available from the GMI runs used in this study, passive ozone from Lagrangian Chemistry and Transport Model ATLAS was used to quantify NO_x-driven ozone loss during these events.

7.2 Severe Ozone Depletion above PEARL

7.2.1 Timeseries of Ozone, NO_2, and OClO

The 1999-2011 timeseries of ozone, NO_2, OClO, T_{490K}, and sPV_{490} is shown in Figure 7.2. In 2000, 2005, 2007 and 2011, low ozone columns were measured above Eureka when the polar vortex was overhead. These years are shown in colour, while the other measurement years are shown in grey. Low ozone coincides with low NO_2, low T_{490K}, and time periods when the instruments are sampling inside the polar vortex.

For 23 February - 21 March 2011 (days 54-80), the DOAS instruments sample lower stratospheric air inside the polar vortex. OClO DSCDs of 0.8-2.0x10^{14} mol/cm^2 are within the range of previous elevated Arctic OClO measurements [e.g., *Tornkvist et al.*, 2002], suggesting chlorine activation. All elevated OClO DSCDs, from 8-22 March 2011 (days 67-81) and 2-5 March 2007 (days 61-64), are measured inside the polar vortex when the high-latitude minimum temperature (calculated by *Manney et al.* [2011], not shown here) is below the threshold for PSC formation (T_{NAT}) (Figure 7.2d). During the period of elevated OClO in 2011, ozone, NO_2, and T_{490K} all reach minima in the 11-year record, with ozone values of 247 DU (237 DU) measured by the GBS (SAOZ) on 18 March (day 77).

High OClO measurements do not always correspond with local $T_{490K} < T_{NAT}$, because the time-scale for vortex mixing (~5-7 days) is shorter than the time-scale for chlorine deactivation (~weeks)*. OClO is approximately representative of the ClO_x ($ClO + 2xCl_2O_2 + Cl + OClO$) concentration and not of local conditions†. Therefore, the ClO_x lifetime is the effective lifetime for OClO concentration. The lifetime of ClO_x is on the order of weeks in the winter polar vortex and drops when ozone is completely depleted, due to increasing efficiency of the $Cl+CH_4$ reaction. Circulation once around the vortex takes only ~5-7 days. Therefore, ClO_x will circulate around the vortex several times during its lifetime. Inside the vortex, there are regions

* This argument for the dependence of OClO on local temperature is based on a personal communication with Markus Rex on 4 November, 2011.

† Note that OClO is also dependent on SZA and Br_y, but these effects are small.

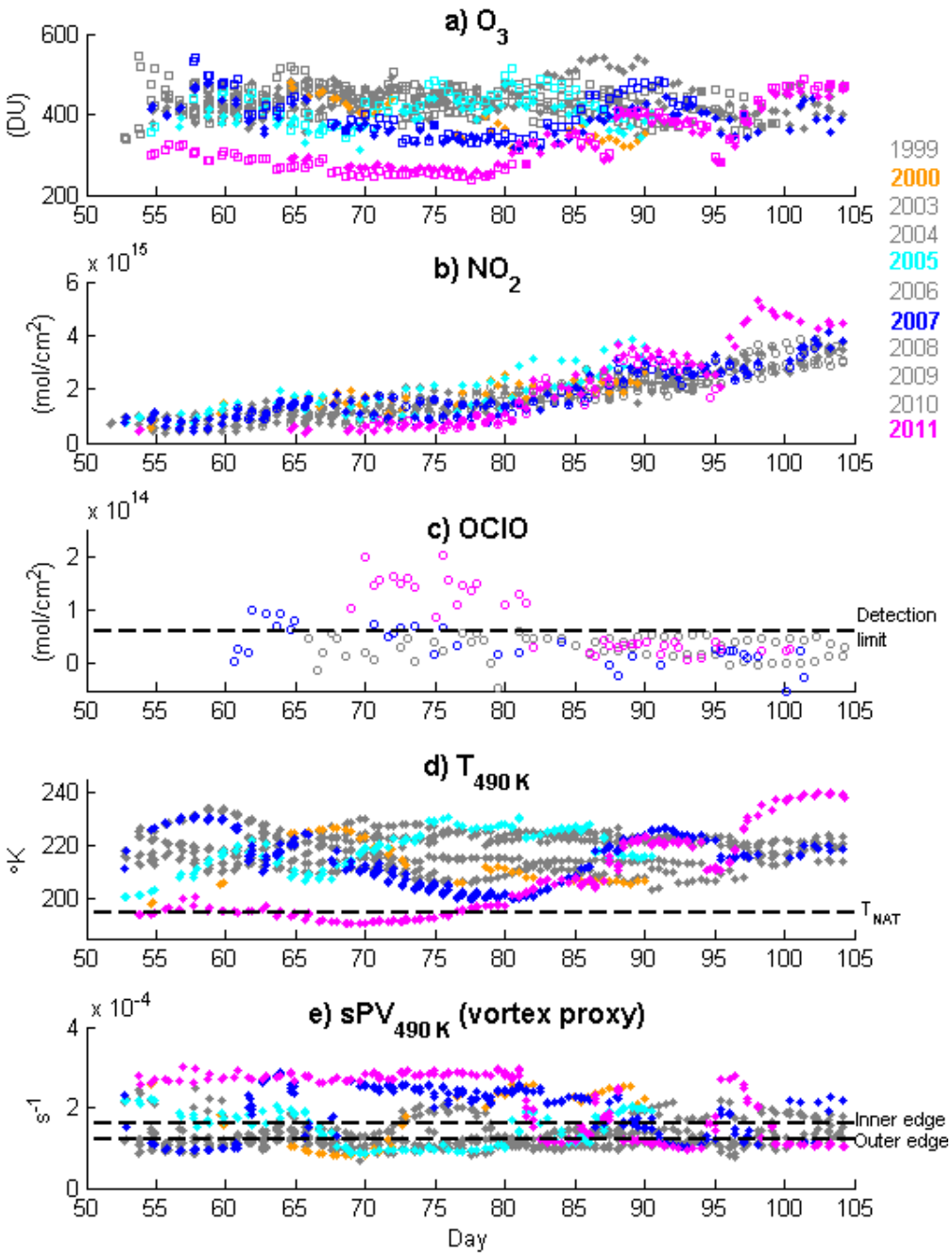

Figure 7.2**:** Timeseries of measurements and dynamical parameters along the DOAS line-of-sight for 1999-2011 versus day of year. Year 2000 is shown in orange, 2005 in cyan, 2007 in blue, 2011 in magenta, and all other years are shown in grey. (a) Ozone total columns measured by the GBS (closed diamonds) and SAOZ (open squares). (b) NO_2 partial columns (17 km to top of atmosphere) measured by GBS-vis (closed diamonds) and GBS-UV (open circles). (c) OClO DSCDs measured by the GBS. (d) T_{490K} and (e) sPV_{490K}.

of high and low temperatures, which are often relatively fixed spatially and are determined by large scale atmospheric waves. Therefore, during its lifetime, ClO_x will typically pass through both warm and cold regions of the vortex. Thus chlorine activation depends on whether ClO_x has passed through a cold region in its history, which is more dependent on the vortex minimum temperature than on the local temperature.

After 22 March 2011 (day 81), the instruments primarily sample the lower stratosphere outside the polar vortex. During this period, ozone and NO_2 increase to levels that are normal in the context of the 11-year data record. On 5 April (day 87) and 28 March (day 95), ozone and NO_2 columns and T_{490K} decrease sharply, as the instruments sample airmasses inside the vortex. After 5 April (day 95), T_{490K} and NO_2 increase to maxima in the 11-year dataset. This increase is investigated further in Section 7.3.

7.2.2 Dynamical and Chemical Contributions to Low Ozone

As is evident in the DOAS timeseries (Figure 7.2), 2011 is extremely different from previous years. Ozone, NO_2, and OClO measurements taken inside the polar vortex ($sPV_{490K} > 1.6x10^{-4}$ s^{-1}) for days 55-80 (24 February to 19/20 March) were selected to investigate this further. The time period was limited in order to reduce the impact of seasonal variation on the results. NO_2 measurements were scaled to local solar noon using a photochemical model [*McLinden et al.*, 2000], initialized with Eureka ozonesonde profiles from the nearest available date. See Appendix E for a description of the photochemical model.

Figure 7.3 shows histograms of ozone, NO_2, and OClO for 1999-2010 (grey) and 2011 (transparent with thick black outline). In 2011, the mean vortex ozone column measured by the GBS (SAOZ) is 28±13% (32±14%) lower than the mean column from other years, where the error denotes the 1σ statistical uncertainty. Similarly, GBS-vis (GBS-UV) NO_2 is 46±30% (45±27%) lower and GBS OClO is three times higher in 2011 than in previous years.

The unusually low 2011 ozone and NO_2 columns are a result of both chemistry and transport, which contribute approximately equally to year-to-year total ozone column variability in the Arctic [*Tegtmeier et al.*, 2008]. Figure 7.4 shows the correlation between vortex ozone/NO_2 measurements and the local T_{490K}. Correlation between ozone and local lower stratospheric

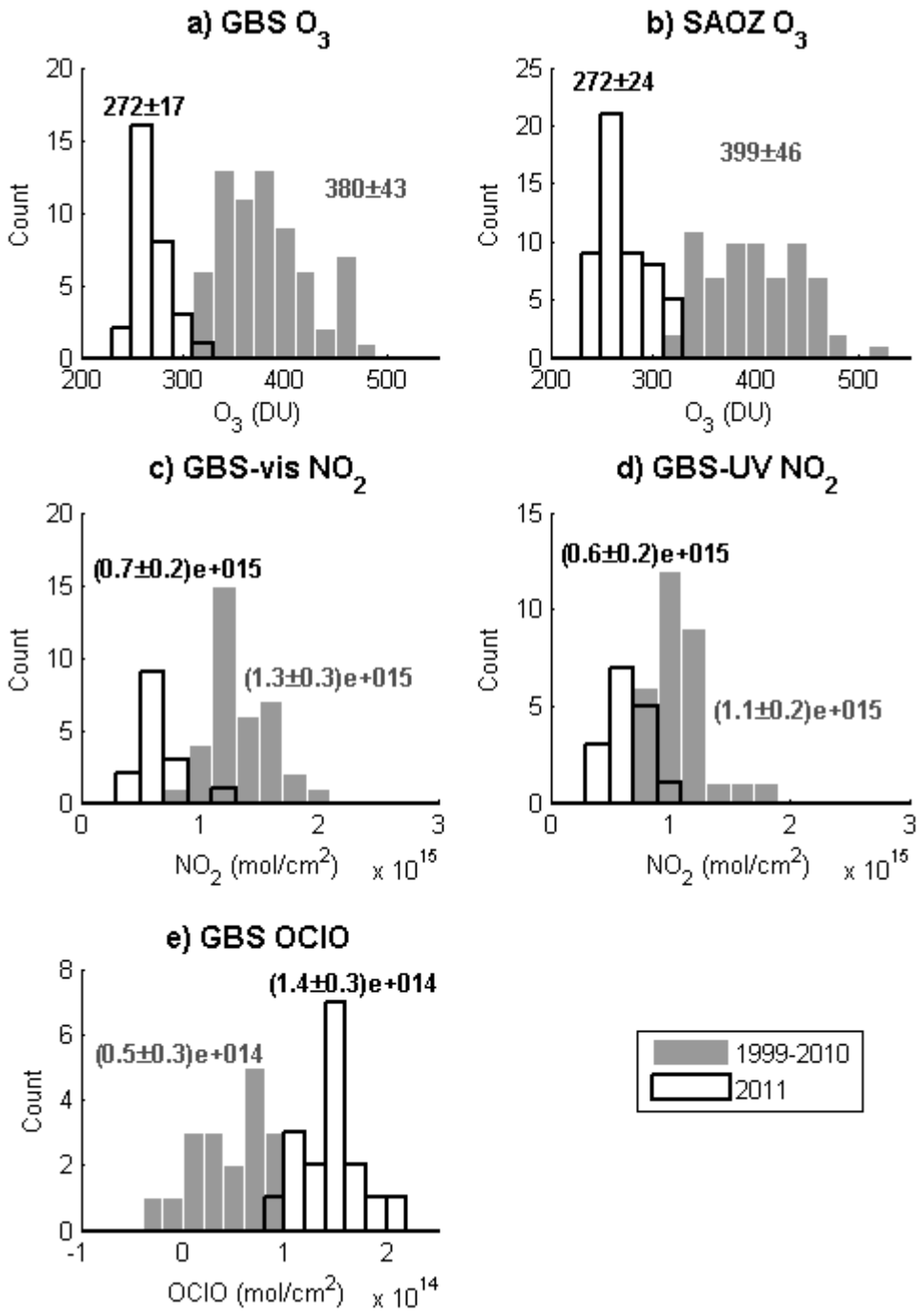

Figure 7.3**:** Histograms of (a) GBS ozone, (b) SAOZ ozone, (c) GBS-vis NO_2, (d) GBS-UV NO_2, and (e) GBS OClO. Measurements were taken inside the vortex for days 55-80 (24 February to 19/20 March), with 1999-2010 in gray and 2011 transparent with thick black lines. N±M denotes the average (N) and 1σ standard deviation (M) in the measurements.

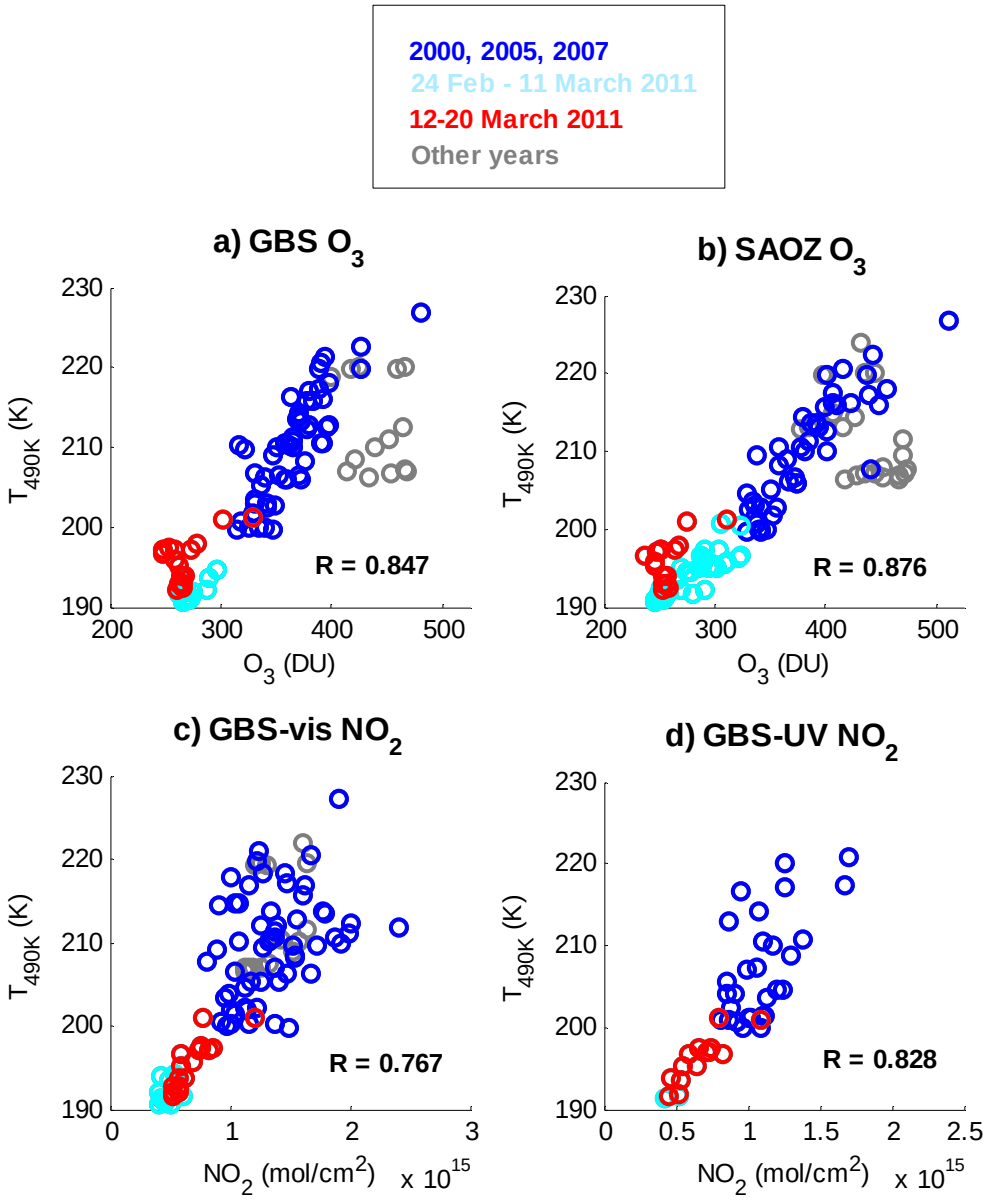

Figure 7.4: Correlation between T_{490K} and (a) GBS ozone, (b) SAOZ ozone, (c) GBS-vis NO_2, and (d) GBS-UV NO_2. Measurements were taken inside the vortex for days 55-80 (24 February to 19/20 March). Data are shown for 2000, 2005, 2007 (blue); 24 February to 11 March 2011 (cyan); 12-20 March 2011 (red); and other years (grey). R and R_{all} are correlation coefficients for data indicated by blue only and for all data in the figure, respectively.

temperature has been observed in previous studies and points to replenishing of ozone through vertical descent, horizontal mixing across the vortex edge, and adiabatic compression of the column, which all increase with higher stratospheric temperatures [e.g., supplementary material in *Manney et al.*, 2011, and references therein]. In the present study, the strongest correlation between ozone and T_{490K} was observed when data were excluded from years with few vortex measurements above Eureka (grey) and 12-20 March 2011 (days 71-79, red). The outliers for years with few vortex measurements may result from errors in matching T_{490K} and sPV_{490K} to measurements both spatially and temporally when the vortex edge is near Eureka. For 12-20 March 2011, the ozone columns remain low, despite the rise in the local T_{490K}. This deviation from the correlation between T_{490K} and ozone suggests chemical depletion [supplementary material in *Manney et al.*, 2011]. NO_2 is also correlated with local lower stratospheric temperature, as has been observed in previous studies [e.g., *Pommereau and Goutail*, 1988; *Dirksen et al.*, 2011]. The correlation for NO_2 is weaker than for ozone, likely due to the seasonal increase in NO_2 as it is released from night-time reservoirs. Vortex ozone and NO_2 measurements were also correlated (not shown here), with R values of 0.6-0.7.

Investigation of complementary datasets provides further evidence of chemical ozone depletion and denitrification above Eureka in 2011. For 9-18 March (days 68-77), low HNO_3 and $ClONO_2$ columns over Eureka were measured by the CANDAC Bruker FTIR [*Lindenmaier et al.*, 2012]. This suggests that the extremely low NO_2 columns measured during the same period are not caused by conversion to HNO_3 or $ClONO_2$. During this period of low $ClONO_2$, HNO_3, and NO_2, OClO DSCDs are elevated, reinforcing that chlorine remains activated. Furthermore, PSCs were measured above Eureka with the CANDAC Rayleigh-Mie-Raman Lidar between 8-18 March (days 67-77) [*Lindenmaier et al.*, 2012]. These measurements agree with photochemical model runs by *Manney et al.* [supplementary material, 2011], which indicate that prolonged denitrification by sedimentation of PSCs delayed chlorine deactivation, leading to the record ozone loss.

7.2.3 Ozone Loss Estimates

Ozone loss was estimated using the passive subtraction method [e.g., *Manney et al.*, 1995b; *WMO*, 2003; *Feng et al.*, 2007]. Passive ozone was calculated using the SLIMCAT 3-

dimensional offline chemical transport model [*Chipperfield*, 2006], where ozone was treated as a passive dynamical tracer with no chemistry. The SLIMCAT passive ozone columns were calculated daily directly above Eureka and interpolated to the measurement times of the instruments. The passive subtraction method involves subtracting measured ozone columns from modeled passive ozone columns. The DOAS (GBS and SAOZ) instruments sample along a line-of-sight along the path of scattered light to the instrument. When the vortex edge is near Eureka, spatial and temporal differences between SLIMCAT passive ozone and DOAS measurements could lead to errors in the ozone loss estimates.

Agreement between SLIMCAT passive ozone and the DOAS instruments was assessed using December ozonesonde measurements. The DOAS instruments do not operate during polar night, before chemical ozone depletion occurs, and therefore could not be compared directly with the passive ozone. The mean difference and standard error for SLIMCAT passive ozone minus ozonesonde total columns was 89.3±11.4 DU for December 2001-2011. This bias may be due in part to the coarse vertical resolution in the SLIMCAT model for altitudes below the 350-K potential temperature level [*Feng et al.*, 2007]. Inside the vortex, for spring 1999-2011, the mean difference for GBS (SAOZ) minus ozonesonde total columns was -31±4 DU (-28±3 DU). To correct for these offsets, 119 DU was subtracted from the SLIMCAT passive ozone prior to the analysis.

Figure 7.5 shows the timeseries of the ozone loss calculations for 1999-2011. Outlying ozone loss estimates may occur when the DOAS and SLIMCAT data sample different airmasses. Furthermore, for large ozone columns, GBS measurements are biased low compared with other instruments [*Adams et al.*, 2012a], which can lead to overestimates of ozone loss. For most of the timeseries, the largest ozone loss is observed in 2011. The average ozone loss for 12-20 March 2011 (days 71-79) was 27% (29%) or 99 DU (108 DU), as estimated from GBS (SAOZ) data using the passive tracer technique. During this period, ozone columns were very low and there was evidence of chemical ozone loss above Eureka in supporting datasets, as discussed in Sections 7.2.1 and 7.2.2. The maximum percent ozone loss was calculated from GBS (SAOZ) data on 5 April 2011 (day 95) at 47% (47%) or 250 DU (251 DU).

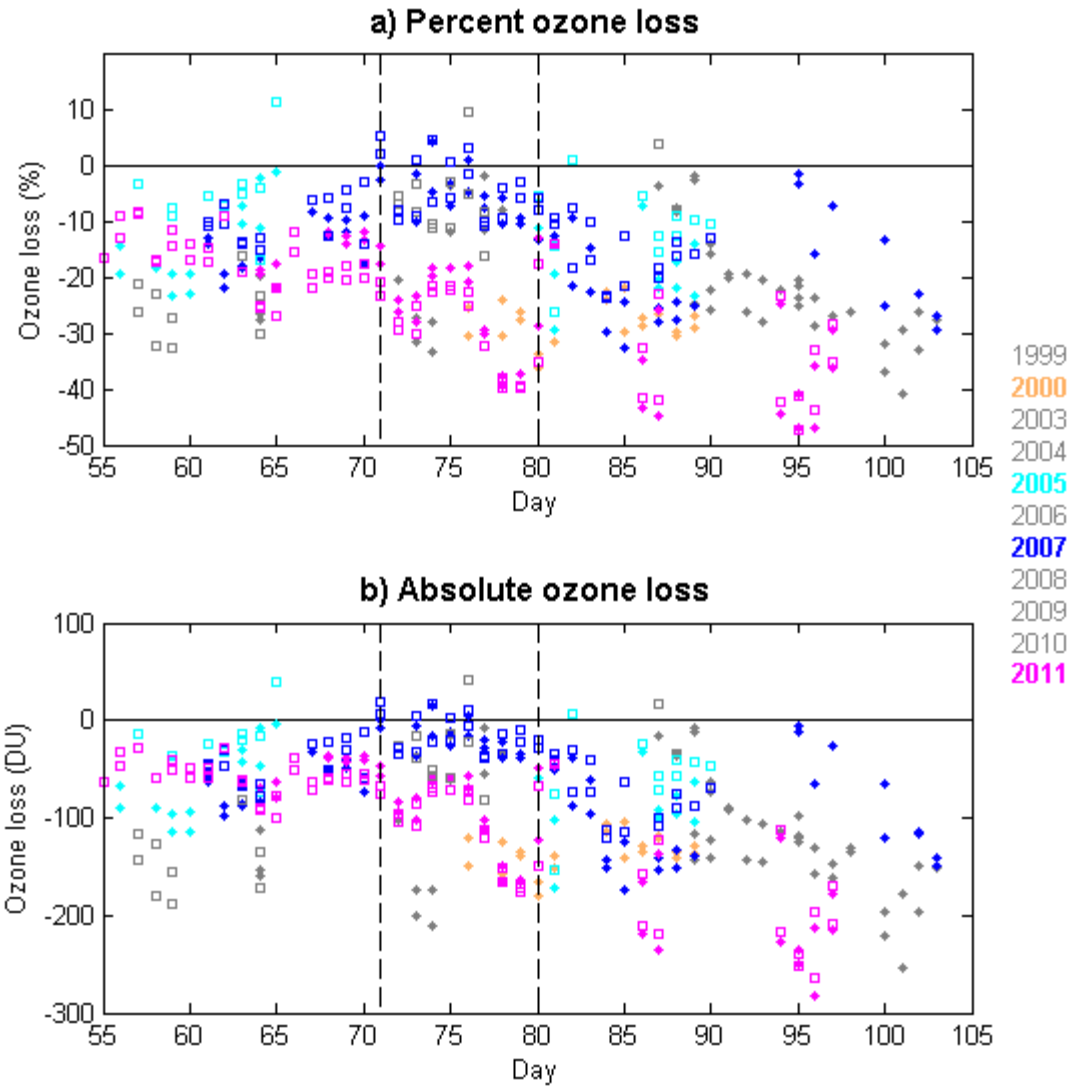

Figure 7.5: Timeseries of (a) percent ozone loss and (b) absolute ozone loss for 1999-2011 versus day of year for GBS (closed circles) and SAOZ (open squares). Ozone loss was calculated using the passive tracer technique. Year 2000 is shown in orange, 2005 in cyan, 2007 in blue, 2011 in magenta, and all other years are shown in grey. The black line indicates zero. The black dashed lines enclose days 71-79 (March 11/12 to 19/20).

7.3 Ozone and NO_2 during the Vortex Breakup

During the break-up of the strong spring 2011 vortex, ozone and NO_2 columns above Eureka were unusual. This section describes these measurements and interprets them using satellite, model, and dynamical datasets. Temperature, PV, EqL, and tropopause height are all considered. N_2O and aerosol are also used as dynamical tracers, with low N_2O/aerosol indicating vortex airmasses and high N_2O/aerosol indicating mid-latitude airmasses [e.g., *Ruth et al.*, 1994; *Harvey et al.*, 1999].

7.3.1 The 2011 Stratospheric Warming above Eureka

April/May 2011 were dynamically atypical above Eureka, compared with previous years. GEOS-5 temperatures and EqLs above Eureka for 2004-2011 are shown in Figure 7.6, with 2011 in red and 2004-2010 in grey. Temperatures above Eureka (panel a) in 2011 reached the largest values in the record from 400 to 1000 K. Average April/May 2011 temperatures (blue line) are also larger than average temperatures in previous years (black line) for 400-1400 K. EqLs (panel b) in 2011 reach < 20°N for 850-900 K and ~450 K, suggesting the transport of lower-latitude air above Eureka.

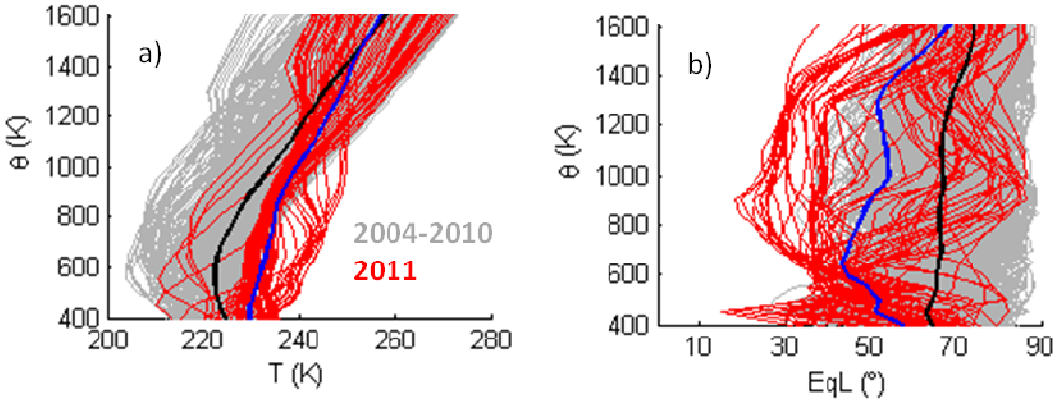

Figure 7.6: Profiles of (a) temperature and (b) EqL from GEOS-5 DMPs at 12:00 UTC above Eureka for 1 April to 31 May. Grey and black lines indicate individual profiles and average profiles, respectively for 2004-2010. Red and blue lines indicate individual profiles and average profiles, respectively for 2011.

Figure 7.7 shows the evolution of temperature (panel a) and EqL (panel b) above Eureka during spring 2011. The white contour lines indicate sPV = 1.6×10^{-4} s^{-1}, which can be used to approximate the inner vortex edge. Air masses within these contour lines are considered to be inside the polar vortex. On 4 April, the vortex is above Eureka from 550 to 1450 K. Above 600 K, the vortex is displaced from Eureka on 5 April. This coincides with an increase in temperature and a sharp decrease in EqL to values < 50°. This suggests that the vortex has moved away and that an anticyclone has moved overhead. EqLs are < 30° for ~10-20 April for ~700-1100 K. The altitude range of low EqL narrows throughout April and May, remaining only at ~600 K by the end of May. At altitudes below 600 K, the vortex moves away from Eureka until 13 April. Following 13 April, there are intervals of high and low EqL, suggesting that vortex and midlatitude air are moving above Eureka. The three dates of interest, labelled A, B, and C, are discussed in Sect. 7.3.2.

The timeseries of NO_2 and ozone columns above Eureka from GBS ground-based measurements, OMI satellite overpasses, and GMI model output is shown in Figure 7.8. Good agreement is observed between the three datasets. Note that for NO_2, only qualitative agreement is expected because the columns were sampled at different SZAs and for different altitude ranges.

In years prior to 2011 (grey), NO_2 columns rise throughout the spring as hours of sunlight at Eureka increase (SZAs decrease). This is expected as NO_x is released from night-time reservoirs through photochemical reactions. Ozone columns decrease throughout the spring, as descent in the polar vortex ceases.

In 2011 (red), NO_2 and ozone columns are significantly different from previous years. In all three datasets, NO_2 and ozone columns are small on 4 April, when the polar vortex briefly passes above Eureka. On 8 April (event A), NO_2 increases to values that are nearly two times larger than in previous years in all three datasets. After 8 April, NO_2 columns decrease for ~4 days in the GBS and OMI data and ~8 days in the GMI data. Throughout the rest of April/May, NO_2 columns gradually return to values that are comparable to past years. Ozone total columns also increase in early April, reaching maxima on ~10-15 April. They then decrease throughout the rest of April/May. Between 15 April and 20 May, ozone columns decrease by more than

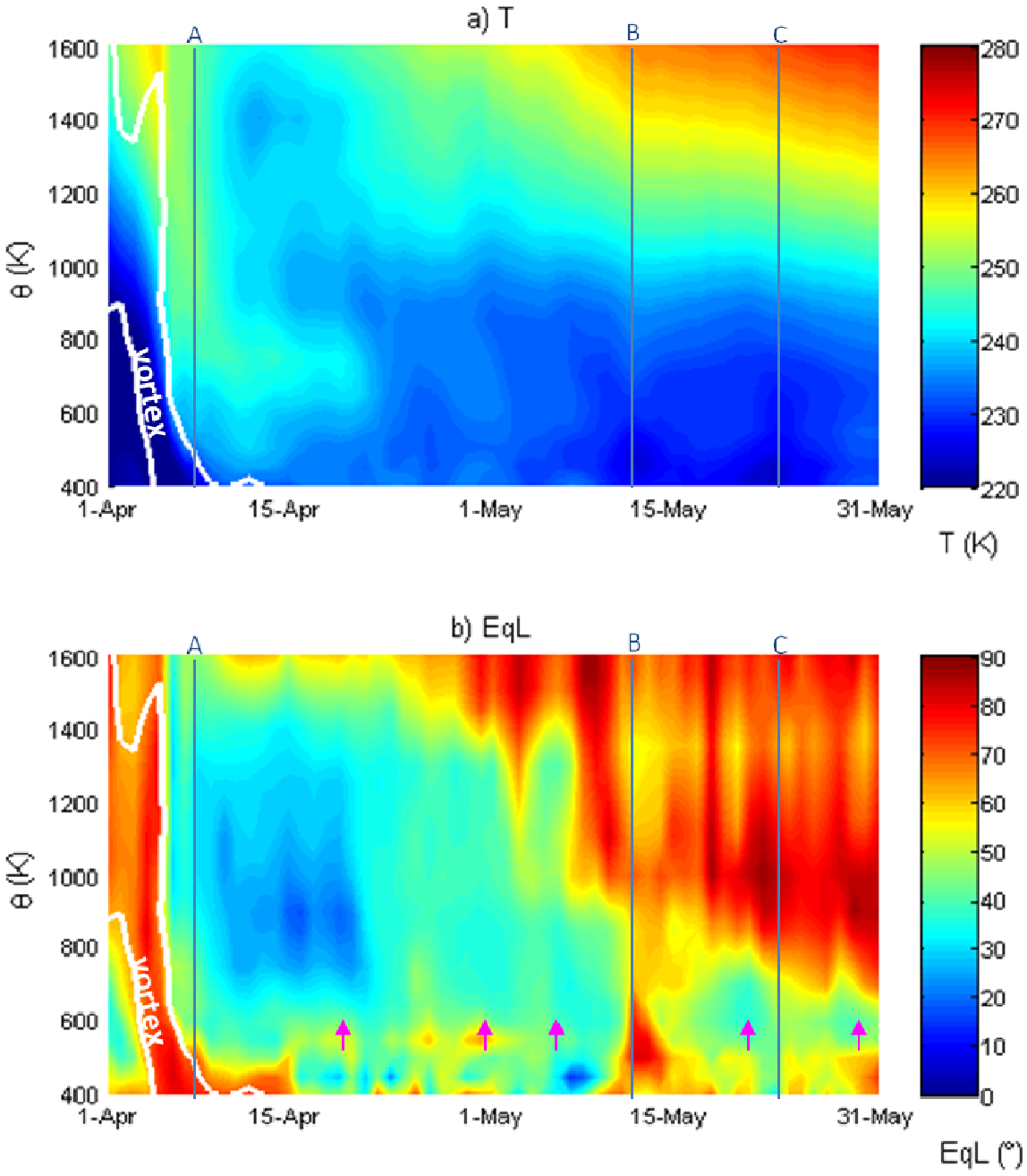

Figure 7.7: Daily (a) temperature (T) and (b) EqL. Thick white lines indicate boundaries of the polar vortex determined by sPV = 1.6×10^{-4} s^{-1}. Data are from GEOS-5 DMPs at 12:00 UTC above Eureka and are plotted against day in 2011 and potential temperature. The blue vertical lines labelled A, B, C indicate 8 April, 13 May, and 22 May respectively. Magenta arrows indicate 20 April, and 1, 6, 21, and 29 May.

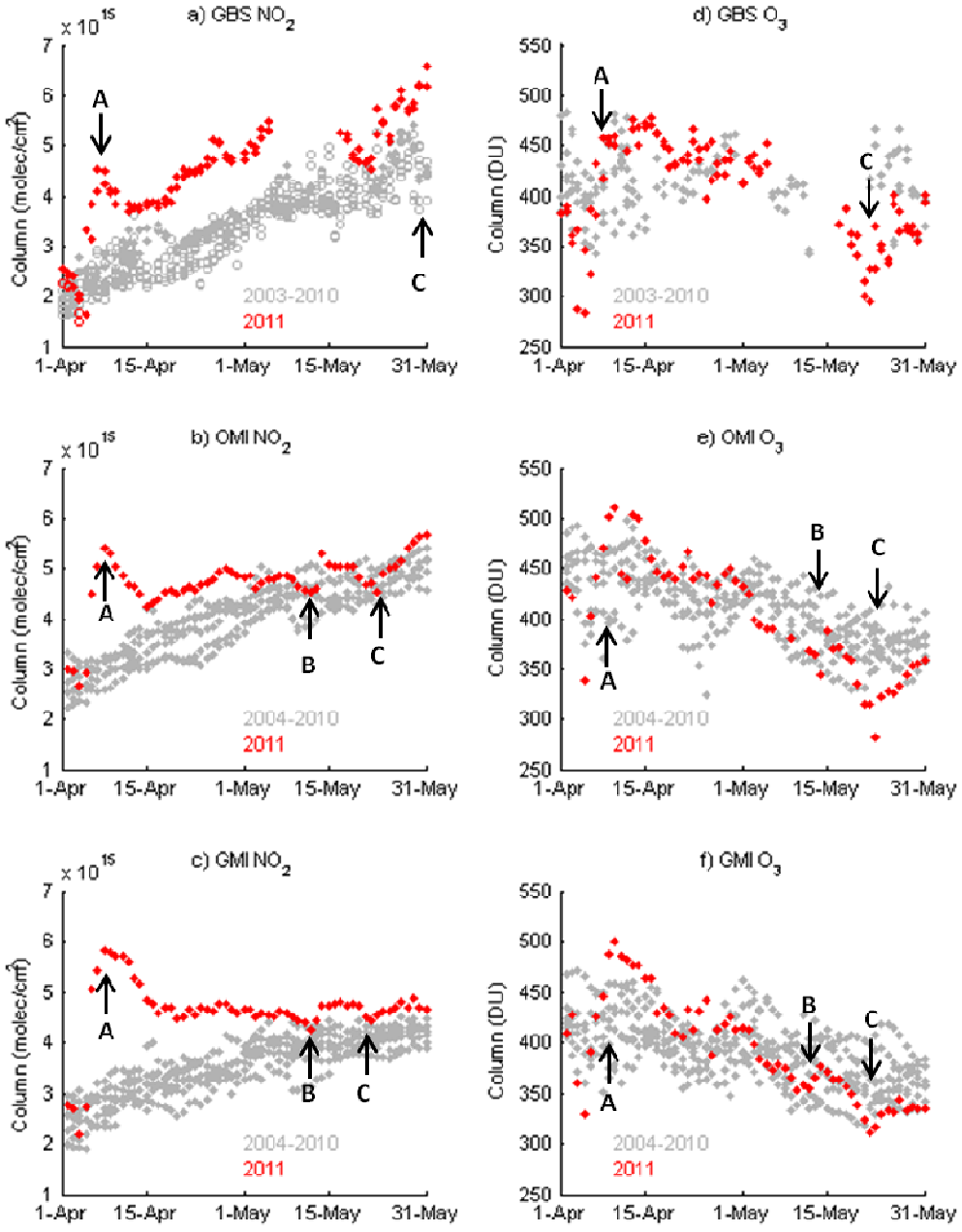

Figure 7.8: Timeseries of NO_2 and ozone columns above Eureka for 1 April to 31 May in 2011 (red) and in previous years (grey). (a) GBS-vis (closed circles) and GBS-UV (open circles) NO_2 partial columns (17 km to top of atmosphere) and (b) GBS ozone total columns, both measured both in morning and evening twilights. (c) OMI stratospheric NO_2 columns and (d) OMI total ozone columns averaged daily within 500 km of Eureka. (e) NO_2 and (f) ozone total columns from daily GMI output from 10-10:30 am local time at Eureka. Note that there are fewer ozone than NO_2 GBS measurements because, for some years, spring-time dedicated BrO measurements excluded the visible wavelengths used to measure ozone. Black arrows labelled A, B, C indicate 8 April, 13 May, and 22 May, respectively.

100 DU in all three datasets. Ozone columns are small on 13-14 May (event B) and 22-23 May (event C), reaching < 300 DU in the GBS and OMI datasets.

Figure 7.9 shows trace gas and aerosol profiles measured by OSIRIS within 500 km of Eureka for 2002-2011 and sampled directly above Eureka from the GMI runs for 2004-2011. For OSIRIS, number density versus altitude, with approximate potential temperature indicated on the right y-axis, and VMR versus potential temperature are both shown.

Average 2011 OSIRIS NO_2 number densities (panel a) are larger and peak ~4 km lower in the atmosphere (blue) than in previous years (black). For 500-1400 K, average NO_2 VMRs in both OSIRIS (panel b) and GMI (panel c) datasets are enhanced. Above 1400 K, OSIRIS and GMI NO_2 profiles differ. The large peak in the GMI NO_2 VMRs at ~850 K corresponds to the NO_2 maximum observed in the column datasets around 8 April (Figure 7.8, event A). This is not observed in the OSIRIS profiles because OSIRIS was turned off during 4-11 April for annual satellite maintenance.

Ozone number densities and VMRs (panels d, e, f) in 2011 (blue) are on average smaller than in previous years (black), with lower average number densities (panel d) for ~11-35 km (~350-1050 K). 2011 average VMRs (panels e, f) are smaller than in previous years for potential temperature levels below 1300 K in OSIRIS profiles and below 1500 K in GMI profiles.

OSIRIS aerosol extinction and GMI N_2O VMRs (panels g, h) are larger in 2011 than previous years above ~650 K, suggesting transport of lower-latitude air over Eureka. Average GMI NO_x ($NO+NO_2$) (panel i) is larger in 2011 than previous years for potential temperature levels > 500 K. For potential temperature levels > 700 K, many of the April/May 2011 NO_x profiles are larger than in any other year.

The evolution of 2011 GMI NO_2, ozone, N_2O, and NO_x VMRs and of OSIRIS NO_2 and ozone VMRs above Eureka is shown in Figure 7.10 and Figure 7.11. Good qualitative agreement is observed between GMI and OSIRIS, with both datasets reproducing the gradual descent of low ozone VMRs through the middle stratosphere. This decrease in ozone and events A, B, and C are discussed in Sect. 7.3.2.

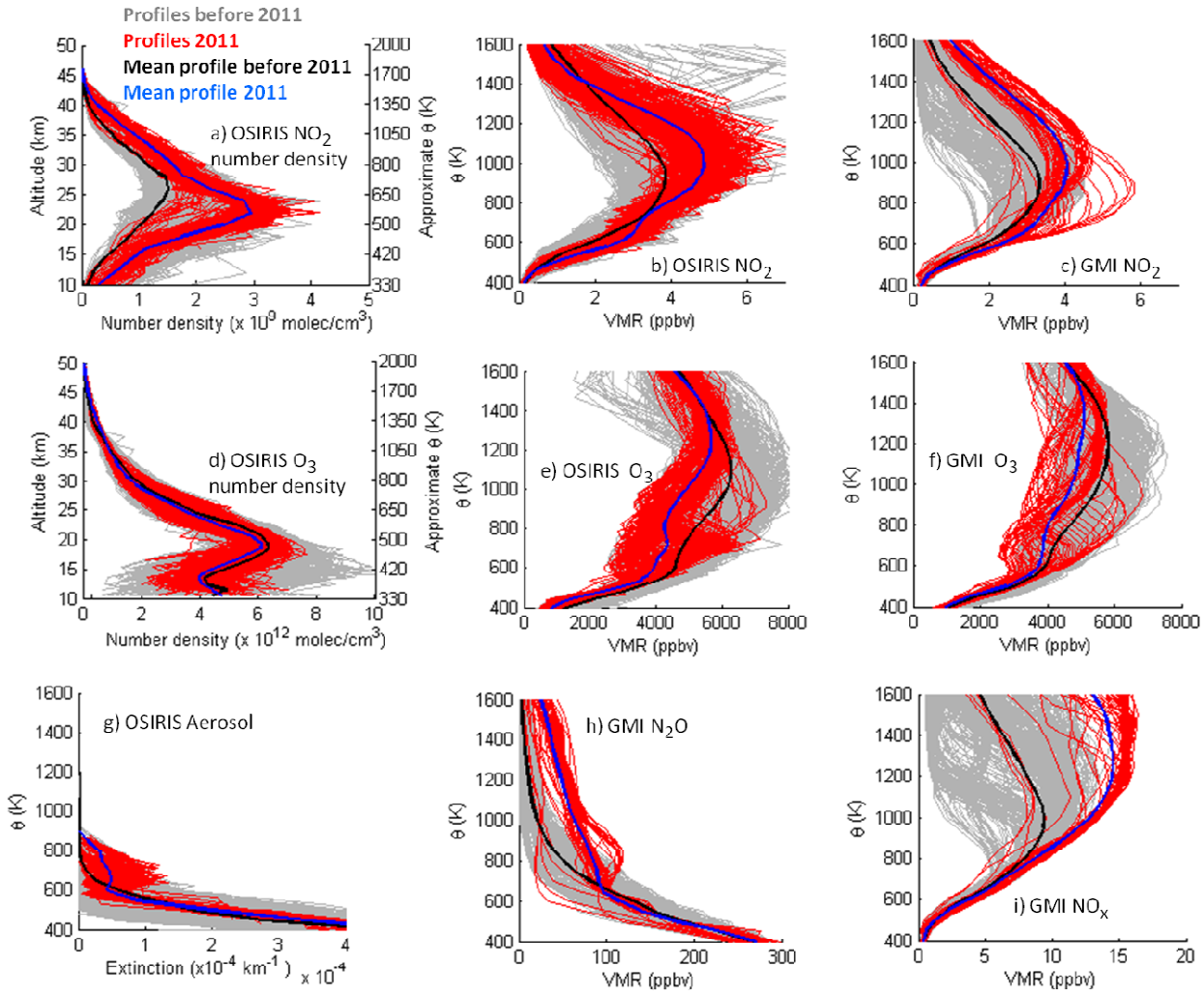

Figure 7.9: Profiles from OSIRIS and GMI above PEARL for 1 April to 31 May. Grey and black lines indicate individual profiles and average profiles, respectively for years before 2011 (2002-2010 for OSIRIS and 2004-2010 for GMI). Red and blue lines indicate individual profiles and average profiles, respectively for 2011. OSIRIS profiles have 25-km tangent heights within 500 km of Eureka. GMI profiles are sampled daily directly above Eureka. OSIRIS number densities are plotted against measurement altitude (left y-axis) and approximate potential temperature (right y-axis). OSIRIS and GMI VMRs and OSIRIS aerosol extinction profiles are plotted against potential temperature.

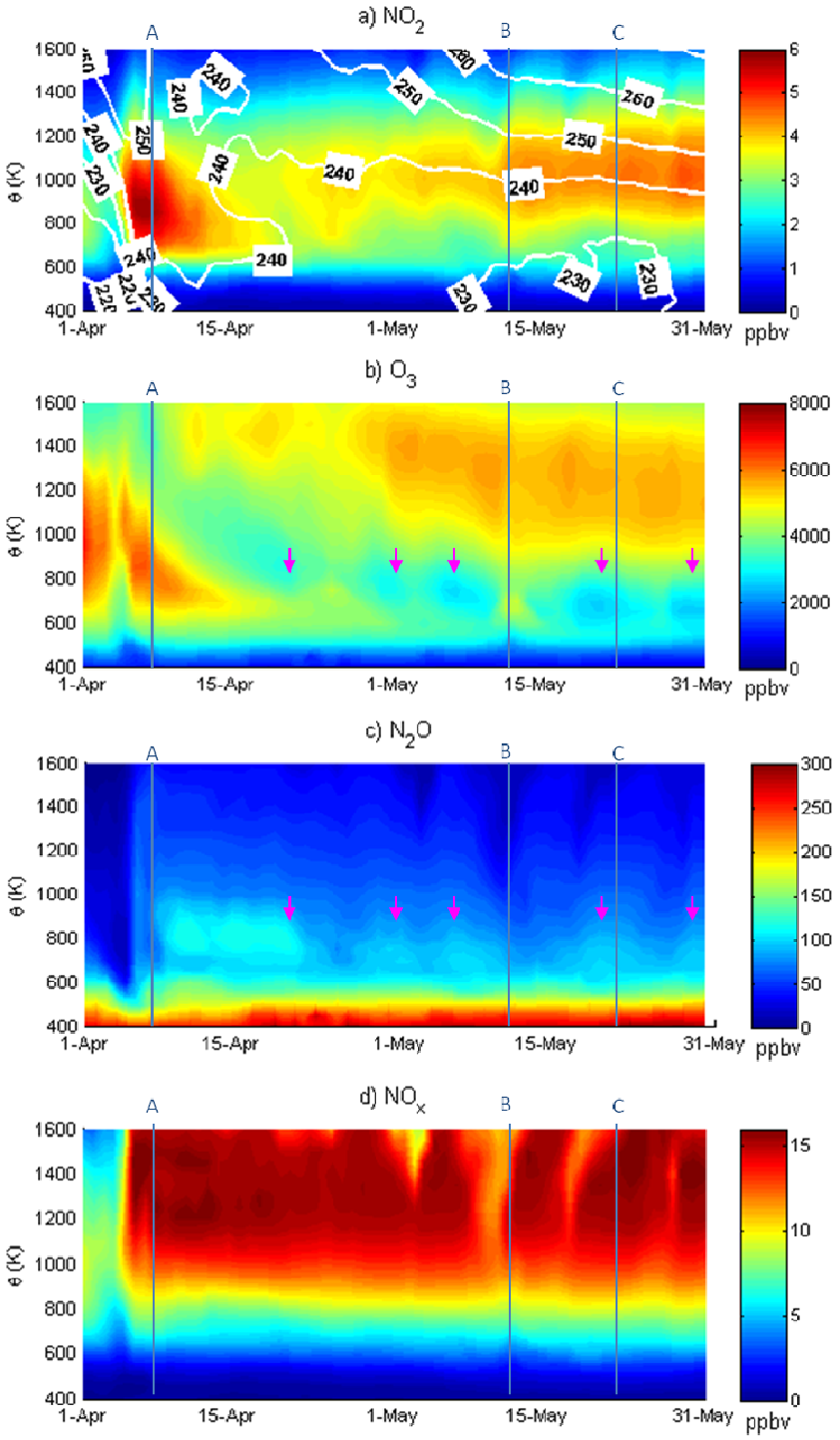

Figure 7.10: Curtain plots of GMI (a) NO_2, (b) ozone, (c) N_2O, and (d) NO_x VMRs above Eureka for 1 April to 31 May 2011. White contours indicate temperature in K. The blue vertical lines labelled A, B, C indicate 8 April, 13 May, and 22 May, respectively. Magenta arrows indicate 20 April and 1, 6, 21, and 29 May.

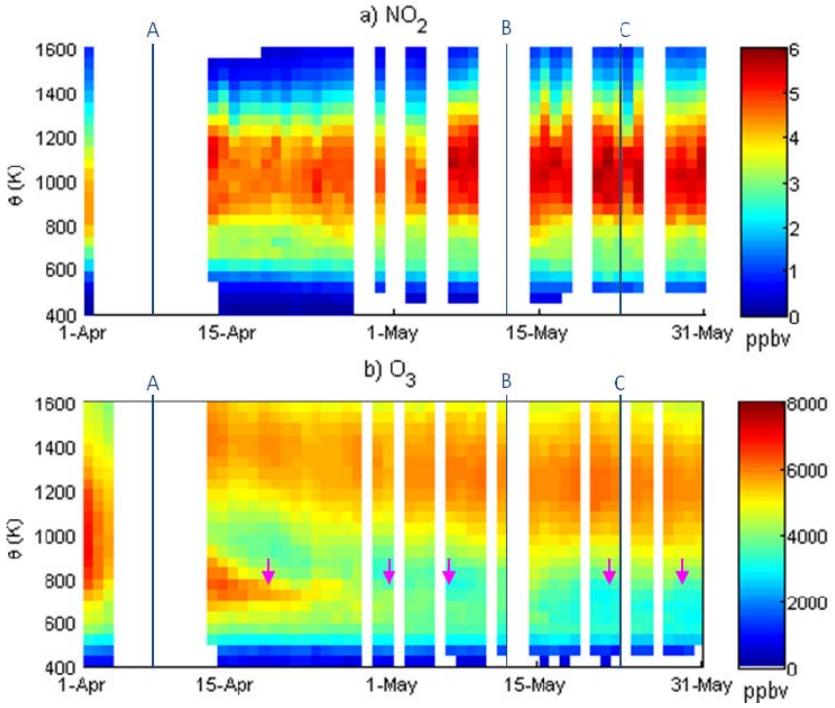

Figure 7.11: Curtain plots of OSIRIS NO_2 and ozone daily average VMR profiles within 500 km of Eureka for 1 April to 31 May 2011. The blue vertical lines labelled A, B, C indicate 8 April, 13 May, and 22 May, respectively. Magenta arrows indicate 20 April and 1, 6, 21, and 29 May.

7.3.2 Discussion

7.3.2.1 NO_2 Maximum on 8 April

A large maximum in NO_2 was observed in the column timeseries on 8 April (Figure 7.8, event A). NO_2 increases can be caused by transport of NO_x-rich air from lower latitudes or from higher altitudes. There is evidence of NO_x transport in the enhanced GMI NO_x VMRs above 500 K (Figure 7.9i). Furthermore, NO_2 can increase via changes in the partitioning between NO and NO_2, as shown in Equations 1.4 and 1.5. The production of NO_2 from Equation 1.5 has a strong temperature dependence [e.g., *Sander et al.*, 2011]. Therefore, high temperatures can cause the NO/NO_2 ratio to change by up to a factor of two, favouring NO_2. Furthermore, increases in ozone VMRs also favour NO_2 production. Large GMI NO_2 VMRs (Figure 7.10a) correspond to high temperatures (white contours) and ozone VMRs (Figure 7.10b), suggesting that chemistry

does indeed play a role in the enhanced NO_2. The relative roles of chemistry and transport on the large NO_2 columns are further investigated using maps of OMI total columns and GMI VMRs at various potential temperature levels. Note that OSIRIS data are not used here because OSIRIS was turned off for 4-11 April.

Figure 7.12 shows polar maps of OMI ozone total columns and NO_2 stratospheric partial columns for 1, 3, 5, and 8 April 2011. sPV=1.6×10^{-4} s^{-1} contours, which approximately enclose the polar vortex, are also shown for various potential temperature levels. On 1 April, low ozone and NO_2 columns reside over Siberia and Northern Europe, coinciding with the location of the polar vortex. On 3 and 5 April, low ozone and NO_2 columns stretch toward Eureka as the polar vortex shifts and stretches overhead. By 8 April, the low NO_2 columns have stretched into a "C" shape, with Eureka and very high NO_2 columns at its centre. The low in ozone remains across the pole from Eureka. Low NO_2 columns coincide approximately with the location of the polar vortex in the middle stratosphere (~850 K), while low ozone columns coincide with the lower stratosphere vortex (~500 K). This is consistent with the differences between the altitudes of the ozone and NO_2 number density maxima (Figure 7.9a,d).

Polar maps of GMI NO_2, ozone, N_2O, and NO_x for 1, 3, 5, and 8 April at 600 K (~22 km) are shown in Figure 7.13. This is the altitude of the NO_2 number density maximum above Eureka in 2011 according to OSIRIS profiles (Figure 7.9a) and therefore yields the largest contribution to the NO_2 columns. The polar vortex (bounded by the white PV contours), encloses low NO_2, ozone, N_2O, and NO_x. At this level, the vortex moves over Eureka on 5 April as a pocket of warm air (enclosed by the purple contour line) appears between Alaska and Siberia. On 8 April (event A), the pocket of warm air is situated directly above Eureka and the vortex has stretched away. The movement of this warm air corresponds to enhanced NO_2, suggesting chemical production from NO_x. However, NO_x is also enhanced above Eureka on 8 April, suggesting that transport also plays a role. North of Eureka, NO_x-rich air is located along the vortex edge, where N_2O is low, suggesting the downward transport of higher-altitude NO_x-rich and N_2O-poor air.

Transport of lower-latitude air, indicated by high N_2O, is located southwest of Eureka. This suggests that the NO_x-rich air that has been transported downward along the vortex edge was drawn over Eureka between the polar vortex to the north and lower-latitude air to the south.

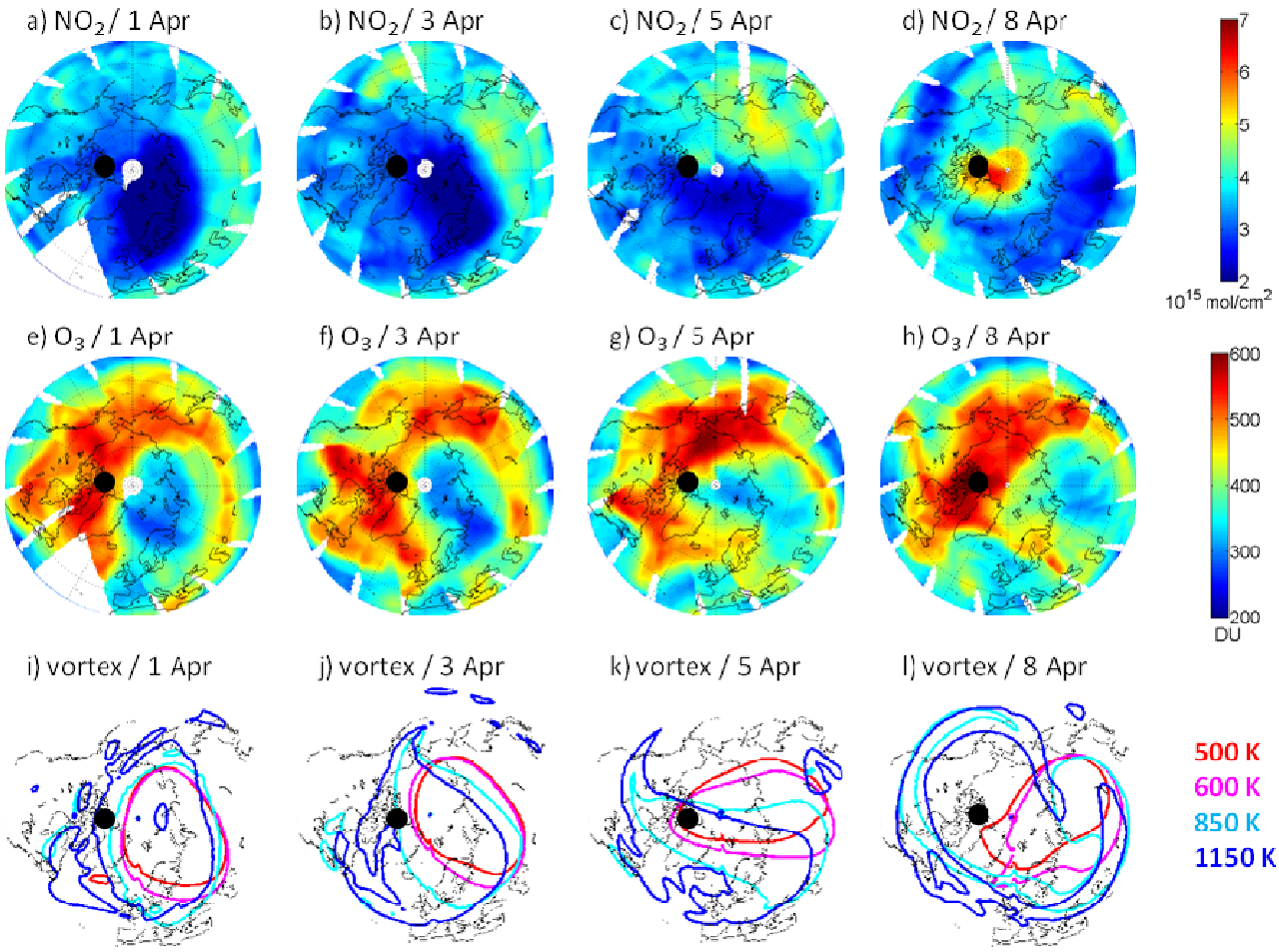

Figure 7.12: Polar maps of OMI NO_2 stratospheric columns (top row), OMI ozone total columns (middle row) and the approximate inner vortex edge (bottom row) for 1, 3, 5 and 8 April 2011. Eureka is indicated by the black circle. The inner vortex edge is approximated at sPV = 1.6×10^{-4} s^{-1} for 500-K (red), 600-K (magenta), 850-K (cyan), and 1150-K (blue) potential temperature levels.

Figure 7.14 shows polar maps of GMI NO_2, ozone, N_2O and NO_x at 850 K (~32 km), the altitude of the large increase in GMI NO_2 VMRs (Figure 7.9c). This is above the NO_2 maximum, but number densities are still large enough to contribute significantly to total columns (Figure 7.9a). Low-latitude air, indicated by high N_2O, is transported from Northern Europe, wrapping counter-clockwise around the vortex. By 8 April, the vortex has shifted to a "C" shape, with high temperatures and NO_2 at its center, directly above Eureka. NO_x is slightly enhanced indicating

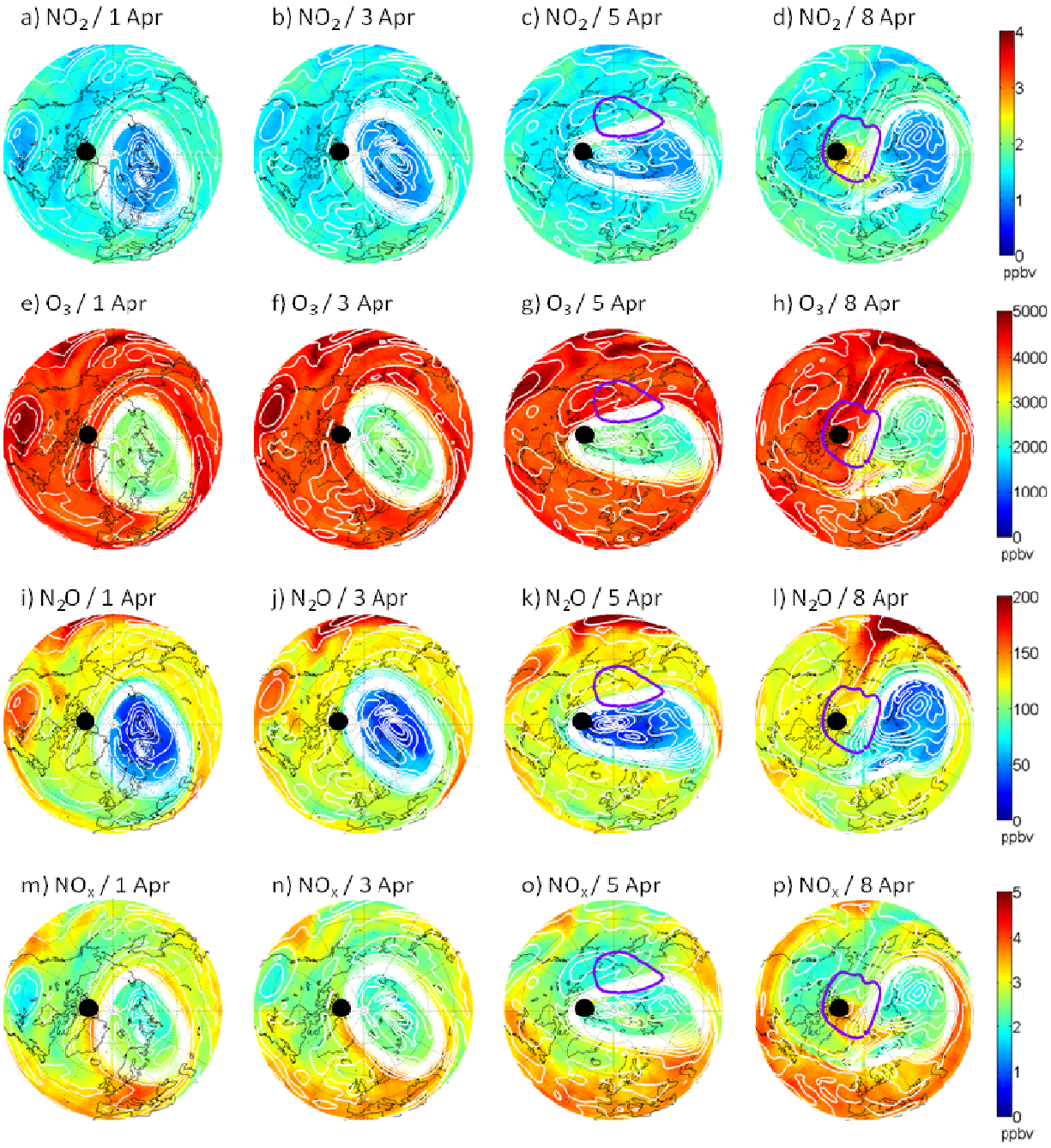

Figure 7.13: Polar maps at the 600-K (~22-km) potential temperature of GMI NO_2 (top row), ozone (top middle row), N_2O (bottom middle row), and NO_x (bottom row) VMRs for 1, 3, 5 and 8 April 2011. White lines indicate PV contours. The area enclosed by the purple contour indicates T > 235 K. Eureka is indicated by the black circle.

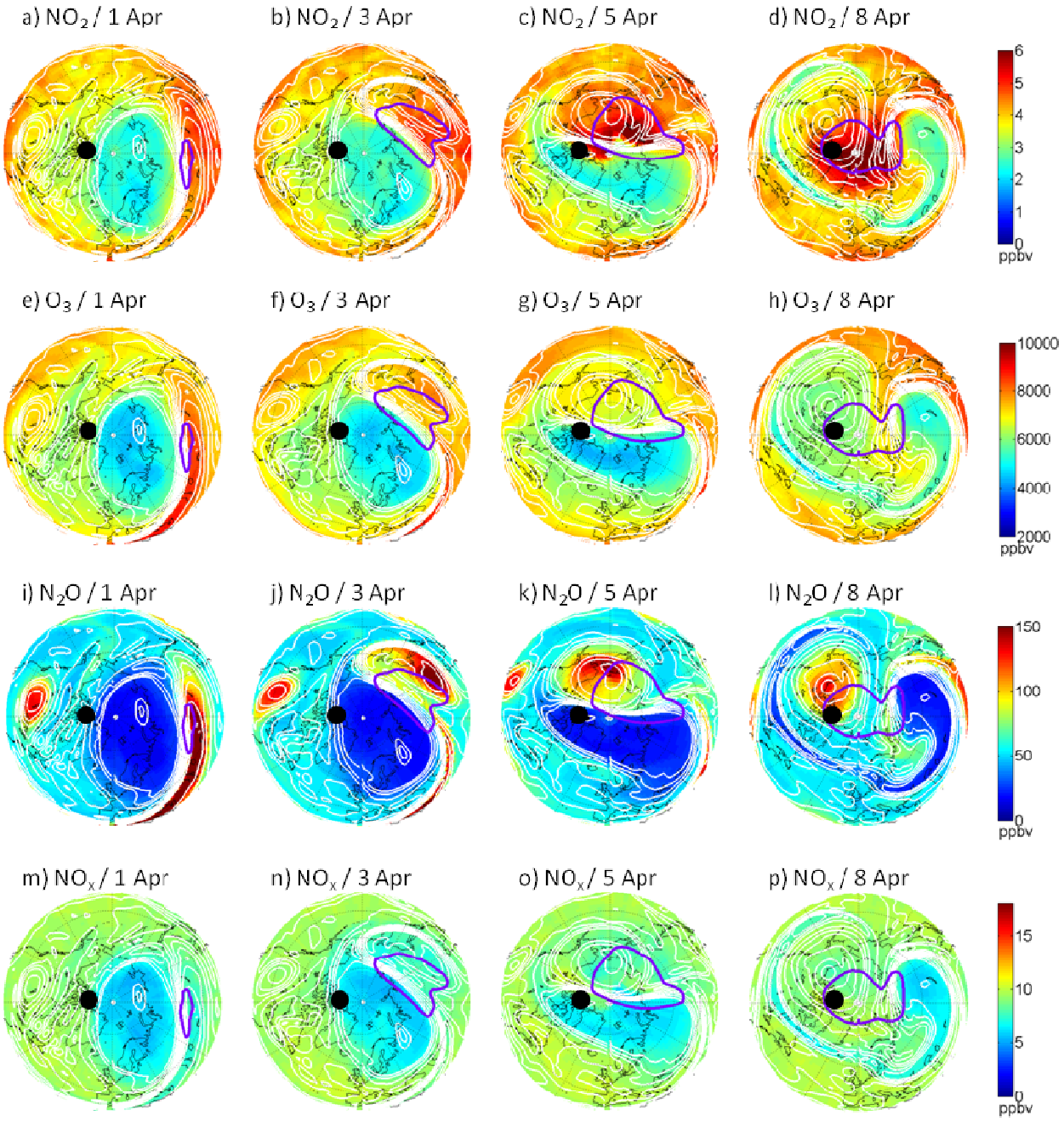

Figure 7.14: As for Figure 7.13 at the 850-K (~32-km) potential temperature level. The area enclosed by the purple contour indicates T > 245 K. Note that colour scales are different from Figure 7.13.

some transport, but the NO_2 increase at this level appears to be dominated by production from NO, due to the high temperatures.

Polar maps of GMI NO_2, ozone, N_2O and NO_x at 1150 K (~37 km) are shown in Figure 7.15. Number densities at this elevation are large enough to contribute significantly to total column amounts, even though they are well above the NO_2 maximum (Figure 7.9a). High N_2O and NO_x, enclosed by PV contour lines, move from lower latitudes to Eureka, indicating the transport of lower-latitude air within an anticyclone. NO_2 peaks above Eureka on 8 April and coincides also with high temperatures, again suggesting some chemical production of NO_2 from NO.

Thus at 600 K, 850 K, and 1150 K, high NO_2 values are concentrated above Eureka on 8 April (event A). Enhanced NO_2 coincides with high temperatures at all levels, suggesting the chemical production of NO_2 from NO. Additionally, transport of NO_x-rich air masses is also observed over Eureka, with descent of higher-altitude air masses at 600 K and transport of lower-latitude air masses at 1150 K. Therefore, the high NO_2 values observed above Eureka on 8 April were caused by both chemistry and transport.

7.3.2.2 FrIAC and Middle-Stratosphere Ozone Loss

In early April, an anticyclone transported lower-latitude air above Eureka (see Sect. 7.3.2.1). This section presents evidence that this anticyclone became frozen-in until at least the end of May and that gas-phase ozone loss occurred within it.

The early evolution of this anticyclone is evident in the GMI fields at 850 K, shown in Figure 7.14. Low-latitude air, identified by high N_2O enclosed by PV contours, wraps counter-clockwise around the polar vortex. By 8 April, the edge of this anticyclone is above Eureka. Ozone inside the anticyclone on 1 April is high, as is consistent with the transport of ozone-rich lower-latitude air. However, as the anticyclone moves over Eureka, the ozone VMRs within it decrease, suggesting chemical ozone loss.

The anticyclone persists at 850 K in PV contours and high N_2O throughout April, as shown in Figure 7.16. OSIRIS and GMI ozone agree well, both showing filaments of high-ozone lower-latitude air being drawn around the anticyclone, with low ozone within the anticyclone. The

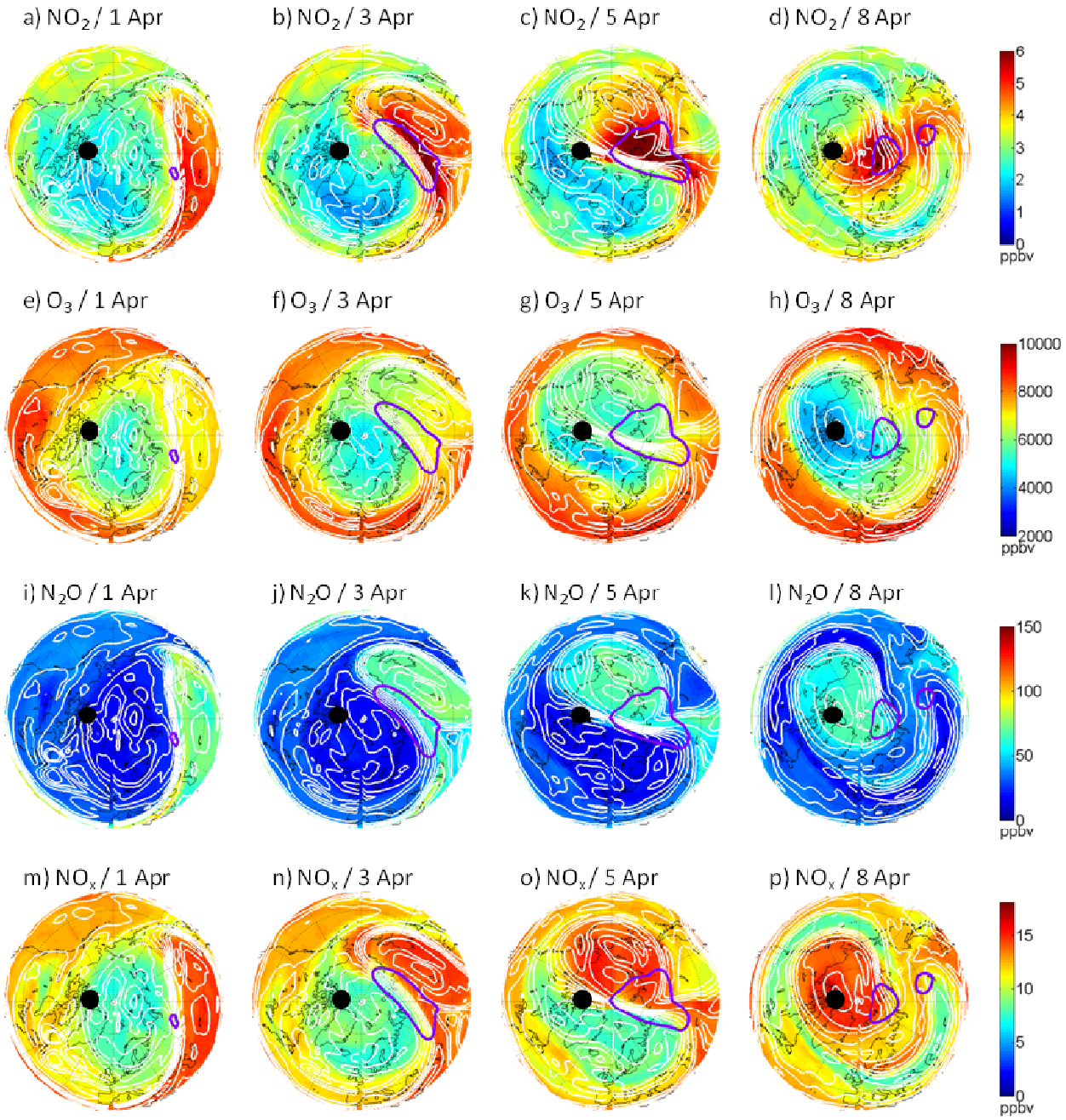

Figure 7.15: As for Figure 7.13 at the 1150-K (~37-km) potential temperature level. The area enclosed by the purple contour indicates T > 260 K. Note that colour scales are different from Figure 7.13.

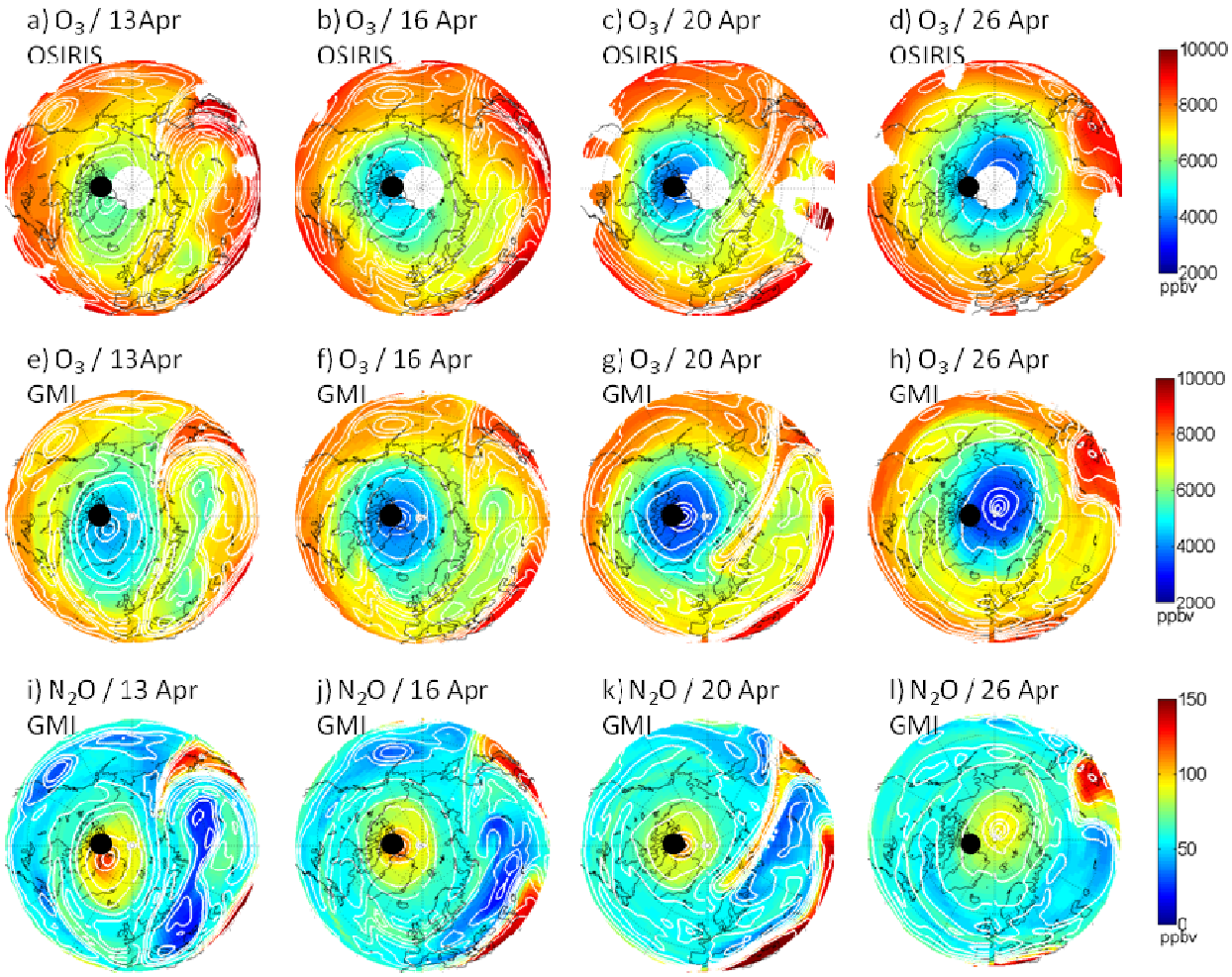

Figure 7.16: Polar maps at the 850-K potential temperature level of OSIRIS ozone (top row), GMI ozone (middle row), and GMI N2O (bottom row) VMRs for 13, 16, 20, 26 April 2011. White lines indicate PV contours.

anticyclone at 850 K remains centred above Eureka for 13-20 April and is then advected by easterly winds and begins to rotate around the pole, with the edge of the anticyclone remaining above Eureka.

This feature persists until at least the end of May, suggesting a 2011 FrIAC. This is evident in Figure 7.10c. N_2O is enhanced until ~20 April (magenta arrow) as the anticyclone sits above Eureka. Following the advection of the anticyclone, N_2O maxima pass over Eureka on 1, 6, 21,

and 29 May (magenta arrows). These large N_2O values coincide with low EqLs (Figure 7.7b, magenta arrows) and low ozone (Figure 7.10b). Therefore the FrIAC has remained intact until at least the end of May in both tracer and dynamical fields.

Low ozone VMRs (< 4000 ppbv) are observed in GMI (Figure 7.10b) and OSIRIS (Figure 7.11b) data above Eureka. The small ozone VMRs are first observed at ~1400 K on 6 April and gradually descend and are centered at ~1150 K on 12 April, ~850 K on 22 April, and ~700 K on 7 May, reaching altitudes at which ozone number densities are larger (Figure 7.9d). Therefore the total ozone columns above Eureka decrease (Figure 7.8b, d, f).

The reduction in ozone was due to NO_x-driven ozone loss within the FrIAC. SZAs above PEARL range from ~75-95° on 1 April to ~60-80° on 31 May and are therefore frequently within the 80-95° SZA range for which catalytic ozone destruction cycles (dominated by NO_x) lead to maximum ozone loss [*Sinnhuber et al.*, 1999]. Furthermore, NO_x was enhanced in 2011 compared with previous years (Figure 7.9i).

Ozone loss above Eureka was estimated using the passive tracer technique [*Manney et al.*, 1995b; *WMO*, 2003; e.g., *Konopka et al.*, 2007] with ATLAS passive ozone, which was initialized on 1 December 2010 with MLS ozone data. Figure 7.17a shows the 2011 timeseries of ozone VMRs at 600 K from ATLAS passive ozone, OSIRIS, and GMI. Good agreement is observed between OSIRIS and GMI. The low ozone VMRs in early April coincide with the vortex passing above Eureka.

The timeseries of ATLAS passive ozone minus OSIRIS and GMI ozone at 600 K is shown in Figure 7.17b. Prior to 15 April, much of the variability in ozone loss can be attributed to transport, as the polar vortex passes briefly over Eureka and an anticyclone moves overhead (see Sect. 7.3.2.1). On 15 April 2010, ozone losses are at ~2 ppmv. This is likely due to NO_x cycles since 1 December 2010, as low EqL values (see Figure 7.7b) suggest that the air mass at 600 K originates from lower latitudes. Around 12/13 May (labelled B) an isolated vortex air mass passes over Eureka (see Sect. 7.3.2.3). Therefore, the reduction in ozone loss during this period is also due to transport. The maximum ozone loss at 600 K since 1 December 2010 is observed on 20 May 2011 at 4.4 ppmv (61%) for GMI and 4.2 ppmv (58%) for OSIRIS. Ozone losses of ~3 ppmv between 1 December 2010 and 1 May 2011 are comparable to the losses observed by

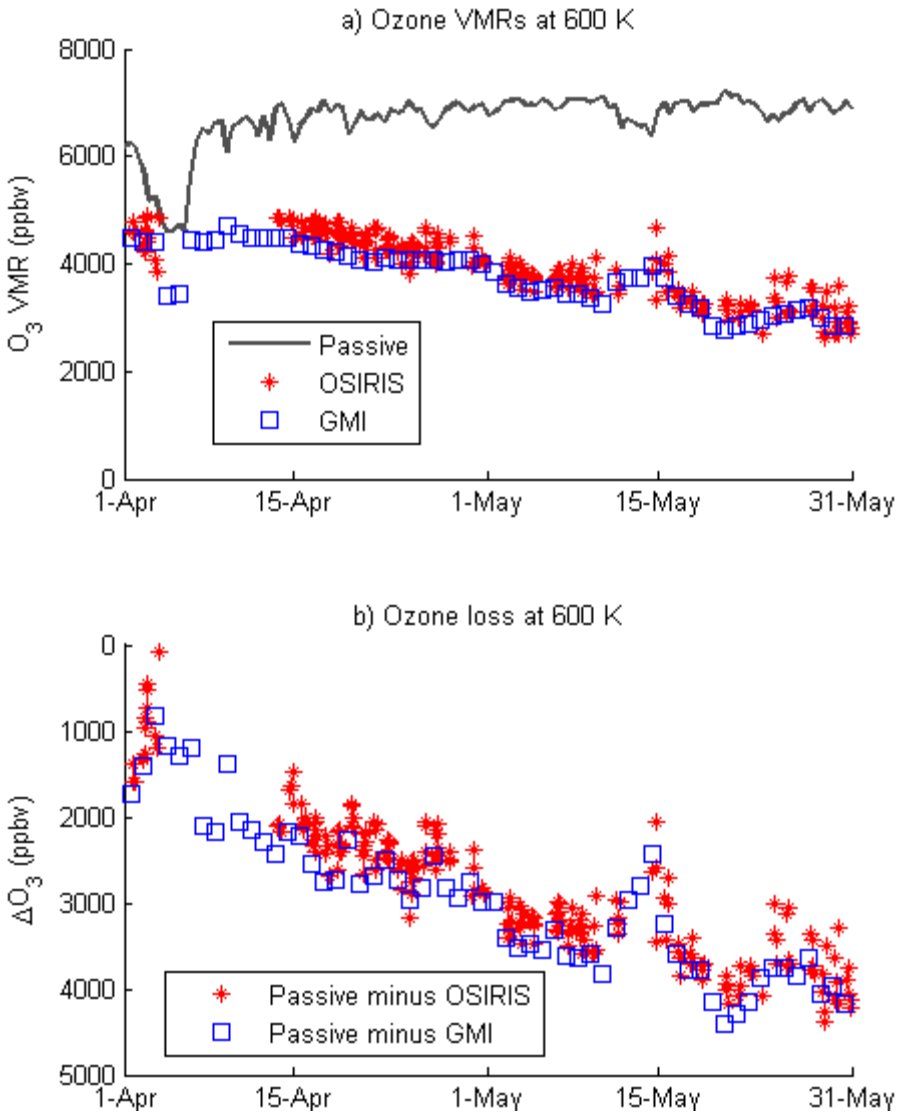

Figure 7.17: (a) 2011 ozone VMRs at the 600-K potential temperature level from ATLAS passive ozone above Eureka (black line), OSIRIS ozone measurements within 500 km of Eureka (red stars), and GMI ozone above Eureka (blue squares). (b) Ozone loss calculated for ATLAS passive ozone minus OSIRIS (red stars) and ATLAS passive ozone minus GMI (blue squares). The black arrow labelled B indicates 13 May. The grey dashed lines indicate 15 April and 20 May.

Konopka et al. [2007] at 600 K between 1 December 2002 and 1 May 2003. Konopka et al. [2007] attributed this ozone loss to transport of NO_x during several stratospheric warmings earlier in the year.

Ozone loss due to NO_x chemistry above Eureka were calculated between 1 April and 31 May for 2004-2011, using GMI monthly average O_x loss rates due to $NO_2 + O \rightarrow NO + O_2$. Note that these average loss rates include processes inside the polar vortex in early April and within the vortex fragment on 12/13 May, as well as within the FrIAC. NO_x-driven ozone loss was larger in 2011 than in any previous year from the tropopause to 18 hPa (~700 K) and above 6.9 hPa (~1000 K). At 37 hPa (~600 K), there was 1.2 ppmv of ozone loss due to NO_x chemistry above Eureka in 2011 compared with 0.7-0.9 ppmv in previous years. This is smaller than the apparent ~2 ppmv of ozone lost between between 1 April and 31 May 2011 above Eureka, calculated using ATLAS passive ozone and GMI and OSIRIS ozone VMRs (Figure 7.17). This suggests that some of the ozone loss observed in the passive ozone timeseries occurred before the air mass reached Eureka. This is consistent with Figure 7.14 and Figure 7.15, which show ozone VMRs decreasing as air masses are transported from lower latitudes toward Eureka.

7.3.2.3 Vortex Fragment on 12/13 May

Ozone and NO_2 columns decreased on 12/13 May (Figure 7.8, event B). These low columns coincided with high EqLs, low temperatures (Figure 7.7, event B), and low ozone VMRs at ~500 K (Figure 7.10b, event B). Figure 7.18 shows the evolution of this event at 500 K through OSIRIS ozone and aerosol and GMI ozone and N_2O. Good agreement is observed between GMI and OSIRIS ozone. Low ozone, N_2O, and aerosol enclosed by PV contour lines indicate that vortex air sits across the pole from Eureka on 26 April. This air mass is stretched and a fragment is ejected over Northern Europe in early May. On 13 May, the fragment passes over Eureka, leading to the low ozone column measurements. This is consistent with other studies that have observed confined fragments of vortex air during and following the spring stratospheric final warming [e.g., *Hess*, 1991].

7.3.2.4 Ozone Mini-Hole on 22/23 May

Minimum ozone columns of 294 DU, 283 DU, and 311 DU are observed above Eureka in the GBS, OMI and GMI datasets around 22/23 May 2011 (Figure 7.8, event C). On 22 May, a large pocket of low ozone (< 300 DU) is observed in OMI total column data over the pole and Ellesmere Island (Figure 7.19, top row). This coincides with low GMI ozone VMRs and high

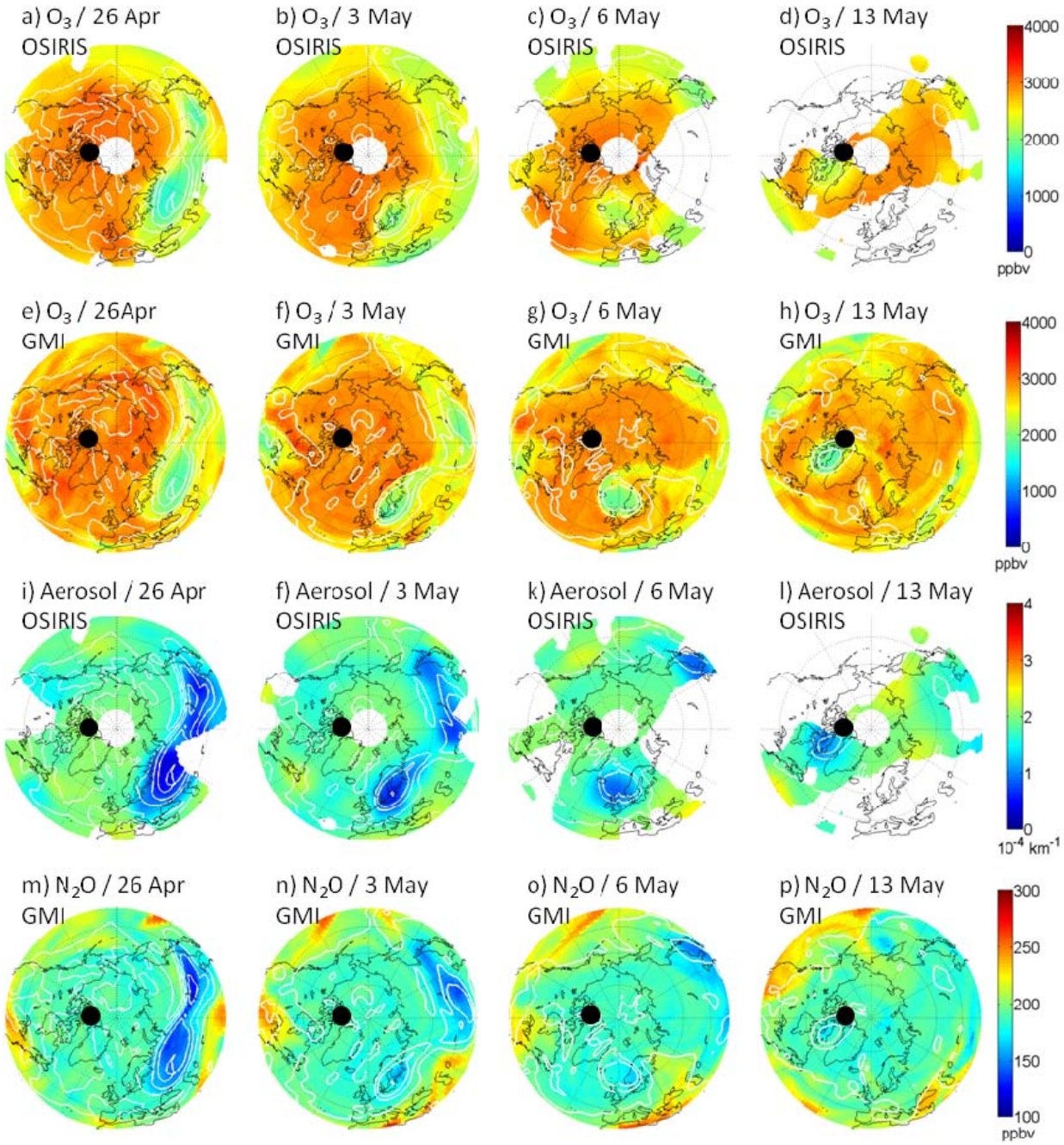

Figure 7.18: Polar maps at the 500-K potential temperature level of OSIRIS ozone (top row), GMI ozone (top middle row) VMRs, OSIRIS aerosol extinction at 750 nm (bottom middle row), and GMI N_2O VMR (bottom row) for 26 April and 3, 6, 13 May 2011. White lines indicate PV contours.

GMI N_2O VMRs at 450 K (Figure 7.19, middle rows), suggesting the transport of air masses containing low ozone. Equivalent latitudes above Eureka (Figure 7.7b) are < 50° for the 350-700 K level on 22 May. This suggests that ozone-poor lower-latitude air has been transported above Eureka. Furthermore, the tropopause (Figure 7.19, bottom row) is elevated, suggesting that more ozone-poor tropospheric air is contributing to the total column. This is consistent with the formation of an ozone mini-hole, which can lead to large decreases in the ozone column over a short time period [*Peters et al.*, 1995; *James*, 1998; e.g., *Hood et al.*, 2001; *Iwao and Hirooka*, 2006]. Ozone mini-holes are caused by dynamical processes [e.g., *Hood et al.*, 2001], usually resulting from a combination of the transport of lower-latitude ozone-poor air masses and a rise in the tropopause, as shown for event C.

7.4 Summary

Unprecedentedly low ozone and NO_2 columns were measured above Eureka in 2011 and correspond to elevated OClO, suggesting chlorine activation and ozone depletion. The OClO and NO_2 measurements complement the work of *Lindenmaier et al.* [2012] who measured ozone, HNO_3, HCl, $ClONO_2$, and HF above Eureka with the CANDAC Bruker FTIR and provide further evidence of denitrification above Eureka. Vortex ozone and NO_2 total columns from 1999-2011 are correlated with the lower stratospheric temperature above Eureka. This indicates that transport also contributes to the low ozone and NO_2 measurements because, e.g., downwelling is reduced when temperatures are low. However, this correlation is weaker for 12-20 March 2011, pointing to chemical ozone depletion. *Manney et al.* [supplementary material, 2011] found a similar reduction in the spatial correlation between ozone and temperature in 2011. Using the SLIMCAT passive tracer model, a maximum percent ozone loss of 47% was observed on 5 April 2011.

The evolution of ozone and NO_2 was observed above Eureka during and after the final warming of the record-strong polar vortex in spring 2011. Good qualitative agreement was observed between ground-based DOAS, OMI and OSIRIS satellite, and GMI model ozone and NO_2 during this period.

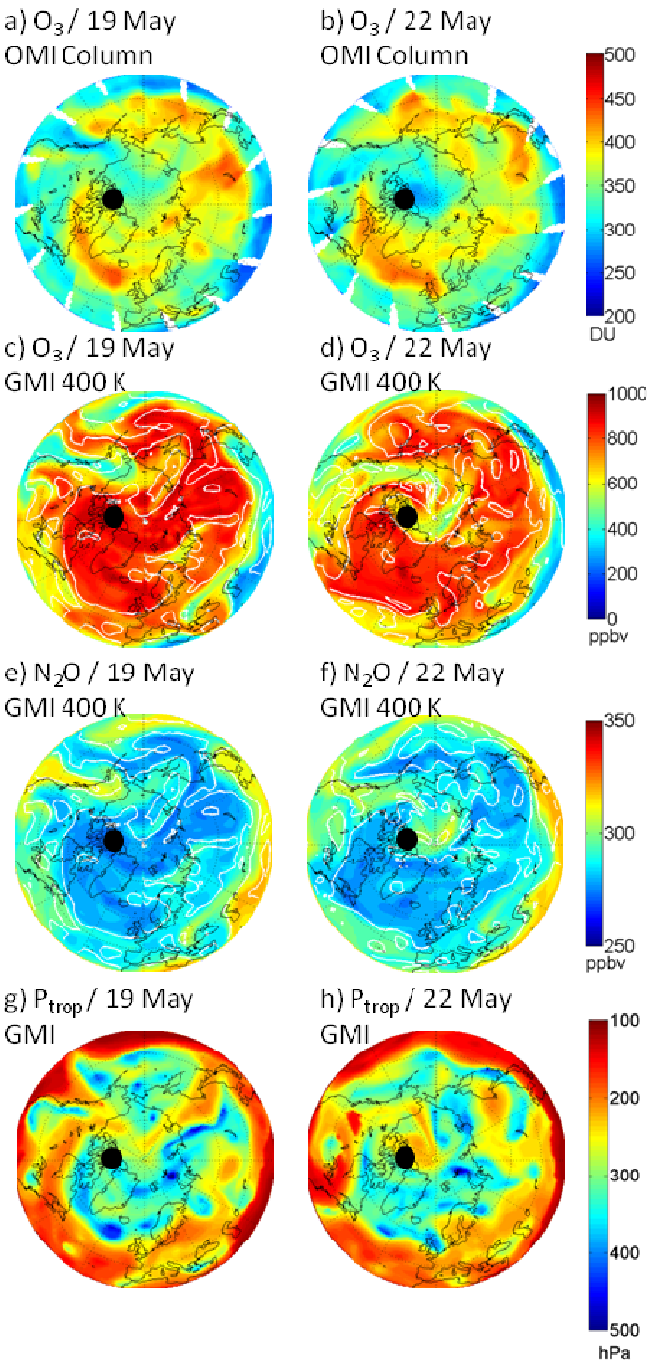

Figure 7.19: Formation of ozone mini-hole above Eureka: (top row) OMI ozone total columns, (top middle row) GMI ozone VMR at 400 K, (bottom middle row) GMI N_2O VMR at 400 K, and (bottom row) GMI tropopause pressure. Note that the colour scale for the tropopause pressure is reversed so that low pressures (high altitudes) are in red and high pressures (low altitudes) are in blue.

As the vortex moved away from Eureka on 8 April 2011, NO_2 columns were nearly twice as large as in previous years during the same period. This coincided with high temperatures and large ozone VMRs, suggesting chemical production of NO_2. Furthermore, GMI NO_x and N_2O fields suggest that at 600 K, near the NO_2 maximum, NO_x descended from higher altitudes along the vortex edge and became trapped above Eureka between a lower-latitude air mass and the vortex. Above the NO_2 maximum, NO_x-rich air was transported over Eureka from mid-latitudes into an anticyclone. This anticyclone became frozen-in and persisted until the end of the measurement period on 31 May 2011.

Ozone was trapped within this FrIAC and depleted by the enhanced NO_x. GMI ozone loss due to NO_x for 1 April to 31 May was larger in 2011 than for any other year in the dataset (2004-2010) for most of the stratosphere, including the region containing the bulk of the ozone column, from the tropopause to 18 hPa (~700 K). Therefore, ozone columns decreased more rapidly in April/May 2011 than in previous years. Chemical ozone loss between 1 December and 20 May 2011, calculated using ATLAS passive ozone, reached 4.4 ppmv (61%) in GMI data and 4.2 ppmv (58%) in OSIRIS data at 600 K above Eureka.

On 12/13 May, a vortex fragment at ~500 K passed over Eureka, leading to a reduction in the ozone columns. Low ozone columns were also observed on 22/23 May and were consistent with the formation of an ozone mini-hole due to horizontal transport of lower-latitude ozone-poor air and a rise in the tropopause height.

As halogen concentrations decrease and N_2O emissions increase, N_2O, as a precursor to stratospheric NO_x, is becoming a significant contributor to anthropogenic ozone loss [e.g., *Ravishankara et al.*, 2009; *WMO*, 2011a]. Furthermore, dynamical variability in the Arctic stratosphere appears to be increasing, with warm winters getting warmer and cold winters getting colder: the four warmest and the two coldest winters since the 1970s have occurred within the last decade [e.g., *Manney et al.*, 2011]. Substantial transport of lower-latitude NO_x and subsequent middle stratospheric ozone loss via gas-phase chemistry was previously observed in spring 2003, following a warm winter that was perturbed by a minor stratospheric warming in December and a major warming in January [*Konopka et al.*, 2007]. In the present study, similar middle-stratospheric ozone losses were observed during the break-up of the record-strength

vortex in April/May 2011, indicating that significant NO_x transport and subsequent ozone loss can also follow an unusually cold, dynamically quiescent winter.

This chapter presented a new perspective on the severe 2011 ozone depletion and evidence that the 2011 vortex breakup was also unusual compared with previous years. This highlights the usefulness of consistent long-term ground-based datasets for the identification and quantification of rare atmospheric events.

8 BrO above Eureka

The amount of BrO in the atmosphere and the contributions of source gases to the stratospheric bromine budget are not well known (see Section 1.1.1.1). Measurements of BrO are difficult as the absorption cross-section is weak and the diurnal variation of BrO is strong [e.g., *Aliwell et al.*, 2002; *Schofield et al.*, 2004b]. Furthermore, there are large uncertainties in the altitude sensitivity of satellite BrO total column measurements, particularly in the Arctic [e.g., *Salawitch et al.*, 2010], as the tropopause height and boundary-layer bromine explosions (see Section 1.2.2) both contribute significantly to the BrO total column.

Ground-based UV-visible measurements with various viewing geometries (see Section 1.3.4) have some sensitivity to the altitude distribution of BrO. Zenith-sky measurements can be used to infer stratospheric [e.g., *Solomon et al.*, 1989; *Aliwell et al.*, 2002; *Tornkvist et al.*, 2002] and, for a fixed summer-time reference spectrum, tropospheric BrO contributions [*Hendrick et al.*, 2007]. *Schofield et al.* [2006] combined direct-sun and zenith-sky measurements to retrieve stratospheric and tropospheric BrO partial columns and to identify bromine explosions. MAX-DOAS measurements have also been used in numerous studies to measure boundary layer BrO [e.g., *Honninger and Platt*, 2002; *Wagner et al.*, 2007; *Pohler et al.*, 2010].

This chapter presents GBS stratospheric and tropospheric BrO measurements. The UT-GBS recorded high resolution zenith-sky measurements for spring 2008-2010. Stratospheric BrO was retrieved from UT-GBS spring 2008 measurements and compared against OMI and OSIRIS satellite data, as discussed in Section 8.1. Furthermore, the PEARL-GBS took high resolution zenith-sky measurements for springs 2007, 2010, and 2011; direct-sun measurements for springs 2008-2011; and MAX-DOAS measurements for springs 2010-2011. Direct-sun DSCDs were not retrieved due to technical difficulties (see Section 9.3). However, MAX-DOAS DSCDs were successfully retrieved for spring 2010 and are presented in Section 8.2.

8.1 Stratospheric BrO in Spring 2008

BrO measurements are difficult, as concentrations are low and the absorption signal is weak. Furthermore, BrO has a large diurnal variation, as shown in the top panels of Figure 8.1 (see Section 8.1.2 for further description of these *a priori* profiles). BrO number densities calculated

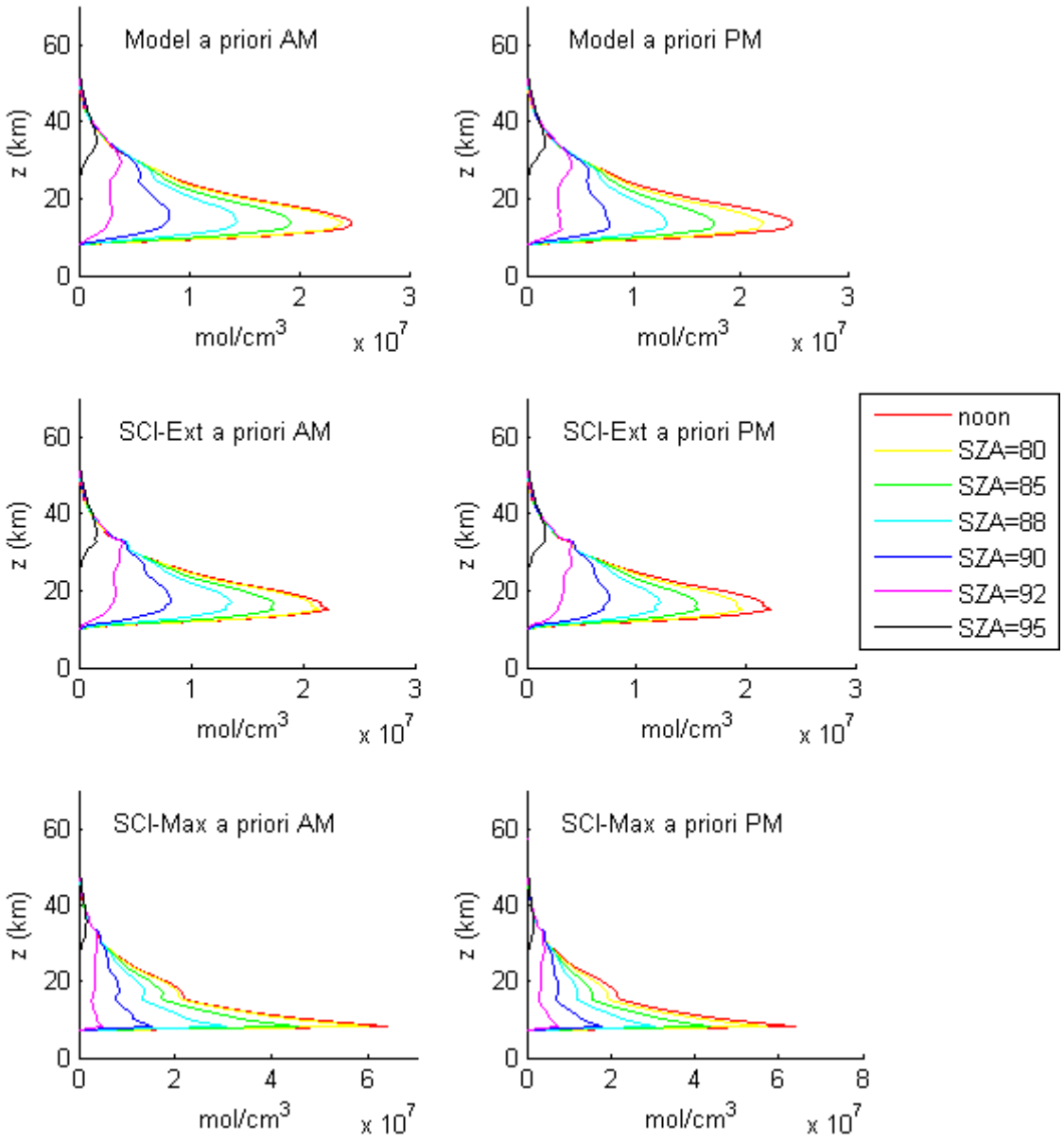

Figure 8.1: BrO profiles at various SZA. (Top) From photochemical model [*McLinden et al.*, 2000], initialized with climatological values at 80°N on day 100. (Middle) From a SCIAMACHY profile extrapolated to zero at 10-km and scaled diurnally using the photochemical model. (Bottom) From a SCIAMACHY profile extrapolated to a maximum in the lower stratosphere and scaled to various SZA using the photochemical model. Note differences in the x-axis scale.

with a photochemical model (Appendix E) reach maxima near noon and decrease rapidly during twilight. This makes DSCD retrievals difficult as the amount of BrO decreases during twilight, as the DOAS slant paths become longer. Furthermore, VCDs cannot be retrieved using Langley plots, which assume that the trace gas does not vary diurnally. Diurnal variability introduces small errors to NO_2 VCD retrievals [e.g., *Roscoe et al.*, 2001], but larger errors to BrO, which varies more rapidly [e.g., *Schofield*, 2003].

8.1.1 DSCD Retrievals

UT-GBS DSCDs were retrieved for days 65-120 of 2008 using two sets of analysis software and cross-sections. The settings for these retrievals are summarized in Table 8.1. The DOAS method is described in Section 1.3.2 and retrievals were performed using the WinDOAS software [*Fayt and Roozendael*, 2001], using the recommended settings of *Aliwell et al.* [2002]. The direct-fit method involves fitting Equation 1.28 directly, as discussed in Section 1.3.2 and was implemented using the "BOAS" software* and OMI BrO retrieval settings [*OMI*, 2008]. When "common mode" is used, the DSCD retrieval is run, the average fit residual for each day is calculated and subtracted from the measurements, then the DSCD retrieval is run again. The average fitting errors for these analyses were calculated for all retrieved DSCDs taken from 8 March to 30 April 2008 at SZA < 91°. The average fitting error for the WinDOAS analysis was 28%. The average fitting error for the direct-fit DSCDs was 12% when common mode was used and 16% when it was not used.

VCDs were retrieved using the optimal estimation method described in Section 8.1.2 for both the direct-fit and DOAS DSCDs. Comparisons between DSCDs and VCDs from the two DSCD retrieval methods are shown in Table 8.2 for three SZAs. The direct-fit DSCDs were systematically lower than the DOAS DSCDs by 8-24%. The VCD retrievals were found to have a moderating effect on the data, yielding 4-8.5% differences between the direct-fit and DOAS datasets. The R correlation coefficient between the VCDs from the two DSCD retrieval methods at various SZA ranges from 0.63 - 0.79. For the remainder of this study, the direct-fit common

* This software was developed by K. Chance at the Harvard Smithsonian Observatory, who also helped implement the software for GBS retrievals.

Table 8.1: DSCD retrieval settings for DOAS and direct-fit.

	DOAS	Direct-fit
Reference spectrum	Daily at noon	Daily at noon
Wavelength range	345-360 nm	345-360 nm
Wavelength calibration	Calibrated against the solar Atlas	Calibrated against the solar Atlas
Cross-sections	BrO at 228 K [*Wilmouth et al.*, 1999] O_3 at 221 K [*Burrows et al.*, 1999a] O_3 at 241 K [*Burrows et al.*, 1999a] NO_2 at 220 K [*Vandaele et al.*, 1998] OClO at 204 K [*Wahner et al.*, 1987] O_4 at 298 K [*Greenblatt et al.*, 1990] Ring [*Chance and Spurr*, 1997]	BrO at 228 K [*Wilmouth et al.*, 1999] O_3 at 228 K [*Malicet et al.*, 1995] NO_2 at 220 K [*Vandaele et al.*, 1998] OClO at 213 K [*Kromminga et al.*, 2003] O_4 at 294 K [*Hermans*, 2004] Ring [*Chance and Spurr*, 1997]
Additional corrections?	First-order offset correction	"Common mode" subtraction of mean residual

Table 8.2: Comparisons of DSCDs and VCDs retrieved using direct-fit and DOAS retrieval methods for days 65-120 of 2008.

DOAS minus direct-fit	SZA = 80°	SZA = 85°	SZA = 88°
mean relative difference in DSCD	8.1%	14.6%	24%
mean relative difference in VCD	5.4%	8.5%	4%
R of retrieved VCDs	0.79	0.77	0.63

mode DSCDs were used because they had the lowest fitting errors. The discrepancy between the two methods may be due to differences in the treatment of the Ring cross-section or spectral wavelength calibration.

8.1.2 Optimal Estimation Profile Retrievals

Direct-fit DSCDs were converted to number density profiles using the optimal estimation software of *Schofield et al.* [2004a], which is based on the technique of *Rodgers* [2000]. There are two main components of the software: the "retrieval model" and the "forward model". Figure 8.2 shows a flow-chart of the software, which executes the following steps.

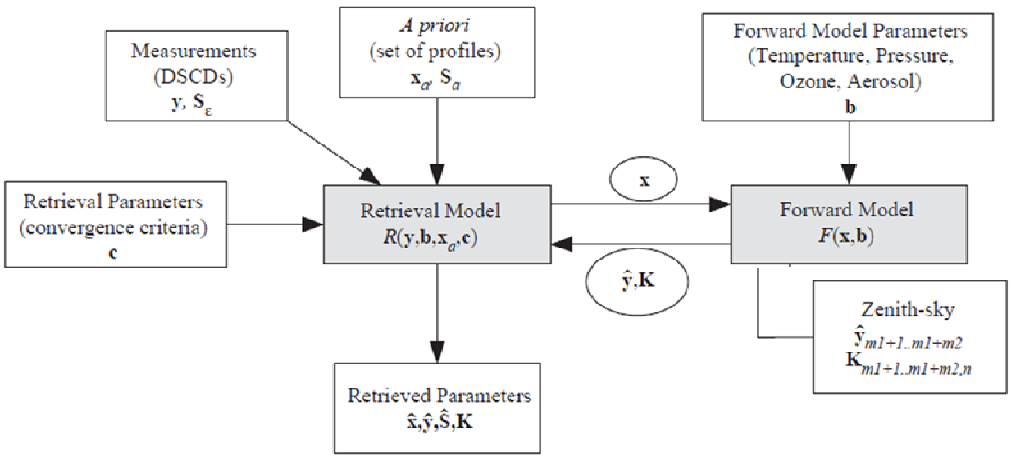

Figure 8.2: Flow-chart describing optimal estimation profile retrievals. Figure adapted from *Schofield et al.* [2004a].

1. The measured DSCDs, convergence criteria, and a first-guess set of number density profiles at various SZA, called the *a priori* are entered into the retrieval model.
2. The number density profiles and forward model parameters are entered into the forward model, which calculates radiative transfer and outputs a set of DSCDs versus SZA. These calculated DSCDs are returned to the retrieval model.
3. The retrieval model determines whether the calculated and measured DSCDs agree given the measurement and *a priori* errors and convergence criteria.
4. If they agree, the number density profiles are returned to the user as the final output. If they do not agree, the number density profiles are modified and steps 2-4 are repeated.

The forward model, F, converts the number density profile state of the atmosphere, $\mathbf{x}$, into measurement DSCDs, $\mathbf{y}$, through

$$\mathbf{y} = F(\mathbf{x},\mathbf{b}) + \varepsilon \,, \tag{8.1}$$

where ε is the error in the measurement and $\mathbf{b}$ is a set of forward model parameters, including ozone, temperature, and pressure profiles derived from ozonesondes launched above Eureka. The forward model is a spherical shell radiative transfer model, which includes refraction,

Rayleigh scattering, Mie scattering, and molecular absorption. The weighting function matrix is given as,

$$\mathbf{K} = \frac{\partial F}{\partial \mathbf{x}} \tag{8.2}$$

and describes the sensitivity of the measured DSCDs to changes in the number density profiles.

The retrieval model evaluates the agreement between the measured and calculated DSCDs as well as error covariance matrices for the measurements, $\mathbf{S}_\varepsilon$, and the *a priori* $\mathbf{S}_a$. The averaging kernel matrix, **A**, describes the sensitivity of the retrieved number density profiles ($\hat{\mathbf{x}}$) to the true state of the atmosphere (**x**). **A** is calculated from the error covariance matrices and the weighting functions,

$$\mathbf{A} = \frac{\partial \hat{\mathbf{x}}}{\partial \mathbf{x}} = (\mathbf{K}^{\mathrm{T}}\mathbf{S}_\varepsilon^{-1}\mathbf{K} + \mathbf{S}_a^{-1})^{-1}\mathbf{K}^{\mathrm{T}}\mathbf{S}_\varepsilon^{-1}\mathbf{K} \quad . \tag{8.3}$$

The rows of **A** are called the averaging kernels. The averaging kernels describe the dependence of the retrieved profiles on the state of the true atmosphere. The sum of the diagonal elements of **A** gives the degrees of freedom for signal (DOFS), which indicate the number of independent pieces of information in a given profile.

8.1.3 Altitude Sensitivity Tests

The sensitivity of the retrievals was tested using three *a priori* profiles, which are shown in Figure 8.1. The *a priori* profiles were constructed from BrO profiles at SZA 76°. The "Model" *a priori* was constructed from a photochemical model profile [*McLinden et al.*, 2000] from 10-60 km for 1 April at 80°N, initialized with climatological temperature and ozone [*McPeters et al.*, 2007]. The "SCI-Ext" and "SCI-Max" profiles* were constructed from a SCIAMACHY profile measured from 15-33 km on 1 April 2008. The SCI-Ext profile was created by extrapolating the SCIAMACHY profile at 15 km to zero at the tropopause. The SCI-Max profile was created by stretching the SCIAMACHY BrO mixing ratio at 15 km to the tropopause and then converting to

* SCI-Ext and SCI-Max profiles at SZA 76.01° were provided by S. Choi at Georgia Tech.

concentration. Above 33 km, all three *a priori* profiles were constructed from photochemical model number densities. From these three profiles at SZA 76°, morning and afternoon *a priori* profiles were obtained at SZA 60°, 80°, 85°, 88°, 90°, 92°, and 95° using the diurnal variation from the photochemical model for 1 April at 80°N.

The *a priori* error covariance matrix $\mathbf{S}_a$ was constructed by placing 50% of the maximum of the *a priori* profile along the diagonal of an *n* x *n* matrix, where *n* is the number of entries in the *a priori* profiles (number of altitude layers times number of SZAs). This covariance error was determined using an L-curve optimization [e.g., *Schofield*, 2003], as follows. Retrievals were run for $\mathbf{S}_a$ constructed from various percentages of the *a priori* profile maxima. The RMS of the retrieved DSCDs minus measured DSCDs was calculated. As the error in the *a priori* profile is increased, the constraint on the retrieval is reduced, leading to smaller RMS values. However, for *a priori* errors greater than 50% of the *a priori* profile maximum, the improvements were smaller.

In order to investigate the altitude sensitivity of the measurements, the forward model was run using the three sets of *a priori* profiles as input. The weighting functions for the SCI-Ext profile are shown in Figure 8.3 for a profile retrieved at SZA 85° (panel a) and SZA 80° (panel b). For smaller SZA, the DSCDs (**y**) are more sensitive to changes in the profiles (**x**) in the lower stratosphere. This is because for zenith-sky measurements, the scattering height is lower in the atmosphere for higher sun [e.g., *Solomon et al.*, 1987], leading to longer paths through the lower stratosphere. For SZA 85°, stronger scattering occurs in the middle stratosphere, leading to a sharper peak in sensitivity. For SZA > 85°, weighting functions peak at increasingly higher altitudes.

The DSCDs calculated from the three *a priori* profiles, using the forward model are shown in Figure 8.4 in red, green and blue. The 9 April 2008 DSCD versus SZA measured by the UT-GBS are shown in black with error bars. Within the measurement errors, it is difficult to distinguish the three sets of profiles. Although the SCI-Max *a priori* contains a much larger BrO column than the other *a priori* profiles, the calculated DSCDs at twilight are smaller. This is due to the change in altitude sensitivity with SZA. The RCD (measured at noon) is more sensitive to the lower stratosphere than the SCD (measured at twilight). Therefore, the RCD increases when

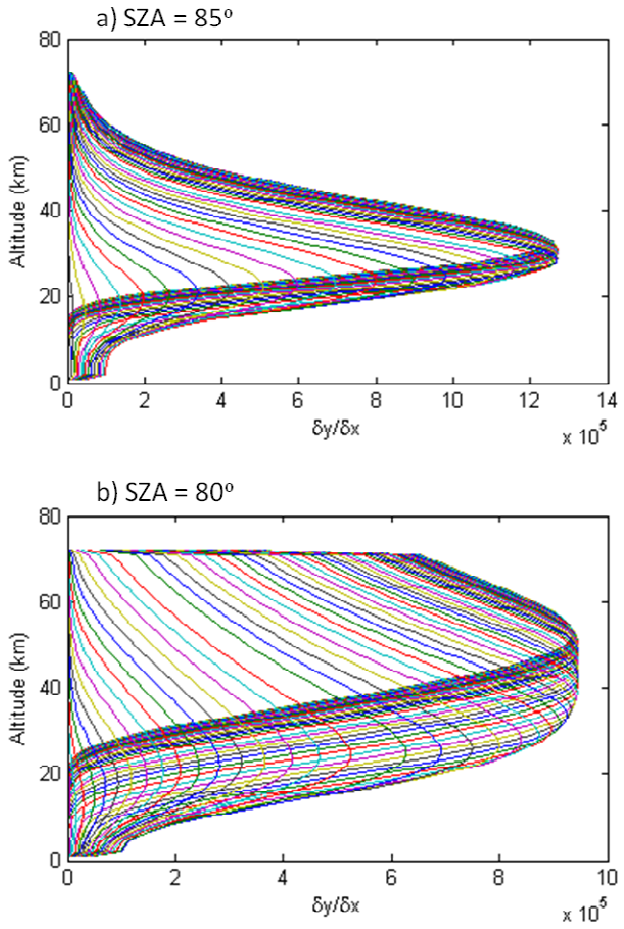

Figure 8.3: Weighting functions derived from the perturbation of the state vector at SZA 85° (top panel) and 80° (bottom panel) on afternoon twilight of day 100, using SCI-Ext *a priori* profiles. Each colour corresponds to a different SZA.

stratospheric BrO is elevated, while the SCD is less affected. Therefore the DSCD=SCD-RCD for SCI-Ext profiles is only large for SZA < 85°, when sensitivity to the lower stratosphere increases. Therefore zenith-sky retrievals have limited sensitivity to lower stratospheric BrO.

UT-GBS DSCDs from spring 2008 were then used to retrieve stratospheric BrO partial columns using the three *a priori* profiles. The measurement error covariance matrix, $\mathbf{S}_{\varepsilon}$, was constructed by placing the DSCD fitting error from 8 April 2008 along the diagonal of an m x m matrix, where m is the number of DSCDs.

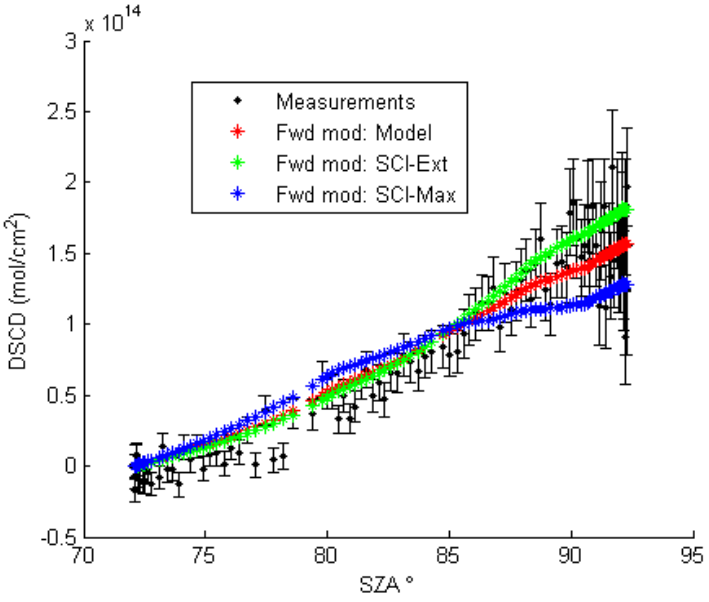

Figure 8.4: DSCD versus SZA for the measurements of 9 April 2010 (black with error bars), and the forward model for the model (red), SCI-Ext (green), and SCI-Max (blue) *a priori* profiles.

The averaging kernel matrices of these retrievals were used in order to further evaluate the altitude sensitivity of these measurements. Figure 8.5 shows a simplified schematic of the averaging kernel matrices produced by the optimal estimation software, with useful components highlighted. These interpretations of the averaging kernel matrix are explained in the paragraphs below, using the averaging kernel matrix from the SCI-Ext *a priori* on 1 April 2008 morning twilight. Qualitatively consistent results were obtained for the other *a priori* profiles on other twilights.

Each row of the averaging kernel corresponds to a retrieval point at a given altitude level and SZA. The row of the averaging kernel (red box in Figure 8.5) shows the dependence of each retrieval point on other layers of the atmosphere and at other SZA. Figure 8.6 shows the rows of the averaging kernel for six retrieval points at SZA 85°. Note that these rows have been rearranged according to SZA and stacked into a matrix so that they can be more easily visualized. The retrieval at 0-km altitude is mostly derived from information higher in the

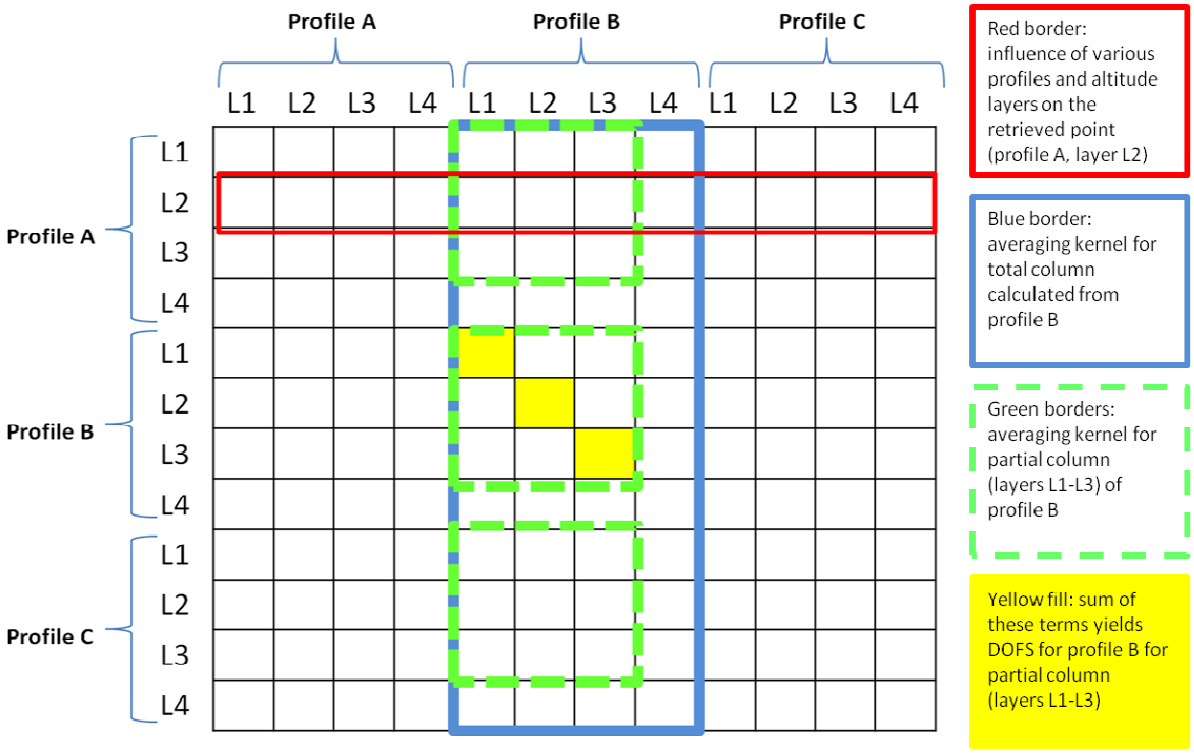

Figure 8.5: Schematic of averaging kernel matrix for simplified retrieval at three SZAs (A, B, C) for a four-layer atmosphere (L1-L4). The coloured boxes indicate various uses of the averaging kernel matrix. Note that the averaging kernels include information at various altitudes and SZAs because this software retrieves BrO profiles at a series of SZAs.

atmosphere. This suggests that retrievals at this altitude are of low quality, which is expected as the zenith-sky viewing geometry has very little sensitivity to the troposphere. At 20-km, the averaging kernel maxima are centred on the retrieval point, indicating good measurement quality at that altitude. As higher altitudes are reached, information appears to be coming from profiles at higher SZA. This is consistent with larger SZA having more sensitivity to higher altitudes.

Averaging kernels for the column and partial column measurements can also be calculated from the averaging kernel matrix (blue and green boxes in Figure 8.5). Sample 10-60 km partial column averaging kernels are shown in Figure 8.7. The retrieved columns have good sensitivity

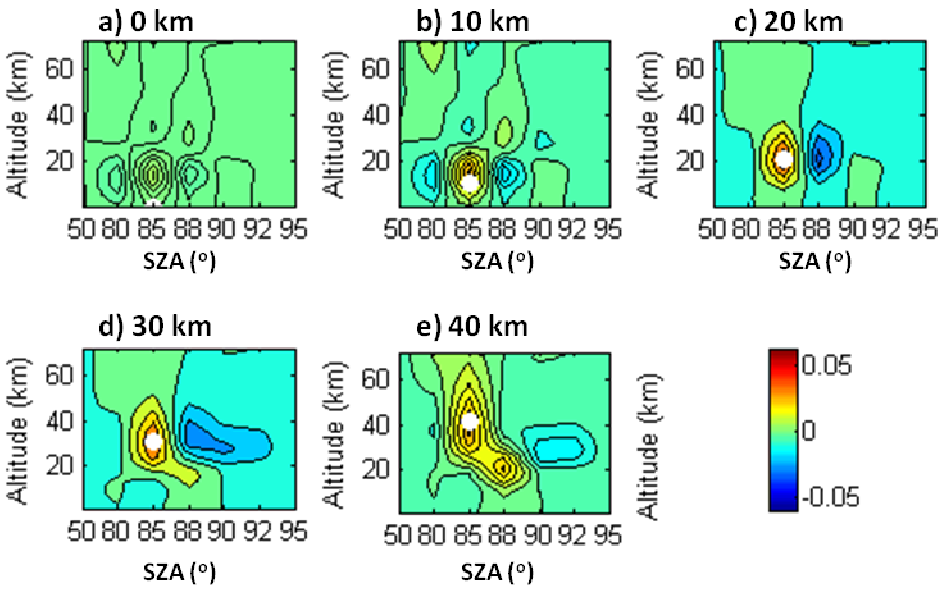

Figure 8.6: Rows of an averaging kernel matrix for profile retrieved at SZA 85°, calculated for morning measurements on 1 April 2008 and the SCI-Ext *a priori*. The retrieved point is indicated by the white dot and given in the figure labels.

to the measurements for profiles at SZA 80°, 85°, and 88°. As suggested by the weighting functions, retrievals at SZA 80° have sensitivity to a larger altitude range, with sensitivity > 0.6 for ~15-55 km. Profiles retrieved at SZA 85° and SZA 88° are sensitive to smaller altitude ranges, with sensitivities > 0.6 for ~17-52 km and ~22-35 km, respectively.

The DOFS can be calculated by taking the sum of the diagonals in the averaging kernel matrix (yellow boxes in Figure 8.5). For 10-60 km partial columns, DOFS > 1 were obtained for most profiles retrieved at SZA 80°, 85°, and 88°. This indicates that a column amount can be calculated from the data. *Hendrick et al.* [2007] also retrieved BrO from ground-based zenith-sky measurements using an optimal estimation approach. They retrieved profiles of BrO with 3.5 DOFS. This is larger than the 1-2 DOFS obtained in the present study. This may be because the errors in the DSCDs used by *Hendrick et al.* [2007] were smaller than those used in the present study. Furthermore, *Hendrick et al.* [2007] retrieved BrO profiles at a single SZA only,

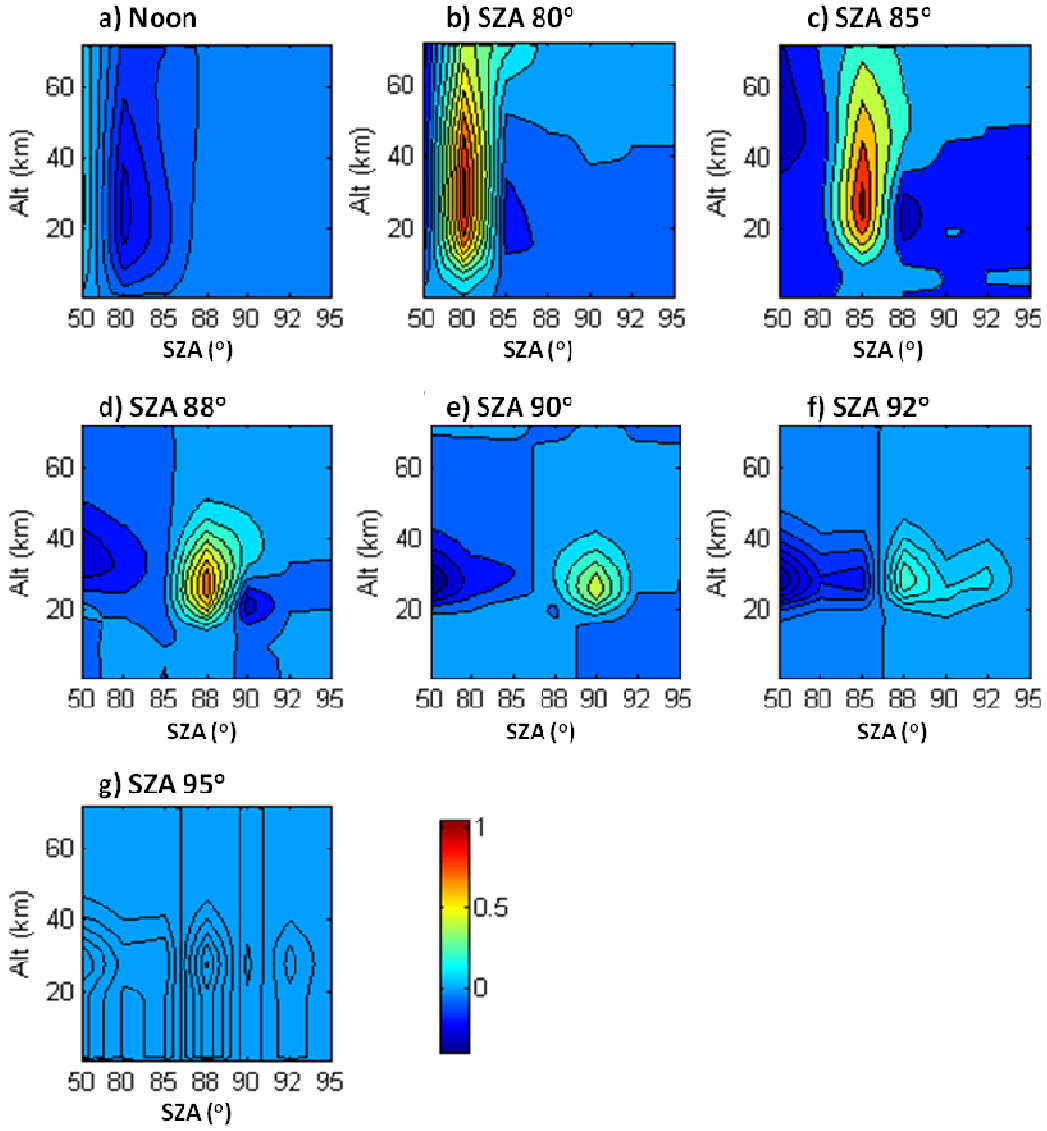

Figure 8.7: 10-60-km partial column averaging kernels for the profile retrieved at SZA indicated by titles calculated for morning measurements on 1 April 2008 and the SCI-Ext *a priori* profiles.

and therefore drew information from DSCDs at all SZA to construct a BrO profile. This would likely increase the DOFS, but relies on the accurate calculation of the diurnal variation of BrO.

The weighting functions and averaging kernels suggest that profiles retrieved at SZA 80° yield better sensitivity to the lower stratosphere, while profiles retrieved at SZA 85° and 88° yield

better sensitivity to the middle stratosphere. This information was used to select partial column ranges and profile SZAs for validation of OMI and OSIRIS BrO measurements, as discussed in Section 8.1.4.

8.1.4 Validation of OMI and OSIRIS BrO

UT-GBS BrO columns derived from the direct-fit DSCDs were compared against OSIRIS and OMI satellite BrO measurements, which are described in Appendix D. OSIRIS zonal averages of 75-85°N partial columns (15-35 km) [*McLinden et al.*, 2010] were calculated. OMI [*Chance*, 1998; *Salawitch et al.*, 2010] total columns were measured daily at ±0.25° latitude and longitude of Eureka. In order to account for diurnal variation, OSIRIS and OMI columns were scaled to the GBS measurement SZA using a photochemical model [*McLinden et al.*, 2000], initialized with ozone, temperature and pressure profiles measured by ozonesondes launched above Eureka in 2008. Photochemical model columns were also calculated and represent climatological values only; they do not account for transport in 2008. Measurements taken on the same day (UTC) were considered coincident.

A timeseries of OSIRIS and GBS BrO partial columns is given in Figure 8.8. GBS 15-35 km partial columns were calculated at SZA 85°, as this SZA yielded the best sensitivity to the middle stratosphere. The profiles selected for comparison had DOFS 0.6-0.9, indicating a strong reliance on the *a priori*. The GBS columns are shown for the model *a priori* and the SCI-Ext *a priori*. The SCI-Max data are not shown, as they are nearly identical to the SCI-Ext data because the *a priori* profiles are the same above 15 km. The photochemical model and OSIRIS columns decrease throughout the spring as NO_2 is released from night-time reservoirs and converts BrO to $BrONO_2$. The GBS columns do not decrease through the spring, likely because the GBS DOFS are small and the GBS *a priori* is fixed. On the other hand, the OSIRIS retrievals have better altitude resolution and were performed using seasonally varying *a priori* profiles, calculated from the same photochemical model. Furthermore, OSIRIS measurements, were also scaled with the photochemical model to SZA 85°.

The top section of Table 8.3 shows mean absolute and relative differences between the GBS and OSIRIS data (see Section 5.2 for definitions of mean absolute and relative differences). The mean relative difference for GBS minus OSIRIS columns is +47% to +52%. Correlations

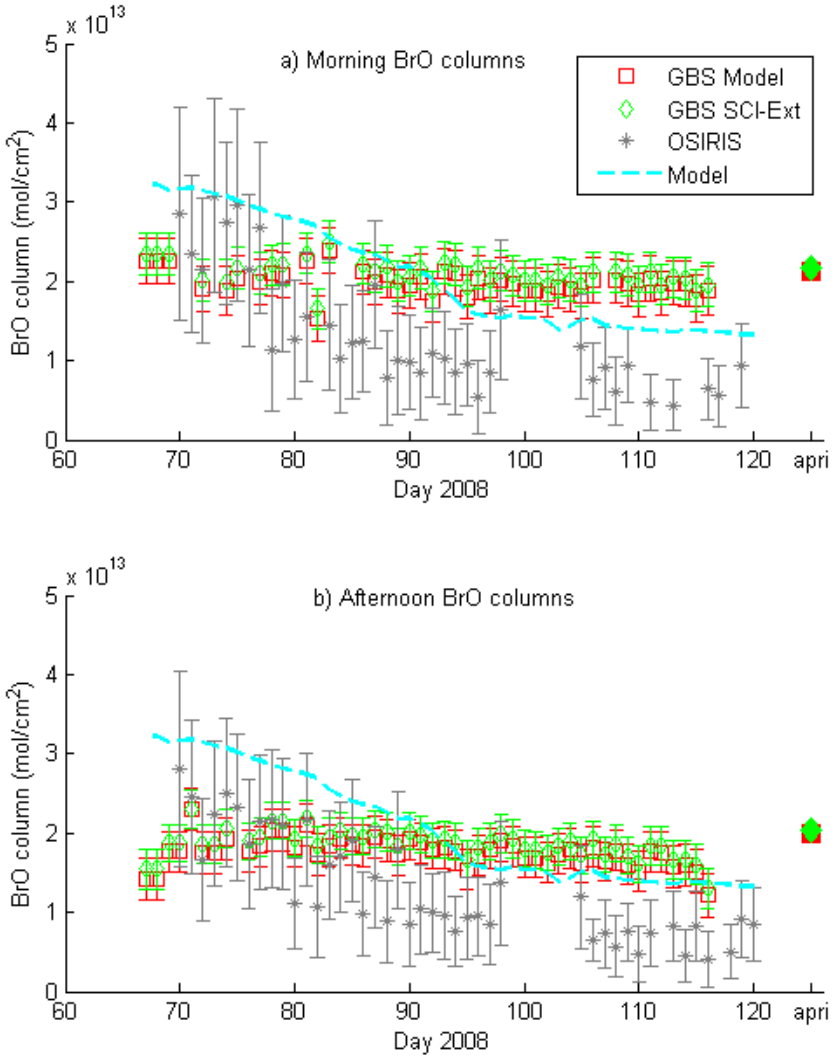

Figure 8.8: BrO 15-35 km columns for (a) morning and (b) afternoon twilights at SZA 85°. GBS columns are shown as retrieved using model (red open squares), SCI-Ext (green open diamonds) *a priori* profiles. The *a priori* column amounts are indicated by closed symbols. GBS error bars were calculated from the optimal estimation retrieval from random errors in the measured DSCDs. OSIRIS columns (grey stars) were scaled to SZA 85° using a photochemical model. OSIRIS error bars indicate precision. Photochemical model columns are also shown (cyan dashed line).

Table 8.3: Number of coincidences (N), mean absolute difference (Δ_{abs}) and mean relative difference (Δ_{rel}) between BrO measurements with respective standard deviation (σ) and standard error (err). GBS measurements are for various *a priori* profiles.

	N	Δ_{abs} (10^{13} mol/cm^2)	σ_{abs} (10^{13} mol/cm^2)	err_{abs} (10^{13} mol/cm^2)	Δ_{rel} (%)	σ_{rel} (%)	err_{rel} (%)
GBS 15-35 km partial columns versus OSIRIS 15-35 km partial columns at SZA 85°							
GBS-Model minus OSIRIS	134	0.60	0.64	0.06	47	44	4
GBS-SCI-Ext minus OSIRIS	134	0.71	0.64	0.06	52	44	4
GBS 10-60 km partial columns versus OMI total columns at SZA 80°							
GBS-Model minus OMI	65	-2.67	0.71	0.08	-61	16	2
GBS-SCI-Ext minus OMI	62	-3.02	0.71	0.09	-71	17	2
GBS-SCI-Max minus OMI	68	-2.32	0.73	0.09	-50	16	2

between the GBS and OSIRIS measurements were poor ($R^2 < 0.1$). This may be due in part to large differences in sampled airmasses, as OSIRIS measures zonally averaged BrO. Furthermore, errors are likely introduced in the diurnal variation scaling factors and the GBS BrO measurements have large systematic uncertainties that are not accounted for in the error bars.

A timeseries of GBS and OMI columns is shown in Figure 8.9. For comparison against OMI total columns, GBS 10-60 km partial columns were calculated at SZA 80°. This SZA maximized GBS sensitivity to the lower stratosphere. Only GBS measurements with DOFS > 1 were included in the comparison. GBS columns retrieved from the three *a priori* profiles are similar. The SCI-Max retrieved columns are slightly larger than for the other profiles, but are smaller than the SCI-Max *a priori* columns. The GBS BrO partial columns range from approximately 2.5-4.5x10^{13} mol/cm^2. These values are comparable to the spring-time stratospheric BrO partial columns measured at the same SZA by *Hendrick et al.* [2007] at Harestua, Norway (60°N, 11°E) using a DOAS instrument.

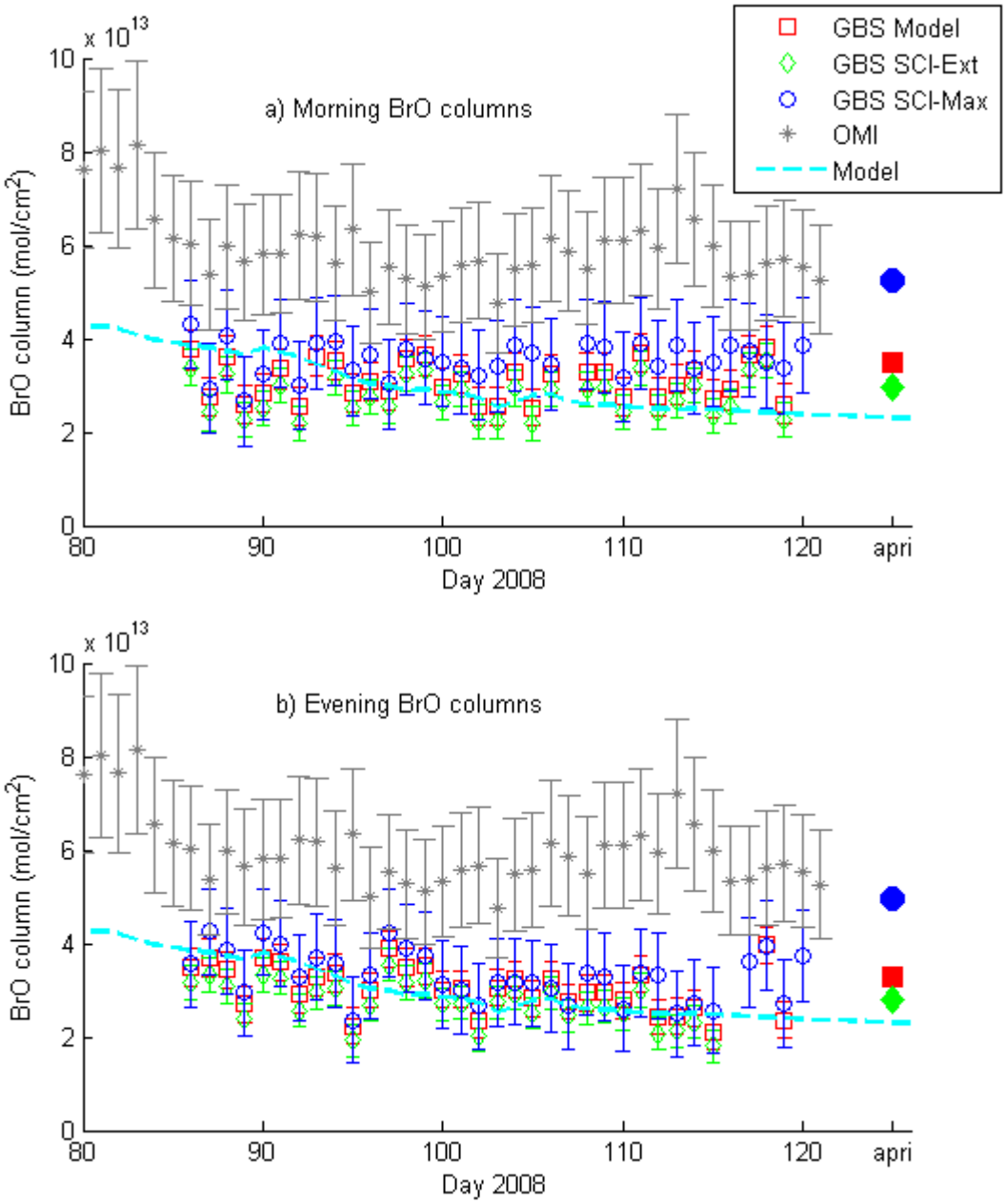

Figure 8.9: BrO columns for (a) morning and (b) afternoon twilights at SZA 80°. GBS 10-60 km columns are shown as retrieved using model (red open squares), SCI-Ext (green open diamonds), and SCI-Max (blue open circles) *a priori* profiles. The *a priori* column amounts are indicated by closed symbols. GBS error bars were calculated from the optimal estimation retrieval from random errors in the measured DSCDs. OMI total columns (grey stars) were scaled to SZA 80° using a photochemical model. OMI error bars are 22%, reflecting uncertainties in DSCD fits [*Salawitch et al.*, 2010]. Photochemical model 10-60 km partial columns are also shown (cyan dashed line).

Mean absolute and relative differences between the GBS and OMI data are summarized in the bottom section of Table 8.3. The GBS columns are much lower than the OMI columns, with mean relative differences of -50% to -61%. This bias may be caused partly by the wavelength range of the SCD retrievals. Several research groups have found that the 319-347.5 nm window,used for OMI, yields larger SCDs than the 345-360 nm window used for GBS retrievals*. Furthermore, this may be caused by differences in the altitude ranges of the columns, as OMI measures the total column, while the GBS measures stratospheric BrO only.

Correlations between GBS and OMI data are poor ($R^2 < 0.1$). This may be due to bromine explosions, which would be captured by OMI total column measurements, but not by GBS stratospheric columns. Furthermore, bromine explosions can be highly localized and can appear or disappear over the course of hours. Ozone mixing ratios from ozonesondes launched above Eureka in 2008 (see Appendix C) are shown in Figure 8.10. Low boundary layer ozone concentrations, likely due to bromine explosions, were observed around days 80 and 115. OMI measures elevated BrO around days 83-84 and for days 110-115, suggesting that it captures these events.

8.2 MAX-DOAS Measurements in 2010

In order to measure tropospheric BrO, MAX-DOAS measurement routines were implemented using the PEARL-GBS and UT Suntracker. Measurements in the UV-wavelength region were acquired for days 90-180 in 2010 at elevations of 1°, 2°, 4°, 10°, 15°, 30°, and 90°. BrO was retrieved using QDOAS in the 345-360 nm wavelength region and O_4 was retrieved in the 350-380 nm wavelength region, with a daily noon-time reference spectrum. For both BrO and O_4, wavelengths were calibrated against the solar spectrum daily based on the reference solar Atlas [*Kurucz et al.*, 1984]. Ozone measured at 223 K [*Bogumil et al.*, 2003], NO_2 measured at 295 K [*Vandaele et al.*, 1998], O_4 [*Greenblatt et al.*, 1990] with corrected wavelengths, BrO measured at 223 K [*Fleischmann et al.*, 2004] and OClO measured at 204 K [*Wahner et al.*, 1987], and Ring [*Chance and Spurr*, 1997] cross-sections were all fit using QDOAS, with a third

* Personal communication with K. Chance on 7 January 2009.

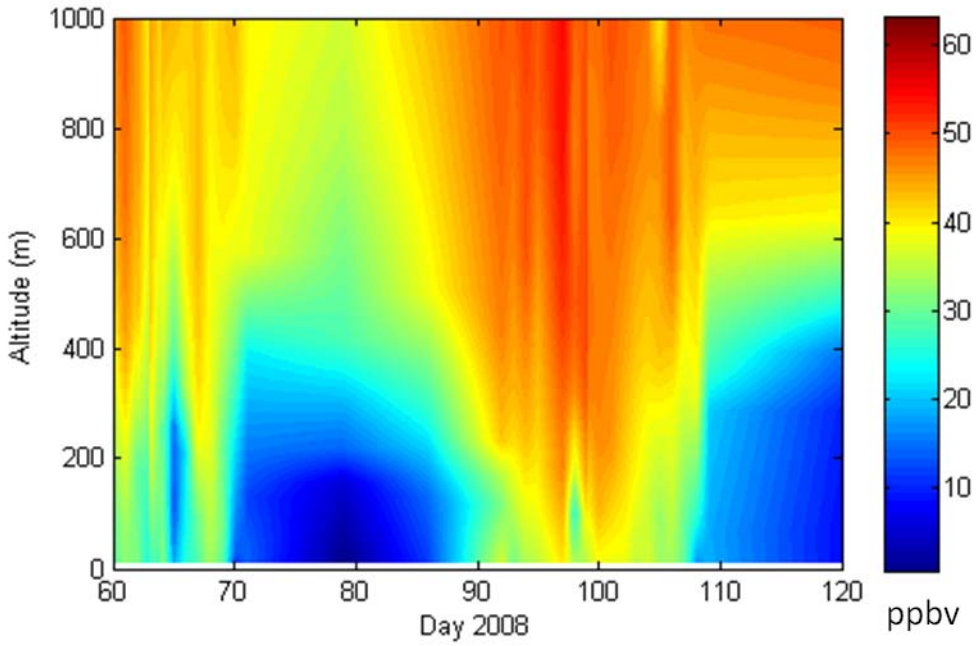

Figure 8.10: Ozonesonde mixing ratio profiles above Eureka for spring 2008.

order polynomial. A first order offset correction was also applied to correct for dark current and stray light. Measurements were filtered for RMS < 0.001. The timeseries of the MAX-DOAS BrO and O_4 DSCDs are shown in Figure 8.11. O_4 can be used to identify path enhancement by clouds, as described in Section 1.3.5. Note that only 90°, 15°, and 1° elevations for SZA < 80° are shown here, so that measurements can be more easily distinguished. The evolution of the DSCD at elevation 1° gives the strongest indication of boundary layer BrO. A large peak in BrO is observed around day 102. Elevated values are also observed for days ~127 and ~139. These values do not coincide with high values of O_4, suggesting that the peaks are caused by enhanced BrO and not enhanced scattering.

Figure 8.12 shows ozonesonde profiles above Eureka in 2010, with the elevation of the PEARL Ridge Lab marked by the black dotted line. Low ozone mixing ratios are observed during much of the spring. Ozonesondes were not launched on days 102 and 127. However, a sonde launched on day 139 indicates low ozone mixing ratios above PEARL. This is consistent with elevated tropospheric BrO during a bromine explosion leading to lower ozone mixing ratios.

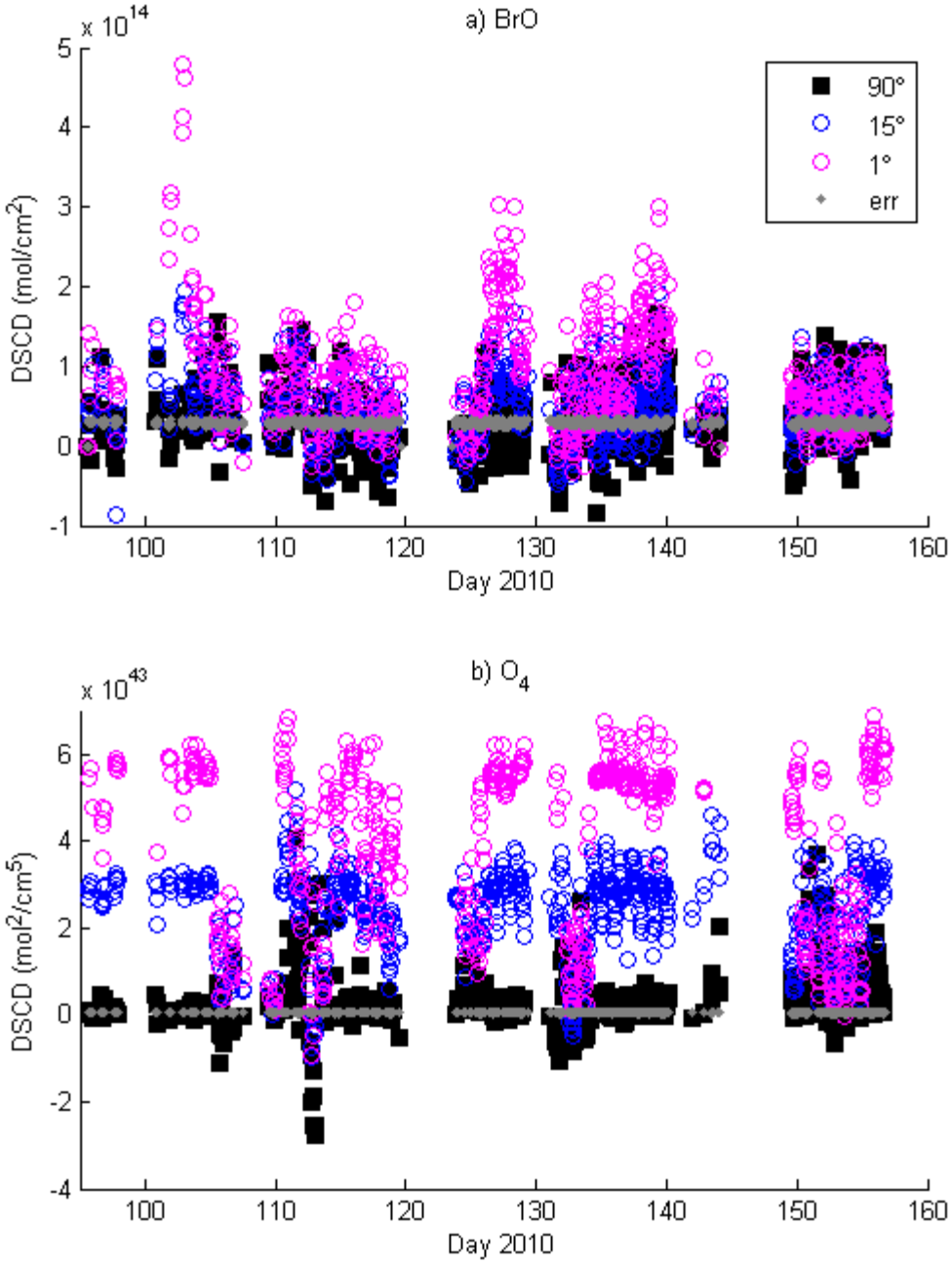

Figure 8.11: PEARL-GBS MAX-DOAS (a) BrO and (b) O_4 measurements for spring 2010. Note that DSCDs were also measured for elevations 2, 4, 10 and 30, but are not shown here to enhance visibility.

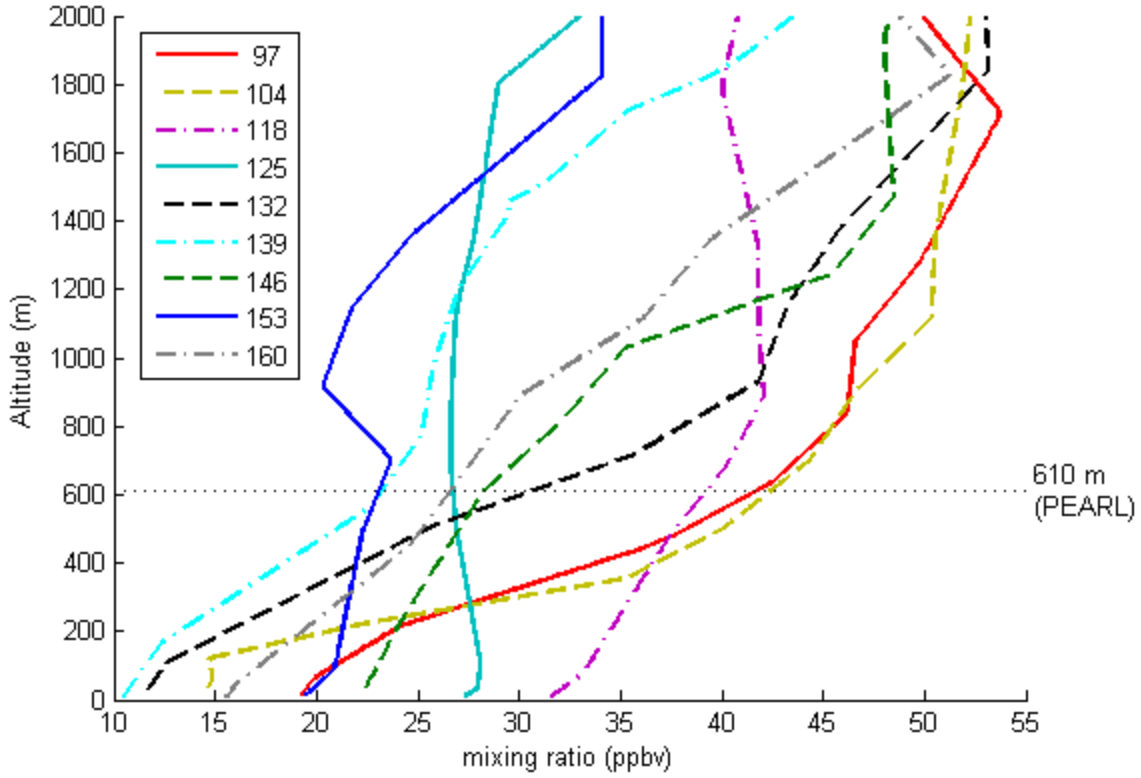

Figure 8.12: Ozonesonde measurements above Eureka in spring 2010 for days indicated in legend. The elevation of PEARL Ridge Lab is indicated by the horizontal dashed line.

8.3 Summary

Stratospheric and tropospheric BrO were measured above Eureka using the GBS instruments. For spring 2008, UT-GBS zenith-sky measurements, BrO DSCDs were retrieved using DOAS and direct-fit analysis methods. The direct-fit analysis yielded lower fitting errors. BrO columns were retrieved using an optimal estimation method for three *a priori* profiles. Forward model tests and averaging kernels indicate that columns have limited sensitivity to the lower stratosphere when SZA > 85°, as expected for the zenith-sky viewing geometry.

GBS 15-35 km partial columns at SZA 85° were compared with OSIRIS zonally averaged 15-35 km partial columns. SZA 85° was selected because this yielded good sensitivity to the middle

stratosphere. The GBS measurements were systematically larger than the OSIRIS measurements, with a mean relative difference of +47% to +52%. Poor correlation ($R^2 < 0.1$) was observed between these datasets, perhaps because the OSIRIS measurements were zonally averaged and therefore did not represent measurements directly above Eureka.

GBS 10-60 km partial columns were compared against OMI total column measurements within ±0.25° of Eureka. GBS partial columns were systematically lower than the OMI columns, with mean relative differences of approximately -50 to -71%, depending on the GBS *a priori* profile. Furthermore, poor correlation ($R^2 < 0.1$) was observed between GBS and OMI measurements. The bias between the GBS and OMI may be caused partly by the different wavelength ranges of the GBS and OMI DSCD retrievals. Furthermore, tropospheric bromine, and in particular boundary layer bromine explosions, likely lead to discrepancies between the GBS 10-60 km partial columns, which are not sensitive to the troposphere, and OMI total column measurements.

This demonstrates some of the challenges of BrO measurement and validation. DSCD and column retrievals are complicated by low signal and the strong diurnal variation of BrO. Furthermore, the validation of BrO is difficult as instruments sample BrO at different SZAs and the altitude sensitivities and footprints of remote sensing instruments vary.

Tropospheric BrO was measured in spring 2010 using PEARL-GBS MAX-DOAS measurements. These are the first Arctic MAX-DOAS measurements taken by the GBS. Several episodes of elevated BrO were observed, suggesting that bromine explosions occurred above PEARL. In the future, the MAX-DOAS measurements may be combined with direct-sun and zenith-sky measurements to calculate the bromine budget from the boundary layer to the stratosphere above Eureka.

9 Conclusions

9.1 Summary of Thesis

Measurements of ozone, NO_2, OClO, BrO, and HCHO were obtained using two ground-based UV-visible spectrometers. An accurate and well-characterized dataset was produced through instrument testing, consistent data analysis and quality control, and extensive validation against other instruments. Using the resulting 11-year dataset, the following scientific questions were addressed:

- How well do ACE and OSIRIS satellite ozone and NO_2 measurements agree with ground-based measurements at Eureka?
- Is our current understanding of stratospheric odd-nitrogen photochemistry correct?
- How did the record 2011 Arctic ozone depletion compare to previous years?
- How much BrO is there above Eureka and how is it distributed in altitude?

The UT-GBS and PEARL-GBS are UV-visible triple-grating spectrometers. The UT-GBS has been deployed at Eureka on a campaign basis since 1999. The PEARL-GBS was permanently installed at Eureka in August 2006. Several changes were made to the GBSs between 2008 and 2011. In 2008, the UT Suntracker was installed above the PEARL-GBS, allowing for new direct-sun and MAX-DOAS measurements. In 2009, light leaks to both instruments were corrected and, in 2010, the resolution of both instruments was improved through modifications to the input optics.

The PEARL-GBS was accepted as an NDACC instrument in 2009. NDACC is a network committed to the long-term monitoring of atmospheric composition. Therefore, the UT-GBS participated in a formal NDACC intercomparison campaign, CINDI, in Cabauw, Netherlands in summer 2009. UT-GBS zenith-sky NO_2 DSCDs, measured during the formal semi-blind part of the campaign, agreed well with other DOAS instruments. Therefore, the UT-GBS was deemed a suitable NDACC instrument. Following the formal part of the campaign, the UT Suntracker was installed above the UT-GBS and the first ever GBS MAX-DOAS measurements were taken.

GBS MAX-DOAS NO_2 and HCHO DSCDs agreed well with other MAX-DOAS instruments. The comparisons performed during CINDI contribute to the assessment of the accuracy of remote-sensing trace gas measurements.

GBS ozone and NO_2 columns above Eureka were retrieved for 1999-2011, using a consistent data analysis technique. Data analysis software and data quality thresholds were developed so that data could be analyzed quickly and consistently over a long time-period. Fitting parameters were monitored, leading to the identification several data quality problems, such as decreased measurement quality in the summer, systematic errors introduced by neutral density filters, and polarization errors. A new error budget was calculated to take these uncertainties into account. Ozone total columns measured by the GBS and SAOZ DOAS instruments, and retrieved with the new NDACC guidelines for ozone [*Hendrick et al.*, 2011], agree to within 3.2%. The DOAS ozone columns agree with the Brewer spectrophotometers with mean relative differences that are smaller than 1.5%. This suggests that, for the GBS and SAOZ, the new NDACC data guidelines were successful in producing a homogenous and accurate ozone dataset at 80°N.

Ozone and NO_2 measured at Eureka by the GBS, SAOZ, Brewer spectrophotometers, and Bruker FTIR were used to validate OSIRIS and ACE, which have been taking measurements from space since 2001 and 2003 respectively. Satellite 14-52 km ozone and 17-40 km NO_2 partial columns within 500 km of Eureka were calculated for ACE-FTS v2.2 plus updates, ACE-FTS v3.0, ACE-MAESTRO v1.2 and OSIRIS SaskMART v5.0x ozone and Optimal Estimation v3.0 NO_2 data products. The new ACE-FTS v3.0 and the validated ACE-FTS v2.2 partial columns are nearly identical, with mean relative differences of 0.0±0.2% for ozone and -0.2±0.1% for v2.2 minus v3.3 NO_2. Ozone columns were constructed from 14-52 km satellite and 0-14 km ozonesonde partial columns and compared with the ground-based total column measurements. The satellite-plus-sonde measurements agree with the ground-based ozone total columns with mean relative differences of 0.1-7.3%. For NO_2, partial columns from 17 km upward were scaled to noon using a photochemical model. Mean relative differences between OSIRIS, ACE-FTS and ground-based NO_2 measurements do not exceed 20%. ACE-MAESTRO measures more NO_2 than the other instruments, with mean relative differences of 25-52%. Seasonal variation in the differences between NO_2 partial columns is observed, suggesting that there are systematic errors in the measurements, the photochemical model corrections, and/or in

the coincidence criteria. The differences between satellite and ground-based measurements do not show any obvious trends over the missions, indicating that both the ACE and OSIRIS instruments continue to perform well. Continued long-term validation of datasets such as these is essential for the study of stratospheric variability under climate change.

On 1 August 2008, a solar eclipse of 98% totality passed over Eureka. During the eclipse, the PEARL-GBS measured SCDs and VCDs of ozone up to 82% occultation and NO_2 up to 96% occultation, beyond which low light intensities and changes in the solar spectrum due to limb-darkening compromised data quality. Ozone VCDs during the eclipse remained within natural variability. Measured NO_2 SCDs increased and decreased symmetrically around the eclipse maximum. NO_2 SCDs were also calculated using a photochemical model and a one-dimensional radiative transfer model. The modeled ratio of eclipse day SCDs to the previous day's SCDs was compared to the measurements. They agreed within error bars leading up to maximum occultation, but the model ratio was systematically larger than the measured ratio for the second half of the eclipse, perhaps due to changing cloud conditions throughout the eclipse. The measured NO_2 SCD ratio of $1.84^{+0.12}_{-0.43}$ at 96% totality is larger than observed in past studies and agrees with modeled ratio of 1.91. Therefore our current understanding of stratospheric photochemistry and NO_x rate constants are sufficient to predict the evolution of NO_x chemistry through a solar eclipse.

Unusually cold conditions in Arctic winter 2010/11 led to large stratospheric ozone loss. We investigated this with UV-visible measurements made at Eureka, Canada (80.05°N, 86.42°W) from 1999-2011. For 8-22 March 2011, OClO was enhanced, indicating chlorine activation above Eureka. Ozone columns were lower than in any other year in the record, reaching minima of 237 DU and 247 DU in two datasets. The average NO_2 column inside the vortex, measured at visible and UV wavelengths, was 46±30% and 45±27% lower in 2011 than the average NO_2 column from previous years. Ozone column loss was estimated from two ozone datasets, using a modeled passive ozone tracer. For 12-20 March 2011, the average ozone loss was 27% and 29% (99 DU and 108 DU). The largest percent ozone loss in the 11-year record of 47% (250 DU and 251 DU) was observed on 5 April 2011. This work complements other studies on the topic of the severe

2011 ozone depletion [*Balis et al.*, 2011; *Manney et al.*, 2011; *Lindenmaier et al.*, 2012], through the inclusion of NO_2 and OClO measurements.

As the polar vortex moved away from Eureka and broke up in 2011, unusual ozone and NO_2 columns were measured. This was investigated using OSIRIS and OMI satellite data, dynamical parameters, and GMI model output. In April, NO_x was enhanced due to descent from higher altitudes and horizontal transport from lower latitudes. Due to high temperatures, chemical NO_2 production was favoured. This led to NO_2 total columns above Eureka that were approximately two times larger than in previous years. Elevated NO_x resulted in more ozone loss in the middle stratosphere, causing ozone columns above Eureka to decrease more rapidly through April/May than in previous years. Vortex fragments, a frozen-in anticyclone, and an ozone mini-hole were also observed above Eureka in April/May 2011. Therefore, the 2011 stratospheric warming was also unusual in the context of previous years due to chemical and dynamical effects.

BrO was also retrieved from GBS spectra. For spring 2008, zenith-sky DSCDs were retrieved using both QDOAS and a direct-fit technique. The direct-fit DSCDs were 8-24% smaller than the DOAS DSCDs. Due to smaller fitting errors, the direct-fit DSCDs were used. Stratospheric partial columns were calculated using an optimal estimation profile retrieval. The altitude sensitivity of these measurements was investigated using several *a priori* profiles and limitations of the retrieval, particularly in the lower stratosphere, were identified. These partial columns were then compared with OMI and OSIRIS satellite BrO measurements. The mean relative difference between GBS and OSIRIS 15-35 km partial columns was +47% to +52%. Discrepancies between these measurements may be due in part to the low 0.6-0.9 DOFS in the GBS 15-35 km partial columns and heavy reliance on the fixed *a priori* profile. The mean relative difference between GBS 10-60 km partial columns and OMI total columns was -50% to +71%. This may be due partly to the wavelength regions selected for the GBS and OMI DOAS retrievals. Furthermore, some of the discrepancies between these measurements may be attributed to bromine explosions in the boundary layer, to which the GBS zenith-sky measurements are not sensitive. In order to address this, MAX-DOAS BrO measurements, which are sensitive to the boundary layer, were acquired in spring 2010 and 2011. In 2010, MAX-DOAS BrO was elevated during several periods, suggesting that these measurements

captured bromine explosions. Therefore, progress was made toward measuring the BrO profile above Eureka.

9.2 Implications

This thesis demonstrates several ways in which long-term ground-based datasets are of value. In Chapters 3, 5 and 8, ozone, NO_2, and BrO measurements are used to evaluate the quality of other ground-based and satellite datasets, particularly those made on the ACE and Odin missions. This is particularly important in the High Arctic, where measurements are challenging due to, e.g., available sunlight and logistics, and are therefore scarce. Chemical reaction rates, such as the NO_2 photolysis rate, are measured in the laboratory, often with large uncertainties, particularly at stratospheric temperatures [e.g., *Sanders et al.*, 2011]. In this thesis, NO_2 photolysis rates are assessed using field measurements throughout the diurnal cycle (Figure 5.3) and during a solar eclipse (Chapter 6). A chemistry transport model dataset was also compared with the ground-based measurements (Figure 7.8). Therefore, this thesis demonstrates the usefulness of long-term datasets for the evaluation of satellite, lab-based, and model datasets.

Additionally, atmospheric processes can be investigated with consistent long-term datasets. The severe ozone depletion in spring 2011 was largely unexpected. The assessment of this event with ground-based ozone, NO_2, and OClO measurements in the context of previous years supported suggestions that the low ozone could be explained given the low temperatures in spring 2011 [e.g., *Manney et al.*, 2011]. Furthermore, this dataset was used to identify the unusual NO_2 increases as the polar vortex warmed in April/May 2011. These data were then complemented by satellite and chemistry transport model profiles and the evolution of ozone and NO_2 through this warming were assessed. Therefore, contributions were made toward identifying and understanding unusual events in the polar stratosphere.

There are many open questions about BrO, as discussed in Section 1.1.1.1. Measurements of BrO columns from various satellite and ground-based instruments often disagree by a factor of two, depending on basic analysis parameters, such the wavelength fitting interval of the retrievals. Furthermore, the altitude distribution of BrO is often unknown as boundary layer bromine explosions can contribute significantly to satellite measurements. Since BrO has absorption features at UV wavelengths, DOAS instruments are well suited for the measurement

of BrO. Furthermore, direct-sun and MAX-DOAS viewing geometries can be used in order to gain altitude information. While these techniques are challenging, the ground-based BrO measurements presented in Chapter 8 of this thesis have the potential to tackle some of these questions.

9.3 Suggested Future Work

A long-term GBS ozone and NO_2 dataset was retrieved and validated against other instruments at PEARL. This dataset was used to investigate the unusual spring 2011 in the context of previous years. Spring-time ozone and NO_2 also show large variability in 2000, 2005 and 2007 (see Figure 4.10 and Figure 4.11), years in which the polar vortex was above Eureka. Summertime NO_2 is also variable (see Figure 4.9), with lower values observed in August 2007 and 2009 than in 2008 and 2010. These events could be investigating using other datasets at PEARL, including long-term FTIR measurements [*Lindenmaier et al.*, 2012], and NDACC DOAS measurements at other sites. Furthermore, as demonstrated in Section 7.3, satellite, dynamical, and model data can be combined to interpret ground-based total column measurements.

The GBSs do not currently measure during the three months of polar night. Using the UT Suntracker, lunar measurements were tested for one twilight in 2008 and DSCDs of ozone were successfully retrieved. Unfortunately, various instrument failures and housing challenges prevented acquisition of lunar measurements in subsequent winters. This technique could be used in the future to measure ozone, and perhaps NO_3 [*Wagner et al.*, 2000] during polar night.

Recently, significant disagreement was observed between OClO from measurements and a photochemical model (see Section 1.1.1.1; *Oetjen et al.* [2011]). GBS OClO, BrO, NO_2, and ozone at various SZAs; Bruker FTIR measurements of ozone, HCl, HNO_3, and $ClONO_2$; and a photochemical model could be used to assess these discrepancies. Furthermore, PSCs could be retrieved from the GBS measurements, using the colour index technique [*Sarkissian et al.*, 1991].

BrO stratospheric partial columns and MAX-DOAS DSCDs were successfully retrieved from GBS data. In the future, a timeseries of stratospheric BrO partial columns for spring 2007-2011 should be retrieved. These partial columns could be compared with satellite and model datasets

in order to determine the stratospheric BrO budget and the contributions from very short-lived substances. Boundary layer partial columns of BrO could be retrieved from MAX-DOAS measurements using optimal estimation techniques. This tropospheric information could be used to improve interpretation of satellite total column measurements. Furthermore, boundary layer partial columns could be used to identify the mechanisms by which bromine explosions evolve. Eureka is an excellent location for these studies because bromine explosions occur regularly [*Tarasick and Bottenheim*, 2002] and several other boundary layer datasets, including ozonesondes, weather data, and PEARL instrumentation, are available.

Despite recent improvements to the GBS instruments, the residuals of GBS DOAS fits are still larger than for some research groups. Several changes could be made to the instruments in order to improve the quality of GBS BrO measurements. Temperature control would reduce wavelength shifts and stretches between noon and twilight spectra. Furthermore, the input optics of the instruments, particularly the UT-GBS, cause optical aberrations. Therefore, the removal of the F# matcher is currently being tested by Xiaoyi Zhao through the direct coupling of a fibre bundle to the slit of the instrument. This may also increase the signal-to-noise ratio, which, based on the large improvements in OClO fits after averaging spectra, should significantly improve data quality. Finally, the polarization effects in the spectra could be tested and, if possible, corrected.

New direct-sun measurements were acquired from spring 2008-2011. However, BrO was not retrieved from these measurements due to large residuals in the DOAS retrievals. This may be caused by drift in the passive tracking throughout the day. This could be reduced through improved correction algorithms [*Merlaud*, 2011] or through active tracking, which has been implemented for FTIR instruments by Dalhousie University. Furthermore, neutral density filters that are used to attenuate direct-sunlight were found to significantly reduce the quality of zenith-sky measurements and could be tested, and perhaps replaced. If direct-sun BrO measurements are successfully obtained, stratospheric and tropospheric partial columns of BrO can be retrieved [*Schofield et al.*, 2004a]. This would yield the lower-stratospheric and upper-tropospheric information that is missing from the zenith-sky and MAX-DOAS measurements. Therefore, low-resolution BrO profiles could be derived above Eureka and used to evaluate the Arctic bromine budget.

Overall, this thesis presents a new 11-year ground-based dataset that can be used to assess the variability of the stratosphere and troposphere. These measurements have been carefully characterized and validated and data analysis has been automated and standardized. Hopefully, this marks the beginning of a consistent multi-decade dataset that will be used to assess Arctic composition trends.

References

Abalakin, V. K. (Ed.) (1981), *Astronomical calendar - constant part*, Science Publishing House, Moscow.

Adams, C., C. A. McLinden, K. Strong, and V. Umlenski (2010), Ozone and NO_2 variations measured during the 1 August 2008 solar eclipse above Eureka, Canada with a UV-visible spectrometer, *J. Geophys. Res.*, *115*, D19310, doi:10.1029/2010JD014424.

Adams, C., K. Strong, R. L. Batchelor, P. F. Bernath, S. Brohede, C. Boone, D. Degenstein, W. H. Daffer, J. R. Drummond, P. F. Fogal, E. Farahani, C. Fayt, A. Fraser, F. Goutail, F. Hendrick, F. Kolonjari, R. Lindenmaier, G. Manney, C. T. McElroy, C. A. McLinden, J. Mendonca, J.-H. Park, B. Pavlovic, A. Pazmino, C. Roth, V. Savastiouk, K. A. Walker, D. Weaver, and X. Zhao (2012a), Validation of ACE and OSIRIS ozone and NO_2 measurements using ground-based instruments at 80°N, *Atmos. Meas. Tech.*, *5*, 927-953, doi:10.5194/amt-5-927-2012.

Adams, C., K. Strong, X. Zhao, M. R. Bassford, M. P. Chipperfield, W. Daffer, J. R. Drummond, E. E. Farahani, W. Feng, A. Fraser, F. Goutail, G. Manney, C. A. McLinden, A. Pazmino, M. Rex, and K. A. Walker (2012b), Severe 2011 ozone depletion assessed with 11 years of ozone, NO_2, and OClO measurements at 80°N, *Geophys. Res. Lett.*, *39*, L05806, doi:10.1029/2011GL050478.

Adams, C., K. Strong, X. Zhao, A. E. Bourassa, W. H. Daffer, D. Degenstein, J. R. Drummond, E. E. Farahani, A. Fraser, N. D. Lloyd, G. L. Manney, C. A. McLinden, M. Rex, C. Roth, S. E. Strahan, K. A. Walker, and I. Wohltmann (2012c), NO_x-driven ozone loss and a frozen-in anticyclone observed during the Arctic spring 2011 stratospheric warming, *in prep for Atmos. Chem. Phys.*

Aliwell, S. R., M. Van Roozendael, P. V. Johnston, A. Richter, T. Wagner, D. W. Arlander, J. P. Burrows, D. J. Fish, R. L. Jones, K. K. Tornkvist, J. C. Lambert, K. Pfeilsticker, and I. Pundt (2002), Analysis for BrO in zenith-sky spectra: An intercomparison exercise for analysis improvement, *J. Geophys. Res.*, *107*, D14, doi:10.1029/2001JD000329.

Allen, D., K. Pickering, B. Duncan, and M. Damon (2010), Impact of lightning NO emissions on North American photochemistry as determined using the Global Modeling Initiative (GMI) model, *J. Geophys. Res.*, *115*.

Allen, D. R., A. R. Douglass, G. L. Manney, S. E. Strahan, J. C. Krosschell, J. V. Trueblood, J. E. Nielsen, S. Pawson, and Z. Zhu (2011), Modeling the Frozen-In Anticyclone in the 2005 Arctic Summer Stratosphere, *Atmos. Chem. Phys.*, *11*, 4557-4576, doi:10.5194/acp-11-4557-2011.

Anderson, P. S., and W. D. Neff (2008), Boundary layer physics over snow and ice, *Atmos. Chem. Phys.*, *8*, 3563-3582.

Balis, D., I. S. A. Isaksen, C. Zerefos, I. Zyrichidou, K. Eleftheratos, K. Tourpali, R. Bojkov, B. Rognerud, F. Stordal, O. A. Sovde, and Y. Orsolini (2011), Observed and modelled record ozone decline over the Arctic during winter/spring 2011, *Geophys. Res. Lett.*, *38*, L23801, doi:10.1029/2011GL049259.

Barona, I. (2001), USPP (Universal Serial Port Python Library), <*http://sites.google.com/site/ibarona/uspp*>.

Barrie, L. A., J. W. Bottenheim, R. C. Schnell, P. J. Crutzen, and R. A. Rasmussen (1988), Ozone Destruction and Photochemical-Reactions at Polar Sunrise in the Lower Arctic Atmosphere, *Nature*, *334*, 138-141.

Bassford, M. R., C. A. McLinden, and K. Strong (2001), Zenith-sky observations of stratospheric gases: the sensitivity of air mass factors to geophysical parameters and the influence of tropospheric clouds, *J. Quant. Spectrosc. Radiat. Transfer*, *68*, 657-677.

Bassford, M. R., K. Strong, C. A. McLinden, and C. T. McElroy (2005), Ground-based measurements of ozone and NO_2 during MANTRA 1998 using a zenith-sky spectrometer, *Atmos.-Ocean*, *43*, 325-338.

Bassford, M. R., K. Strong, and J. Rebello (2000), An automated spectrometer for monitoring Arctic ozone depletion, *Spectroscopy*, *15*, 42-46.

Batchelor, R. L., F. Kolonjari, R. Lindenmaier, R. L. Mittermeier, W. Daffer, H. Fast, G. Manney, K. Strong, and K. A. Walker (2010), Four Fourier transform spectrometers and the Arctic polar vortex: instrument intercomparison and ACE-FTS validation at Eureka during the IPY springs of 2007 and 2008, *Atmos. Meas. Tech.*, *3*, 51-66, doi:10.5194/amt-3-51-2010.

Batchelor, R. L., K. Strong, R. Lindenmaier, R. L. Mittermeier, H. Fast, J. R. Drummond, and P. F. Fogal (2009), A New Bruker IFS 125HR FTIR Spectrometer for the Polar Environment Atmospheric Research Laboratory at Eureka, Nunavut, Canada: Measurements and Comparison with the Existing Bomem DA8 Spectrometer, *J. Atmos. Ocean. Technol.*, *26*, 1328-1340, doi:10.1175/2009JTECHA1215.1.

Bates, D. R., and M. Nicolet (1950), Atmospheric Hydrogen, *Publications of the Astronomical Society of the Pacific*, *62*, 106-110.

Bernath, P. F., C. T. McElroy, M. C. Abrams, C. D. Boone, M. Butler, C. Camy-Peyret, M. Carleer, C. Clerbaux, P. F. Coheur, R. Colin, P. DeCola, P. F. Bernath, C. T. McElroy, M. C. Abrams, C. D. Boone, M. Butler, C. Camy-Peyret, M. Carleer, C. Clerbaux, P. F. Coheur, R. Colin, P. DeCola, M. DeMaziere, J. R. Drummond, D. Dufour, W. F. J. Evans, H. Fast, D. Fussen, K. Gilbert, D. E. Jennings, E. J. Llewellyn, R. P. Lowe, E. Mahieu, J. C. McConnell, M. McHugh, S. D. McLeod, R. Michaud, C. Midwinter, R. Nassar, F. Nichitiu, C. Nowlan, C. P. Rinsland, Y. J. Rochon, N. Rowlands, K. Semeniuk, P. Simon, R. Skelton, J. J. Sloan, M. A. Soucy, K. Strong, P. Tremblay, D. Turnbull, K. A. Walker, I. Walkty, D. A. Wardle, V. Wehrle, R. Zander, and J. Zou (2005), Atmospheric Chemistry Experiment (ACE): Mission overview, *Geophys. Res. Lett.*, *32*, L15S01, doi:10.1029/2005GL022386.

Blumthaler, M., A. Bais, A. Webb, S. Kazadzis, R. Kift, N. Kouremeti, B. Schallhart, and A. Kazantzidis (2006), Variations of solar radiation at the Earth's surface during the total solar eclipse of 29 March 2006, in *Remote Sensing of Clouds and the Atmosphere XI*, edited by J. R. Slusser et al., pp. U126-U133, SPIE International Society Optical Engineering, Bellingham.

Boersma, K. F., R. Braak, and R. Van Der A (2011), Dutch OMI NO_2 (DOMINO) data product v2.0, <*http://www.temis.nl/docs/OMI_NO2_HE5_2.0_2011.pdf*>.

Boersma, K. F., H. J. Eskes, J. P. Veefkind, E. J. Brinksma, R. J. van der A, M. Sneep, G. H. J. van den Oord, P. F. Levelt, P. Stammes, J. F. Gleason, and E. J. Bucsela (2007), Near-real time retrieval of tropospheric NO2 from OMI, *Atmos. Chem. Phys.*, *7*, 2103-2118.

Bogumil, K., J. Orphal, T. Homann, S. Voigt, P. Spietz, O. C. Fleischmann, A. Vogel, M. Hartmann, H. Kromminga, H. Bovensmann, J. Frerick, and J. P. Burrows (2003), Measurements of molecular absorption spectra with the SCIAMACHY pre-flight model: instrument characterization and reference data for atmospheric remote-sensing in the 230-2380 nm region, *J. Photochem. Photobiol. A-Chem.*, *157*, 167-184, doi:10.1016/S1010-6030(03)00062-5.

Bojkov, R. D. (1968), Ozone variations during solar eclipse of 20 May 1966, *Tellus*, *20*, 417-421.

Boone, C. D., R. Nassar, K. A. Walker, Y. Rochon, S. D. McLeod, C. P. Rinsland, and P. F. Bernath (2005), Retrievals for the Atmospheric Chemistry Experiment Fourier-Transform Spectrometer, *Appl. Opt.*, *44*, 7218-7231, doi:10.1364/AO.44.007218.

Bottenheim, J. W., A. G. Gallant, and K. A. Brice (1986), Measurements of NO_y Species and O_3 at 82°N Latitude, *Geophys. Res. Lett.*, *13*, 113-116.

Bourassa, A. E., D. A. Degenstein, R. L. Gattinger, and E. J. Llewellyn (2007), Stratospheric aerosol retrieval with optical spectrograph and infrared imaging system limb scatter measurements, *J. Geophys. Res.*, *112*, D10217, doi:10.1029/2006JD008079.

Bourassa, A. E., L. A. Rieger, N. D. Lloyd, and D. A. Degenstein (2012), Odin-OSIRIS stratospheric aerosol data product and SAGE III intercomparison, *Atmos. Chem. Phys.*, *12*, 605-614.

Brewer, A. W. (1949), Evidence for a World Circulation Provided by the Measurements of Helium and Water Vapour Distribution in the Stratosphere, *Q. J. R. Meteorol. Soc.*, *75*, 351-363.

Brinksma, E. J., G. Pinardi, H. Volten, R. Braak, A. Richter, A. Schonhardt, M. van Roozendael, C. Fayt, C. Hermans, R. J. Dirksen, T. Vlemmix, A. J. C. Berkhout, D. P. J. Swart, H. Oetjen, F. Wittrock, T. Wagner, O. W. Ibrahim, G. de Leeuw, M. Moerman, R. L. Curier, E. A. Celarier, A.

Cede, W. H. Knap, J. P. Veefkind, H. J. Eskes, M. Allaart, R. Rothe, A. J. M. Piters, and P. F. Levelt (2008), The 2005 and 2006 DANDELIONS NO_2 and aerosol intercomparison campaigns, *J. Geophys. Res.*, *113*, D16S46, doi:10.1029/2007JD008808.

Brohede, S., C. S. Haley, C. A. McLinden, C. E. Sioris, D. P. Murtagh, S. V. Petelina, E. J. Llewellyn, A. Bazureau, F. Goutail, C. E. Randall, J. D. Lumpe, G. Taha, L. W. Thomasson, and L. L. Gordley (2007), Validation of Odin/OSIRIS stratospheric NO_2 profiles, *J. Geophys. Res.*, *112*, D07310, doi:10.1029/2006JD007586.

Brohede, S., C. A. McLinden, J. Urban, C. S. Haley, A. I. Jonsson, and D. Murtagh (2008), Odin stratospheric proxy NO_y measurements and climatology, *Atmos. Chem. Phys.*, *8*, 5731-5754, doi:10.5194/acp-8-5731-2008.

Burrows, J. P., A. Richter, A. Dehn, B. Deters, S. Himmelmann, and J. Orphal (1999a), Atmospheric remote-sensing reference data from GOME—2. Temperature-dependent absorption cross sections of O-3 in the 231-794 nm range, *J. Quant. Spectrosc. Radiat. Transfer*, *61*, 509-517.

Burrows, J. P., M. Weber, M. Buchwitz, V. Rozanov, A. Ladstatter-Weissenmayer, A. Richter, R. DeBeek, R. Hoogen, K. Bramstedt, K. U. Eichmann, and M. Eisinger (1999b), The global ozone monitoring experiment (GOME): Mission concept and first scientific results, *J. Atmos. Sci.*, *56*, 151-175.

Butchart, N., and E. E. Remsberg (1986), The Area of the Stratospheric Polar Vortex as a Diagnostic for Tracer Transport on an Isentropic Surface, *J. Atmos. Sci.*, *43*, 1319-1339.

Chakrabarty, D. K., S. K. Peshin, S. K. Srivastav, N. C. Shah, and K. V. Pandya (2001), Further evidence of total ozone variation during the solar eclipse of 1995, *J. Geophys. Res.*, *106*, 3213-3218.

Chakrabarty, D. K., N. C. Shah, and K. V. Pandya (1997), Fluctuation in ozone column over Ahmedabad during the solar eclipse of 24 October 1995, *Geophys. Res. Lett.*, *24*, 3001-3003.

Chance, K. (1998), Analysis of BrO measurements from the Global Ozone Monitoring Experiment, *Geophys. Res. Lett.*, *25*, 3335-3338.

Chance, K. V., and R. J. D. Spurr (1997), Ring effect studies: Rayleigh scattering, including molecular parameters for rotational Raman scattering, and the Fraunhofer spectrum, *Appl. Opt.*, *36*, 5224-5230.

Chapman, S. (1930), On ozone and atomic oxygen in the upper atmosphere, *Philos. Mag.*, *10*, 369-383.

Charlton, A. J., and L. M. Polvani (2007), A new look at stratospheric sudden warmings. Part I: Climatology and modeling benchmarks, *J. Clim.*, *20*, 449-469.

Chernetenko, Y. A., V. N. L'vov, V. A. Shor, R. I. Smekhacheva, and S. D. Zeckmeister (1992), CERES: the integrated software package for minor planets research, paper presented at Second international workshop on positional astronomy and celestial mechanics, Spain.

Chimonas, G., and C. O. Hines (1971), Atmospheric gravity waves induced by a solar eclipse, 2, *J. Geophys. Res.*, *76*, 7003-7005.

Chipperfield, M. P. (1999), Multiannual simulations with a three-dimensional chemical transport model, *J. Geophys. Res.*, *104*, 1781-1805.

Chipperfield, M. P. (2006), New version of the TOMCAT/SLIMCAT off-line chemical transport model: Intercomparison of stratospheric tracer experiments, *Q. J. R. Meteorol. Soc.*, *132*, 1179-1203, doi:10.1256/qj.05.51.

Chipperfield, M. P., and J. A. Pyle (1998), Model sensitivity studies of Arctic ozone depletion, *J. Geophys. Res.*, *103*, 28389-28403.

Comiso, J. C., C. L. Parkinson, R. Gersten, and L. Stock (2008), Accelerated decline in the Arctic Sea ice cover, *Geophys. Res. Lett.*, *35*, L01703, doi:10.1029/2007GL031972.

Crutzen, P. J. (1970), Influence of Nitrogen Oxides on Atmospheric Ozone Content, *Q. J. R. Meteorol. Soc.*, *96*, 320-325.

Dani, K. K., and P. C. S. Devara (2002), Aerosol optical depth and ozone variations during the total solar eclipse of 24 October 1995, *Atmospheric Research*, *65*, 1-15.

Dee, D. P., S. M. Uppala, A. J. Simmons, P. Berrisford, P. Poli, S. Kobayashi, U. Andrae, M. A. Balmaseda, G. Balsamo, P. Bauer, P. Bechtold, A. C. M. Beljaars, L. van de Berg, J. Bidlot, N. Bormann, C. Delsol, R. Dragani, M. Fuentes, A. J. Geer, L. Haimberger, S. B. Healy, H. Hersbach, E. V. Holm, L. Isaksen, P. Kallberg, M. Koehler, M. Matricardi, A. P. McNally, B. M. Monge-Sanz, J. J. Morcrette, B. K. Park, C. Peubey, P. de Rosnay, C. Tavolato, J. N. Thepaut, and F. Vitart (2011), The ERA-Interim reanalysis: configuration and performance of the data assimilation system, *Q. J. R. Meteorol. Soc.*, *137*, 553-597.

Degenstein, D. A., A. E. Bourassa, C. Z. Roth, and E. J. Llewellyn (2009), Limb scatter ozone retrieval from 10 to 60 km using a multiplicative algebraic reconstruction technique, *Atmos. Chem. Phys.*, *9*, 6521-6529, doi:10.5194/acp-9-6521-2009.

Dirksen, R. J., K. F. Boersma, H. J. Eskes, D. V. Ionov, E. J. Bucsela, P. F. Levelt, and H. M. Kelder (2011), Evaluation of stratospheric NO_2 retrieved from the Ozone Monitoring Instrument: Intercomparison, diurnal cycle, and trending, *J. Geophys. Res.*, *116*, D08305, doi:10.1029/2010JD014943.

Dobson, G. M. B. (1956), Origin and Distribution of the Polyatomic Molecules in the Atmosphere, *Proceedings of the Royal Society of London. Series A, Mathematical and Physical Sciences*, *236*, 187-193.

Donovan, D. P., H. Fast, Y. Makino, J. C. Bird, A. I. Carswell, J. Davies, T. J. Duck, J. W. Kaminski, C. T. McElroy, R. L. Mittermeier, S. R. Pal, V. Savastiouk, D. Velkov, and J. A. Whiteway (1997), Ozone, column ClO, and PSC measurements made at the NDSC Eureka observatory (80 degrees N, 86 degrees W) during the spring of 1997, *Geophys. Res. Lett.*, *24*, 2709-2712.

Duncan, B. N., S. E. Strahan, Y. Yoshida, S. D. Steenrod, and N. Livesey (2007), Model study of the cross-tropopause transport of biomass burning pollution, *Atmos. Chem. Phys.*, *7*, 3713-3736.

Dunkerton, T. J., and D. P. Delisi (1986), Evolution of Potential Vorticity in the Winter Stratosphere of January February 1979, *J. Geophys. Res.*, *91*, 1199-1208.

Dupuy, E., K. A. Walker, J. Kar, C. D. Boone, C. T. McElroy, P. F. Bernath, J. R. Drummond, R. Skelton, S. D. McLeod, R. C. Hughes, C. R. Nowlan, D. G. Dufour, J. Zou, F. Nichitiu, K. Strong, P. Baron, R. M. Bevilacqua, T. Blumenstock, G. E. Bodeker, T. Borsdorff, A. E. Bourassa, H. Bovensmann, I. S. Boyd, A. Bracher, C. Brogniez, J. P. Burrows, V. Catoire, S. Ceccherini, S. Chabrillat, T. Christensen, M. T. Coffey, U. Cortesi, J. Davies, C. De Clercq, D. A. Degenstein, M. De Mazière, P. Demoulin, J. Dodion, B. Firanski, H. Fischer, G. Forbes, L. Froidevaux, D. Fussen, P. Gerard, S. Godin-Beekmann, F. Goutail, J. Granville, D. Griffith, C. S. Haley, J. W. Hannigan, M. Höpfner, J. J. Jin, A. Jones, N. B. Jones, K. Jucks, A. Kagawa, Y. Kasai, T. E. Kerzenmacher, A. Kleinböhl, A. R. Klekociuk, I. Kramer, H. Kullmann, J. Kuttippurath, E. Kyrölä, J. C. Lambert, N. J. Livesey, E. J. Llewellyn, N. D. Lloyd, E. Mahieu, G. L. Manney, B. T. Marshall, J. C. McConnell, M. P. McCormick, I. S. McDermid, M. McHugh, C. A. McLinden, J. Mellqvist, K. Mizutani, Y. Murayama, D. P. Murtagh, H. Oelhaf, A. Parrish, S. V. Petelina, C. Piccolo, J. P. Pommereau, C. E. Randall, C. Robert, C. Roth, M. Schneider, C. Senten, T. Steck, A. Strandberg, K. B. Strawbridge, R. Sussmann, D. P. J. Swart, D. W. Tarasick, J. R. Taylor, C. Tétard, L. W. Thomason, A. M. Thompson, M. B. Tully, J. Urban, F. Vanhellemont, C. Vigouroux, T. von Clarmann, P. von der Gathen, C. von Savigny, J. W. Waters, J. C. Witte, M. Wolff, and J. M. Zawodny (2009), Validation of ozone measurements from the Atmospheric Chemistry Experiment (ACE), *Atmos. Chem. Phys.*, *9*, 287-343, doi:10.5194/acp-9-287-2009.

Eckermann, S. D., D. Broutman, M. T. Stollberg, J. Ma, J. P. McCormack, and T. F. Hogan (2007), Atmospheric effects of the total solar eclipse of 4 December 2002 simulated with a high-altitude global model, *J. Geophys. Res.*, *112*, D14105, doi:10.1029/2006JD007880.

Elansky, N. F., and A. Y. Arabov (1983), Measurements of nitrogen dioxide content in the atmosphere during the solar eclipse of July 31, 1981, *Izv. Acad. Sci. USSR Atmos. Oceanic Phys., Eng. Trans.*, *18*, 511-513.

Elansky, N. F., and A. S. Elokhov (1993), Variation of stratospheric NO_2 during the solar eclipse, *Ozone in the troposphere and the stratosphere, part 2, NASA Conf. Publ. 326, Proc. of 1992 Quadrenn. Ozone Symp.*, *3266*, 699-702.

Emde, C., and B. Mayer (2007), Simulation of solar radiation during a total eclipse: a challenge for radiative transfer, *Atmos. Chem. Phys.*, *7*, 2259-2270.

Eskes, H. J., and K. F. Boersma (2003), Averaging kernels for DOAS total-column satellite retrievals, *Atmos. Chem. Phys.*, *3*, 1285-1291.

Espenak, F., and J. Anderson (2007), Total solar eclipse of 2008 August 01, *NASA Technical Publication*, *214149*.

Eyring, V., I. Cionni, G. E. Bodeker, A. J. Charlton-Perez, D. E. Kinnison, J. F. Scinocca, D. W. Waugh, H. Akiyoshi, S. Bekki, M. P. Chipperfield, M. Dameris, S. Dhomse, S. M. Frith, H. Garny, A. Gettelman, A. Kubin, U. Langematz, E. Mancini, M. Marchand, T. Nakamura, L. D. Oman, S. Pawson, G. Pitari, D. A. Plummer, E. Rozanov, T. G. Shepherd, K. Shibata, W. Tian, P. Braesicke, S. C. Hardiman, J. F. Lamarque, O. Morgenstern, J. A. Pyle, D. Smale, and Y. Yamashita (2010), Multi-model assessment of stratospheric ozone return dates and ozone recovery in CCMVal-2 models, *Atmos. Chem. Phys.*, *10*, 9451-9472.

Fahey, D. W., and A. R. Ravishankara (1999), Summer in the stratosphere, *Science*, *285*, 208-210.

Farahani, E. (2006), Stratospheric composition measurements in the Arctic and at mid-latitudes and comparison with chemical fields from atmospheric models, PhD Thesis, University of Toronto, Toronto, Canada.

Farman, J. C., B. G. Gardiner, and J. D. Shanklin (1985a), Large Losses of Total Ozone in Antarctica Reveal Seasonal ClO_x/NO_x Interaction, *Nature*, *315*, 207-210.

Farman, J. C., R. J. Murgatroyd, A. M. Silnickas, and B. A. Thrush (1985b), Ozone Photochemistry in the Antarctic Stratosphere in Summer, *Q. J. R. Meteorol. Soc.*, *111*, 1013-1025.

Fayt, C., I. De Smedt, V. Letocart, A. Merlaud, G. Pinardi, and M. Van Roozendael (2011), QDOAS Software user manual version 1.00, <http://uv-vis.aeronomie.be/software/QDOAS/index.php>.

Fayt, C., and M. V. Roozendael (2001), WinDOAS 2.1 - Software user manual, Uccle, Belgium.

Feng, W., M. P. Chipperfield, H. K. Roscoe, J. J. Remedios, A. M. Waterfall, G. P. Stiller, N. Glatthor, M. Hopfner, and D. Y. Wang (2005), Three-dimensional model study of the Antarctic ozone hole in 2002 and comparison with 2000, *J. Atmos. Sci.*, *62*, 822-837.

Feng, W., M. P. Chipperfield, D. S., P. von der Gathen, E. Kyro, C. A. Volk, A. Ulanovsky, and G. Belyaev (2007), Large chemical ozone loss in 2004/05 Arctic winter/spring, *Geophys. Res. Lett.*, *34*, L09803, doi:10.1029/2006GL029098.

Fish (1994), Measurements of stratospheric composition using ultraviolet and visible spectroscopy, PhD Thesis, University of Cambridge, Cambridge, UK.

Fish, D. J., and R. L. Jones (1995), Rotational Raman-Scattering And The Ring Effect In Zenith-Sky Spectra, *Geophys. Res. Lett.*, *22*, 811-814.

Fish, D. J., R. L. Jones, and E. K. Strong (1995), Midlatitude Observations Of The Diurnal-Variation Of Stratospheric Bro, *J. Geophys. Res.*, *100*, 18863-18871.

Fleischmann, O. C., M. Hartmann, J. P. Burrows, and J. Orphal (2004), New ultraviolet absorption cross-sections of BrO at atmospheric temperatures measured by time-windowing Fourier transform spectroscopy, *J. Photochem. Photobiol. A-Chem.*, *168*, 117-132.

Fogal, P. F., R. D. Blatherwick, F. J. Murcray, and J. R. Olson (2005), Infra-red FTS measurements of CH_4, N_2O, O_3, HNO_3, HCl, CFC-11 and CFC-12 from the MANTRA balloon campaign, *Atmos.-Ocean*, *43*, 351-359.

Fraser, A. (2008), Arctic and Midlatitude Stratospheric Trace Gas Measurements Using Ground-based UV-visible Spectroscopy, PhD Thesis, University of Toronto, Toronto, Canada.

Fraser, A., C. Adams, J. R. Drummond, F. Goutail, G. Manney, and K. Strong (2009), The Polar Environment Atmospheric Research Laboratory UV-visible ground-based spectrometer: first measurements of O_3, NO_2, BrO, and OClO columns, *J. Quant. Spectrosc. Radiat. Transfer*, *110*, 986-1004, doi:10.1016/j.jqsrt.2009.02.034.

Fraser, A., P. F. Bernath, R. D. Blatherwick, J. R. Drummond, P. F. Fogal, D. Fu, F. Goutail, T. E. Kerzenmacher, C. T. McElroy, C. Midwinter, J. R. Olson, K. Strong, K. A. Walker, D. Wunch, and I. J. Young (2007a), Intercomparison of ground-based ozone and NO_2 measurements during the MANTRA 2004 campaign, *Atmos. Chem. Phys.*, *7*, 5489-5499, doi:10.5194/acp-7-5489-2007.

Fraser, A., F. Goutail, C. A. McLinden, S. M. L. Melo, and K. Strong (2007b), Lightning-produced NO_2 observed by two ground-based UV-visible spectrometers at Vanscoy, Saskatchewan in August 2004, *Atmos. Chem. Phys.*, *7*, 1683-1692.

Fraser, A., F. Goutail, K. Strong, P. F. Bernath, C. Boone, W. H. Daffer, J. R. Drummond, D. G. Dufour, T. E. Kerzenmacher, G. L. Manney, C. T. McElroy, C. Midwinter, C. A. McLinden, F. Nichitiu, C. R. Nowlan, J. Walker, K. A. Walker, H. Wu, and J. Zou (2008), Intercomparison of UV-visible measurements of ozone and NO_2 during the Canadian Arctic ACE validation campaigns: 2004-2006, *Atmos. Chem. Phys.*, *8*, 1763-1788, doi:10.5194/acp-8-1763-2008.

Friedl, R. R., and S. P. Sander (1989), Kinetics And Product Studies Of The Reaction ClO + BrO Using Discharge-Flow Mass-Spectrometry, *J. Phys. Chem.*, *93*, 4756-4764.

Friess, U., T. Deutschmann, B. S. Gilfedder, R. Weller, and U. Platt (2010), Iodine monoxide in the Antarctic snowpack, *Atmos. Chem. Phys.*, *10*, 2439-2456.

Friess, U., J. Hollwedel, G. Konig-Langlo, T. Wagner, and U. Platt (2004), Dynamics and chemistry of tropospheric bromine explosion events in the Antarctic coastal region, *J. Geophys. Res.*, *109*, D06305, doi:10.1029/2003JD004133.

Fritts, D. C., and Z. G. Luo (1993), Gravity-wave forcing in the Middle Atmosphere due to reduced ozone heating during a solar eclipse, *J. Geophys. Res.*, *98*, 3011-3021.

Fu, D. J., K. A. Walker, R. L. Mittermeier, K. Strong, K. Sung, H. Fast, P. F. Bernath, C. D. Boone, W. H. Daffer, P. Fogal, F. Kolonjari, P. Loewen, G. L. Manney, O. Mikhailov, and J. R. Drummond (2011), Simultaneous trace gas measurements using two fourier transform spectrometers at Eureka, Canada during spring 2006, and comparison with the ACE-FTS, *Atmos. Chem. Phys.*, *11*, 5383-5405.

Fu, D. J., K. A. Walker, K. Sung, C. D. Boone, M. A. Soucy, and P. F. Bernath (2007), The portable atmospheric research interferometric spectrometer for the infrared, PARIS-IR, *J. Quant. Spectrosc. Radiat. Transfer*, *103*, 362-370, doi:10.1016/j.jqsrt.2006.05.006.

GCOS (2012), GCOS-Global Climate Observing System, <*http://www.wmo.int/pages/prog/gcos/*>.

Gil, M., O. Puentedura, M. Yela, and E. Cuevas (2000), Behavior of NO_2 and O_3 columns during the eclipse of February 26, 1998, as measured by visible spectroscopy, *J. Geophys. Res.*, *105*, 3583-3593.

Gilman, J. B., J. F. Burkhart, B. M. Lerner, E. J. Williams, W. C. Kuster, P. D. Goldan, P. C. Murphy, C. Warneke, C. Fowler, S. A. Montzka, B. R. Miller, L. Miller, S. J. Oltmans, T. B. Ryerson, O. R. Cooper, A. Stohl, and J. A. de Gouw (2010), Ozone variability and halogen oxidation within the Arctic and sub-Arctic springtime boundary layer, *Atmos. Chem. Phys.*, *10*, 10223-10236.

Grainger, J. F., and J. Ring (1962), Anomalous Fraunhofer line profiles, *Nature*, *193*, 762.

Greenblatt, G. D., J. J. Orlando, J. B. Burkholder, and A. R. Ravishankara (1990), Absorption-measurements of oxygen between 330nm and 1140nm, *J. Geophys. Res.*, *95*, 18577-18582.

Hains, J. C., K. F. Boersma, M. Kroon, R. J. Dirksen, R. C. Cohen, A. E. Perring, E. Bucsela, H. Volten, D. P. J. Swart, A. Richter, F. Wittrock, A. Schoenhardt, T. Wagner, O. W. Ibrahim, M. van Roozendael, G. Pinardi, J. F. Gleason, J. P. Veefkind, and P. Levelt (2010), Testing and improving OMI DOMINO tropospheric NO_2 using observations from the DANDELIONS and INTEX-B validation campaigns, *J. Geophys. Res.*, *115*, D05301, doi:10.1029/2009JD012399.

Hansen, J., M. Sato, R. Ruedy, K. Lo, D. W. Lea, and M. Medina-Elizade (2006), Global temperature change, *Proc. Natl. Acad. Sci. U. S. A.*, *103*, 14288-14293.

Harvey, V. L., M. H. Hitchman, R. B. Pierce, and T. D. Fairlie (1999), Tropical aerosol in the Aleutian High, *J. Geophys. Res.*, *104*, 6281-6290.

Harvey, V. L., R. B. Pierce, T. D. Fairlie, and M. H. Hitchman (2002), A climatology of stratospheric polar vortices and anticyclones, *J. Geophys. Res.*, *107*, 4442, doi:10.1029/2001JD001471.

Harvey, V. L., R. B. Pierce, M. H. Hitchman, C. E. Randall, and T. D. Fairlie (2004), On the distribution of ozone in stratospheric anticyclones, *J. Geophys. Res.*, *109*, D24308, doi:10.1029/2004JD004992.

Harvey, V. L., C. E. Randall, G. L. Manney, and C. S. Singleton (2008), Low-ozone pockets observed by EOS-MLS, *J. Geophys. Res.*, *113*, D17112, doi:10.1029/2007JD009181.

Hausmann, M., and U. Platt (1994), Spectroscopic Measurement of Bromine Oxide and Ozone in the High Arctic During Polar Sunrise Experiment 1992, *J. Geophys. Res.*, *99*, 25399-25413.

Hecht, E. (1987), *Optics*, 2 ed., 220-241 pp., Addison-Wesley, USA.

Hendrick, F., J.-P. Pommereau, F. Goutail, R. D. Evans, D. Ionov, A. Pazmino, E. Kyrö, G. Held, P. Eriksen, V. Dorokhov, M. Gil, and M. V. Roozendael (2011), NDACC/SAOZ UV-visible total ozone measurements: improved retrieval and comparison with correlative satellite and ground-based observations, *Atmos. Chem. Phys.*, *11*, 5975-5995, doi:10.5194/acp-11-5975-2011.

Hendrick, F., M. Van Roozendael, M. P. Chipperfield, M. Dorf, F. Goutail, X. Yang, C. Fayt, C. Hermans, K. Pfeilsticker, J. P. Pommereau, J. A. Pyle, N. Theys, and M. De Maziere (2007), Retrieval of stratospheric and tropospheric BrO profiles and columns using ground-based zenith-sky DOAS observations at Harestua, 60 degrees N, *Atmos. Chem. Phys.*, *7*, 4869-4885.

Hendrick, F., M. Van Roozendael, A. Kylling, A. Petritoli, A. Rozanov, S. Sanghavi, R. Schofield, C. von Friedeburg, T. Wagner, F. Wittrock, D. Fonteyn, and M. De Mazière (2006),

Intercomparison exercise between different radiative transfer models used for the interpretation of ground-based zenith-sky and multi-axis DOAS observations, *Atmos. Chem. Phys.*, *6*, 93-108, doi:10.5194/acp-6-93-2006.

Herman, J. R. (1979), Response of stratospheric constituents to a solar eclipse, sunrise, and sunset, *J. Geophys. Res.-Atmos.*, *84*, 3701-3710.

Herman, J. R., P. K. Bhartia, O. Torres, C. Hsu, C. Seftor, and E. Celarier (1997), Global distribution of UV-absorbing aerosols from Nimbus 7/TOMS data, *J. Geophys. Res.*, *102*, 16911-16922.

Hermans, C. (2004), O_2 and its collisonal induced absorption, <*http://spectrolab.aeronomie.be/o2.htm*>.

Hess, P. G. (1991), Mixing Processes Following the Final Stratospheric Warming, *J. Atmos. Sci.*, *48*, 1625-1641.

Holton, J. R., P. H. Haynes, M. E. McIntyre, A. R. Douglass, R. B. Rood, and L. Pfister (1995), Stratosphere-Troposphere Exchange, *Reviews Of Geophysics*, *33*, 403-439.

Honninger, G., and U. Platt (2002), Observations of BrO and its vertical distribution during surface ozone depletion at Alert, *Atmos. Environ.*, *36*, 2481-2489.

Honninger, G., C. von Friedeburg, and U. Platt (2004), Multi axis differential optical absorption spectroscopy (MAX-DOAS), *Atmos. Chem. Phys.*, *4*, 231-254.

Hood, L. L., B. E. Soukharev, M. Fromm, and J. P. McCormack (2001), Origin of extreme ozone minima at middle to high northern latitudes, *J. Geophys. Res.*, *106*, 20925-20940.

Horiba (2012), Optics Tutorial - Section 1: Diffraction Gratings Ruled & Holographic, <*http://www.horiba.com/scientific/products/optics-tutorial/diffraction-gratings/*>.

IPCC (2007), Climate Change 2007: The Physical Science Basis. Contribution of Working Group 1 to the 4th Assessment Report of the Intergovernmental Panel on Climate Change.

Iwao, K., and T. Hirooka (2006), Dynamical quantifications of ozone minihole formation in both hemispheres, *J. Geophys. Res.*, *111*.

Jacob, D. J. (1999), *Introduction to atmospheric chemistry*, Princeton University Press, Princeton, N.J.

Jacob, D. J. (2000), Heterogeneous chemistry and tropospheric ozone, *Atmos. Environ.*, *34*, 2131-2159.

James, P. M. (1998), A climatology of ozone mini-holes over the northern hemisphere, *Int. J. Climatol.*, *18*, 1287-1303.

Jones, A. E., P. S. Anderson, M. Begoin, N. Brough, M. A. Hutterli, G. J. Marshall, A. Richter, H. K. Roscoe, and E. W. Wolff (2009), BrO, blizzards, and drivers of polar tropospheric ozone depletion events, *Atmos. Chem. Phys.*, *9*, 4639-4652.

Kaleschke, L., A. Richter, J. Burrows, O. Afe, G. Heygster, J. Notholt, A. M. Rankin, H. K. Roscoe, J. Hollwedel, T. Wagner, and H. W. Jacobi (2004), Frost flowers on sea ice as a source of sea salt and their influence on tropospheric halogen chemistry, *Geophys. Res. Lett.*, *31*, L16114, doi:10.1029/2004GL020655.

Kar, J., C. T. McElroy, J. R. Drummond, J. Zou, F. Nichitiu, K. A. Walker, C. E. Randall, C. R. Nowlan, D. G. Dufour, C. D. Boone, P. F. Bernath, C. R. Trepte, L. W. Thomason, and C. McLinden (2007), Initial comparison of ozone and NO_2 profiles from ACE-MAESTRO with balloon and satellite data, *J. Geophys. Res.*, *112*, D16301, doi:10.1029/2006JD008242.

Kerzenmacher, T. E., K. A. Walker, K. Strong, R. Berman, P. F. Bernath, S. J. Bingham, C. D. Boone, J. R. Drummond, H. Fast, P. F. Fogal, A. Fraser, D. Fu, F. Goutail, M. Harwood, P. Loewen, K. MacQuarrie, C. T. McElroy, O. Mikhailov, C. Midwinter, R. Mittermeier, V. Savastiouk, R. Skelton, K. Strawbridge, K. Sung, J. Walker, and H. Wu (2006), Results from the Three Canadian Arctic Validation of ACE Campaigns Conducted at Eureka from 2004 to 2006, 6 pp, Frascati, Italy.

Kerzenmacher, T. E., K. A. Walker, K. Strong, R. Berman, P. F. Bernath, C. D. Boone, J. R. Drummond, H. Fast, A. Fraser, K. MacQuarrie, C. Midwinter, K. Sung, C. T. McElroy, R. L. Mittermeier, J. Walker, and H. J. Wu (2005), Measurements of O_3, NO_2 and temperature during the 2004 Canadian Arctic ACE Validation Campaign, *Geophys. Res. Lett.*, *32*, L16S07, doi:10.1029/2005GL023032.

Kerzenmacher, T. E., M. A. Wolff, K. Strong, E. Dupuy, K. A. Walker, L. K. Amekudzi, R. L. Batchelor, P. F. Bernath, G. Berthet, T. Blumenstock, C. D. Boone, K. Bramstedt, C. Brogniez, S. Brohede, J. P. Burrows, V. Catoire, J. Dodion, J. R. Drummond, D. G. Dufour, B. Funke, D. Fussen, F. Goutail, D. W. T. Griffith, C. S. Haley, F. Hendrick, M. Höpfner, N. Huret, N. Jones, J. Kar, I. Kramer, E. J. Llewellyn, M. López-Puertas, G. Manney, C. T. McElroy, C. A. McLinden, S. Melo, S. Mikuteit, D. Murtagh, F. Nichitiu, J. Notholt, C. Nowlan, C. Piccolo, J. P. Pommereau, C. Randall, P. Raspollini, M. Ridolfi, A. Richter, M. Schneider, O. Schrems, M. Silicani, G. P. Stiller, J. Taylor, C. Tétard, M. Toohey, F. Vanhellemont, T. Warneke, J. M. Zawodny, and J. Zou (2008), Validation of NO_2 and NO from the Atmospheric Chemistry Experiment (ACE), *Atmos. Chem. Phys.*, *8*, 5801-5841, doi:10.5194/acp-8-5801-2008.

Koepke, P., J. Reuder, and J. Schween (2001), Spectral variation of the solar radiation during an eclipse, *Meteorologische Zeitschrift*, *10*, 179-186.

Konopka, P., A. Engel, B. Funke, R. Mueller, J.-U. Grooss, G. Guenther, T. Wetter, G. Stiller, T. von Clarmann, N. Glatthor, H. Oelhaf, G. Wetzel, M. Lopez-Puertas, M. Pirre, N. Huret, and M. Riese (2007), Ozone loss driven by nitrogen oxides and triggered by stratospheric warmings can outweigh the effect of halogens, *J. Geophys. Res.*, *112*, D05105, doi:10.1029/2006JD007064.

Konor, C. S., and A. Arakawa (1997), Design of an atmospheric model based on a generalized vertical coordinate, *Mon. Weather Rev.*, *125*, 1649-1673.

Kovalenko, L. J., N. L. Livesey, R. J. Salawitch, C. Camy-Peyret, M. P. Chipperfield, R. E. Cofield, M. Dorf, B. J. Drouin, L. Froidevaux, R. A. Fuller, F. Goutail, R. F. Jarnot, K. Jucks, B. W. Knosp, A. Lambert, I. A. MacKenzie, K. Pfeilsticker, J. P. Pommereau, W. G. Read, M. L. Santee, M. J. Schwartz, W. V. Snyder, R. Stachnik, P. C. Stek, P. A. Wagner, and J. W. Waters

(2007), Validation of Aura Microwave Limb Sounder BrO observations in the stratosphere, *J. Geophys. Res.*, *112*.

Kromminga, H., J. Orphal, P. Spietz, S. Voigt, and J. P. Burrows (2003), New measurements of OClO absorption cross-sections in the 325-435 nm region and their temperature dependence between 213 and 293 K, *J. Photochem. Photobiol. A-Chem.*, *157*, 149-160.

Krueger, A. J., and R. A. Minzner (1976), Mid-Latitude Ozone Model for the 1976 U.S. Standard Atmosphere, *J. Geophys. Res.*, *81*, 4477-4481.

Kurucz, R. L., I. Furenlid, J. Brault, and L. Testerman (1984), *Solar flux atlas from 296 to 1300 nm*, National Solar Observatory, Sunspot, New Mexico, USA.

Kurylo, M. J., and R. J. Zander (2000), The NDSC - Its status after ten years of operation., paper presented at Proceedings of the Quadrennial Ozone Symposium, Sapporo, Japan, 3-8 July, 2000.

Lahoz, W. A., A. J. Geer, and Y. J. Orsolini (2007), Northern Hemisphere stratospheric summer from MIPAS observations, *Q. J. R. Meteorol. Soc.*, *133*, 197-211.

Lam, K. S., V. Savastiouk, W. Y. Fung, T. K. Chan, and K. Lamb (2007), Recalculation of 11-year total ozone of Brewer spectrophotometer 115, *J. Geophys. Res.*, *112*, D15104, doi:10.1029/2006JD008178.

Lambert, J.-C., J. Granville, M. Van Roozendael, A. Sarkissian, F. Goutail, J.-F. Müller, J.-P. Pommereau, and J. M. Russell III (1999), A climatology of NO_2 profile for improved Air Mass Factors for ground-based vertical column measurements, Stratospheric Ozone 1999, Air Pollution Research Report 73 (CEC DG XII), 703-706 pp.

Lambert, J.-C., J. Granville, M. Van Roozendael, A. Sarkissian, F. Goutail, J.-F. Müller, J.-P. Pommereau, and J. M. Russell III (2000), Global Behaviour of Atmospheric NO_2 as Derived from the Integrated Use of Satellite, Ground-based Network and Balloon Observations, paper presented at Proeedings 19th Quad. Ozone Symp., Sapporo, Japan.

Lesins, G., T. J. Duck, and J. R. Drummond (2010), Climate Trends at Eureka in the Canadian High Arctic, *Atmos.-Ocean*, *48*, 59-80.

Levelt, P. F., G. H. J. Van den Oord, M. R. Dobber, A. Malkki, H. Visser, J. de Vries, P. Stammes, J. O. V. Lundell, and H. Saari (2006), The Ozone Monitoring Instrument, *IEEE Trans. Geosci. Remote Sensing*, *44*, 1093-1101.

Lindenmaier, R., R. L. Batchelor, K. Strong, H. Fast, F. Goutail, F. Kolonjari, C. T. McElroy, R. L. Mittermeier, and K. A. Walker (2010), An evaluation of infrared microwindows for ozone retrievals using the Eureka Bruker 125HR Fourier transform spectrometer, *J. Quant. Spectrosc. Radiat. Transfer*, *111*, 569-585, doi:10.1016/j.jqsrt.2009.10.013.

Lindenmaier, R., K. Strong, R. L. Batchelor, P. F. Bernath, S. Chabrillat, M. Chipperfield, W. H. Daffer, J. R. Drummond, W. Feng, A. I. Jonsson, F. Kolonjari, G. L. Manney, C. A. McLinden, R. Menard, and K. A. Walker (2011), A study of the NO_y budget above Eureka, Canada, *J. Geophys. Res.*, *116*, D23302, doi:10.1029/2011JD016207.

Lindenmaier, R., K. Strong, R. L. Batchelor, M. Chipperfield, W. Daffer, J. R. Drummond, T. J. Duck, H. Fast, W. Feng, P. F. Fogal, F. Kolonjari, G. L. Manney, A. Manson, C. Meek, R. Mittermeier, G. J. Nott, C. Perro, and K. A. Walker (2012), Unusually low ozone, HCl, and HNO_3 column measurements at Eureka, Canada during winter/spring 2011, *Atmos. Chem. Phys.*, *12*, 3821-3835, doi:10.5194/acp-12-3821-2012.

Liou, N. K. (2002), *An Introduction to Atmospheric Radiation*, Academic Press, New York.

Llewellyn, E., N. D. Lloyd, D. A. Degenstein, R. L. Gattinger, S. V. Petelina, A. E. Bourassa, J. T. Wiensz, E. V. Ivanov, I. C. McDade, B. H. Solheim, J. C. McConnell, C. S. Haley, C. von Savigny, C. E. Sioris, C. A. McLinden, E. Griffioen, J. Kaminski, W. F. J. Evans, E. Puckrin, K. Strong, V. Wehrle, R. H. Hum, D. J. W. Kendall, J. Matsushita, D. P. Murtagh, S. Brohede, J. Stegman, G. Witt, G. Barnes, W. F. Payne, L. Piche, K. Smith, G. Warshaw, D. L. Deslauniers, P. Marchand, E. H. Richardson, R. A. King, I. Wevers, W. McCreath, E. Kyrola, L. Oikarinen, G. W. Leppelmeier, H. Auvinen, G. Megie, A. Hauchecorne, F. Lefevre, J. de La Noe, P. Ricaud, U. Frisk, F. Sjoberg, F. von Scheele, and L. Nordh (2004), The OSIRIS instrument on the Odin spacecraft, *Can. J. Phys.*, *82*, 411-422.

Lundh, F. (2005), Python Imaging Library Handbook, <http://www.pythonware.com/library/pil/handbook/index.htm>.

Mackay, C. (1986), Charge-coupled devices in astronomy, *Annual Review of Astronomy and Astrophysics*, *24*, 255-283.

Malicet, J., D. Daumont, J. Charbonnier, C. Parisse, A. Chakir, and J. Brion (1995), Ozone UV Spectroscopy 2: Absorption Cross-Sections and Temperature-Dependence, *J. Atmos. Chem.*, *21*, 263-273.

Manney, G. L., W. H. Daffer, J. M. Zawodny, P. F. Bernath, K. W. Hoppel, K. A. Walker, B. W. Knosp, C. Boone, E. E. Remsberg, M. L. Santee, V. L. Harvey, S. Pawson, D. R. Jackson, L. Deaver, C. T. McElroy, C. A. McLinden, J. R. Drummond, H. C. Pumphrey, A. Lambert, M. J. Schwartz, L. Froidevaux, S. McLeod, L. L. Takacs, M. J. Suarez, C. R. Trepte, D. C. Cuddy, N. J. Livesey, R. S. Harwood, and J. W. Waters (2007), Solar occultation satellite data and derived meteorological products: Sampling issues and comparisons with Aura Microwave Limb Sounder, *J. Geophys. Res.*, *112*, D24S50, doi:10.1029/2007JD008709.

Manney, G. L., L. Froidevaux, J. W. Waters, R. W. Zurek, J. C. Gille, J. B. Kumer, J. L. Mergenthaler, A. E. Roche, A. Oneill, and R. Swinbank (1995a), Formation Of Low-Ozone Pockets In The Middle Stratospheric Anticyclone During Winter, *J. Geophys. Res.*, *100*, 13939-13950.

Manney, G. L., N. J. Livesey, C. J. Jimenez, H. C. Pumphrey, M. L. Santee, I. A. MacKenzie, and J. W. Waters (2006), EOS Microwave Limb Sounder observations of "frozen-in" anticyclonic air in arctic summer, *Geophys. Res. Lett.*, *33*, L06810, doi:10.1029/2005GL025418.

Manney, G. L., M. L. Santee, M. Rex, N. J. Livesey, M. C. Pitts, P. Veefkind, E. R. Nash, I. Wohltmann, R. Lehmann, L. Froidevaux, L. R. Poole, M. R. Schoeberl, D. P. Haffner, J. Davies, V. Dorokhov, H. Gernandt, B. Johnson, R. Kivi, E. Kyro, N. Larsen, P. F. Levelt, A. Makshtas, C. T. McElroy, H. Nakajima, M. C. Parrondo, D. W. Tarasick, P. von der Gathen, K. A. Walker, and N. S. Zinoviev (2011), Unprecedented Arctic ozone loss in 2011, *Nature*, *478*, 469-475, doi:10.1038/nature10556.

Manney, G. L., R. W. Zurek, L. Froidevaux, J. W. Waters, A. Oneill, and R. Swinbank (1995b), Lagrangian Transport Calculations Using UARS Data. 2. Ozone, *J. Atmos. Sci.*, *52*, 3069-3081.

Manney, G. L., R. W. Zurek, A. Oneill, and R. Swinbank (1994), On The Motion of Air Through the Stratospheric Polar Vortex, *J. Atmos. Sci.*, *51*, 2973-2994.

McConnell, J. C., G. S. Henderson, L. Barrie, J. Bottenheim, H. Niki, C. H. Langford, and E. M. J. Templeton (1992), Photochemical Bromine Production Implicated in Arctic Boundary-Layer Ozone Depletion, *Nature*, *355*, 150-152.

McElroy, C. T. (1995), A Spectroradiometer for the Measurement of Direct and Scattered Solar Irradiance from On-Board The NASA ER-2 High-Altitude Research Aircraft, *Geophys. Res. Lett.*, *22*, 1361-1364.

McElroy, C. T., C. R. Nowlan, J. R. Drummond, P. F. Bernath, D. V. Barton, D. G. Dufour, C. Midwinter, R. B. Hall, A. Ogyu, A. Ullberg, D. I. Wardle, J. Kar, J. Zou, F. Nichitiu, C. D. Boone, K. A. Walker, and N. Rowlands (2007), The ACE-MAESTRO instrument on SCISAT: description, performance, and preliminary results, *Appl. Opt.*, *46*, 4341-4356, doi:10.1364/AO.46.004341.

McElroy, M. B., and R. J. Salawitch (1989), Changing Composition of the Global Stratosphere, *Science*, *243*, 763-770.

McElroy, M. B., R. J. Salawitch, S. C. Wofsy, and J. A. Logan (1986), Reductions of Antarctic Ozone due to Synergistic Interactions of Chlorine and Bromine, *Nature*, *321*, 759-762.

McLinden, C. A., C. S. Haley, N. D. Lloyd, F. Hendrick, A. Rozanov, B. M. Sinnhuber, F. Goutail, D. A. Degenstein, E. J. Llewellyn, C. E. Sioris, M. Van Roozendael, J. P. Pommereau, W. Lotz, and J. P. Burrows (2010), Odin/OSIRIS observations of stratospheric BrO: Retrieval methodology, climatology, and inferred Br_y, *J. Geophys. Res.*, *115*, D15308, doi:10.1029/2009JD012488.

McLinden, C. A., C. S. Haley, and C. E. Sioris (2006), Diurnal effects in limb scatter observations, *J. Geophys. Res.*, *111*, D14302, doi:10.1029/2005JD006628.

McLinden, C. A., J. C. McConnel, E. Griffioen, and C. T. McElroy (2002), A vector radiative-transfer model for the Odin/OSIRIS project, *Can. J. Phys.*, *80*, 375-393, doi:10.1139/P01-156.

McLinden, C. A., S. C. Olsen, B. Hannegan, O. Wild, M. J. Prather, and J. Sundet (2000), Stratospheric ozone in 3-D models: A simple chemistry and the cross-tropopause flux, *J. Geophys. Res.*, *105*, 14653-14665.

McPeters, R., M. Kroon, G. Labow, E. Brinksma, D. Balis, I. Petropavlovskikh, J. P. Veefkind, P. K. Bhartia, and P. F. Levelt (2008), Validation of the Aura Ozone Monitoring Instrument total column ozone product, *J. Geophys. Res.*, *113*, D15S14, doi:10.1029/2007JD008802.

McPeters, R. D., G. J. Labow, and J. A. Logan (2007), Ozone climatological profiles for satellite retrieval algorithms, *J. Geophys. Res.*, *112*, D05308, doi:10.1029/2005JD006823.

Meller, R., and G. K. Moortgat (2000), Temperature dependence of the absorption cross sections of formaldehyde between 223 and 323 K in the wavelength range 225-375 nm, *J. Geophys. Res.*, *105*, 7089-7101.

Melo, S. M. L., E. Farahani, K. Strong, M. R. Bassford, K. E. Preston, and C. A. McLinden (2004), NO_2 vertical profiles retrieved from ground-based measurements during spring 1999 in the Canadian Arctic, *Adv. Space Res.*, *34*, 786-792.

Melo, S. M. L., K. Strong, M. R. Bassford, K. E. Preston, C. T. McElroy, E. V. Rozanov, and T. Egorova, G. (2005), Retrieval of stratospheric NO_2 vertical profiles from ground- based zenith-sky DOAS measurements: Results for the MANTRA 1998 field campaign, *Atmos.-Ocean*, *43*, 339–350.

Melsheimer, C., G. Heygster, and J. Notholt (2011), Arctic warming: Sea-ice minimum is not a one-off, *Nature*, *478*, 188.

Merlaud, A. (2011), Equations for solar tracking, <*http://arxiv.org/abs/1102.3825v1*>.

Mims, F. M., and E. R. Mims (1993), Fluctuations in column ozone during the total solar eclipse of July 11, 1991, *Geophys. Res. Lett.*, *20*, 367-370.

Molina, L. T., and M. J. Molina (1987), Production of Cl_2O_2 from the self-reaction of the ClO radical, *J. Phys. Chem.*, *91*, 433-436.

Molina, M. J., and F. S. Rowland (1974), Stratospheric Sink for Chlorofluoromethanes - Chlorine Atomic-Catalysed Destruction of Ozone, *Nature*, *249*, 810-812.

Montzka, S. A., J. H. Butler, B. D. Hall, D. J. Mondeel, and J. W. Elkins (2003), A decline in tropospheric organic bromine, *Geophys. Res. Lett.*, *30*, 1826-1830, doi:10.1029/2003GL017745.

Morris, G. A., S. R. Kawa, A. R. Douglass, M. R. Schoeberl, L. Froidevaux, and J. Waters (1998), Low-ozone pockets explained, *J. Geophys. Res.*, *103*, 3599-3610.

Murtagh, D., U. Frisk, F. Merino, M. Ridal, A. Jonsson, J. Stegman, G. Witt, P. Eriksson, C. Jimenez, G. Megie, J. de la Noe, P. Ricaud, P. Baron, J. R. Pardo, A. Hauchcorne, E. J. Llewellyn, D. A. Degenstein, R. L. Gattinger, N. D. Lloyd, W. F. J. Evans, I. C. McDade, C. S. Haley, C. Sioris, C. von Savigny, B. H. Solheim, J. C. McConnell, K. Strong, E. H. Richardson, G. W. Leppelmeier, E. Kyrola, H. Auvinen, and L. Oikarinen (2002), An overview of the Odin atmospheric mission, *Can. J. Phys.*, *80*, 309-319.

Nagatani, R. M., and J. E. Rosenfield (1993), Temperature, net heating and circulation, *The Atmospheric Effects of Stratospheric Aircraft: Report of the 1992 Models and Measurements Workshop*, A1-A47.

Nair, H., M. Allen, L. Froidevaux, and R. W. Zurek (1998), Localized rapid ozone loss in the northern winter stratosphere: An analysis of UARS observations, *J. Geophys. Res.*, *103*, 1555-1571.

NDACC (2009), Appendix VII - UV/Vis Instruments, <*http://www.ndacc.org/*>.

Newchurch, M. J., M. Allen, M. R. Gunson, R. J. Salawitch, G. B. Collins, K. H. Huston, M. M. Abbas, M. C. Abrams, A. Y. Chang, D. W. Fahey, R. S. Gao, F. W. Irion, M. Loewenstein, G. L. Manney, H. A. Michelsen, J. R. Podolske, C. P. Rinsland, and R. Zander (1996), Stratospheric NO and NO_2 abundances from ATMOS solar-occultation measurements, *Geophys. Res. Lett.*, *23*, 2373-2376.

Newchurch, M. J., E. S. Yang, D. M. Cunnold, G. C. Reinsel, J. M. Zawodny, and J. M. Russell (2003), Evidence for slowdown in stratospheric ozone loss: First stage of ozone recovery, *J. Geophys. Res.*, *108*, 4507-4520, doi:10.1029/2003JD003471.

Newport (2011), Oriel Pencil Style Calibration Lamps, <*http://assets.newport.com/pdfs/e5395.pdf*>.

Noxon, J. F. (1975), Nitrogen-dioxide in stratosphere and troposphere measured by ground-based absorption spectroscopy, *Science*, *189*, 547-549.

Noxon, J. F., E. C. Whipple, and R. S. Hyde (1979), Stratospheric NO_2 1: Observational Method and Behavior at Mid-Latitude, *J. Geosphys. Res.*, *84*, 5047-5065.

NSIDC (2011), Arctic Sea Ice News & Analysis, <*http://nsidc.org/arcticseaicenews/*>.

Oetjen, H., F. Wittrock, A. Richter, M. P. Chipperfield, T. Medeke, N. Sheode, B. M. Sinnhuber, M. Sinnhuber, and J. P. Burrows (2011), Evaluation of stratospheric chlorine chemistry for the Arctic spring 2005 using modelled and measured OClO column densities, *Atmos. Chem. Phys.*, *11*, 689-703.

Olsen, S. C., C. A. McLinden, and M. J. Prather (2001), Stratospheric N_2O-NO_y system: Testing uncertainties in a three-dimensional framework, *J. Geophys. Res.*, *106*, 771-784.

OMI (2008), OMBRO readme file, <*https://www.cfa.harvard.edu/~tkurosu/SatelliteInstruments/OMI/PGEReleases/READMEs/OMBRO_README.pdf*>.

Orsolini, Y. J., H. Eskes, G. Hansen, U. P. Hoppe, A. Kylling, E. Kyro, J. Notholt, R. Van Der A, and P. Von Der Gathen (2003), Summertime low-ozone episodes at northern high latitudes, *Q. J. R. Meteorol. Soc.*, *129*, 3265-3275.

Orsolini, Y. J., and G. Nikulin (2006), A low-ozone episode during the European heatwave of August 2003, *Q. J. R. Meteorol. Soc.*, *132*, 667-680.

OSIRIS (2011), Odin-OSIRIS NO_2 data product, <*http://osirus.usask.ca/?q=node/245*>.

Perliski, L. M., S. Solomon, and J. London (1989), On the Interpretation of Seasonal-Variations of Stratospheric Ozone, *Planet. Space Sci.*, *37*, 1527-1538.

Perrin, F. H. (1948), Whose absorption law? *J. Opt. Soc. Am.*, *38*, 78-74.

Peters, D., J. Egger, and G. Entzian (1995), Dynamical Aspects of Ozone Mini-Hole Formation, *Meteorol. Atmos. Phys.*, *55*, 205-214.

Pfeilsticker, K., F. Erle, O. Funk, L. Marquard, T. Wagner, and U. Platt (1998), Optical path modifications due to tropospheric clouds: Implications for zenith sky measurements of stratospheric gases, *J. Geophys. Res.*, *103*, 25323-25335.

Pfeilsticker, K., F. Erle, and U. Platt (1999), Observation of the stratospheric NO_2 latitudinal distribution in the northern winter hemisphere, *J. Atmos. Chem.*, *32*, 101-120.

Pierce, A. K. (1968), Chromospheric spectrum outside of eclipse, λλ 3040 to 9266 A^o, *Astrophysical Journal Supplement Series*, *17*, 1-370.

Pinardi, G., M. Van Roozendael, C. Adams, S. Beirle, A. Cede, K. Clémer, C. Fayt, U. Friess, M. Gil, C. Hermans, F. Hendrick, H. Irie, A. Merlaud, E. Peters, A. Piters, O. Puentedura, A. Richter, R. Shaigan, E. Spinei, K. Strong, H. Takashima, T. Wagner, F. Wittrock, and S. Yilmaz (2012), Intercomparison of MAXDOAS formaldehyde slant columns during the CINDI campaign, *in preparation, Atmos. Meas. Tech.*

Piters, A. J. M., K. F. Boersma, M. Kroon, J. C. Hains, M. Van Roozendael, F. Wittrock, N. Abuhassan, C. Adams, M. Akrami, M. A. F. Allaart, A. Apituley, J. B. Bergwerff, A. J. C. Berkhout, D. Brunner, A. Cede, J. Chong, K. Clémer, C. Fayt, U. Frieß, L. F. L. Gast, M. Gil-Ojeda, F. Goutail, R. Graves, A. Griesfeller, K. Großmann, G. Hemerijckx, F. Hendrick, B. Henzing, J. Herman, C. Hermans, M. Hoexum, G. R. van der Hoff, H. Irie, P. V. Johnston, Y. Kanaya, Y. J. Kim, H. Klein Baltink, K. Kreher, G. de Leeuw, R. Leigh, A. Merlaud, M. M. Moerman, P. S. Monks, G. H. Mount, M. Navarro-Comas, H. Oetjen, A. Pazmino, M. Perez-Camacho, E. Peters, A. du Piesanie, G. Pinardi, O. Puentadura, A. Richter, H. K. Roscoe, A. Schönhardt, B. Schwarzenbach, R. Shaiganfar, W. Sluis, E. Spinei, A. P. Stolk, K. Strong, D. P. J. Swart, H. Takashima, T. Vlemmix, M. Vrekoussis, T. Wagner, C. Whyte, K. M. Wilson, M.

Yela, S. Yilmaz, P. Zieger, and Y. Zhou (2012), The Cabauw Intercomparison campaign for Nitrogen Dioxide measuring Instruments (CINDI): design, execution, and early results, *Atmos. Meas. Tech.*, *5*, 457-485, doi:10.5194/amt-5-457-2012.

Platt, U., D. Perner, and H. W. Patz (1979), Simultaneous measurement of atmospheric CH_2O, O_3, and NO_2 by differential optical-absorption, *J. Geophys. Res.*, *84*, 6329-6335.

Platt, U., and J. Stutz (2008), *Differential Optical Absorption Spectroscopy (DOAS)*, Springer, Germany.

Pohler, D., L. Vogel, U. Friess, and U. Platt (2010), Observation of halogen species in the Amundsen Gulf, Arctic, by active long-path differential optical absorption spectroscopy, *Proc. Natl. Acad. Sci. U. S. A.*, *107*, 6582-6587.

Polvani, L. M., D. W. Waugh, G. J. P. Correa, and S.-W. Son (2011), Stratospheric Ozone Depletion: The Main Driver of Twentieth-Century Atmospheric Circulation Changes in the Southern Hemisphere, *J. Clim.*, *24*, 795-812.

Pommereau, J. P., and F. Goutail (1988), O_3 and NO_2 ground-based measurements by visible spectrometry during Arctic winter and spring 1988, *Geophys. Res. Lett.*, *15*, 891-894.

Pommereau, J. P., A. Hauchecorne, and G. Souchon (1976), Variation of atmospheric NO_2 total content observed during a solar eclipse - diurnal-variation in tropics, *C. R. Seances Acad. Sci., Ser. B*, *283*, 163-165.

Pougatchev, N. S., B. J. Connor, and C. P. Rinsland (1995), Infrared Measurements of the Ozone Vertical Distribution Above Kitt Peak, *J. Geophys. Res.*, *100*, 16689-16697.

Prather, M. (1992), Catastrophic Loss of Stratospheric Ozone in Dense Volcanic Clouds, *J. Geophys. Res.*, *97*, 10187-10191.

Prather, M., and A. H. Jaffe (1990), Global Impact of the Antarctic Ozone Hole - Chemical-Propagation, *J. Geophys. Res.*, *95*, 3473-3492.

Preston, K. E., R. L. Jones, and H. K. Roscoe (1997), Retrieval of NO_2 vertical profiles from ground-based UV-visible measurements: Method and validation, *J. Geophys. Res.*, *102*, 19089-19097.

Randel, W. J., K. P. Shine, J. Austin, J. Barnett, C. Claud, N. P. Gillett, P. Keckhut, U. Langematz, R. Lin, C. Long, C. Mears, A. Miller, J. Nash, D. J. Seidel, D. W. J. Thompson, F. Wu, and S. Yoden (2009), An update of observed stratospheric temperature trends, *J. Geophys. Res.*, *114*, D02107, doi:10.1029/2008JD010421.

Rankin, A. M., E. W. Wolff, and S. Martin (2002), Frost flowers: Implications for tropospheric chemistry and ice core interpretation, *J. Geophys. Res.*, *107*, 4683-4698, doi:10.1029/2002JD002492.

Ravishankara, A. R., J. S. Daniel, and R. W. Portmann (2009), Nitrous Oxide (N_2O): The Dominant Ozone-Depleting Substance Emitted in the 21st Century, *Science*, *326*, 123-125.

Reinecker, M. M., M. J. Suarez, R. Todling, J. Bacmeister, L. L. Takacs, H.-C. Liu, W. Gu, M. Sienkiewicz, R. D. Koster, R. Gelaro, I. Stajner, and J. E. Nielsen (2008), The GEOS-5 data assimilation system - Documentation of versions 5.0.1, 5.1.0, and 5.2.0, *NASA Tech. Memo., TM-2008-104606*, *27*, 1-118.

Rex, M., R. J. Salawitch, P. von der Gathen, N. R. P. Harris, M. P. Chipperfield, and B. Naujokat (2004), Arctic ozone loss and climate change, *Geophys. Res. Lett.*, *31*, L04116, doi:10.1029/2003GL018844.

Rhodes, B. C. (2010), PyEphem, <*http://rhodesmill.org/pyephem/*>.

Rienecker, M. M., M. J. Suarez, R. Gelaro, R. Todling, J. Bacmeister, E. Liu, M. G. Bosilovich, S. D. Schubert, L. Takacs, G.-K. Kim, S. Bloom, J. Chen, D. Collins, A. Conaty, A. da Silva, W. Gu, J. Joiner, R. D. Koster, R. Lucchesi, A. Molod, T. Owens, S. Pawson, P. Pegion, C. R. Redder, R. Reichle, F. R. Robertson, A. G. Ruddick, M. Sienkiewicz, and J. Woollen (2011), MERRA: NASA's Modern-Era Retrospective Analysis for Research and Applications, *J. Clim.*, *24*, 3624-3628.

Rienecker, M. M., M. J. Suarez, R. Todling, J. Bacmeister, L. L. Takacs, H.-C. Liu, W. Gu, M. Sienkiewicz, R. D. Koster, R. Gelaro, I. Stajner, and J. E. Nielsen (2008), The GEOS-5 data assimilation system - Documentation of versions 5.0.1, 5.1.0, and 5.2.0, *NASA Tech. Memo., TM-2008-104606*, *27*, 1-118.

Rind, D., D. Shindell, P. Lonergan, and N. K. Balachandran (1998), Climate change and the middle atmosphere. Part III: The doubled CO_2 climate revisited, *J. Clim.*, *11*, 876-894.

Rodgers, C. D. (2000), *Inverse methods for atmospheric sounding: theory and practice*, World Scientic Co. Pte. Ltd.

Rodgers, C. D., and B. J. Connor (2003), Intercomparison of remote sounding instruments, *J. Geophys. Res.*, *108*, 4116, doi:10.1029/2002JD002299.

Roscoe, H. K., A. J. Charlton, D. J. Fish, and J. G. T. Hill (2001), Improvements to the accuracy of measurements of NO_2 by zenith-sky visible spectrometers II: errors in zero using a more complete chemical model, *J. Quant. Spectrosc. Radiat. Transfer*, *68*, 337-349.

Roscoe, H. K., D. J. Fish, and R. L. Jones (1996), Interpolation errors in UV-visible spectroscopy for stratospheric sensing: Implications for sensitivity, spectral resolution, and spectral range, *Appl. Opt.*, *35*, 427-432.

Roscoe, H. K., P. V. Johnston, M. Van Roozendael, A. Richter, A. Sarkissian, J. Roscoe, K. E. Preston, J. C. Lambert, C. Hermans, W. Decuyper, S. Dzienus, T. Winterrath, J. Burrows, F. Goutail, J. P. Pommereau, E. D'Almeida, J. Hottier, C. Coureul, R. Didier, I. Pundt, L. M. Bartlett, C. T. McElroy, J. E. Kerr, A. Elokhov, G. Giovanelli, F. Ravegnani, M. Premuda, I. Kostadinov, F. Erle, T. Wagner, K. Pfeilsticker, M. Kenntner, L. C. Marquard, M. Gil, O. Puentedura, M. Yela, D. W. Arlander, B. A. K. Hoiskar, C. W. Tellefsen, K. K. Tornkvist, B. Heese, R. L. Jones, S. R. Aliwell, and R. A. Freshwater (1999), Slant column measurements of O_3 and NO_2 during the NDSC intercomparison of zenith-sky UV-visible spectrometers in June 1996, *J. Atmos. Chem.*, *32*, 281-314.

Roscoe, H. K., M. Van Roozendael, C. Fayt, A. du Piesanie, N. Abuhassan, C. Adams, M. Akrami, A. Cede, J. Chong, K. Clémer, U. Friess, M. Gil Ojeda, F. Goutail, R. Graves, A.

Griesfeller, K. Grossmann, G. Hemerijckx, F. Hendrick, J. Herman, C. Hermans, H. Irie, P. V. Johnston, Y. Kanaya, K. Kreher, R. Leigh, A. Merlaud, G. H. Mount, M. Navarro, H. Oetjen, A. Pazmino, M. Perez-Camacho, E. Peters, G. Pinardi, O. Puentedura, A. Richter, A. Schönhardt, R. Shaiganfar, E. Spinei, K. Strong, H. Takashima, T. Vlemmix, M. Vrekoussis, T. Wagner, F. Wittrock, M. Yela, S. Yilmaz, F. Boersma, J. Hains, M. Kroon, and A. Piters (2010), Intercomparison of slant column measurements of NO_2 and O_4 by MAX-DOAS and zenith-sky UV and visible spectrometers, *Atmos. Meas. Tech.*, *3*, 1629-1646, doi:10.5194/amt-3-1629-2010.

Rothman, L. S., A. Barbe, D. C. Benner, L. R. Brown, C. Camy-Peyret, M. R. Carleer, K. Chance, C. Clerbaux, V. Dana, V. M. Devi, A. Fayt, J. M. Flaud, R. R. Gamache, A. Goldman, D. Jacquemart, K. W. Jucks, W. J. Lafferty, J. Y. Mandin, S. T. Massie, V. Nemtchinov, D. A. Newnham, A. Perrin, C. P. Rinsland, J. Schroeder, K. M. Smith, M. A. H. Smith, K. Tang, R. A. Toth, J. Vander Auwera, P. Varanasi, and K. Yoshino (2003), The HITRAN molecular spectroscopic database: edition of 2000 including updates through 2001, *J. Quant. Spectrosc. Radiat. Transfer*, *82*, 5-44, doi:10.1016/S0022-4073(03)00146-8.

Rothman, L. S., D. Jacquemart, A. Barbe, D. C. Benner, M. Birk, L. R. Brown, M. R. Carleer, C. Chackerian, K. Chance, L. H. Coudert, V. Dana, V. M. Devi, J. M. Flaud, R. R. Gamache, A. Goldman, J. M. Hartmann, K. W. Jucks, A. G. Maki, J. Y. Mandin, S. T. Massie, J. Orphal, A. Perrin, C. P. Rinsland, M. A. H. Smith, J. Tennyson, R. N. Tolchenov, R. A. Toth, J. Vander Auwera, P. Varanasi, and G. Wagner (2005a), The HITRAN 2004 molecular spectroscopic database, *J. Quant. Spectrosc. Radiat. Transfer*, *96*, 139-204.

Rothman, L. S., N. Jacquinet-Husson, C. Boulet, and A. M. Perrin (2005b), History and future of the molecular spectroscopic databases, *Molecular spectroscopy and planetary atmospheres*, *6*, 897-907.

Ruth, S. L., J. J. Remedios, B. N. Lawrence, and F. W. Taylor (1994), Measurements of N_2O by the UARS Improved Stratospheric and Mesospheric Sounder during the Early Northern Winter 1991/92, *J. Atmos. Sci.*, *51*, 2818-2833.

Saiz-Lopez, A., K. Chance, X. Liu, T. P. Kurosu, and S. P. Sander (2007a), First observations of iodine oxide from space, *Geophys. Res. Lett.*, *34*, L12812, doi:10.1029/2007GL030111.

Saiz-Lopez, A., A. S. Mahajan, R. A. Salmon, S. J. B. Bauguitte, A. E. Jones, H. K. Roscoe, and J. M. C. Plane (2007b), Boundary layer halogens in coastal Antarctica, *Science*, *317*, 348-351.

Salawitch, R. J., T. Canty, T. Kurosu, K. Chance, Q. Liang, A. da Silva, S. Pawson, J. E. Nielsen, J. M. Rodriguez, P. K. Bhartia, X. Liu, L. G. Huey, J. Liao, R. E. Stickel, D. J. Tanner, J. E. Dibb, W. R. Simpson, D. Donohoue, A. Weinheimer, F. Flocke, D. Knapp, D. Montzka, J. A. Neuman, J. B. Nowak, T. B. Ryerson, S. Oltmans, D. R. Blake, E. L. Atlas, D. E. Kinnison, S. Tilmes, L. L. Pan, F. Hendrick, M. Van Roozendael, K. Kreher, P. V. Johnston, R. S. Gao, B. Johnson, T. P. Bui, G. Chen, R. B. Pierce, J. H. Crawford, and D. J. Jacob (2010), A new interpretation of total column BrO during Arctic spring, *Geophys. Res. Lett.*, *37*, L21805, doi:10.1029/2010GL043798.

Sander, S. P., R. R. Friedl, J. R. Barker, D. M. Golden, M. J. Kurylo, P. H. Wine, J. Abbatt, J. B. Brukholder, C. E. Kolb, G. K. Moortgat, R. E. Huie, and V. L. Orkin (2009), Chemical Kinetics and Photochemical Data for Use in Atmospheric Studies Evaluation Number 16, 1-523 pp, JPL Publication 09-31, Jet Propulsion Laboratory, California Institude of Technology, Pasadena, California.

Sander, S. P., R. R. Friedl, J. R. Barker, D. M. Golden, M. J. Kurylo, P. H. Wine, J. Abbatt, J. B. Brukholder, C. E. Kolb, G. K. Moortgat, R. E. Huie, and V. L. Orkin (2011), Chemical Kinetics and Photochemical Data for Use in Atmospheric Studies Evaluation Number 17, 1-684 pp, JPL Publication 10-6, Jet Propulsion Laboratory, California Institude of Technology, Pasadena, California.

Sander, S. P., R. R. Friedl, D. M. Golden, M. J. Kurylo, G. K. Moortgat, H. Keller-Rudek, P. H. Wine, A. R. Ravishankar, C. E. Kolb, M. J. Molina, B. J. Finlayson-Pitts, R. E. Huie, and V. L. Orkin (2006), Chemical Kinetics and Photochemical Data for Use in Atmospheric Studies Evaluation Number 15, 1-523 pp, JPL Publication 06-2, Jet Propulsion Laboratory, California Institude of Technology, Pasadena, California.

Sarkissian, A., J. P. Pommereau, and F. Goutail (1991), Identification of Polar Stratospheric Clouds from the Ground by Visible Spectrometry, *Geophys. Res. Lett.*, *18*, 779-782.

Savastiouk, V., and C. T. McElroy (2005), Brewer spectrophotometer total ozone measurements made during the 1998 Middle Atmosphere Nitrogen Trend Assessment (MANTRA) campaign, *Atmos.-Ocean*, *43*, 315-324, doi:10.3137/ao.430403.

Scherhag, R. (1952), Die explosionsartigen Stratosphärenerwärmungen des Spätwinters, *Ber. Dtsch. Wetterdienst (US Zone)*, *6*, 51-63.

Schiller, C., and A. Wahner (1996), Stratospheric OClO measurements as a poor quantitative indicator of chlorine activation - Comment, *Geophys. Res. Lett.*, *23*, 1053-1054.

Schiller, C., A. Wahner, U. Platt, H. P. Dorn, J. Callies, and D. H. Ehhalt (1990), Near UV Atmospheric Absorption-Measurements of Column Abundances During Airborne Arctic Stratospheric Expedition, January - February 1989. 2: OClO Observations, *Geophys. Res. Lett.*, *17*, 501-504.

Schofield, R. (2003), The Vertical Distribution of Atmospheric BrO from Ground-Based Measurements, PhD Thesis, University of Auckland, Auckland, New Zealand.

Schofield, R., B. J. Connor, K. Kreher, P. V. Johnston, and C. D. Rodgers (2004a), The retrieval of profile and chemical information from ground-based UV-visible spectroscopic measurements, *J. Quant. Spectrosc. Radiat. Transfer*, *86*, 115-131.

Schofield, R., P. V. Johnston, A. Thomas, K. Kreher, B. J. Connor, S. Wood, D. Shooter, M. P. Chipperfield, A. Richter, R. von Glasow, and C. D. Rodgers (2006), Tropospheric and stratospheric BrO columns over Arrival Heights, Antarctica, 2002, *J. Geophys. Res.*, *111*.

Schofield, R., K. Kreher, B. J. Connor, P. V. Johnston, A. Thomas, D. Shooter, M. P. Chipperfield, C. D. Rodgers, and G. H. Mount (2004b), Retrieved tropospheric and stratospheric BrO columns over Lauder, New Zealand, *J. Geophys. Res.*, *109*, D14304, doi:10.1029/2003JD004463.

Schonhardt, A., A. Richter, F. Wittrock, H. Kirk, H. Oetjen, H. K. Roscoe, and J. P. Burrows (2008), Observations of iodine monoxide columns from satellite, *Atmos. Chem. Phys.*, *8*, 637-653.

Sessler, J., M. P. Chipperfield, J. A. Pyle, and R. Toumi (1995), Stratospheric OClO measurements as a poor quantitative indicator of chlorine activation, *Geophys. Res. Lett.*, *22*, 687-690.

Sessler, J., M. P. Chipperfield, J. A. Pyle, and R. Toumi (1996), Stratospheric OClO measurements as a poor quantitative indicator of chlorine activation - Reply, *Geophys. Res. Lett.*, *23*, 1055-1055.

Shaw, G. E. (1978), Sky radiance during a total solar eclipse - theoretical-model, *Appl. Opt.*, *17*, 272-276.

Shepherd, T. G. (2003), Large-Scale Atmospheric Dynamics for Atmospheric Chemists, *Chemical Reviews*, *103*, 4509-4531.

Shepherd, T. G. (2007), Dynamics, Stratospheric Ozone, and Climate Change, *Atmos.-Ocean*, *46*, 117-138, doi:10.3137/ao.460106.

Sica, R. J., M. R. M. Izawa, K. A. Walker, C. Boone, S. V. Petelina, P. S. Argall, P. Bernath, G. B. Burns, V. Catoire, R. L. Collins, W. H. Daffer, C. De Clercq, Z. Y. Fan, B. J. Firanski, W. J. R. French, P. Gerard, M. Gerding, J. Granville, J. L. Innis, P. Keckhut, T. Kerzenmacher, A. R. Klekociuk, E. Kyro, J. C. Lambert, E. J. Llewellyn, G. L. Manney, I. S. McDermid, K. Mizutani, Y. Murayama, C. Piccolo, P. Raspollini, M. Ridolfi, C. Robert, W. Steinbrecht, K. B. Strawbridge, K. Strong, R. Stuebi, and B. Thurairajah (2008), Validation of the Atmospheric Chemistry Experiment (ACE) version 2.2 temperature using ground-based and space-borne measurements, *Atmos. Chem. Phys.*, *8*, 35-62, doi:10.5194/acp-8-35-2008.

Simpson, W. R., D. Carlson, G. Honninger, T. A. Douglas, M. Sturm, D. Perovich, and U. Platt (2007a), First-year sea-ice contact predicts bromine monoxide (BrO) levels at Barrow, Alaska better than potential frost flower contact, *Atmos. Chem. Phys.*, *7*, 621-627.

Simpson, W. R., R. von Glasow, K. Riedel, P. Anderson, P. Ariya, J. Bottenheim, J. Burrows, L. J. Carpenter, U. Friess, M. E. Goodsite, D. Heard, M. Hutterli, H. W. Jacobi, L. Kaleschke, B. Neff, J. Plane, U. Platt, A. Richter, H. Roscoe, R. Sander, P. Shepson, J. Sodeau, A. Steffen, T.

Wagner, and E. Wolff (2007b), Halogens and their role in polar boundary-layer ozone depletion, *Atmos. Chem. Phys.*, *7*, 4375-4418.

Sinnhuber, B. M., R. Muller, J. Langer, H. Bovensmann, V. Eyring, U. Klein, J. Trentmann, J. P. Burrows, and K. F. Kunzi (1999), Interpretation of mid-stratospheric Arctic ozone measurements using a photochemical box-model, *J. Atmos. Chem.*, *34*, 281-290.

Sinnhuber, B. M., N. Sheode, M. Sinnhuber, M. P. Chipperfield, and W. Feng (2009), The contribution of anthropogenic bromine emissions to past stratospheric ozone trends: a modelling study, *Atmos. Chem. Phys.*, *9*, 2863-2871.

Solomon, S., R. R. Garcia, and A. R. Ravishankara (1994), On the Role of Iodine in Ozone Depletion, *J. Geophys. Res.*, *99*, 20491-20499.

Solomon, S., R. R. Garcia, F. S. Rowland, and D. J. Wuebbles (1986), On the Depletion of Antarctic Ozone, *Nature*, *321*, 755-758.

Solomon, S., G. H. Mount, R. W. Sanders, R. O. Jakoubek, and A. L. Schmeltekopf (1988), Observations of the Nighttime Abundance of OClO in the Winter Stratosphere Above Thule, Greenland, *Science*, *242*, 550-555.

Solomon, S., R. W. Sanders, M. A. Carroll, and A. L. Schmeltekopf (1989), Visible and Near-Ultraviolet Spectroscopy at Mcmurdo Station, Antarctica.5. Observations of the Diurnal-Variations of BrO and OClO, *J. Geophys. Res.*, *94*, 11393-11403.

Solomon, S., A. L. Schmeltekopf, and R. W. Sanders (1987), On the interpretation of zenith sky absorption measurements, *J. Geophys. Res.*, *92*, 8311-8319.

Starr, W. L., R. A. Craig, M. Loewenstein, and M. E. McGhan (1980), Measurements of NO, O_3, and temperature at 19.8 km during the total solar elipse of 26 February 1979, *Geophys. Res. Lett.*, *7*, 553-555.

Stolarski, R. S., and R. J. Cicerone (1974), Stratospheric Chlorine - Possible Sink for Ozone, *Can. J. Chem.-Rev. Can. Chim.*, *52*, 1610-1615.

Strahan, S. E., B. N. Duncan, and P. Hoor (2007), Observationally derived transport diagnostics for the lowermost stratosphere and their application to the GMI chemistry and transport model, *Atmos. Chem. Phys.*, *7*, 2435-2445.

Strong, K., G. Bailak, D. Barton, M. R. Bassford, R. D. Blatherwick, S. Brown, D. Chartrand, J. Davies, J. R. Drummond, P. F. Fogal, E. Forsberg, R. Hall, A. Jofre, J. Kaminski, J. Kosters, C. Laurin, J. C. McConnell, C. T. McElroy, A. McLinden, S. M. L. Melo, K. Menzies, C. Midwinter, F. J. Murcray, C. Nowlan, J. R. Olson, B. M. Quine, V. Savastiouk, B. Solheim, D. Sommerfeldt, A. Ullberg, S. Werchohlad, H. Wu, and D. Wunch (2005), MANTRA - A balloon mission to study the odd-nitrogen budget of the stratosphere, *Atmos.-Ocean*, *43*, 283-299.

Stutz, J., and U. Platt (1993), Problems in using diode arrays for open path DOAS measurements of atmospheric species, *Proceedings at SPIE*, *1715*, 329-340, doi:10.1117/12.140192.

Sung, K., R. Skelton, K. A. Walker, C. D. Boone, D. Fu, and P. F. Bernath (2007), N_2O and O_3 arctic column amounts from PARIS-IR observations: Retrievals, characterization, and error analysis, *J. Quant. Spectrosc. Radiat. Transfer*, *107*, 385-406.

Tarasick, D. W., and J. W. Bottenheim (2002), Surface ozone depletion episodes in the Arctic and Antarctic from historical ozonesonde records, *Atmos. Chem. Phys.*, *2*, 197-205.

Tarasick, D. W., V. E. Fioletov, D. I. Wardle, J. B. Kerr, and J. Davies (2005), Changes in the vertical distribution of ozone over Canada from ozonesondes: 1980-2001, *J. Geophys. Res.*, *110*, D02304, doi:10.1029/2004JD004643.

Tegtmeier, S., M. Rex, I. Wohltmann, and K. Kruger (2008), Relative importance of dynamical and chemical contributions to Arctic wintertime ozone, *Geophys. Res. Lett.*, *35*, L17801, doi:10.1029/2008GL034250.

Tétard, C., D. Fussen, C. Bingen, N. Capouillez, E. Dekemper, N. Loodts, N. Mateshvili, F. Vanhellemont, E. Kyrola, J. Tamminen, V. Sofieva, A. Hauchecorne, F. Dalaudier, J. L. Bertaux, O. F. d'Andon, G. Barrot, M. Guirlet, T. Fehr, and L. Saavedra (2009), Simultaneous measurements of OClO, NO_2 and O_3 in the Arctic polar vortex by the GOMOS instrument, *Atmos. Chem. Phys.*, *9*, 7857-7866.

Thieblemont, R., N. Huret, Y. J. Orsolini, A. Hauchecorne, and M. A. Drouin (2011), Frozen-in anticyclones occurring in polar Northern Hemisphere during springtime: Characterization, occurrence and link with quasi-biennial oscillation, *J. Geophys. Res.*, *116*.

Toon, G. C. (1991), The JPL MkIV Interferometer, *Optical Photonics News*, *2*, 19-21.

Tornkvist, K. K., D. W. Arlander, and B. M. Sinnhuber (2002), Ground-based UV measurements of BrO and OClO over Ny-Alesund during winter 1996 and 1997 and Andoya during winter 1998/99, *J. Atmos. Chem.*, *43*, 75-106.

Tung, K. K., M. K. W. Ko, J. M. Rodriguez, and N. D. Sze (1986), Are Antarctic Ozone Variations a Manifestation of Dynamics or Chemistry, *Nature*, *322*, 811-814.

Van Roozendael, M., and F. Hendrick (2012), Recommendations for NO2 column retrieval from NDACC zenith-sky UV-VIS spectrometers, edited, pp. 1-7, Belgian Institute for Space Aeronomy (BIRA-IASB).

Vandaele, A. C., C. Fayt, F. Hendrick, C. Hermans, F. Humbled, M. Van Roozendael, M. Gil, M. Navarro, O. Puentedura, M. Yela, G. Braathen, K. Stebel, K. Tornkvist, P. Johnston, K. Kreher, F. Goutail, A. Mieville, J. P. Pommereau, S. Khaikine, A. Richter, H. Oetjen, F. Wittrock, S. Bugarski, U. Friess, K. Pfeilsticker, R. Sinreich, T. Wagner, G. Corlett, and R. Leigh (2005), An intercomparison campaign of ground-based UV-visible measurements of NO_2, BrO, and OClO slant columns: Methods of analysis and results for NO_2, *J. Geophys. Res.*, *110*, D08305, doi:10.1029/2004JD005423.

Vandaele, A. C., C. Hermans, P. C. Simon, M. Carleer, R. Colin, S. Fally, M. F. Merienne, A. Jenouvrier, and B. Coquart (1998), Measurements of the NO_2 absorption cross-section from 42 000 cm^{-1} to 10 000 cm^{-1} (238-1000 nm) at 220 K and 294 K, *J. Quant. Spectrosc. Radiat. Transfer*, *59*, 171-184.

Vandaele, A. C., C. Hermans, P. C. Simon, M. VanRoozendael, J. M. Guilmot, M. Carleer, and R. Colin (1996), Fourier transform measurement of NO_2 absorption cross-section in the visible range at room temperature, *J. Atmos. Chem.*, *25*, 289-305.

Vaughan, G., H. K. Roscoe, L. M. Bartlett, F. M. Oconnor, A. Sarkissian, M. VanRoozendael, J. C. Lambert, P. C. Simon, K. Karlsen, B. A. K. Hoiskar, D. J. Fish, R. L. Jones, R. A. Freshwater, J. P. Pommereau, F. Goutail, S. B. Andersen, D. G. Drew, P. A. Hughes, D. Moore, J. Mellqvist, E. Hegels, T. Klupfel, F. Erle, K. Pfeilsticker, and U. Platt (1997), An intercomparison of ground-based UV-visible sensors of ozone and NO_2, *J. Geophys. Res.*, *102*, 1411-1422.

Veefkind, J. P., J. R. de Haan, E. J. Brinksma, M. Kroon, and P. F. Levelt (2006), Total ozone from the Ozone Monitoring Instrument (OMI) using the DOAS technique, *IEEE Trans. Geosci. Remote Sensing*, *44*, 1239-1244.

Veefkind, P., and M. Sneep (2009), OMDOA03 README FILE, <*http://disc.sci.gsfc.nasa.gov/Aura/data-holdings/OMI/documents/v003/OMDOAO3_README_V003.shtml*>.

Vogt, R., P. J. Crutzen, and R. Sander (1996), A mechanism for halogen release from sea-salt aerosol in the remote marine boundary layer, *Nature*, *383*, 327-330.

Voulgarakis, A., X. Yang, and J. A. Pyle (2009), How different would tropospheric oxidation be over an ice-free Arctic? *Geophys. Res. Lett.*, *36*, L23807, doi:10.1029/2009GL040541.

Wagner, T., O. Ibrahim, R. Sinreich, U. Friess, R. von Glasow, and U. Platt (2007), Enhanced tropospheric BrO over Antarctic sea ice in mid winter observed by MAX-DOAS on board the research vessel Polarstern, *Atmos. Chem. Phys.*, *7*, 3129-3142.

Wagner, T., C. Leue, M. Wenig, K. Pfeilsticker, and U. Platt (2001), Spatial and temporal distribution of enhanced boundary layer BrO concentrations measured by the GOME instrument aboard ERS-2, *J. Geophys. Res.*, *106*, 24225-24235.

Wagner, T., C. Otten, K. Pfeilsticker, I. Pundt, and U. Platt (2000), DOAS moonlight observation of atmospheric NO_3 in the Arctic winter, *Geophys. Res. Lett.*, *27*, 3441-3444.

Wagner, T., C. von Friedeburg, M. Wenig, C. Otten, and U. Platt (2002), UV-visible observations of atmospheric O_4 absorptions using direct moonlight and zenith-scattered sunlight

for clear-sky and cloudy sky conditions, *J. Geophys. Res.*, *107*, 4424, doi:10.1029/2001JD001026.

Wahner, A., G. S. Tyndall, and A. R. Ravishankara (1987), Absorption cross-sections for OClO as a function of temperature in the wavelength range 240-480 nm, *J. Phys. Chem.*, *91*, 2734-2738.

Wamsley, P. R., J. W. Elkins, D. W. Fahey, G. S. Dutton, C. M. Volk, R. C. Myers, S. A. Montzka, J. H. Butler, A. D. Clarke, P. J. Fraser, L. P. Steele, M. P. Lucarelli, E. L. Atlas, S. M. Schauffler, D. R. Blake, F. S. Rowland, W. T. Sturges, J. M. Lee, S. A. Penkett, A. Engel, R. M. Stimpfle, K. R. Chan, D. K. Weisenstein, M. K. W. Ko, and R. J. Salawitch (1998), Distribution of halon-1211 in the upper troposphere and lower stratosphere and the 1994 total bromine budget, *J. Geophys. Res.*, *103*, 1513-1526.

Weatherhead, E. C., and S. B. Andersen (2006), The search for signs of recovery of the ozone layer, *Nature*, *441*, 39-45.

Wilmouth, D. M., T. F. Hanisco, N. M. Donahue, and J. G. Anderson (1999), Fourier Transform Ultraviolet Spectroscopy of the A 2Π3/2 ← X 2Π3/2 Transition of BrO, *J. Phys. Chem. A*, *103*, 8935-8945.

WMO (2003), Scientific Assessment of Ozone Depletion: 2002, Rep. 50, Global Ozone Research and Monitoring Project, World Meteorological Society, Geneva, Switzerland.

WMO (2007), Scientific Assessment of Ozone Depletion: 2006, Rep. 51, Global Ozone Research and Monitoring Project, World Meteorological Society, Geneva, Switzerland.

WMO (2011a), Scientific Assessment of Ozone Depletion: 2010, Rep. 52, Global Ozone Research and Monitoring Project, World Meteorological Society, Geneva, Switzerland.

WMO (2011b), Systematic Observation Requirements for Satellite-Based Data Products for Climate - 2011 Update, <*http://www.wmo.int/pages/prog/gcos/documents/SatelliteSupplement2011Update.pdf*>.

Wofsy, S. C., M. B. McElroy, and Y. L. Yung (1975), Chemistry of Atmospheric Bromine, *Geophys. Res. Lett.*, *2*, 215-218.

Wohltmann, I., R. Lehmann, and M. Rex (2010), The Lagrangian chemistry and transport model ATLAS: simulation and validation of stratospheric chemistry and ozone loss in the winter 1999/2000, *Geosci. Model Dev.*, *3*, 585-601.

Wohltmann, I., and M. Rex (2009), The Lagrangian chemistry and transport model ATLAS: validation of advective transport and mixing, *Geosci. Model Dev.*, *2*, 153-173.

Wuebbles, D., and J. S. Chang (1979), Theoretical-study of stratospheric trace species variations during a solar eclipse, *Geophys. Res. Lett.*, *6*, 179-182.

Wunch, D., C. Midwinter, J. R. Drummond, C. T. McElroy, and A. F. Bages (2006), University of Toronto's balloon-borne Fourier transform spectrometer, *Rev. Sci. Instrum.*, *77*, 093104, doi:10.1063/1.2338289.

Yang, E. S., D. M. Cunnold, R. J. Salawitch, M. P. McCormick, J. Russell, J. M. Zawodny, S. Oltmans, and M. J. Newchurch (2006), Attribution of recovery in lower-stratospheric ozone, *J. Geophys. Res.*, *111*, D17309, doi:10.1029/2005JD006371.

Yang, X., J. A. Pyle, and R. A. Cox (2008), Sea salt aerosol production and bromine release: Role of snow on sea ice, *Geophys. Res. Lett.*, *35*, L16815, doi:10.1029/2008GL034536.

Yung, Y. L., J. P. Pinto, R. T. Watson, and S. P. Sander (1980), Atmospheric Bromine and Ozone Perturbations in the Lower Stratosphere, *J. Atmos. Sci.*, *37*, 339-353.

Zerefos, C. S., D. S. Balis, C. Meleti, A. F. Bais, K. Tourpali, K. Kourtidis, K. Vanicek, F. Cappellani, U. Kaminski, T. Colombo, R. Stubi, L. Manea, P. Formenti, and M. O. Andreae (2000), Changes in surface solar UV irradiances and total ozone during the solar eclipse of August 11, 1999, *J. Geophys. Res.*, *105*, 26463-26473.

Zerefos, C. S., E. Gerasopoulos, I. Tsagouri, B. E. Psiloglou, A. Belehaki, T. Herekakis, A. Bais, S. Kazadzis, C. Eleftheratos, N. Kalivitis, and N. Mihalopoulos (2007), Evidence of gravity

waves into the atmosphere during the March 2006 total solar eclipse, *Atmos. Chem. Phys.*, *7*, 4943-4951.

Zong, Y. Q., S. W. Brown, B. C. Johnson, K. R. Lykke, and Y. Ohno (2006), Simple spectral stray light correction method for array spectroradiometers, *Appl. Opt.*, *45*, 1111-1119.

Appendices

A. Useful Dynamical Parameters

Several dynamical parameters are used throughout this work in order to assess stratospheric dynamics. The *potential vorticity* (PV) is a conserved quantity under adiabatic processes. PV is defined as

$$PV = \left(\frac{1}{\rho}\right)\eta \cdot \nabla\theta, \tag{A.1}$$

where ρ is the density and η is the absolute vorticity, a measure of rotation. The gradient of the potential temperature gives a measure of the stratification. Since PV is conserved, it is a useful quantity to follow the air-flow of parcels.

PV increases with altitude. Therefore, *scaled PV* (sPV) [*Dunkerton and Delisi*, 1986] is calculated to yield similar values at potential temperature levels throughout the stratosphere. sPV values used in this thesis were calculated by dividing PV by $\partial\theta/\partial p$, assuming that the lapse rate dT/dz is 1 K/km and the pressure at the 500-K potential temperature level is 54 hPa [*Manney et al.*, 1994]. sPV values of $1.6\text{x}10^{-4}$ s^{-1} and $1.2\text{x}10^{-4}$ s^{-1} are used to define the inner and outer vortex edges, respectively [*Manney et al.*, 2007].

Equivalent latitude (EqL) is a vortex-centred coordinate system [*Butchart and Remsberg*, 1986], for which the centre of the vortex is located at 90° EqL and the vortex edge is located at approximately 60° EqL. If there were no waves, in Northern Hemisphere winter, constant PV contours would coincide with latitude bands, with higher PV at higher latitudes. Therefore, these PV contours can be associated with an EqL. Waves cause these PV contours (and therefore EqL contours) to move away from the pole, so that they are no longer symmetric in latitude.

B. Treatment of Systematic Residuals in Ozone DSCDs

For both the UT-GBS and PEARL-GBS, intermittent systematic residuals appeared in the DOAS ozone fits. In order to quantify the impact of this residual and correct for it, DOAS analyses were performed on the data without any cross-sections, including only a third order polynomial. A clear day from summer 2007 was analyzed. Residuals from other clear-sky days, in other years, were consistent with the one selected. The residuals of this analysis were observed for near-noon SZA, to avoid contributions from atmospheric trace gases. These residuals are shown in Figure B.1 in red for the UT-GBS (panel a) and the PEARL-GBS (panel b) for the 600 gr/mm gratings. The DODs of these residuals are on the same order as twilight ozone DODs at Eureka during the summertime. Therefore, they introduce significant errors to the measurements.

In order to characterize and correct for these residuals, they were smoothed using running averages and included as cross-sections in the ozone DOAS analysis. These will be referred to as "residual cross-sections", and the magnitude of their fit will be referred to as the "residual DSCD". The DOAS ozone fits with the smallest RMS corresponded to the residual cross-sections shown in black in Figure B.1. These were calculated using a running average of 100 points (~10 nm) for the UT-GBS (panel a) and 20 points (~2 nm) for the PEARL-GBS (panel b). The PEARL-GBS residual cross-section could not be smoothed further due to the sharp peak in at 490 nm.

These residual cross-sections were fit in the ozone retrievals for the full UT-GBS and PEARL-GBS time-series 600 gr/mm datasets. They fit the entire time-series very well, indicating that the shape of the residual is constant. The residual DSCDs were scaled so that a residual DSCD of 1 corresponds to a DOD of 0.01. In order to identify the cause of these residuals, they were plotted against various parameters, such as dark current and exposure time. The largest systematic trends were observed against SZA and solar azimuth angle, as shown in Figure B.2 for UT-GBS measurements in 2007 (panel a), 2008 (panel c), 2009 (panel e), and 2010 (panel g) and for PEARL-GBS measurements in 2007 (panel b), 2008 (panel d), 2009 (panel f), and 2010 (panel h). The PEARL-GBS residual DSCDs are much larger in 2007 and 2008 than in 2009 and 2010. This may be because light-leaks to the instrument were corrected in

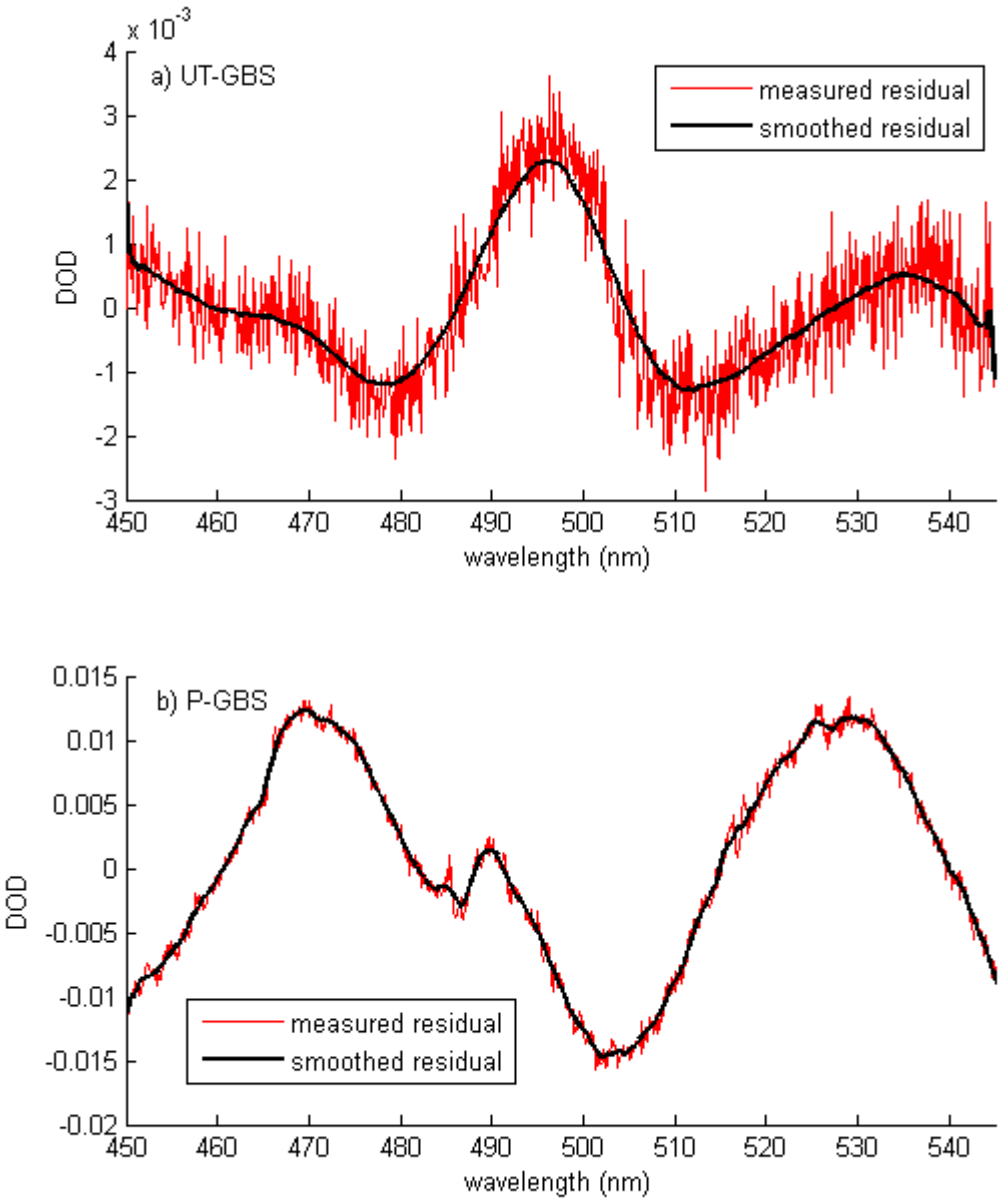

Figure B.1: Systematic residual in 600 gr/mm grating UT-GBS on (panel a) and PEARL-GBS (panel b) ozone measurements (red) and smoothed (black). The smoothed residuals were fit in the DOAS analysis.

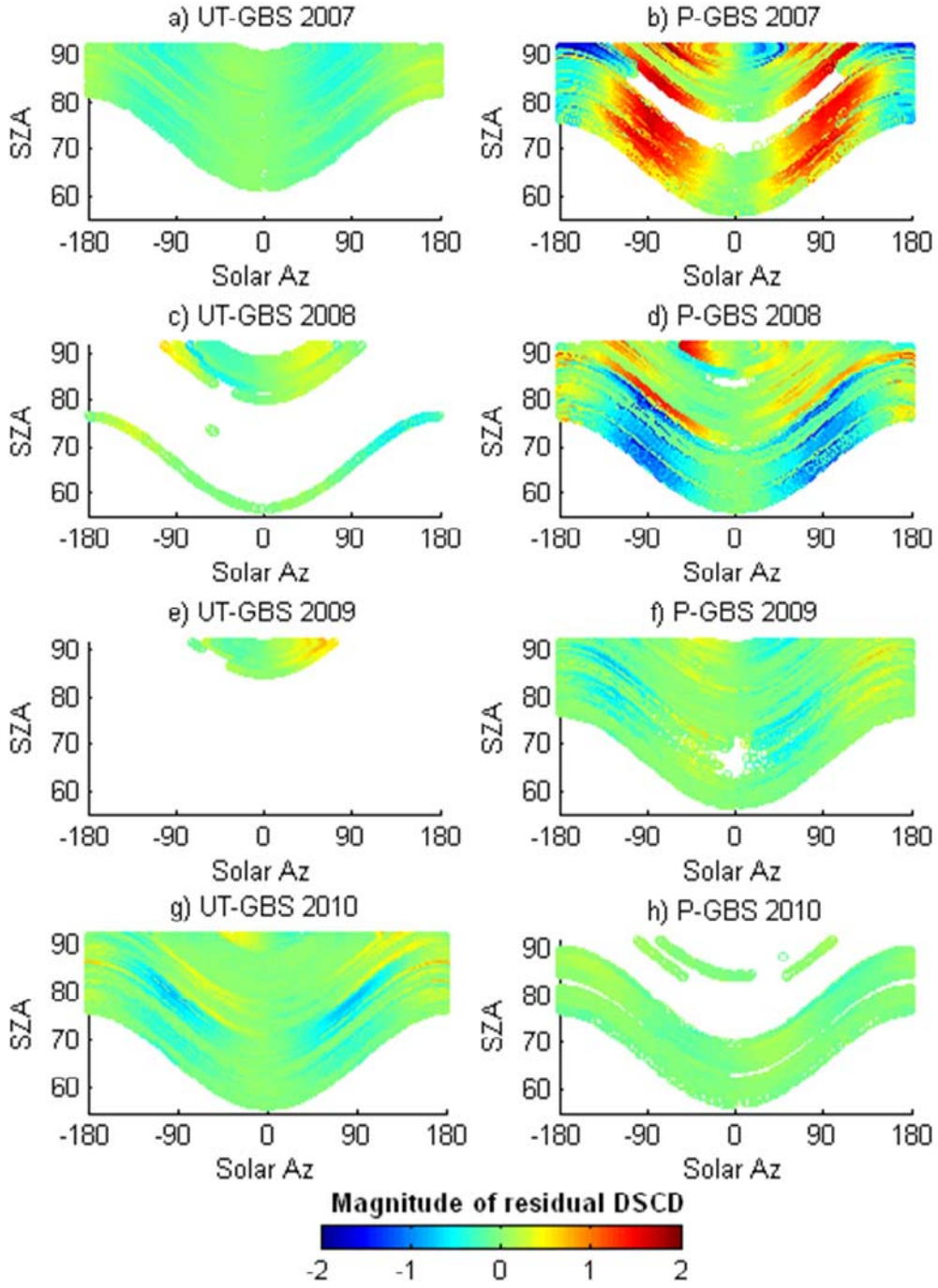

Figure B.2: Magnitude of the residual DSCD shown in colour-scale, plotted against SZA and solar azimuth angle for UT-GBS measurements in 2007 (panel a), 2008 (panel c), 2009 (panel e), and 2010 (panel g) and for PEARL-GBS measurements in 2007 (panel b), 2008 (panel d), 2009 (panel f), and 2010 (panel h).

Spring 2009, as discussed in Section 2.3.1 or because the instrument was moved and the input optics were readjusted.

For most days, there is a systematic drift in the residual strength with respect to the SZA and solar azimuth angle. The peaks (and minima) in the residual are separated by solar azimuth angles of 180°. This suggests that this error is due to polarization effects in the spectrometer. This is unexpected because polarization tests have never shown strong polarization patterns in either spectrometer [*Farahani*, 2006; *Fraser*, 2008]. Perhaps the polarization effect is a result of light entering in the instrument through light leaks. This would explain why the PEARL-GBS residual DSCDs decrease sharply in 2009, after the light-leaks were covered. Further laboratory tests of instrument polarization are required to properly quantify these problems.

Considerable effort was made to remove this residual from the spectra without including the residual in the DOAS fits. Various wavelength calibration schemes, shifts and stretches, and wavelength intervals were tested in QDOAS and did not improve the quality of the fits. Some of these methods improved results for several days, but none of them consistently improved the datasets over the full time period. By increasing the polynomial from 3 to 5, the RMS of the DOAS fits was improved, but the ozone DSCDs became unrealistic, with large negative values at twilight in summer.

Since a simple solution to this residual problem was not found, a study was performed on the UT-GBS and PEARL-GBS ozone DSCDs for days 54-59 (23-28 February) 2007 when both instruments were taking zenith-sky, 600 gr/mm measurements. Figure B.3 shows ozone DSCDs from February 2007 retrieved including (blue stars) and excluding (red circles) the residual cross-sections in the DOAS fits for the UT-GBS (panel a) and the PEARL-GBS (panel b). The difference between the retrieved DSCDs, including and excluding the residual cross-sections, is also shown for the UT-GBS (panel c) and the PEARL-GBS (panel d). The inclusion or exclusion of the residual cross-section has a small impact on the UT-GBS measurements, which may be due to the small values of the residual DSCD for the UT-GBS (panel e). This means that the UT-GBS for this time period is a good baseline for comparison with the PEARL-GBS. Contrarily, the PEARL-GBS ozone DSCDs are impacted greatly by the exclusion or inclusion of

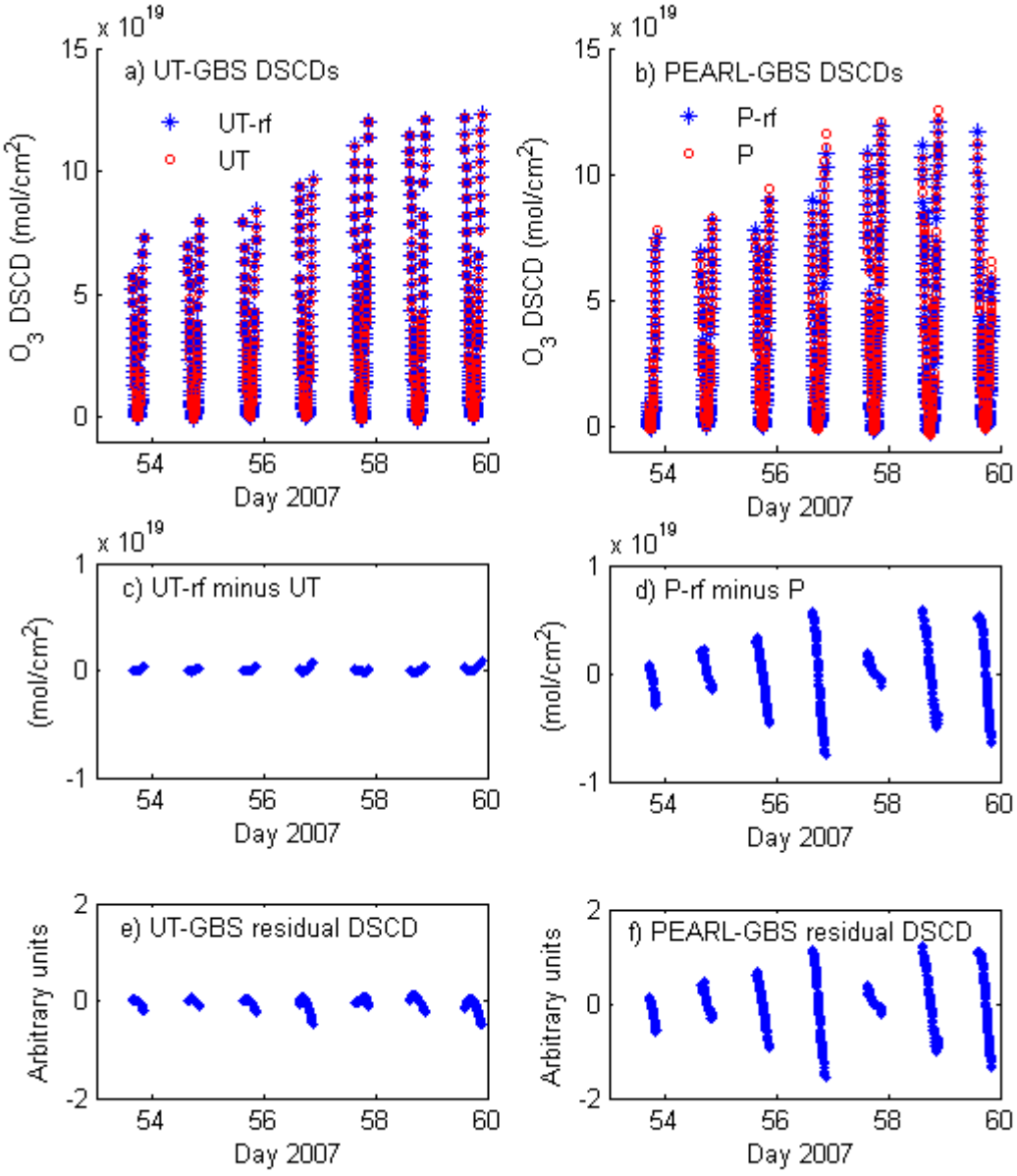

Figure B.3: Ozone DSCDs from February 2007 retrieved including (blue stars) and excluding (red circles) the residual cross-sections in the DOAS fits for (a) the UT-GBS and (b) the PEARL-GBS. The difference between the residual fit ozone DSCD and the non-residual fit DSCD for the UT-GBS (c) and PEARL-GBS (d) and the magnitude of the residual fit DSCD for the UT-GBS (e) and the PEARL-GBS (f).

the residual cross-section. This may be because the magnitude of the fit residual SCD (panel f) is very large.

In order to assess the magnitude of these effects, the UT-GBS ozone DSCDs were subtracted from the PEARL-GBS DSCDs which included the residual fit. These were all plotted against the PEARL-GBS residual DSCD and are shown in Figure B.4. The R^2 value is 0.97, indicating that the PEARL-GBS ozone values are very well correlated with the magnitude of the residual cross-section. Multiple attempts were made to reduce this correlation by building different residual cross-sections, introducing gaps in the DOAS analysis, and orthogonalizing the residual and ozone cross-sections in QDOAS. Unfortunately, none of these techniques worked. Therefore, a linear fit, with the y-intercept forced to 0 mol/cm^2 was applied to the dataset and is shown in black. PEARL-GBS ozone DSCDs from 2006-2010 were corrected by adding the slope of this line (4.4×10^{18} mol/cm^2) multiplied the magnitude of the residual DSCD for each measurement.

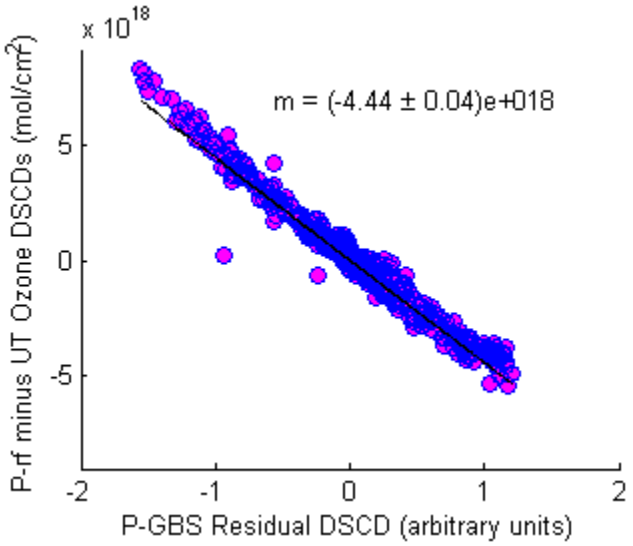

Figure B.4: PEARL-GBS ozone DSCDs retrieved including residual fit minus UT-GBS ozone DSCDs retrieved without residual fit plotted against PEARL-GBS residual DSCD (circles) and linear fit, with y-intercept forced at 0 mol/cm^2 (black line).

Since this method is unusual, the PEARL-GBS and UT-GBS DSCDs were compared extensively (see Section 4.1.4) and VCDs were validated against numerous instruments (see Chapter 5). Good agreement with other instruments was observed, suggesting that this correction method was successful. Furthermore, the magnitudes of the residual fits were taken into account during error analysis (see Section 4.3).

Similar residuals were not apparent in DOAS fits for NO_2, BrO, OClO, or HCHO. This may be because the fitting window for ozone is larger than for the other trace gases or perhaps the polarization effects are only present for wavelengths > 450 nm, for which only ozone is retrieved.

C. Instruments at Eureka

The text below describes the ground-based Eureka datasets that are used throughout this thesis.

SAOZ DOAS Instruments

SAOZ [*Pommereau and Goutail*, 1988] instruments are deployed in a global network for measurements of stratospheric trace gases and are NDACC-certified. A SAOZ instrument was deployed at the PEARL Ridge Lab during each spring for the 2005-2011 Canadian Arctic ACE Validation Campaigns. SAOZ-15 and SAOZ-7 were deployed from 2005-2009 and 2010-2011, respectively. For 2008-2009 and 2011, the SAOZ instrument took measurements outside on the roof of the PEARL Ridge Lab, while in other years the SAOZ instrument was installed inside the PEARL Ridge Lab and took measurements through a UV-visible transparent window.

SAOZ-15 and SAOZ-7 are UV-visible grating spectrometers which measure in the 270-620 nm region with 1.0 nm resolution and a 10° field-of-view. They record spectra on uncooled 1024-pixel linear diode array detectors every fifteen minutes during the day and continuously between SZA 80-95°. SAOZ-15 and SAOZ-7 were both deployed during the CINDI campaign in Cabauw, Netherlands (51.97°N, 4.93°E) [*Roscoe et al.*, 2010; *Piters et al.*, 2012] and showed excellent agreement with each other, despite slight differences in the instrument reference spectra. Therefore, the SAOZ-15 and SAOZ-7 measurements were considered as a single SAOZ throughout this thesis.

SAOZ ozone VCDs were retrieved using the settings recommended by the NDACC UV-visible working group [*Hendrick et al.*, 2011]. Ozone DSCDs were retrieved using in-house software, with a single yearly reference spectrum in the 450-550 nm window. Wavelengths were calibrated against the solar spectrum based on the reference solar atlas [*Kurucz et al.*, 1984]. The following cross-sections were all fit during the DOAS procedure: ozone measured at 223 K [*Bogumil et al.*, 2003], NO_2 measured at 220 K [*Vandaele et al.*, 1998], H_2O [converted from line parameters given in *Rothman et al.*, 2003], O_4 [*Hermans*, 2004], and Ring [*Chance and Spurr*, 1997]. DSCDs were converted to VCDs using the NDACC AMF LUTs [*Hendrick et al.*, 2011]. Daily AMFs were extracted from these LUTs based on the latitude and elevation of the PEARL Ridge Lab, day of year, sunrise or sunset conditions, wavelength, SZA, surface albedo,

and ozone SCD. A single average of monthly average reference column densities was calculated for each spring. For ozone, the estimated total error is 5.9% [*Hendrick et al.*, 2011].

SAOZ NO_2 DSCDs were retrieved using the same methods and cross-sections as for ozone, in the 410-530 nm range, with a gap from 427-433 nm. SAOZ data were analyzed with a single set of AMFs constructed from an average of summer evening composite profiles derived from POAM III (Polar Ozone and Aerosol Measurement) and SAOZ balloon measurements in the Arctic. 30% of the NO_2 in this profile is below 17 km. These SAOZ Arctic AMFs produce total columns of NO_2. For NO_2, the precision and accuracy are estimated at $1.5x10^{14}$ mol/cm^2 and 10%, respectively. When applied to the 2005-2011 Eureka measurements and added in quadrature, this yields an average 13.2% total error in NO_2. SAOZ data were provided by F. Goutail and A. Pazmino.

CANDAC Bruker FTIR

The CANDAC Bruker IFS 125HR FTIR is an NDACC-certified instrument that was installed inside the PEARL Ridge Lab in 2006 and is described in depth by *Batchelor et al.* [2009]. The Bruker FTIR records spectra on either an InSb or HgCdTe detector. A KBr beamsplitter is used and eight narrow-band interference filters cover the range of 600-4300 cm^{-1}. Solar absorption measurements consist of two to four co-added spectra recorded in both the forward and backward direction. Each measurement takes about 6 minutes and has a resolution of 0.0035 cm^{-1}. No apodization is applied to the measurements.

The Bruker FTIR ozone and NO_2 measurements are described by *Batchelor et al.* [2009] and *Lindenmaier et al.* [2010; 2011]. The SFIT2 Version 3.92c (v3.92c) algorithm [*Pougatchev et al.*, 1995] and HITRAN 2004 [*Rothman et al.*, 2005a] with updates were used in order to produce VMR profiles of the species using the optimal estimation technique. Ozone 14-52 km partial columns and total columns were retrieved in the 1000.0-1005 cm^{-1} microwindow. Ozone has uncertainties of 4.3% for total columns and 3.8% for partial columns. NO_2 17-40 km partial columns were retrieved in five microwindows between 2914.590 and 2924.925 cm^{-1} with a mean uncertainty of 15.0%. Only NO_2 partial columns for SZA smaller than 80° were included in this study, due to oscillations in the NO_2 profiles for larger SZA. Bruker data were provided by R. Lindenmaier.

Brewer spectrophotometers

Brewer spectrophotometers measure total ozone columns using direct and scattered sunlight at UV wavelengths [e.g., *Savastiouk and McElroy*, 2005]. Four Brewer spectrophotometers took measurements from 2004-2011 at both the PEARL Ridge Lab and the Eureka Weather Station. Brewers #021 and #192 are both MKIII double monochromaters, which took measurements from 2004-2011 and 2010-2011 respectively. Brewer #069, a MKV single monochromator, took measurements from 2004-2011 and Brewer #007, a MKIV single monochromator, took measurements from 2005-2011. Data were analyzed using the standard Brewer algorithm [*Lam et al.*, 2007], with small changes to the analysis parameters due to the high latitude of the measurements. The AMF was limited to be smaller than 5 instead of 3.5, which is acceptable under low ozone conditions and allows for more days with good data in the winter months. Furthermore, the ozone layer was set at 18 km instead of 22 km to better reflect Arctic conditions. For each day, ozone data from all available instruments were averaged to create one Brewer dataset. The random error in Brewer measurements is typically less than 1% [*Savastiouk and McElroy*, 2005]. Brewer data were provided by V. Savastiouk.

Ozonesondes

Ozonesondes are launched on a weekly basis from the Eureka Weather Station [*Tarasick et al.*, 2005]. During the intensive phase of the Canadian Arctic ACE Validation Campaigns 2004-2011, ozonesondes were launched daily at 23:15 UTC, while, on occasion, the launch time was altered to match a satellite measurement. Additional ozonesondes were launched as a part of Determination of Stratospheric Polar Ozone Losses (Match) campaigns. Total columns derived from ozonesondes have errors of 5% [*Tarasick et al.*, 2005]. Ozonesonde data were provided by Environment Canada.

D. Satellite Instruments

The text below describes the satellite datasets that are used throughout this thesis.

OSIRIS

OSIRIS was launched aboard the Odin spacecraft in February 2001 [*Murtagh et al.*, 2002; *Llewellyn et al.*, 2004]. It observes limb-radiance profiles with a 1-km vertical field-of-view over altitudes ranging from approximately 10-100 km, with coverage of 82.2°N to 82.2°S. The grating Optical Spectrograph measures scattered sunlight from 280-800 nm, with 1-nm spectral resolution. The OSIRIS 25-km tangent height is within 500 km of Eureka several times per day and measurements of ozone, aerosol, and NO_2 are taken during the sunlit part of the year.

The SaskMART Multiplicative Algebraic Reconstruction Technique [*Degenstein et al.*, 2009] v5.0x (v5.0.1 and v5.0.6) ozone and aerosol were used in this study. Ozone absorption information in both the UV and visible parts of the spectrum is used to retrieve number density profiles from 60 km to the cloud tops (down to a minimum of 10 km in the absence of clouds). OSIRIS ozone VMRs, calculated using European Centre for Medium-Range Weather Forecasts (ECMWF) number density and neutral density profiles, are also available. SaskMART v5.0x ozone profiles agree with those from SAGE II (Stratospheric Aerosol and Gas Experiment) to within 2% from 18-53 km [*Degenstein et al.*, 2009]. Random errors due to instrument noise in 14-52 km partial column measurements within 500 km of Eureka, calculated for a subset of the measurements, were 3.7% on average. Systematic and other errors are expected to be on the same order as the instrument noise. SaskMART aerosol extinction at 750 nm [*Bourassa et al.*, 2007] is retrieved with an assumed height profile and particle size distribution. OSIRIS aerosol agrees with SAGE II and SAGE III measurements to within 15% for the lower stratosphere [*Bourassa et al.*, 2012].

For NO_2, the v3.0 Optimal Estimation data product was used. NO_2 slant column densities (SCDs) are retrieved using the DOAS technique in the 435-451 nm range. These SCDs are converted to number density profiles from 10-46 km using an optimal estimation inversion, with high response for 15-42 km [*Brohede et al.*, 2008]. OSIRIS NO_2 VMRs, calculated from ECMWF number density and neutral density profiles, are also available. The precision of these

measurements is 16% between 15-25 km and 6% between 25-35 km based on comparisons with other instruments [*OSIRIS*, 2011]. The average random error in 17-40 km NO_2 partial columns within 500 km of Eureka was 6.8%.

Zonally averaged BrO profiles were retrieved with the DOAS technique in the 346.0-376.6 nm wavelength range [*McLinden et al.*, 2010]. Profiles were retrieved for 16-36 km using an optimal estimation inversion, with *a priori* profiles constructed using a photochemical model [*McLinden et al.*, 2000]. Profiles have a precision of ~30% and vertical resolution of ~3-5 km through most of the retrieval range.

ACE-FTS and ACE-MAESTRO

ACE comprises two instruments, ACE-FTS and ACE-MAESTRO, aboard the Canadian Space Agency's SCISAT-1, a solar occultation satellite launched in August 2003 [*Bernath et al.*, 2005]. SCISAT-1 measures above Eureka near polar sunrise (February-March) and polar sunset (September-October). ACE data are available at http://www.ace.uwaterloo.ca/.

The ACE-FTS is a high-resolution (0.02 cm^{-1}) infrared FTS instrument, operating from 750-4400 cm^{-1}, which measures more than 30 different atmospheric species. Based on a detailed CO_2 analysis, pressure and temperature profiles are calculated from the spectra using a global nonlinear least squares fitting algorithm. Then VMR profiles are retrieved, also using a nonlinear least squares fitting algorithm. ACE-FTS v2.2 data with the ozone update [*Boone et al.*, 2005] as well as preliminary v3.0 data were included in this study.

ACE-MAESTRO is a UV-visible-near-IR double spectrograph, with a resolution of 1.5-2.5 nm, and a wavelength range of 270-1040 nm [*McElroy et al.*, 2007]. ACE-MAESTRO v1.2 visible ozone update and UV NO_2 were used for this study. ACE-MAESTRO VMRs were converted to number densities using pressure, temperature, and density information from the ACE-FTS v2.2 data.

When ACE ozone profiles are compared with other instruments, typical relative differences of +1 to +8% are found for ACE-FTS v2.2 measurements from 16-44 km and ±10% for ACE-MAESTRO measurements from 18-40 km [*Dupuy et al.*, 2009]. For the 14-52 km ozone

partial columns used in this study, the average random errors were 1.4% for ACE-FTS v2.2, 1.6% for ACE-FTS v3.0, and 1.3% for ACE-MAESTRO.

For NO_2, ACE-FTS v2.2 and ACE-MAESTRO typically agree with other satellite measurements to within ~25% from 23-40 km, with ACE-MAESTRO measuring higher VMRs than ACE-FTS [*Kar et al.*, 2007; *Kerzenmacher et al.*, 2008]. The average random error of the 17-40 km partial columns used in this study was 3.7% for ACE-FTS v2.2, 2.7% for ACE-FTS v3.0, and 2.3% for ACE-MAESTRO.

OMI

OMI [*Levelt et al.*, 2006], on board the Earth Observing System Aura satellite, measures backscattered sunlight off of the Earth's surface at UV and visible wavelengths. OMI covers the globe daily, taking measurements in the sunlit part of the globe, with a nadir resolution which varies from 13x24 km^2 to 24-48 km^2.

OMI-DOAS ozone total columns are retrieved using an algorithm that is based on the DOAS technique [*Veefkind et al.*, 2006; *Veefkind and Sneep*, 2009]. Fits are performed in a 5 nm wide fitting window, centred at 334.1 nm. AMFs are determined using a radiative transfer model. OMDOAO3 total columns have been validated extensively against other instruments and have been shown to agree typically within 2% or better, with a slight SZA dependence at high latitudes [e.g., *McPeters et al.*, 2008 and references therein]. *Hendrick et al.* [2011] compared OMI-DOAS columns with high-latitude ground-based DOAS measurements to within ~5%. OMI-DOAS data are publically available at http://www.knmi.nl/omi.

The Dutch OMI NO_2 retrieval (DOMINO) stratospheric NO_2 product was used in this study [*Boersma et al.*, 2007; *Boersma et al.*, 2011; *Dirksen et al.*, 2011]. NO_2 SCDs are retrieved using the DOAS technique in the 405-465 nm range. SCDs are then assimilated in a CTM and assimilated stratospheric partial columns are produced. DOMINO stratospheric NO_2 agrees with ground-based measurements to within $0.3x10^{15}$ mol/cm^2 (13%) [*Dirksen et al.*, 2011]. OMI DOMINO NO_2 is available at http://www.temis.nl/airpollution/no2.html.

OMI BrO SCDs were retrieved in the 319-347.5 nm window, using a direct-fitting technique [*Chance*, 1998; *OMI*, 2008]. SCDs were converted to VCDs using AMFs calculated with a

radiative transfer model, with varying surface albedo. VCD 1σ uncertainties are estimated at ±22% based on fitting residuals and agree with ground-based instrument to 15% [*Salawitch et al.*, 2010]. OMI BrO VCDs were provided by T. Kurosu.

E. Model Datasets

The text below describes the model datasets that are used throughout this thesis.

Photochemical Model

A photochemical stacked box model [*Prather and Jaffe*, 1990; *Prather*, 1992; *McLinden et al.*, 2000] was used to calculate the diurnal variation of NO_2 and BrO throughout this thesis. This model calculates chemical changes in species through at 25 altitude-levels from 10-58 km, by solving the coupled set of chemical reactions throughout the diurnal cycle,

$$\frac{\partial c}{\partial t} = \boldsymbol{P} - \boldsymbol{L} \tag{E.1}$$

where $\partial c/\partial t$ is the rate of change of a given species, P is the production rate, and L is the loss rate. Transport is not considered in the model. Photochemical reaction rates depend on the temperature, density, ozone, and concentrations of other long-lived species and families. Temperatures and ozone can be supplied by climatologies [*Nagatani and Rosenfield*, 1993; *McPeters et al.*, 2007] or by profile measurements from, e.g., ozonesondes and satellite instruments for the case of temperature or ozone. Climatologies of N_2O and NO_y were taken from three dimensional model simulations [*Olsen et al.*, 2001] and total inorganic chlorine (Cl_y) and bromine (Br_y) were taken from tracer correlations with N_2O [*Wamsley et al.*, 1998; *Kovalenko et al.*, 2007]. Reaction rate coefficients and absorption cross-sections were taken from the JPL compendium [*Sander et al.*, 2006]. The model includes heterogeneous stratospheric aerosol chemistry, but no PSCs. Note that for the solar eclipse study (Chapter 6), an updated NO_y climatology [*Brohede et al.*, 2008] and JPL reaction rate coefficients and absorption cross-sections [*Sander et al.*, 2009] were used. With these parameters specified, all remaining species (including NO_2 and BrO) are calculated to be in a 24-hour steady state by integrating the model for 30 days, fixed to the specified Julian day and latitude. The box model has been evaluated using measurements from the JPL MkIV interferometer from 10 balloon flights between 1997-2005 [*Toon*, 1991]. Results of a comparison on the partitioning of stratospheric NOy are presented in *Brohede et al.* [2008] in which good overall agreement is found except for instances near the polar day or polar night boundary, where airmass history becomes a dominant factor.

SLIMCAT

SLIMCAT is an offline 3-D chemical transport model [*Chipperfield*, 1999]. The model runs used in this thesis are described by *Feng et al.* [2007]. Horizontal winds and temperatures were specified from ECMWF meteorological data (ERA-40 reanalysis used for 1999, operational analyses used for 2000-2011). Vertical advection was calculated using diabatic heating rates derived from a radiation scheme with improved vertical transport and age-of-air [*Chipperfield*, 2006]. The model was run on a hybrid σ-θ altitude grid, i.e., isentropic coordinates were used at higher altitudes, but were transformed smoothly to σ coordinates at lower altitudes to prevent intersection with the surface [*Konor and Arakawa*, 1997]. For this study, a model grid of 2.8°x2.8° was used, with 24 σ-θ levels from the surface to ~55 km (~2-km resolution in the lower stratosphere). Passive ozone was calculated by advecting ozone through the model without chemistry. This accounts for dynamical changes in ozone concentrations only (e.g., due to temperature). Active ozone and other trace gases can be calculated using detailed stratospheric chemistry and PSCs [*Feng et al.*, 2005], but were not used for this thesis. SLIMCAT passive ozone columns above Eureka were provided by M. Chipperfield and W. Feng.

GMI

GMI is a 3-D CTM [*Strahan et al.*, 2007] with full chemistry in the troposphere and stratosphere [*Duncan et al.*, 2007]. The GMI CTM is integrated with meteorological fields from the GEOS-5.2.0 Modern Era Retrospective-analysis for Research and Applications (MERRA) [*Rienecker et al.*, 2011]. The GMI chemical mechanism includes 125 species, with 322 thermal chemical reactions, 82 photolysis reactions, including heterogeneous reactions on aerosols and PSCs. Time-varying natural and anthropogenic emissions are included. Tropospheric processes represented in the simulation include convection, wet scavenging, dry deposition, and NO_x produced from lightning [*Allen et al.*, 2010]. The GMI-MERRA simulation is integrated at 2°x2.5° (latitude x longitude) on 72 pressure levels, ranging from the surface to 0.015 hPa. For this study, daily ozone, NO_2, and NO fields used are averages for 10:00-11:00 LT. N_2O, PV, and temperature are model 'snapshots' from 12:00 UTC. These fields are sampled at different times because it was useful to sample NO and NO_2 at the same part of the diurnal cycle throughout the globe (e.g., at a fixed LT), but N_2O was not available for those GMI data files. Profiles were

interpolated to the latitude and longitude of Eureka. Polar maps at various potential temperature levels were also produced. Global GMI data and software were provided by S. Strahan.

ATLAS

Passive ozone was calculated using the Lagrangian Chemistry and Transport Model ATLAS [*Wohltmann and Rex*, 2009; *Wohltmann et al.*, 2010]. Ozone was treated as a passive dynamical tracer with no chemistry. The passive tracer was initialized on 1 December 2010, using profiles from MLS. Meteorological data from the ECMWF ERA-Interim reanalysis are used to drive the model [*Dee et al.*, 2011]. The model resolution is approximately 150 km in the horizontal and 1-2 km in the vertical. The model uses a hybrid vertical coordinate, which is to a good approximation a potential temperature coordinate. Heating rates from the ERA-Interim reanalysis drive the vertical motion.

F. Zenith-Sky Line-of-Sight Calculations

Zenith-sky instruments sample the atmosphere along a line-of-sight which varies in latitude and longitude with altitude, SZA, solar azimuth angle, and wavelength. This appendix outlines a method for calculating the approximate line-of-sight of zenith-scattered measurements, which is used in the calculation of DMPs and the application of additional coincidence criteria.

For measurements above SZA 85°, most light is scattered at an altitude called the scattering height, as shown in Figure F.1. The radiance of sunlight in the zenith as a function of scattering height was calculated by C.A. McLinden with a radiative transfer model [*McLinden et al.*, 2002], using the methods described by *Solomon et al.* [1987].

The zenith-scattered radiance at the surface versus the scattering altitude is shown in Figure F.2a for various SZA and wavelengths. The wavelengths correspond to the GBS DSCD retrieval windows described in Section 4.1 (500 nm for ozone, 425 nm for NO_2-vis, and 365 nm for NO_2-UV). Approximate scattering heights for the various SZAs and wavelengths were

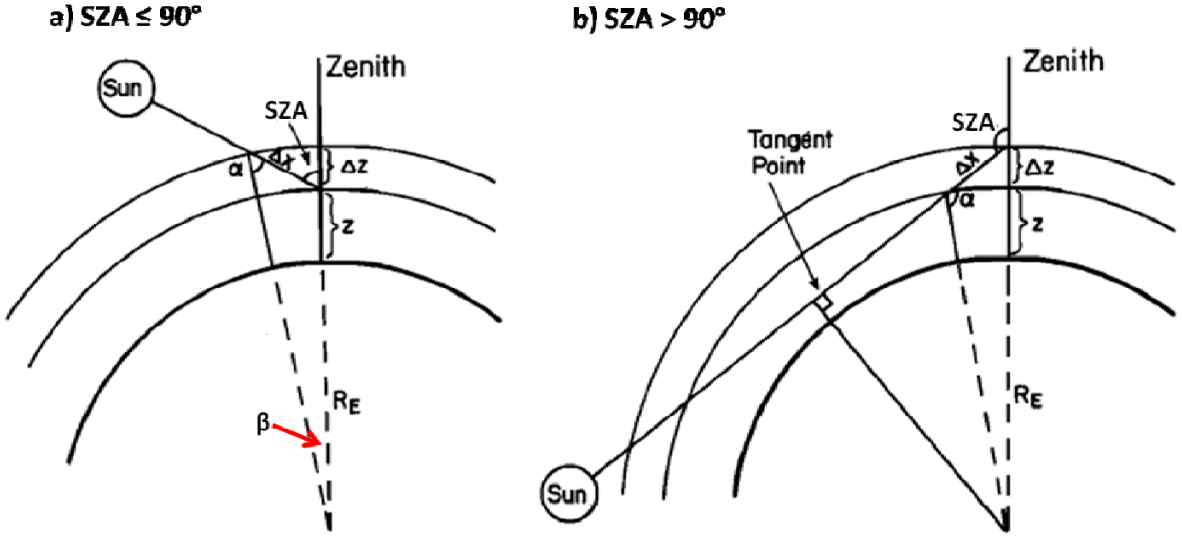

Figure F.1: Schematic of scattered light in zenith-sky viewing geometry for (a) SZA less than or equal to 90° and (b) SZA greater than 90°. Modified from *Solomon et al.* [1987].

calculated by taking the weighted means of the scattered radiances and are shown in Table F.1. The scattering height is lower for longer wavelengths and for smaller SZA, as expected.

Using the scattering height and SZA, the distance between the PEARL Ridge Lab and the ground location directly below the sampled airmass can be calculated, using the geometry in *Solomon et al.* [1987]. The latitude and longitude of the sampled airmass can then be calculated from the distance and the solar azimuth angle. The distances from the PEARL Ridge Lab are shown in Figure F.2b and vary considerably depending on the SZA, altitude, and wavelength. At an altitude of 18 km, in the lower stratosphere where spring-time ozone depletion can occur, measurements can range from directly above the PEARL Ridge Lab for NO_2-UV to 175 km for ozone. At 30 km, DOAS instruments sample airmasses up to 400 km away from the PEARL Ridge Lab.

Table F.1: Mean scattering height for zenith-sky measurements at various SZA and wavelengths.

SZA (°)	*z* (km) at 365 nm	*z* (km) at 425 nm	*z* (km) at 500 nm
86	16.1	12.4	9.8
88	19.1	15.1	11.7
90	23.5	19.5	15.6

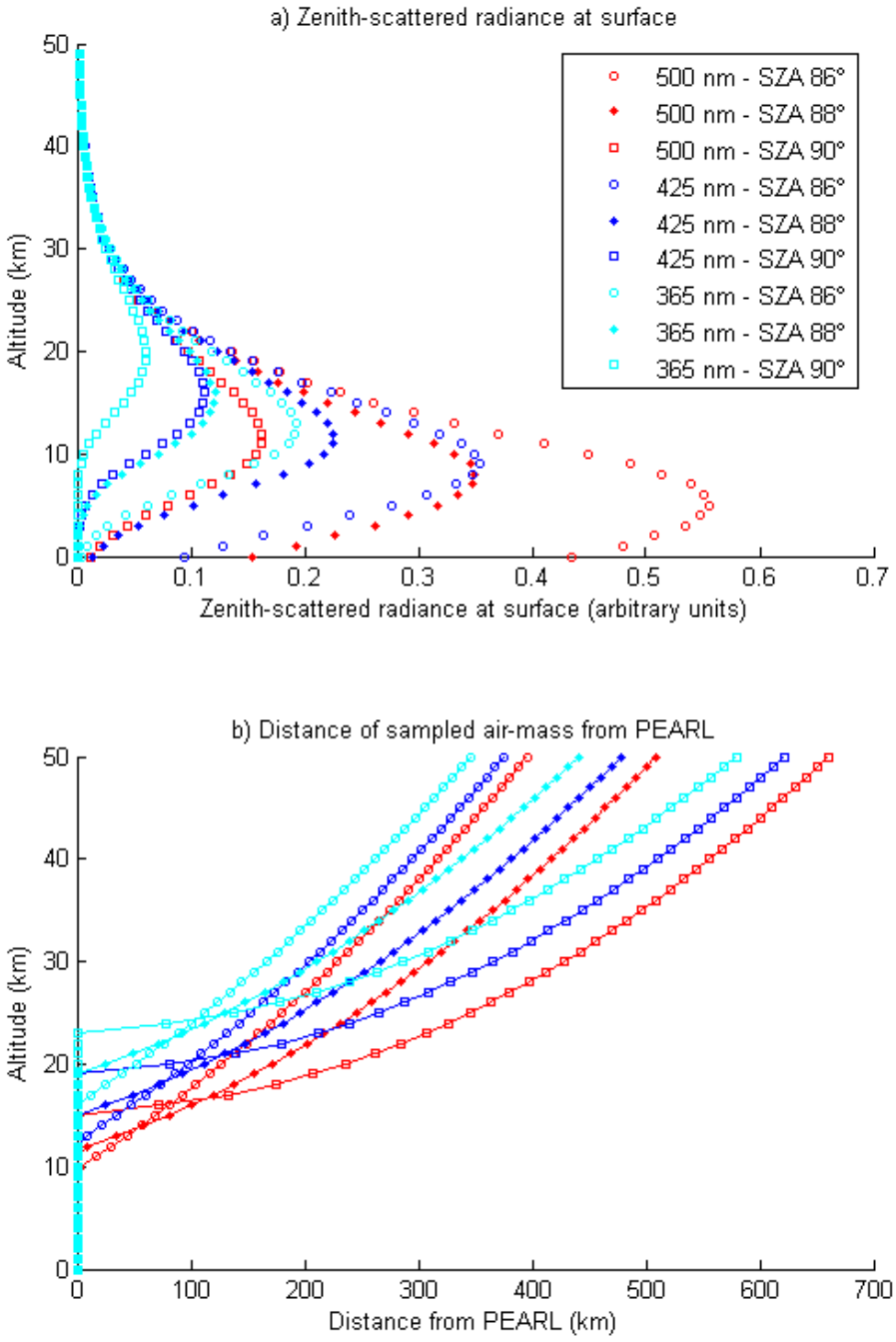

Figure F.2: Schematic of scattered light in zenith-sky viewing geometry for (a) SZA less than or equal to 90° and (b) SZA greater than 90°.